INFORMATION TO USERS

This manuscript has been reproduced from the microfilm master. UMI films the text directly from the original or copy submitted. Thus, some thesis and dissertation copies are in typewriter face, while others may be from any type of computer printer.

The quality of this reproduction is dependent upon the quality of the copy submitted. Broken or indistinct print, colored or poor quality illustrations and photographs, print bleedthrough, substandard margins, and improper alignment can adversely affect reproduction.

In the unlikely event that the author did not send UMI a complete manuscript and there are missing pages, these will be noted. Also, if unauthorized copyright material had to be removed, a note will indicate the deletion.

Oversize materials (e.g., maps, drawings, charts) are reproduced by sectioning the original, beginning at the upper left-hand corner and continuing from left to right in equal sections with small overlaps.

Photographs included in the original manuscript have been reproduced xerographically in this copy. Higher quality 6" x 9" black and white photographic prints are available for any photographs or illustrations appearing in this copy for an additional charge. Contact UMI directly to order.

Bell & Howell Information and Learning
300 North Zeeb Road, Ann Arbor, MI 48106-1346 USA

UMI®
800-521-0600

UNIVERSITY OF OKLAHOMA
GRADUATE COLLEGE

BRANCH-POINT STRUCTURE AND ENERGY LEVEL CALCULATIONS OF DIAMAGNETIC HYDROGEN USING DIMENSIONAL PERTURBATION THEORY

A Dissertation
SUBMITTED TO THE GRADUATE FACULTY
in partial fulfillment of the requirements for the
degree of
Doctor of Philosophy

By
JOHN RANDALL WALKUP
Norman, Oklahoma

2000

BRANCH-POINT STRUCTURE AND ENERGY LEVEL CALCULATIONS OF DIAMAGNETIC HYDROGEN USING DIMENSIONAL PERTURBATION THEORY

A Dissertation APPROVED FOR THE
DEPARTMENT OF PHYSICS AND ASTRONOMY

By

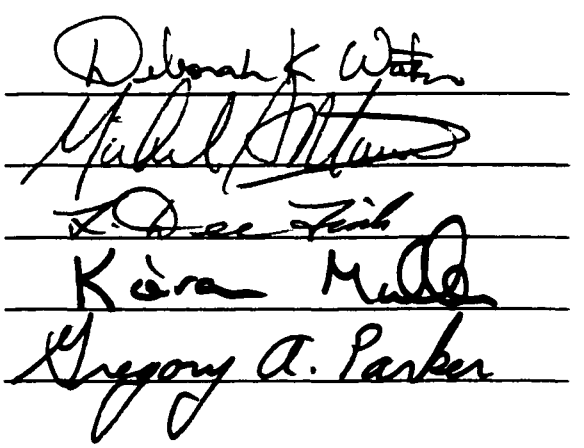

Dedication

This dissertation is dedicated to Mickie and Mikey.

Never give up.

Acknowledgements

There are many that have helped me. For moral support, my family was always there to prod me onwards. My parents, Mike and Laura Walkup, especially were always willing to do whatever they could to make my life a little more manageable during the time it took to write this thesis. My wife, despite working a full schedule, was tireless in helping raise our kids and allowing me time for performing research. As for my kids, well, they made it all worthwhile.

I have been asked by more than a few students what is most important to know about studying at the graduate level. My reply has always been the same, "Find a good advisor." I found one, and I wish to now thank Deborah Watson for raising support from the rest of the faculty to give me one last stab at a Ph.D. My gratitude goes beyond that, of course. Her support for my endeavors has been steady since the day she decided that I had what it took to complete a Ph.D. in theoretical physics.

I was also fortunate to have committee members Greg Parker, Michael Morrison, Kieran Mullen, and Dee Fink. They were always willing to do what they could to make this ordeal as smooth as possible. Kieran Mullen was especially helpful as he not only supervised my Specialist's exam but was also instrumental in developing the new numerical technique described in this dissertation. Among the rest of the faculty, John Cowan allowed me access to his computer which made parts of this research possible, Andy Feldt got me out of several jams which would have severely hindered progress, and Bruce Mason allowed a lot of flexibility when working for him which freed time to write this dissertation. There were also a few friends that I would like to mention because they provided invaluable help

whenever I needed it: Fred Brown and Ted Mansell. Without Fred's help, writing this dissertation would have been far more difficult.

There were a few others who helped in various phases of ths research. John Cowan loaned me the use of his computer on several occasions. Andy Feldt kept the machines going, and I am certainly not the only one grateful for his services. And I especially thank Bruce Mason for not only providing me with a wonderful job but also allowing me time to work on this dissertation. Manfred Bucher, of Fresno State University, was my early mentor and his encouragement helped me get here. And I certainly am not going to forget the skill in which Grettie Bondy guided me through all the academic red tape.

Finally, I want to thank a fellow member of our research group whose brilliance in theoretical physics was the driving force behind much of this research. Martin Dunn, despite having numerous personal responsibilities, managed to find time to help guide me throughout my research career. Clearly, without his expertise this dissertation would not have been possible.

Thanks again, everyone.

Contents

List Of Tables

List Of Figures

Abstract

This dissertation describes the results of research that covers two distinct areas relevant to the field of physics: atomic theory and applied numerical analysis. In the first phase of this research the avoided crossings of diamagnetic hydrogen were examined with dimensional perturbation theory, resulting in a systematic means of understanding the appearance of these avoided crossings and where they will occur in the energy spectrum. In the second phase of this research we turned our attention to the field of approximation theory, developing a more accurate technique for summing divergent perturbation series at specific values of the independent variable. The two phases of research were finally related by applying this new techique to the diamagnetic hydrogen problem, with improved convergence and accuracy when summing the perturbation energy series.

Scientific Advances in this Research

The research that comprises this dissertation has made numerous contributions to the scientific literature. This research spanned six publications, and all original research appearing in this dissertation is published in at least one of the following articles:

(A) D. K. Watson, M. Dunn, T. C. Germann, D. R. Herschbach, D. Z. Goodson, and J. R. Walkup, "Dimensional Expansions for Atomic Systems," From *New Methods in Quantum Theory*, edited by C. A. Tsipis, V. S. Popov, D. R. Herschbach, and J. Avery, NATO Conference Book, Vol. 8 (Kluwer Academic Press, Dordrecht, Holland, 1996).

(B) M. Dunn, D. K. Watson, and J. R. Walkup, "On the Behavior of Padé Approximates in the Vicinity of Avoided Crossings," *Journal of Chemical Physics* **104**, 9870, (1996).

(C) J. R. Walkup, M. Dunn, and D. K. Watson, "Avoided Crossings of Diamagnetic Hydrogen as Functions of Magnetic Field Strength and Angular Momentum," *Physical Review A* **58**, 4668 (1998).

(D) J. R. Walkup, M. Dunn, and D. K. Watson, "Branch-point Structure and the Energy Level Characterization of Avoided Crossings," *Journal of Mathematical Physics* **41**, 218 (2000).

(E) J. R. Walkup, M. Dunn, and D.K. Watson, "Local Optimization of the summation of divergent perturbation series," accepted for publication by *Journal of Mathematical Physics*.

(F) J. R. Walkup, M. Dunn, and D. K. Watson, "Energy Calculations of Low-$|m|$ Diamagnetic Hydrogen States with Dimensional Perturbation Theory," accepted for publication by *Physical Review A*.

The majority of this research is contained in the last four publications. (I have listed the above citations by an alphabetical letter, so as not to confuse the entries with those in the bibliography.)

The following advances in research form the basis of this dissertation:

- We first extended previous results of various researchers, most notably M. Dunn, D.K. Watson, T.C. Germann, and D.R. Herschbach, for calculating the energy levels and branch-point structure of diamagnetic hydrogen to the odd-parity states. These results appear in Ref. (A)

- The fact that avoided crossings appear in the energy spectrum of diamagnetic hydrogen while the magnetic quantum number m is held fixed and the field strength B is swept is well-known. However, we demonstrated in Ref. (C) that avoided crossings appear when B is held fixed and the magnetic quantum number m swept.

- Also in Ref. (C) we demonstrated that the locations of these two types of avoided crossings (that is, the avoided crossing when B is held fixed and m is swept and the avoided crossing when m is held fixed and B is swept) are intimately related.

- In this same article, by plotting the trajectories of the square-root branch points (which connect the energy levels that are attempting to cross) we established a systematic means of predicting the location of avoided crossings, even hidden avoided crossings. This technique was successful for both types of avoided crossings.

- As the field strength B is swept, the square-root branch points move on the complex-parameter plane. We established in Ref. (D) a characterization of this motion that is analytic for all field strengths, even through regions of field strength where the motion is highly non-smooth.

- Avoided crossings can range from broad avoided crossings (indicative of a very strong interaction between energy levels) to narrow avoided crossings (corresponding to a very weak interaction). In Ref. (D) we explained the broadness of avoided crossings in terms of the behavior of the square-root branch points in light of second-order, degenerate perturbation theory.

- The summing of divergent perturbation series is an important area of research in applied numerical analysis, and has important implications in perturbation theory. In Ref. (E) we developed a new numerical technique for summing divergent perturbation series at particular values of the independent variable that is a dramatic improvement over Padé summation, considered to be one of the most robust and powerful techniques available.

- The perturbation series of diamagnetic hydrogen created by dimensional perturbation theory is highly divergent for most field strengths and states. In many cases the series can still be summed to a finite, and accurate, result using Padé summation. In Ref. (F) we successfully applied this new numerical technique to the perturbation series of diamagnetic hydrogen and noted its often dramatic improvement over Padé summation.

- Because the perturbation parameter in dimensional perturbation theory is inversely proportional to $|m|$, it was commonly thought that dimensional perturbation theory would not be nearly as effective at low values of $|m|$. In Ref. (F) we demonstrated and explained why dimensional perturbation theory actually *increases* in effectiveness as $|m|$ is lowered.

- Dimensional perturbation theory is a natural for studying circular Rydberg states. In this same paper we showed that dimensional perturbation theory remains effective for highly *non-circular* states as well.

So let's get on with the show!

What the Critics are Saying about 'Branch-Point Structure'

Bomb! Lowest rating!

— L. A. Times

We are treated to one scene after another where the energy levels approach each other as if to cross, only to avoid each other at the very last moment. The first time this happens may be frightening to some readers (yeah, right!), but by the end of the dissertation all these "terrifying" confrontations come off as big yawners.

— The Daily Grad

Two thumbs down. Waaaaaaay down.

— Siskel (or Ebert)

The scene where the branch points annihilate is completely tasteless and gratuitous. Having the branch points co-exist in peace would have not changed the story line one iota, but gore is what sells these days.

— Dissertation Digest

El stink-a-roo! I hope the readers kept their receipt.

— Rex Reed

This solves the mystery of what happened to Milli Vanilli.

— The Globe

Muddled plot. Halfway through the dissertation the characters of the wave functions exchange identities, producing a puzzling mess.

— Thesis Illustrated

The quadratic $|\mathbf{B}|^2(x^2 + y^2)$ [term] is unimportant for a one-electron atom.

— J. J. Sakurai, *Modern Quantum Mechanics*.

A beautiful piece of work, destined to enchant future generations more. John Walkup has created a masterful dissertation. He's good looking, too.

— An admirer of his work who wishes to remain anonymous.

Part I

Introduction

Chapter 1

The Diamagnetic Hydrogen Problem and its Applications

Those wanting a stark contrast between the words *simple* and *easy* need look no further than the diamagnetic hydrogen problem. While simple in description — after all, it is nothing more than a hydrogen atom placed in a constant magnetic field — such a problem is certainly not easy to solve. In fact, the problem has defied all attempts at an analytic solution[8, 9, 10, 11, 12, 13, 14, 15]. At large field strengths the effects of the diamagnetic term, which is proportional to B^2, begin to have tremendous effects on the wave functions of the system. The Schrödinger equation can now no longer considered to be separable, and once the field strength reaches roughly 10^5 T the effects of the magnetic field and the Coulombic attraction between the electron and proton become comparable. At this point even minor changes in the external field strength can have drastic effects on the wave function characteristics.

Fortunately, recent progress has managed to illuminate some of the more dominate characteristics of diamagnetic hydrogen, especially in the limits of very small and very large B. In the small-field limit an approximate symmetry was discovered that allows one to meaningfully label the energy levels, even past the point where the energy levels from competing n-manifolds begin to mix. In the (very) large-field limit the system separates (at least to a good approximation) so that the motion of the electron due to the magnetic field contributions can be effectively separated from the motion due to the Coulombic attraction. In Chap. 2 we will introduce the physics of the diamagnetic hydrogen in the weak and

strong field limits. This research, however, mostly focused on the behavior of the system in the intermediate-field region. Therefore, in Part II of this dissertation, starting with Chap. 4, we begin discussing our original research on diamagnetic hydrogen in this very complicated part of the energy spectrum.

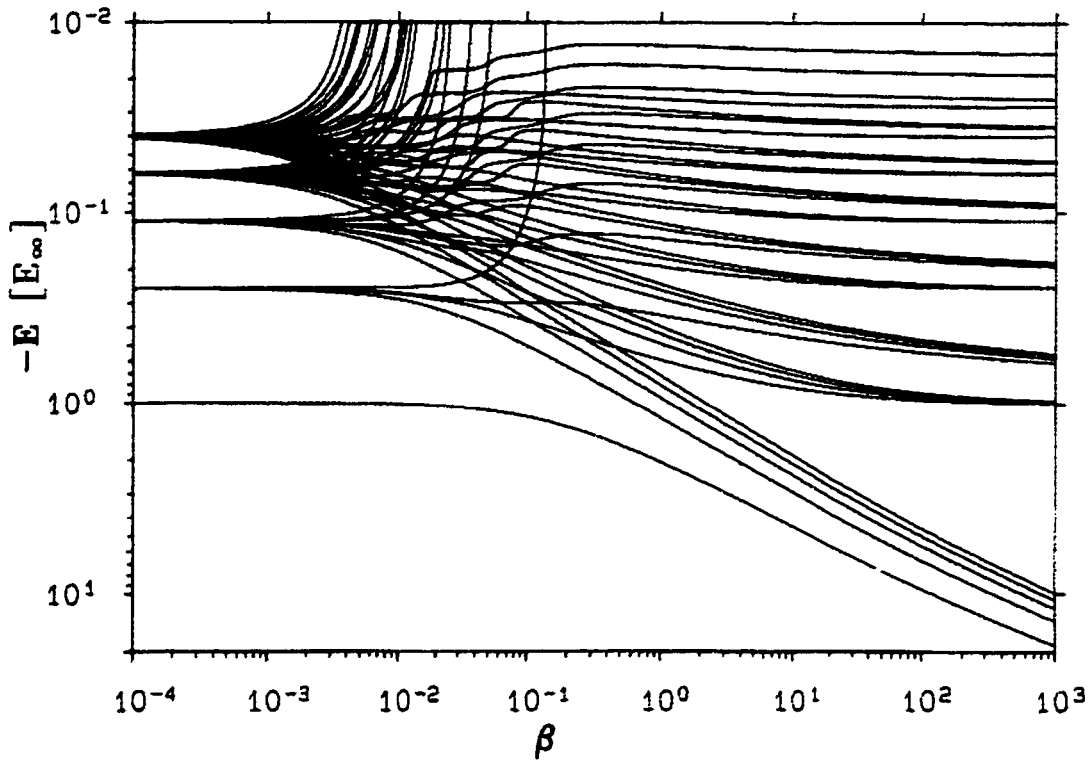

Figure 1.1: The low-lying energy spectrum of diamagnetic hydrogen calculated by Ruder *et al.*[6] In this figure $\beta = 1$ corresponds to 4.701×10^5 T. Some level crossings appear since this spectrum includes both even and odd parity states. Note the avoided crossings appearing between energy levels in the intermediate field-strength region (roughly 10^3–10^5 T). In this region, the diamagnetic hydrogen problem is particularly difficult.

1.1 How strong is "strong"?

The Hamiltonian describing a hydrogen atom in a constant, external magnetic field B can be expressed in terms of the five most frequently discussed contributions:

$$H_{\text{total}} = H_{\text{KE}} + H_{\text{Coul}} + H_{\text{SO}} + H_B + H_{B^2}\,, \tag{1.1}$$

where

- H_{KE} is the contribution from the kinetic energy of the electron,
- H_{Coul} represents the Coulombic attraction between the electron and proton,
- H_{SO} is the spin-orbit coupling of the electron,
- H_B is the linear Zeeman term, which is proportional to mB, where m is the magnetic quantum number,
- H_{B^2} is the diamagnetic term, which is proportional to $\rho^2 B^2$, where ρ is the radial distance to the electron from the z-axis.

Here, we are ignoring those contributions that are extremely weak in comparison to the above terms, such as the hyperfine structure correction and the Lamb shift. Furthermore, there are two other relativistic corrections besides the spin-orbit coupling H_{SO}, namely the Darwin term and the relativistic correction to the kinetic energy, that we are ignoring for now but are discussed in Appendix A.

In most physics textbooks the diamagnetic term, because of its inherent difficulty, is rarely discussed in great detail. (See the quote by J. J. Sakurai in the "Critical Reviews" section on p. 3.) Therefore, weak and strong fields are usually defined according to the relative strengths of the linear Zeeman term and spin-orbit coupling. A strong magnetic field is usually considered to be a field such that the linear Zeeman effect is so large that spin-orbit coupling can be treated as a small perturbation (the *Paschen-Bach effect*). Weak

fields, on the other hand, usually denote fields where the effects of the external field can be treated as a perturbation in relation to the spin-orbit coupling (it is in this region where the *anomalous Zeeman effect* becomes apparent). This is illustrated in the upper half of Fig. 1.2.

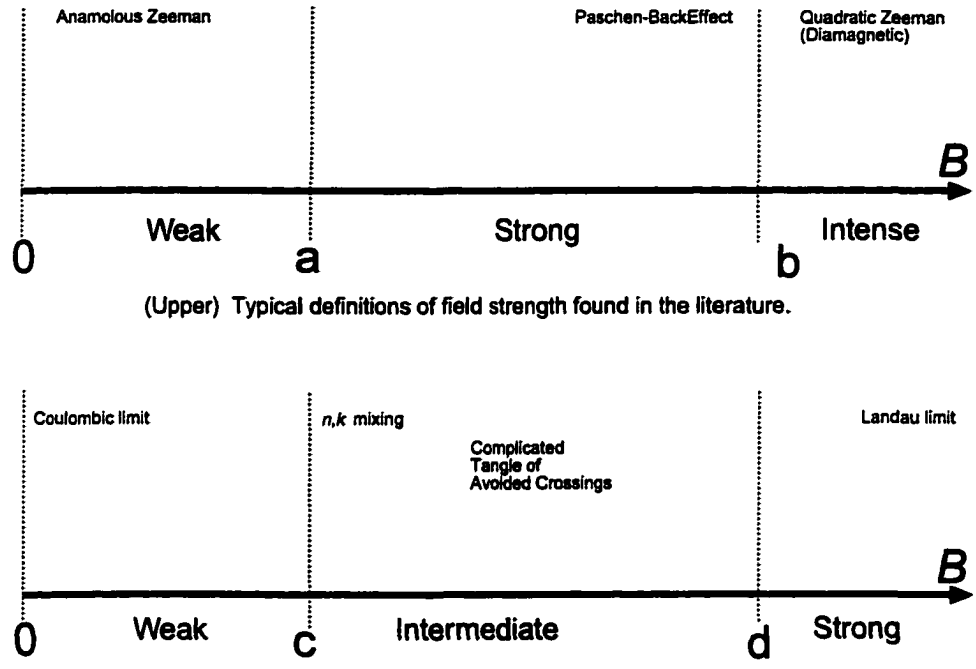

Figure 1.2: (Upper half) Typical descriptions of field strength intensity used in many quantum textbooks. The letters in the upper half refer to specific values: For (a) see Table A.2 in Appendix A. (Lower half) Descriptions of field strength intensity used in this dissertation. The value of field strength that corresponds to pt. (c) is much stronger than that corresponding to pt. (a) in the upper figure.

For a summary of the relative strengths of many of these physical effects, see Appendix A.

In this research we focus solely on the effects of the diamagnetic term, so we will describe the strength of external magnetic fields somewhat differently. Since the linear Zeeman term (which can also be defined to include the spin contribution of the electron) simply shifts the energy levels without affecting their behavior as a function of field strength, we

will largely neglect this effect. This does not imply that the energy shifts of the linear Zeeman term are so small as to be negligible. Rather, we consider the effects of the linear Zeeman term on the energy spectrum, no matter how large they may be, unimportant for the purpose of this research.

A weak field in this research is defined as being sufficiently small that energy levels belonging to different n-subspaces do not mix. Roughly, this mixing can be said to occur when the Lorentz force due to the external magnetic field is comparable to the attractive Coulombic attraction between the two particles. For the situations where the atom is either highly excited or is in a circular state (that is, when $|m|$ is maximized), then we can assume that the electron is in a roughly circular orbit and rotating around the proton at the cyclotron frequency $\omega_c = eB/m_e$. Setting the Lorentz force equal to the Coulombic force,

$$evB = \frac{ke^2}{r^2}, \tag{1.2}$$

where k is the Boltzmann constant, and noting that $v = r\omega_c = reB/m_e$ we find

$$B^2 e = \frac{kem_e}{r^3} = \frac{km_e}{a_0^3 n^6} \quad \Longrightarrow \quad B^2 = \frac{km_e}{a_0^3 n^6}. \tag{1.3}$$

From the Virial theorem for a Coulombic potential energy function we can show that

$$\left\langle \frac{1}{r^3} \right\rangle = \left\langle \frac{Z}{a_0^3 n^2} \right\rangle, \tag{1.4}$$

we get (with $Z = 1$)

$$B = \sqrt{\frac{km_e}{a_0^3}} \frac{1}{n^3} \approx \frac{235\,000}{n^3}, \tag{1.5}$$

Therefore, in Fig. 1.1 we can define

$$B_{(c)} \approx \frac{235,000}{n^3}, \quad (n \gg 1 \text{ or } n \gtrsim m). \tag{1.6}$$

The special field strength $B = 235\,000$ T will become important later, as it defines the characteristic field strength used in this research. Note that this boundary depends strongly on the energy level of the hydrogen atom, and ranges from roughly 50,000 T for first excited state ($n = 2$) down to 6 T for the excited states we are considering heavily in this research ($n = 34$). (The rules of thumb for defining weak and strong fields in this research do not really apply to the ground state, which does not undergo avoided crossings with higher-lying states, as seen in Fig. 1.1.) Clearly, for highly-excited states, extremely strong magnetic fields are *not* necessary in order to experience the complicated mixing of energy levels of diamagnetic hydrogen.

Intermediate field strengths, therefore, begin where this mixing of different energy levels begins. The onset of the strong-field region, as seen in Feg. 1.2, is gradual and difficult to define precisely. A commonly used description relies on the applicability of the *adiabatic approximation*. Qualitatively, the adiabatic approximation maintains that in sufficiently strong fields, the coupling between the ρ and z degrees of freedom becomes sufficiently weak that the frequency Ω_z of motion along the z axis due to the Coulombic attraction is so much lower than the frequency Ω_ρ along the x, y-plane due to the force of the magnetic field that the former motion can be considered to be static with respect to the latter. For highly excited states, Angelié and Deutsch[17] used a WKB approximation to derive a condition that states the adiabatic approximation is valid when

$$\frac{\Omega_z}{\Omega_\rho} \approx \frac{m_e e^2}{\hbar^3 \hat{n}^3 B} \ll 1, \tag{1.7}$$

which roughly means

$$B(T) \gg \frac{18\,000}{\hat{n}^3}, \tag{1.8}$$

where $\hat{n} = n_z + n_\rho + |m| + 1$ and n_z and n_ρ are the excitation levels (nodes) along the z-axis and x, y-plane, respectively. Unfortunately, none of the states considered in this research are sufficiently excited to where this approximation is valid. In summary, for the states considered in this research the strong-field region is not clearly defined.

1.2 Assumptions and justifications

At this point we consider which justifications we should make concerning certain interactions that may or may not be ignorable in regards to the scope of this research. Since this research is only concerned with fields on the order of roughly 10 T and above, we will only concern ourselves with those terms in the Hamiltonian that are not negligible for this region of field strengths.

1.2.1 Finite proton mass

Traditionally, the zero-field hydrogen problem is solved by assuming a separation between the internal and external coordinates of the system. However, an external magnetic field couples these two motions, and the question is now whether the center-of-mass motion can still be considered negligible.

Using a variational calculation, Virtamo and Simola demonstrated that the center-of-mass motion cannot be disregarded for astrophysically-large field strengths. However, O'Connell disagreed[99], and it was not until Wunner, Ruder, and Herold[100] examined the problem that the matter appeared to have been settled — the center-of-mass motion indeed *cannot* be disregarded for sufficiently large field strengths, such as those found on neutron stars. (See also Baye and Vincke, Ref. [82].) The greater the value of $|m|$, the more noticeable the effect — irrespective of whether the momentum of the combined system is nonzero[100]. Furthermore, for nonzero system momentum the motional Stark effect appears, as was mentioned in Sec. 1.4.2. Naturally, the extreme condition occurs with positronium in an external magnetic field, since for this system the center-of-mass is located directly between the two particles. This situation has been discussed in great detail by Schmelcher[84].

In this research we are mostly concerned with studying the underlying mathematical structure of the energy spectrum of diamagnetic hydrogen. Therefore, center-of-mass corrections have been ignored because, while they may shift the energy values a significant

amount in the strong-field limit, they do not affect the *dynamics* of the energy spectrum to a sufficient degree to warrant inclusion. At this time dimensional perturbation theory has not been applied to the problem of finite proton mass and very few theoretical calculations have been performed that incorporate these effects[100, 82, 85]. It remains an issue for future investigation.

1.2.2 Relativistic effects

By expanding each component of the electron spinor in terms of Landau orbitals (in the relativistic treatment of the diamagnetic hydrogen problem the spin-up and spin-down states are no longer uncoupled), Lindgren and Virtamo[86] transformed the Dirac equation into an infinite set of ordinary differential equations, which they then solved numerically. For the ground state in a field strength of roughly 10^9 tesla they found that the energy shifts amounted to a mere $10^{-4}\%$. However, these energy shifts become larger for higher-excited states. (Relativistic effects for motion *parallel* to the magnetic field are especially small and can almost always be ignored for field strengths below 10^{10} T, well below the field strengths considered in this research.)

We must keep in mind that relativistic effects in this research have been ignored, even though the system is certainly relativistic for sufficiently strong magnetic fields. However, we are mostly interested in examining the avoided crossings in the intermediate-field region, where relativistic corrections are minor.

1.3 The importance of the diamagnetic hydrogen problem

Until the 1970s there were few *practical* reasons to study diamagnetic hydrogen. After all, the field strengths at the point where the diamagnetic term becomes important are roughly 200, 000 T, far beyond available laboratory strengths. (For continuous field strengths, 100 T is considered to be on the fringes of what is possible with current technology, while the use of explosives can only push the field strengths over 1000 T for a few milliseconds[19, 20]).

Instead, the motivation for such research was based on the challenge of overcoming the mathematical difficulty of obtaining a complete solution. However, since then enormous field strengths have been discovered in the hydrogenic atmospheres of certain white dwarfs and neutron stars. To understand the atmospheres of both objects (examples of which are known to contain large amounts of hydrogen) an understanding of the energy spectrum of diamagnetic hydrogen is essential.[8, 9, 10, 21]

However, despite the "impossibility" of achieving sufficiently strong field strengths, natural laboratories have been created for studying the diamagnetic hydrogen problem. One way to observe the effects of the diamagnetic term is to effectively "lower" the Coulombic interaction between the electron and proton. Naturally, the charge of the electron and proton are fundamental and not variable, but in solid state physics it is possible in some situations to simulate a weak Coulombic attraction by applying a much weaker field to an electron/hole pair (exciton). In this situation, a laboratory-strength magnetic field (roughly a few tesla) can mimic the effects of a much larger field (say, roughly 10^6 T) on an isolated hydrogen atom.[22, 23, 24, 25]

Another way to produce diamagnetic hydrogen effects is to excite the electron to very large orbits so that the Coulombic interaction is relatively weak in comparison to the external field force. [This can be verified with Eq. 1.6.] In such a system, called a Rydberg state, minor changes in the magnetic field strength can have dramatic effects on the wave functions of the atom which means that, for all practical purposes, the diamagnetic term has become dominant. *Circular* Rydberg states, which are Rydberg states with the magnetic quantum number m increased to its maximal value, $m = n - 1$, have become important because they are relatively long-lived and the effects of the external field occur at even lower, laboratory-accessible, field strengths.[26, 27, 28]

The rest of this chapter discusses these applications of diamagnetic hydrogen in more detail, followed by a discussion of previous attempts to solve the problem. In Chap. 2 we

will discuss the energy level spectrum in both the weak-field limit (Sec. 2.1) and strong-field limit (Sec. 2.2).

Once the diamagnetic hydrogen problem is sufficiently discussed we begin discussing the scope of this research, which is broken into two parts: In Part I, which makes up the majority of this research, dimensional perturbation theory is applied to reveal important characteristics of the mathematical structure of the avoided crossings of diamagnetic hydrogen. Part II examines a new technique in applied numerical analysis developed in this research for summing divergent perturbation series. In the final chapter of Part II, a connection is made between these two disparate issues by applying this new numerical technique to sum the perturbation series corresponding to certain energy levels of diamagnetic hydrogen.

1.4 Applications I: Astrophysics

The presence of magnetic fields in stellar atmospheres is certainly not unusual, but for the most part such field strengths typically measure less than a tesla, well below the region of interest in this research. However, there are two main astrophysical objects, white dwarfs and neutron stars, that deserve mention here because the chemical makeup of their atmospheres and the presence of enormous magnetic field strengths are directly related to this research in diamagnetic hydrogen. Of these two astrophysical objects, white dwarfs are the most relevant to this research, and for this reason most of the following discussion is centered around white dwarfs.

1.4.1 White dwarfs

As of 1997 there were roughly 2000 known examples of white dwarfs[1] in the Universe. These astrophysical objects represent the most common end-point of stellar evolution (neutron stars and black holes being the other end-points). Most white dwarfs fall into two main

types, denoted DA and DB. Both DA and DB white dwarfs have exceptionally pure atmospheres; hydrogen for DA and helium for DB. The purity of their atmospheres is caused mainly by the lack of convectional currents (such as stellar winds, convection, and circulation) which allows the enormous gravitational field strengths, roughly 10^8 cm/s^2, to separate the elements by mass, leaving hydrogen (and helium in the case of Type DB white dwarfs) to make up essentially the entire atmosphere.

On a small number of white dwarfs the presence of magnetic fields up to 10^5 T and electric fields up to 10^9 V/m have been discovered, although all well-identified examples are confined to those with hydrogen atmospheres. The idea that large electric and magnetic field strengths exist on white dwarfs has been postulated to conserve total magnetic field flux as the radius of the star contracts, since this flux is roughly proportional to BR^2, where R is the radius of the star. As the star shrinks towards the dimension of a white dwarf the global field strength must increase quadratically.

Because the surface temperatures of white dwarfs is relatively low, and because there is an absence of convective currents, the motion of the atoms with respect to the external magnetic field is relatively unimportant. For this reason diamagnetic hydrogen research is particularly applicable to this system. There is an important complicating factor, however, from the fact that the magnetic field of a white dwarf is not uniform but rather, like the Earth's magnetic field, strengthens near the poles. This tends to broaden the spectral lines.

The large electric fields present in the atmospheres of white dwarfs are caused by free electrons and ions in the atmosphere as well, but the overwhelming contribution from these electric fields is due mainly to those components parallel to the magnetic field.[29] By including only the parallel contribution of the electric field, the azimuthal symmetry (the symmetry about the axis parallel to the magnetic field) is maintained.[30, 31] As we will now see, this is not the case for neutron stars.

1.4.2 Neutron stars

It was the discovery of extremely large magnetic fields on the surface of a neutron star in the binary system of Hercules X-1 (see Fig. 1.3) by Trümper *et al.*[32] that prompted much of the research in diamagnetic hydrogen. In comparison to white dwarfs, the magnetic fields often found on neutron stars[2] are larger by many orders of magnitude, with fields up to 10^8 T detected. However, unlike white dwarfs, the surface temperatures of neutron stars are extremely high, causing the motion of the atoms with respect to the magnetic field in the atmosphere to be considerable. Since the electron and proton are oppositely charged, the opposing magnetic field forces caused by the motion of the atom tends to try and separate the two particles, thus acting as if the two particles were placed in an electric field orthogonal to the magnetic field. This effective Stark effect (called the *motional Stark effect*) requires an understanding of the behavior of hydrogen in a crossed electric and magnetic field.[33, 34] This is a complicating matter, since the additional electric field destroys the azimuthal symmetry of the diamagnetic hydrogen problem.

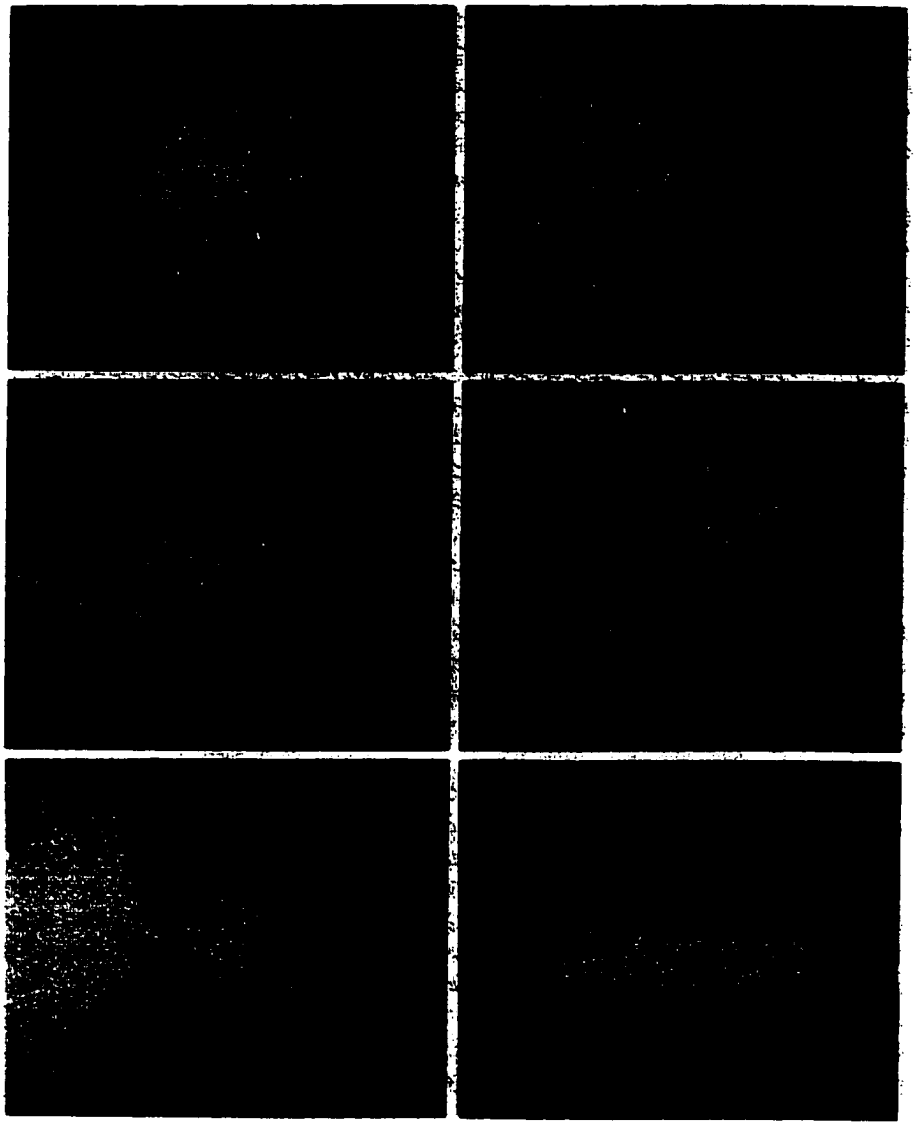

Figure 1.3: Computer simulation of a voyage around the neutron star Hercules X-1.[3]

1.5 Applications II: Solid state physics

An example of a quantum defect occurs when one atom in a crystal lattice is in an excited state. Since the states associated with each lattice atom are strongly coupled, this negative charge density can be effectively passed around to neighboring atoms. The hole that is left behind also represents a state of the atom, and this hole can be passed from one lattice site

to another as well. In this sense, the electron-hole interaction (called an *exciton*) resembles a hydrogen atom, with similar spherical symmetry and discrete, bound energy levels. However, in this case the Coulombic attraction between the electron and hole is typically weaker than for the hydrogen atom. Furthermore, the effective mass of the electron and hole are much less than their hydrogenic counterparts, so external perturbations such as magnetic fields have greater effect on this system than on hydrogen. In this sense, the exciton models the diamagnetic hydrogen problem but at much lower field strengths, which makes it feasible to study in the laboratory.

1.6 Applications III: Rydberg states of atoms

Highly-excited (large n) states of atoms, called *Rydberg* atoms[35, 36, 37], are natural systems to study the effects of external magnetic fields because the diamagnetic term in the Hamiltonian is proportional to ρ^2, and therefore proportional to the orbital area, which scales as n^4. One of the earliest experiments on the effects of magnetic fields on hydrogen concerned Rydberg states.[38] Furthermore, the correspondence principle states that atoms excited to large values of n should share many properties of classical systems.[39, 40, 41]

In this research, our focus was mainly on *circular* Rydberg states because they are very amenable to theoretical examination with dimensional perturbation theory, the method of choice in this research.

1.6.1 Circular Rydberg states

When the magnitude of the magnetic quantum number $|m|$ is maximized for a given n shell, the electron probability distribution takes on the shape of a torus with a radius proportional to m^2. The torus becomes more distinct as the atom is excited to higher levels of n — both the uncertainty in the radius and angular position (that is, the spherical coordinate θ defined with respect to the z-axis) tend to 0 as n increases towards infinity. This torus is naturally centered about the origin, so there is minimal probability that the electron will habitually

come to within close distances of the nucleus. Therefore, in studying circular Rydberg states we are not restricted to hydrogen alone, since the non-penetration of orbitals closer to the nucleus means that atoms in circular Rydberg states are, for all practical purposes, hydrogenic.

Because these states have maximal values of the magnetic quantum number $|m|$ they are of special interest to this research since the perturbation parameter we use in dimensional perturbation theory is inversely proportional to $|m|$. However, circular Rydberg states have some other unusual properties that have aroused much interest in general:

- From an experimental point of view, circular Rydberg states are relatively long-lived. The lifetime of such a state is roughly $10^{-10}n^5$ seconds[27], so even states with $n = 10$ have a lifetime of 10 microseconds.

- Since the angular uncertainty $\Delta\theta$ is small, circular Rydberg states are highly planar, which means that they are highly anisotropic with respect to external perturbations. Therefore, circular states of atoms are useful for studying the role of orientation in collisions involving Rydberg atoms. For example, much attention has been paid to the effect of the orientation of the two bodies in ion/atom collisions. It has been shown for cases where the atom is in a circular Rydberg state that the cross section for charge transfer in such a collision is maximized when the orbital plane is parallel to the relative velocities of the two bodies (in other words, when the incoming ion sees an "edge view" of the incident circular Rydberg target).[42, 43]

- Although the correspondence principle, which relates the behavior of systems in the limit of small $\hbar$ to classical mechanics, is well-accepted in quantum theory, experimental verification is difficult. To explore this relationship it is necessary to construct wave packets that behave like classical systems. Schrödinger[44] first proposed that hydrogenic states constructed to exhibit quasi-classical properties would travel along

a Kepler elliptical orbit in accordance with Ehrenfest's theorem[45], and many researchers have attempted to computationally construct such systems.[40, 41] Circular Rydberg states, because the electronic motion is largely confined to a circular-type orbit, are therefore important systems for studying this region where the distinctions between classical and quantum mechanics blur.[46]

- Since the radius is proportional to m^2, maximizing the magnetic quantum number m reduces the effect of the Coulombic interaction for a given value of n. This means that states of maximal $|m|$ are highly sensitive to small changes in external perturbations, such as an external magnetic field. (Keep in mind that the diamagnetic term is proportional to the average orbital area, which increases as $|m|$ becomes larger.) This reduces the region of field strength at which the complicated mixing of energy eigenstates occurs to laboratory-accessible levels.

1.7 A brief review of diamagnetic hydrogen research

The numerical and theoretical research on the diamagnetic hydrogen problem is vast, and therefore we focus in this section mainly on work that has direct implications on the research discussed in this dissertation. There are two teams of researchers in particular — the French team of Delande and Gay and the German team of Rösner, Wunner, Herold, and Ruder — that have dominated much of the literature on diamagnetic hydrogen, so we will discuss their contributions in separate sections towards the end of this chapter.

Perhaps the earliest work on the diamagnetic hydrogen problem was by Schiff and Snyder[47], who applied first-order perturbation theory to the low-field limit. Other work on the energy levels and transitions of diamagnetic hydrogen, at least for field strengths below 10^7 T, was performed by, among others, Smith *et al.*[48], Brandi *et al.*[23], and Garstang[9]. The latter is particularly important, since his contribution contains a comprehensive review of the previous research on diamagnetic hydrogen. The first large-scale

calculation of energy levels was by Praddaude[49], who expanded the wave function in Laguerre polynomials; numerical results were presented for the first 14 energy levels for the $n = 1, 2$, and 3 subspaces. Beginning with the zero-field case, Cabib, Fabri, and Fiorio expanded the eigensolutions of the Hamiltonian in spherical harmonics and recast the results into a set of difference equations which were then solved numerically for the ground and first-excited state.[25] Pokatilov and Rusanov used a variational approach, assuming exponential dependence on the trial wave functions, that proved successful in the low field limit for the $1s$, $2s$, and $2p$ states.[50]

Canuto and Kelly[51] extended the scope of this research for fields larger than 10^7 T by relying on an adiabatic approximation, discussed in Chap. 2. By introducing a trial wave function that combined the spherical symmetry (good at low field strengths) and cylindrical symmetry (good at large field strengths) Rau and Spruch[52] established upper bounds for the energy levels at arbitrary values of the magnetic field. In this same research they were also one of the first to establish a correspondence between the low-field and high-field quantum numbers. For large field strengths an early variational approach was performed by Yafet, Keyes, and Adams[53] using wave functions having a Gaussian shape, which is a good approximation in the large field limit.

As mentioned in Sec. 1.4.2, by discovering enormous magnetic field strengths in neutron stars Trümper[32] deserves credit for initiating much of the next phase of research in diamagnetic hydrogen. In 1979 Simola and Virtamo, using an approach similar to that of Canuto and Kelly, focused on a few low-lying ($n \leq 5$) states and calculated their energy levels and even established the correct correspondence diagram between the low-field and high-field limits. Bender, Mlodinow, and Papanicolaou[54] used semiclassical perturbation theory to derive expressions for the ground state energy levels in each $|m|$ subspace. Semiclassical treatments were also used by DuVernois, Boorstein, and Uzer[55] to calculate widths of avoided crossings, and by Angelié and Deutsch[17] to investigate quantum number assignments in the weak-field and strong-field limits. Starace and Webster[56]

calculated rigorous upper and lower bounds for low-lying states using an adiabatic approximation for fields below 10^5 T. This work was extended to fields above 10^5 T by Liu and Starace[57]. Later, Shertzer and colleagues calculated highly accurate lower bounds on the binding energies of the ground state[58] and lowest-lying excited states[59]. For Rydberg levels of diamagnetic hydrogen in the weak-field region, Falsaperla and Fonte[60] provided rigorous bound-state error estimates for both the energy levels and wave functions. To match the low-field and high-field regions Wintgen and Friedrich[4, 61] diagonalized the Hamiltonian in the complete basis of two-dimensional harmonic oscillators. This work is discussed in more detail later.

1.7.1 Delande and Gay

From a purely theoretical view, D. Delande and J. C. Gay have long been involved in various approaches to the diamagnetic hydrogen problem, and their early work has been some of the most important. Delande and Gay were one of the first, along with Zimmerman *et al.*[62] and Clark and Taylor[63], to observe exponentially small avoided crossings between states originating from different n-manifolds.[64] This suggested the possibility that there existed within the structure of the diamagnetic hydrogen problem a hidden symmetry that allowed these energy levels to (nearly) cross. Later, they would follow the works of Solov'ev[65] and Herrick[66] in deriving a term in the Hamiltonian that was, within a particular n-space, a first-order invariant with respect to energy.[67] The existence of this operator is crucial to understand these small avoided crossings in the low-field spectrum of diamagnetic hydrogen. Their group theoretical approach is probably the most straightforward and robust of the three approaches, and in Sec. 2.1 and Appendix B we discuss their approach in detail. They quickly followed this important contribution with a more generalized treatment of the derivation which extended the application to a wider variety of perturbing potentials.[68] In 1986 they used their group-theoretical approach to calculate many of the energy levels of diamagnetic hydrogen, although only for very large values of

the principle quantum number n.[13] They even applied a supersymmetric factorization of Rydberg atoms in parallel electric and magnetic fields.[30]

1.7.2 Rösner, Wunner, Herold, Ruder

From a numerical standpoint, the contributions of Rösner, Wunner, Herold, and Ruder are vast. After all, by expanding the eigensolutions in a spherical basis for low field strengths, and a cylindrical basis for large field strengths, they were the first to compile a comprehensive list[69] of highly accurate (low-lying) energy levels as functions of B for $B \leq 10^9$ T. Ruder, Wunner, and Herold (along with F. Geyer) extended this work to a larger number of energy levels and published the seminal *Atoms in Strong Magnetic Fields*,[6] which is the most comprehensive study of diamagnetic hydrogen to date. They also made an early attempt at providing reasonably accurate energy levels in the intermediate field region which successfully connected the energy levels at the two extremes.[70] One of the earliest perturbation treatments of diamagnetic hydrogen was by Ruder, Wunner, Herold, and M. Reinecke.[71] The general problem of two charged bodies interacting in a homogeneous magnetic field was studied by Herold.[72] This team also used an asymptotic potential energy function to find approximate solutions of the diamagnetic hydrogen problem for the strong-field region.[73] We already mentioned the contribution of Wunner, Kost, and Ruder in numerically computing many of the circular states of diamagnetic hydrogen.[74]

Much of Rösner, Wunner, Herold, and Ruder's attention has concentrated on astrophysics, especially white dwarfs. In Ref. [75] they focused their efforts on the (well-studied) white dwarf Grw+70°8247 by comparing results derived from its energy spectrum to wavelengths and dipole strengths of diamagnetic hydrogen in the field strength region from 15 to 35 kT. Wunner and Ruder calculated even more properties, including oscillator strengths, transition probabilities, and sum rules, for field strengths corresponding to neutron stars.[76] At roughly the same time, these two researchers approximated their earlier,

highly accurate, energy values with polynomial approximants. These approximants are capable of providing accurate energy values for field strengths of roughly 10^6 to 10^9 T for the 13 lowest-lying states of diamagnetic hydrogen.[77] Using numerical wave functions, Rösner, Wunner, Herold,and Ruder were able to calculate sum rules and energy values of diamagnetic hydrogen and compare their results to variational treatments.[78]

1.7.3 Books and review articles

The first comprehensive review of the problem of atoms in high magnetic fields was that of Garstang[9], followed rapidly by Bayfield[79] who expanded the focus to include excited states of atoms in both magnetic and electric fields. Since then there have been many books published that focus heavily on the diamagnetic hydrogen problem. The most important is probably *Atoms in Strong Magnetic Fields*[6], which we mentioned in Sec. 1.7.2. *Atoms and Molecules in Strong External Fields*[8] is relatively current (1998) and is especially noteworthy for its in-depth discussions of the astrophysical applications of this research. Friedrich's *Theoretical Atomic Physics*[80] discusses the physics of the diamagnetic hydrogen problem for large field strengths in detail, while *Rydberg Atoms*[81] and *Rydberg States of Atoms and Molecules*[36] extend the discussion to Rydberg states.

Chapter 2

The Energy Level Spectrum of Diamagnetic Hydrogen

A graphical depiction of the diamagnetic hydrogen atom is shown in Fig. 2.1. Because of the cylindrical symmetry of this system we only need to consider motion in the $\hat{\rho}$ and $\hat{\mathbf{z}}$ degrees of freedom because the quantum mechanical equations of motion are invariant under rotations in the angle $\hat{\boldsymbol{\phi}}$.

The Schrödinger equation for a hydrogenic atom placed in a constant magnetic field is given in a.u. by[87]

$$\left[-\frac{1}{2}\nabla^2 + \frac{B}{2}\hat{L}_z + \frac{B^2\rho^2}{8} - \frac{Z}{\sqrt{\rho^2+z^2}}\right]\Phi(\rho,z,\phi) = E\Phi(\rho,z,\phi). \tag{2.1}$$

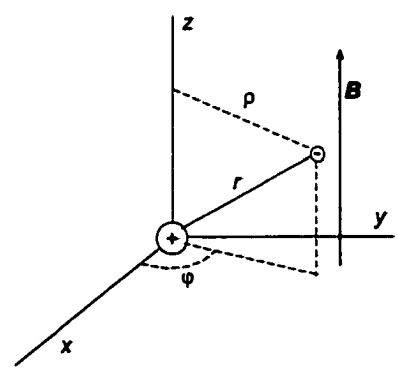

Figure 2.1: The geometry of the diamagnetic hydrogen problem. The magnetic field **B** points along the z-axis. Notice that cylindrical coordinates defined by (ρ, z, ϕ) are natural coordinates to use in this system.

Section 2.1 addresses the challenging problem of describing the energy spectrum of diamagnetic hydrogen in the low-field limit. In contrast, Sec. 2.2 describes the high-field limit, which in many ways is much simpler. Finally, in Sec. 2.3 we will briefly discuss the intermediate-field region. Once we formulate dimensional perturbation theory in Chap. 3, we will be prepared for a discussion of the original research in this dissertation, which begins in Part II.

2.1 Energy level spectrum in the low-field limit.

In a weak magnetic field there is very little mixing between different n levels that arise from a hydrogenic expansion of the wave function. Therefore, n is an approximate quantum number in the very-weak field region. The diamagnetic term though, strongly mixes states of the same n but different l.[88] Using Lie algebra (see Appendix B), we can demonstrate that *in a given n shell*, the diamagnetic term is a first-order invariant in the Hamiltonian. More specifically, ρ^2 in Eq. (2.1) may be replaced as follows:

$$\rho^2 \longrightarrow \frac{n^2}{2Z^2}(n^2 + m^2 + 3 + \Sigma), \tag{2.2}$$

where

$$\Sigma \equiv 4A^2 - 5A_z \tag{2.3}$$

is the first-order invariant and A_z is the component of the *Runge-Lenz vector* (often called the *eccentricity vector*)

$$\mathbf{A} = (-2E)^{-1/2}\left[\frac{1}{2}(\mathbf{L}\times\mathbf{p} - \mathbf{p}\times\mathbf{L}) + Z\hat{\mathbf{r}}\right] \tag{2.4}$$

along the direction of the external field. The three components of $\mathbf{A}$ are three of the six generators of the SO(4) Lie algebra of the zero-B field hydrogen atom. (The other three generators are the Cartesian components of the orbital angular momentum $\mathbf{L}$).

The operator Σ was independently derived using three different methods. Herrick[66] used a momentum-space representation of the diamagnetic hydrogen problem to derive Σ, but this treatment is long and involved. Solovév[65], on the other hand, relied on a semi-classical treatment. In Appendix B, I describe how Delande and Gay[67, 68] used the isomorphism between the SO(4) Lie algebra of the Coulomb problem and the SO(2, 2) Lie algebra of the two-dimensional harmonic oscillator to derive Σ, as I found their treatment to be the most straightforward.

The diamagnetic term breaks the SO(4) group dynamical symmetry of the zero B-field hydrogen in such a way that the quantum number ℓ associated with the angular momentum operator $\mathbf{L}^2$ is no longer a good quantum number. However, since Σ commutes with the zero B-field Hamiltonian, in a given n shell the operator Σ commutes with the diamagnetic Hamiltonian, so in the weak-field limit the eigenvalues s of Σ afford an approximate quantum number to replace the angular-momentum quantum number ℓ.

2.1.1 Vibrator and rotator States

Classically, the Runge-Lenz vector $\mathbf{A}$ determines the orientation and shape of the orbit. The length of $\mathbf{A}$ is directly related to the eccentricity ϵ by

$$\epsilon = (-2E)^{1/2}|\mathbf{A}| \tag{2.5}$$

($\mathbf{A}$ perfect circle corresponds to $\epsilon = |\mathbf{A}| = 0$.) The direction of $\mathbf{A}$ is from the nucleus towards the perihelion of the orbit.

The fact that Σ is constant provides a constraint on the rotation dilation of the Runge-Lenz vector. Although the length of $\mathbf{A}$, and the lengths of its components along the x, y-plane and z-axis, can vary quite considerably, the precession of $\mathbf{A}$ about its average position in the ρ, z-plane is rather small, as shown in Figs. 2.2 and 2.3. The eigenvalue

$$s = 4A^2 - 5A_z^2 \tag{2.6}$$

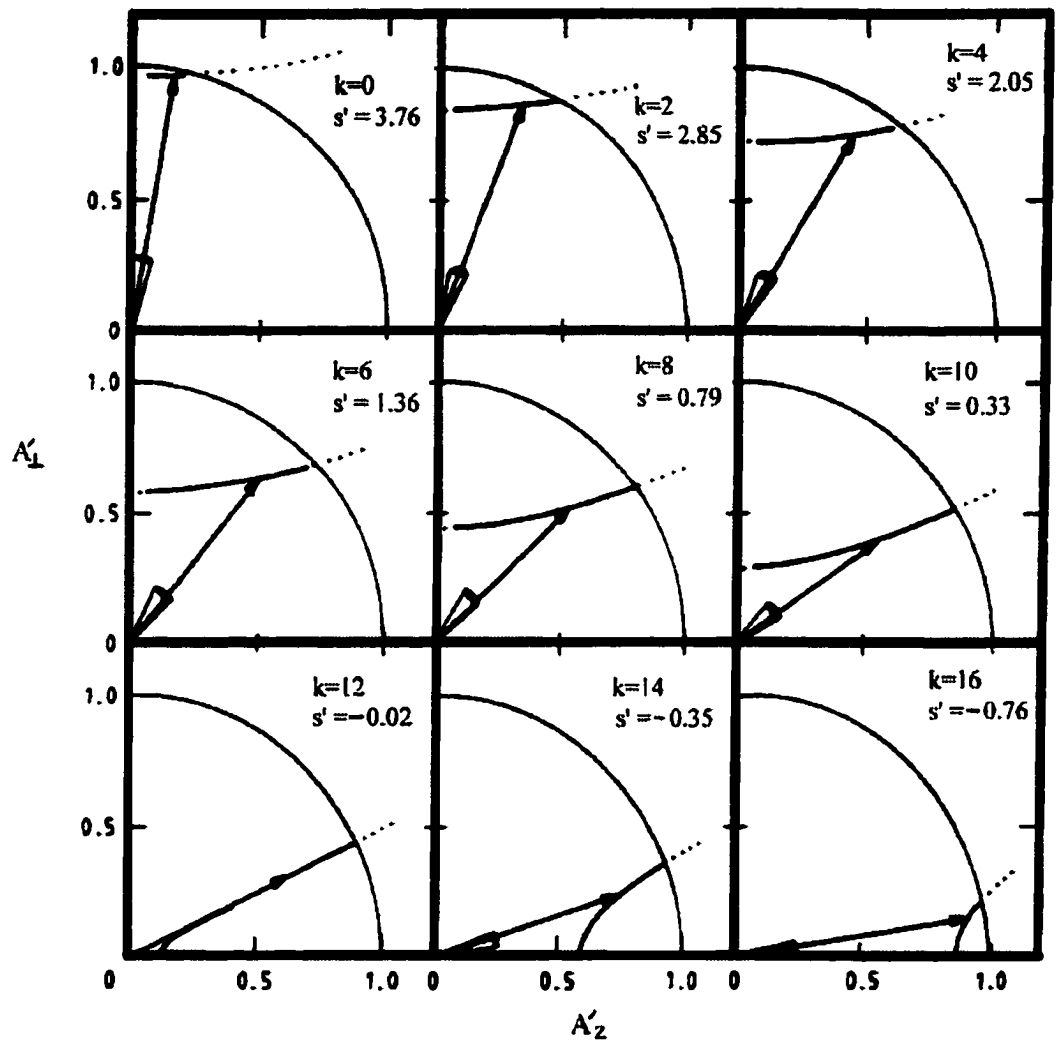

Figure 2.2: Variation of the A_z and $A_\perp$ components of the Runge-Lenz vector **A** for $n = 18$ and $m = 0$ for different values of s' and k, where s' is the eigenstate s of Σ scaled as $s/(n^2 - 1)$. Clearly, neither $A_\perp$, A_z, nor $|\mathbf{A}|$ is even close to being constant, but the precession of **A** (depicted by the small cone emanating from the origin) is very small for all values of s'. Notice that as k gets large, corresponding to a vibrator state, **A** begins to migrate towards the z-axis. From Ref. [4].

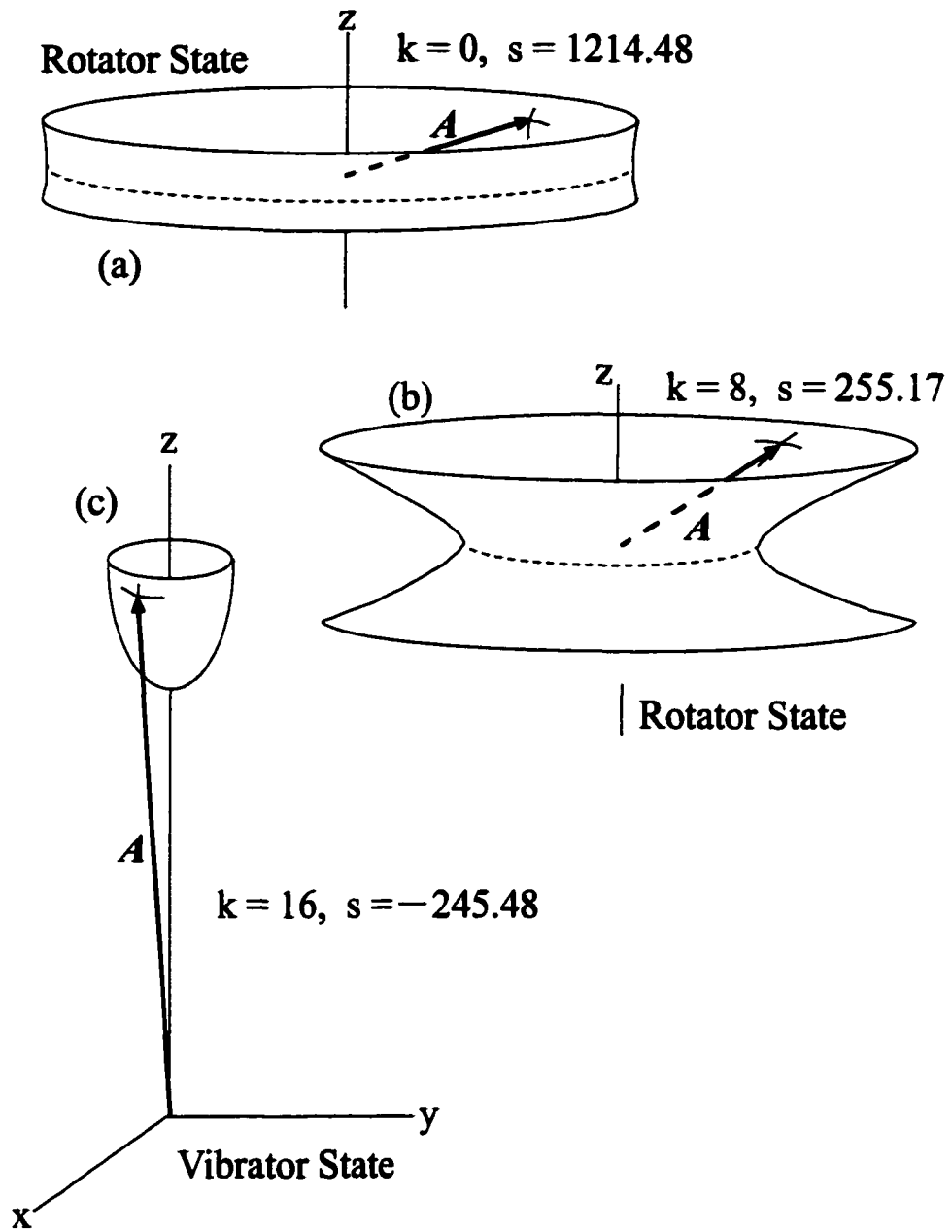

Figure 2.3: A three-dimensional pictorial of the variation in the orientation of the Runge-Lenz vector corresponding to three situations depicted in Fig. 2.2. Because of the azimuthal symmetry of the system, the Runge-Lenz vector is free to rotate about the z-axis. However, neither its length, nor the length of any of its components, can be considered close to constant for all three situations. In (a) the precession of **A** about its average position in the ρ, z-plane is mostly in the z-direction, whereas in the other extreme (c) this precession is mostly in the direction perpendicular to the z-axis. In all three cases, the magnitude of the precession of **A** as the tip of **A** rides along the surface $4A^2 - 5A_z^2$ is roughly the same, and confined to relatively limited motion.

need not be integral; but it is restricted by the requirements[4]

$$A^2 \leq n^2 - |m|(|m|+1) - 1\,, \tag{2.7}$$

and

$$0 \leq |A_z| \leq n - |m| - 1 \,(\text{for } n - |m| \text{ even})\,, \tag{2.8}$$

$$1 \leq |A_z| \leq n - |m| - 1 \,(\text{for } n - |m| \text{ odd})\,. \tag{2.9}$$

The lower lying ($s < 0$) states are termed *vibrator* states and, not surprisingly, the wave functions are localized along a line parallel to the field, with the result that the orbital area is small — the diamagnetic shifts will be small as well.

The spacing between levels corresponding to different values of s are not equal. In fact, the spacing reaches a minimum at $s = 0$. The transition between the two patterns of electron localization becomes increasingly narrow as n becomes larger.

As long as states belonging to different n shells remain well-separated in energy, the states will be dominated by a contribution from a single hydrogenic function labeled by n and s. However, as the field is sufficiently increased, rotator states from one n-shell will cross into the vibrator states of the n-shell above. This gives rise to avoided crossings between rotator and vibrator states and these are seen to be narrow, particularly at higher n.[90] In this case the region of field strength at which the states become mixed in n and s becomes small, so on either side of the avoided crossing there is little mixing between states of differing values of n and s. Therefore the n, s labeling of states can be continued diabatically across avoided crossings into the overlapping n region.[4]

It is not surprising that avoided crossings between vibrator and rotator states would be narrow, indicative of very little interaction between the two states except when they are very close together in energy. After all, with their radically different electron localizations (one localized along the z-axis, the other along the plane perpendicular to this axis) we

would not expect a great deal of interaction between the two states. However, the avoided crossings between rotator states of different n are narrow as well, and clearly this cannot be explained in terms of electron localization.

Wintgen and Friedrich[4, 61] were the first to explain the narrow avoided crossings between rotator states by introducing a more convenient quantum number k to label the states in a given (m, n) shell. In many ways the k quantum number takes on the same role for diamagnetic hydrogen as ℓ does in the zero-field case. For example, k takes on all integer values from 0 (the state of largest s) to a fixed upper bound (the state of lowest s), although in this case the upper bound is $n - |m| - 1$. Conversely to s, states having small values of k are rotator states and have relatively high energy, whereas large values of k denote vibrator states and relatively low energy. The nodal structure remains the same, with $k = 0$ corresponding to the maximum number of nodes along the x, y-plane and maximal k corresponding to the maximal number of nodes about the z-axis. This is summarized in Figs. 2.4 and 2.5. The approximate respective energy shifts as functions of field strength are given by Herrick[66] as

$$\Delta E = \frac{B^2 n^2}{8B_0^2}\left[\frac{9}{2}\lambda(\lambda+1) + \frac{1}{2}n^2 - 3m^2 + \frac{13}{4}\right], \quad \text{(rotator states)}, \tag{2.10}$$

$$\Delta E = \frac{B^2 n^2}{8B_0^2}\Big[2\sqrt{5}n(2\sigma + |m| + 1) - 3(2\sigma + |m| + 1)^2 - m^2 + 1\Big], \quad \text{(vibrator states)}, \tag{2.11}$$

where $B_0 = 2.35 \times 10^5$ T, $\lambda \equiv n - 1 - k$ and

$$2\sigma = n - |m| - 1 - k, \quad (\text{for odd } n - m - k), \tag{2.12}$$

$$2\sigma = n - |m| - 1 - k, \quad (\text{for odd } n - m - k). \tag{2.13}$$

Also, k determines the parity of the system in a similar manner as ℓ, that is

$$\hat{\pi} = (-1)^k. \tag{2.14}$$

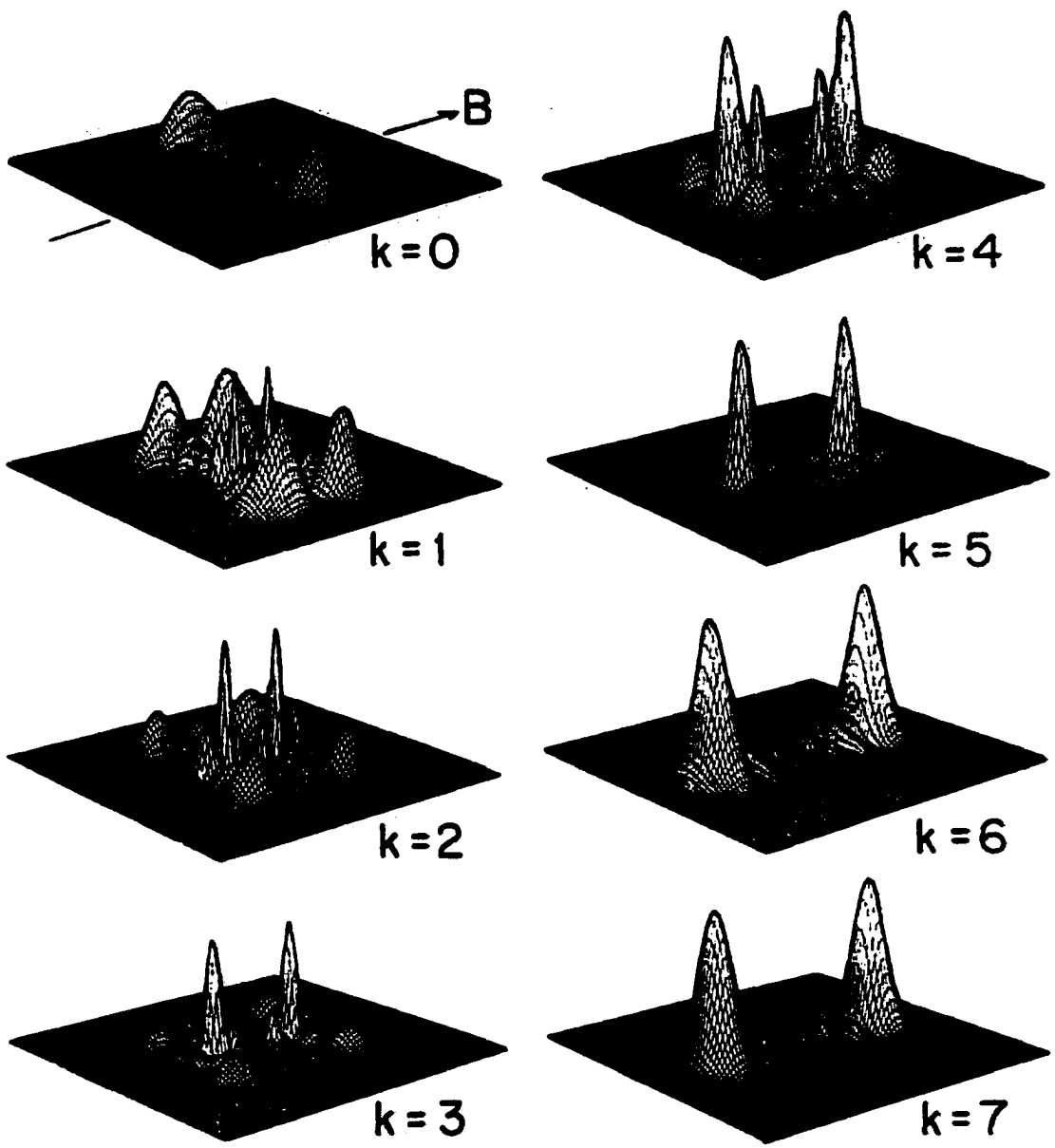

Figure 2.4: Wave functions for various values of the (approximate) quantum number k for $n = 8$, $m = 0$, from Ref. [5]. Notice that as k increases, there is a transfer of nodes from the z-axis to the x, y-plane. We can see clearly why it would appear that there would be very little overlap between the rotator and vibrator states.

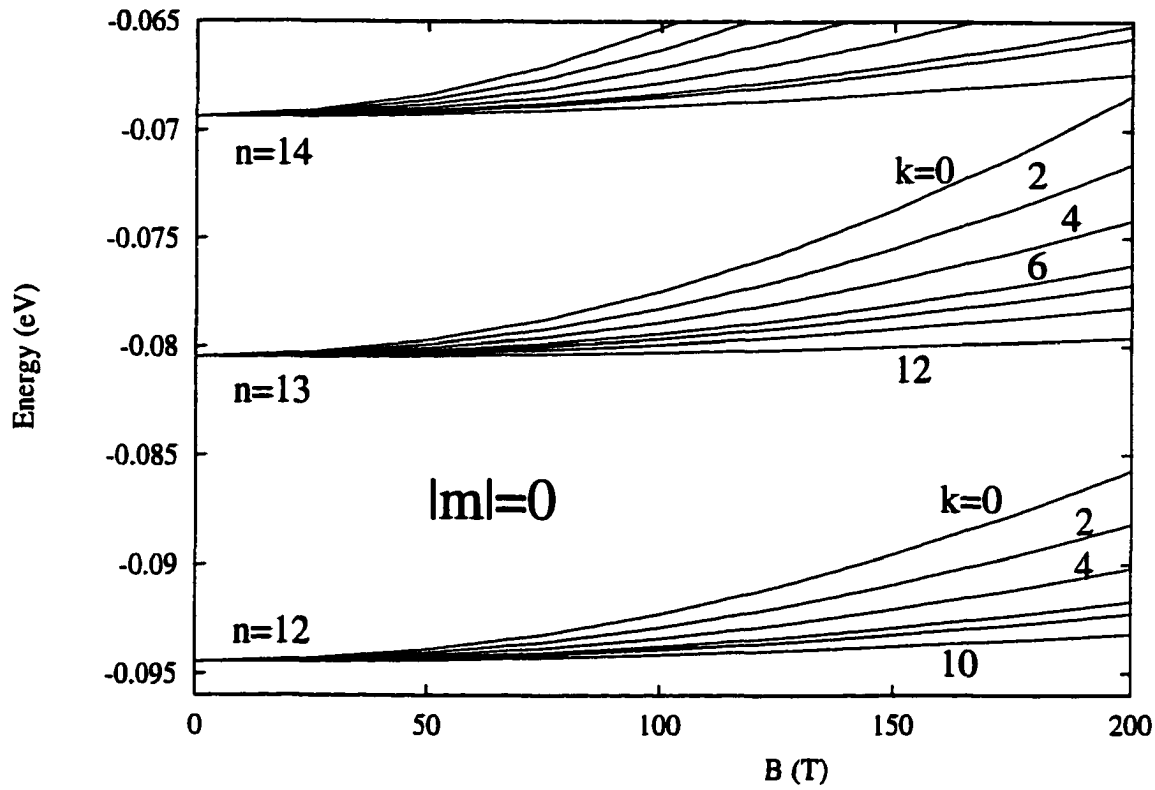

Figure 2.5: An example of how the energy levels of diamagnetic hydrogen corresponding to particular values of the (approximate) quantum number k spread with increasing field strength in the weak-field region. Only the even-parity (even-k) subspace is shown. For clarity, some k labels have been omitted.

In the weak-field region, the k quantum number is merely a way of relabeling the states in a given n-manifold (however, states with different values of n but the same value of k will have differing values of s). Wintgen and Friedrich demonstrated that the Hamiltonian for a magnetic field that is weak but strong enough to allow n mixing is approximately separable into blocks that are diagonal in k, and that the off-diagonal elements between blocks of differing values of k are very small. This means that the "spectral repulsion" between states with differing values of k arising from these very small off-diagonal elements will also be very small, that is, avoided crossings will be very narrow. See Figs. 2.6 and 2.7

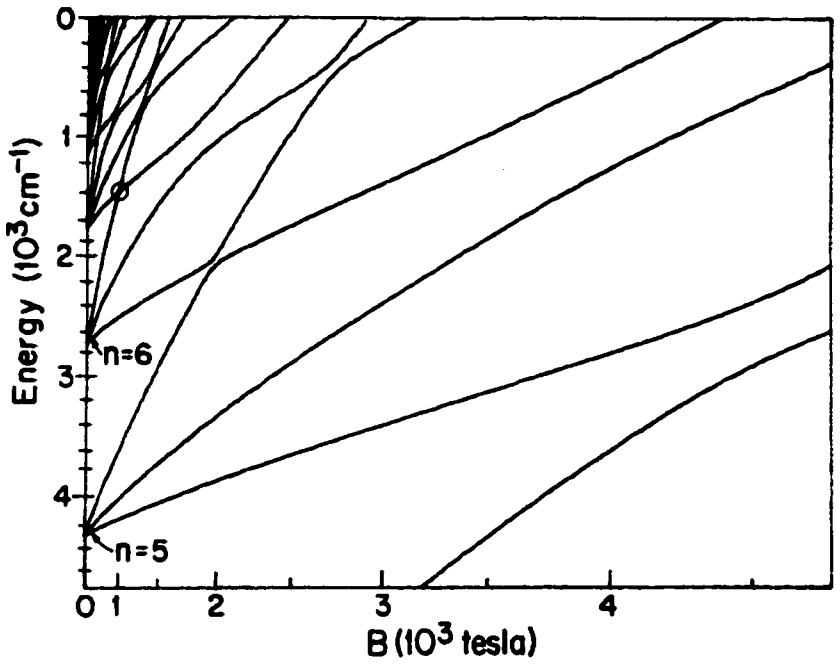

Figure 2.6: Low-field energy spectrum of diamagnetic hydrogen for relatively small values of n. Notice the very broad avoided crossing on the lower left, and that the avoided crossings become narrower as n increases. From Ref. [5].

Off-diagonal matrix elements connecting vibrator states whose values of k differ by 2 are the exception — they are appreciable (off-diagonal matrix elements connecting vibrator states are generally larger than other matrix elements). Thus k remains a good quantum number until the the magnetic field has risen sufficiently that vibrator states start to cross. Wintgen and Friedrich have provided rough estimates as to when this is likely to happen, with the result that the magnetic field at which vibrator states begin to cross is roughly five times that at which the states of adjacent n manifolds begin to cross — well within the region of n mixing.

At this point, we have a reasonable understanding of the low-field energy spectrum of diamagnetic hydrogen. We have two quantum numbers, n and k, that adequately label the characteristics of the wave functions even beyond the point at which levels from different n-subspaces begin to mix. We now turn our attention to the strong-field limit.

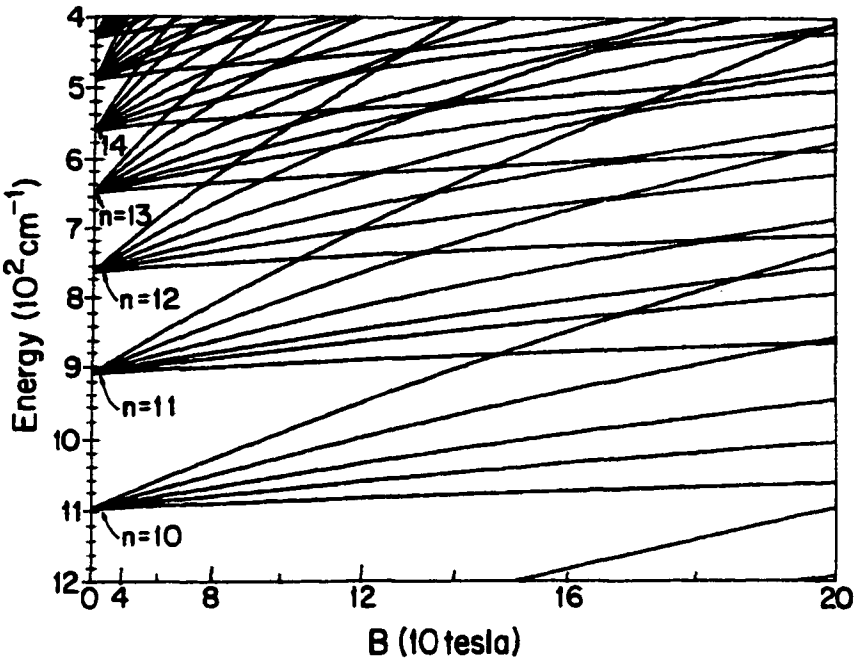

Figure 2.7: Same as Fig. 2.6, but for higher values of n.[5]

2.2 Energy level structure and continuum threshold in the strong and infinite field limit.

In this section we will see that the energy levels in the strong field limit have a structure that resembles that of a free electron in a magnetic field (the *Landau problem*). However, superimposed on that structure is a Coulombic structure caused by the Coulombic attraction, which dominates in the region along the field axis. In Sec. 2.2.1 we derive the Hamiltonians that describe the motion along the field axis (the z-axis) and along the plane perpendicular to that axis (the ρ-axis) in the limit of infinite field strength. In Sec. 2.2.1.1 we will see that the motion in the ρ-plane produces a structure that closely resembles the Landau problem, and in Sec. 2.2.1.2 we go a step further and describe the threshold energy determined by that motion. In Sec. 2.2.1.3 we consider motion along the z-axis.

Up to this point, we will have been considering the motion along the two respective degrees of freedom as independent of each other, which applies when the field strength is

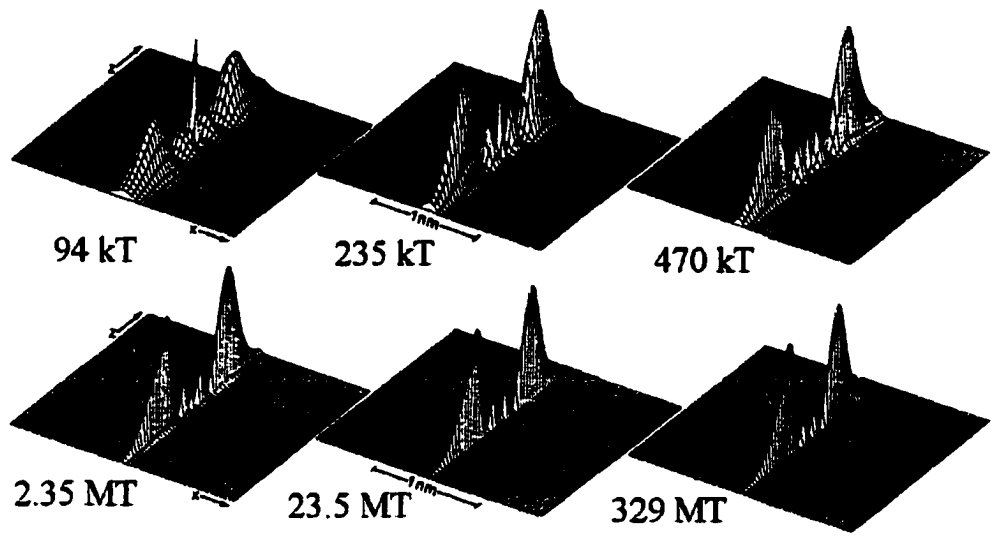

Figure 2.8: Evolution of the $|Nm\nu\rangle = |004\rangle$ large-field probability densities of diamagnetic hydrogen at various field strengths. (From Ref. [6]. The quantum numbers N and ν are defined in Secs. 2.2.1.1 and 2.2.1.3, respectively). Note how the wave function becomes "squeezed" onto the z-axis as the field strength increases.

infinitely large. In Sec. 2.2.2, however, we describe how lowering the field strength to finite values couples the two degrees of freedom and affects the resulting energy spectrum.

2.2.1 The $B \rightarrow \infty$ limit.

It is convenient to rewrite the Schroedinger equation in Eq. (2.1), which describes a hydrogenic atom in a magnetic field oriented along the $\hat{\mathbf{z}}$ axis, as

$$\left[-\frac{1}{2}\nabla^2 + \frac{B}{2}\hat{L}_z + \frac{B^2\rho^2}{8} - \frac{Z}{|z|\sqrt{1+\frac{\rho^2}{z^2}}}\right]\Phi(\rho,z,\phi) = E\Phi(\rho,z,\phi) \qquad (2.15)$$

so that it is easier to analyze the ρ- and z-dependence of the potential energy in the limit of a large magnetic field.

As the magnetic field increases in strength it "squeezes" the wave functions towards the z-axis, as can be seen in Figs. 2.8 and 2.9. Consequently we expect the expectation value

$\langle\rho\rangle$ to decrease rapidly compared to $\langle z\rangle$ as the magnetic field strengthens. Therefore the Coulombic potential energy

$$V(\rho,z)=\frac{Z}{|z|\sqrt{1+\dfrac{\rho^2}{z^2}}}=\frac{Z}{|z|}+\mathcal{O}(\rho^2/z^2)+\ldots\approx\frac{Z}{|z|} \tag{2.16}$$

as $B\rightarrow\infty$, uncoupling the $\hat{\boldsymbol{\rho}}$ and $\hat{\mathbf{z}}$ degrees of freedom in the potential energy. The Schroedinger equation in this limit then separates in ρ and z, as

$$\left[-\frac{1}{2}\nabla_\rho^2+\frac{mB}{2}+\frac{B^2\rho^2}{8}\right]\Omega_{\sigma,m}(\rho)=E_{\sigma,m}\Omega_{\sigma,m}(\rho), \tag{2.17}$$

$$\left[-\frac{1}{2}\nabla_z^2-\frac{Z}{|z|}\right]R_\lambda(z)=E_\lambda R_\lambda(z), \tag{2.18}$$

where $\Phi(\rho,z,\phi)\equiv\Omega(\rho)R(z)e^{-im\phi}$, and σ and λ represent the set of good quantum numbers (besides m) for each respective degree of freedom.

These results can be understood from a more physical approach. Since the force exerted on the electron by the magnetic field is given by

$$\mathbf{F_B}=-\mathbf{v}\times\mathbf{B}=-B\mathbf{v}\times\hat{z}, \tag{2.19}$$

then the magnetic field would not normally affect the motion of the electron along the z-axis; rather it tends to provide a centripetal force that draws the electron in closer to the z-axis. The Coulombic interaction, which is a function of both ρ and z, couples the two degrees of freedom. In the x,y-plane, the region in which the Coulomb interaction is significant compared to the magnetic interaction shrinks to 0 as $B\rightarrow\infty$, so this coupling disappears for infinitely strong B-fields. Therefore, *as far as motion in the x,y-plane is concerned*, the system in this limit models the two-dimensional motion of an isolated electron in a constant magnetic field. Furthermore, the force acting along $\hat{\mathbf{z}}$ is purely Coulombic in this limit and the system along this axis is thus modeled by a one-dimensional hydrogen atom, as implied in Eq. (2.18).

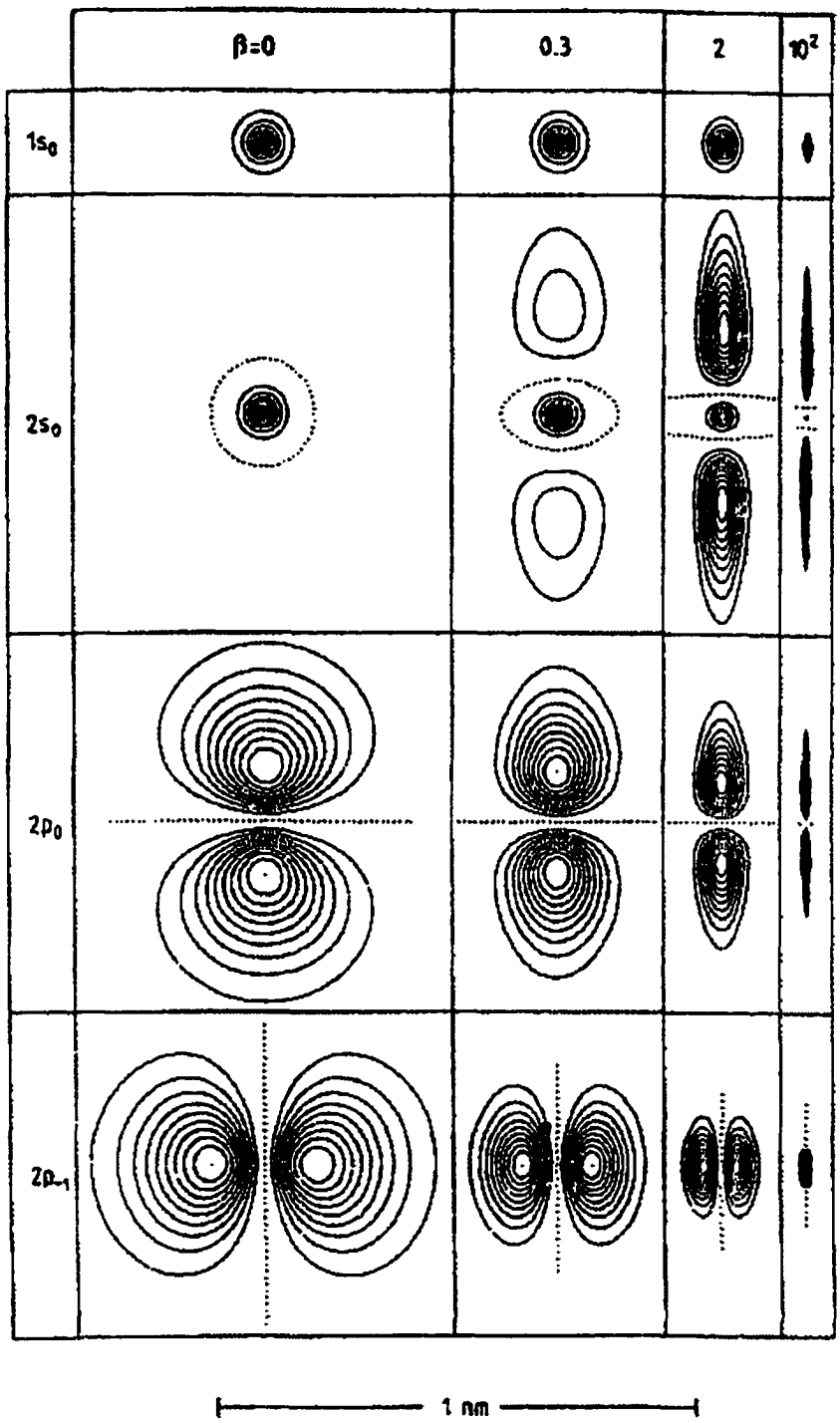

Figure 2.9: Contour view of the nodal structure and probability density of a number of states at low and high field strengths. (The $2s_0$ state appears to have passed through an avoided crossing, since its nodal structure has changed.) From Ref. [6].

2.2.1.1 Energy spectrum related to motion in the x-y plane in the limit $B \to \infty$.

To understand the spectrum in the large-field limit it is necessary to consider the familiar Landau problem, which we now describe.

Consider an isolated electron restricted to an x-y-plane and subjected to a constant magnetic field $\mathbf{B} = B\hat{k}$. For maximum separability of the Hamiltonian we choose the axial gauge

$$\mathbf{A} = -\frac{1}{2}\mathbf{r} \times \mathbf{B} = \frac{B}{2}(-y\hat{\imath} + x\hat{\jmath}). \tag{2.20}$$

The resulting Hamiltonian

$$\begin{aligned}\hat{H} &= \frac{1}{2}[\mathbf{p} + \mathbf{A}(\mathbf{r})]^2 = \frac{1}{2}\sum_{i=1}^{3}[\mathbf{p}_i + \mathbf{A}_i(\mathbf{r})]^2 = \frac{1}{2}\left[\left(\mathbf{p}_x - \frac{yB}{2}\hat{\imath}\right)^2 + \left(\mathbf{p}_y + \frac{xB}{2}\hat{\jmath}\right)^2\right] \\ &= \frac{1}{2}\left[\hat{p}_\rho^2 + B(\hat{x}\hat{p}_y - \hat{y}\hat{p}_x) + \frac{B^2\hat{\rho}^2}{4}\right] = \frac{1}{2}\left[-\nabla_\rho^2 + B\hat{L}_z + \frac{B^2\hat{\rho}^2}{4}\right]\end{aligned} \tag{2.21}$$

commutes with the angular momentum operator $\hat{L}_z$. Therefore, $\hat{L}_z$ and $\hat{H}$ share a complete set of eigenfunctions,

$$B\hat{L}_z|\Phi\rangle = mB|\Phi\rangle, \tag{2.22}$$

$$\hat{H}|\Phi\rangle = E_{\sigma,m}|\Phi\rangle, \tag{2.23}$$

(σ again represents the complete set of good quantum numbers besides m) so that the time-independent Schroedinger equation can be written

$$\frac{1}{2}\left[-\nabla_\rho^2 + mB + \frac{B^2\rho^2}{4}\right]\Omega_{\sigma,m}(\rho) = E_{\sigma,m}\Omega_{\sigma,m}(\rho), \tag{2.24}$$

which exactly matches our previous result in Eq. (2.17), thus demonstrating that in the infinite B-field limit the motion along the x,y-plane is indeed modeled by an isolated electron in a constant magnetic field.

The Schroedinger equation in Eq. (2.17) for the isolated electron in a magnetic field is identical to the Schroedinger equation for a two-dimensional isotropic harmonic oscillator.[80, 91] *As far as motion in the x,y-plane is concerned, a hydrogen atom in an infinite magnetic field behaves like a two-dimensional, isotropic, harmonic oscillator.* The energy eigenvalues of this system are well-known:[80, 91]

$$E_{N,m} = \frac{B}{2}(2N + |m| + m + 1), \quad N = 0, 1, 2, \ldots, \quad N - m = 0, 1, 2, \ldots, \tag{2.25}$$

where the *Landau channel number* N denotes the excitation of the (quantized) energy levels corresponding to radial motion perpendicular to the magnetic field and therefore counts the number of radial nodes in the Landau eigenfunction. As usual we drop the linear Zeeman term $mB/2$:

$$E_{N,m} = \frac{B}{2}(2N + |m| + 1). \tag{2.26}$$

2.2.1.2 Threshold energy and energy spectrum in the $B \to \infty$ limit.

The threshold energy E_T is the maximum total energy the electron can have and remain completely bound (that is, the minimum energy an electron can have once expelled from the atom). The total energy E of the electron has two contributions, one from the radial motion, $E_{N,m}$, and one from the Coulombic interaction, E_z (we will derive the exact form of E_z in Sec. 2.2.1.3). The radial energy $E_{N,m}$ in Eq. (2.26) increases as N increases, and since N is unbounded the bound state spectrum extends all the way to $E_{N,m} \to \infty$.[92] Therefore *the electron is completely bound regarding motion along the x,y-plane.* But it is possible for the electron to escape to $\pm\infty$ along the z-axis as long as it has enough energy to overcome the Coulombic potential energy. However, the energy contribution from the Coulombic interaction, E_z, has no effect on the overall threshold energy of the electron for two reasons:

1. E_z vanishes as $z \to \infty$.

2. E_z is always negative (attractive), but the threshold energy is the *maximum* energy of a bound electron.

Since the energy contributions from the Coulombic interaction are always negative and extend up to $E_z \rightarrow 0$, the overall energy levels of the system will always line up below the Landau threshold $E_{N,m}$ for any given values of N and $|m|$. (See Fig. 2.10.) We can therefore expect the Landau energy in Eq. (2.26) to also be the continuum threshold for the system in a given $\{N,|m|\}$ subspace. Furthermore, as previously stated, the solutions to the Schroedinger equation in Eq. (2.1) are uncoupled in regards to motion along the $\hat{\mathbf{z}}$ and $\hat{\boldsymbol{\rho}}$ directions in the limit $B \rightarrow \infty$. Therefore in this limit a system in an excited Landau state (that is, $N \geq 1$) cannot de-excite simply by transferring energy to motion along the z-axis. Therefore the Landau threshold is also the overall continuum threshold E_T for a given $|m|$ subspace; that is,

$$E_T = E_{N,m} = \frac{B}{2}(2N + |m| + 1) \qquad (B \rightarrow \infty). \tag{2.27}$$

A state in a given Landau level $N > 1$ has a finite probability of de-exciting to a state of lower N. This de-excitation can provide enough kinetic energy to motion along the z-axis to ionize the atom, so thatany excited Landau state is also a resonant state. Therefore, the overall threshold for completely bound energy levels has to assume $N = 0$. However, these de-excitations can only occur when a potential energy exists in the system that couples excitations in the two degrees of freedom, which we will later consider by lowering the magnetic field strength so that the Coulombic interaction along the x-y plane is no longer negligible.

2.2.1.3 Motion along the $\hat{\mathbf{z}}$ axis in the limit $B \rightarrow \infty$.

The potential energy function

$$V(z) = -\frac{Z}{|z|} \tag{2.28}$$

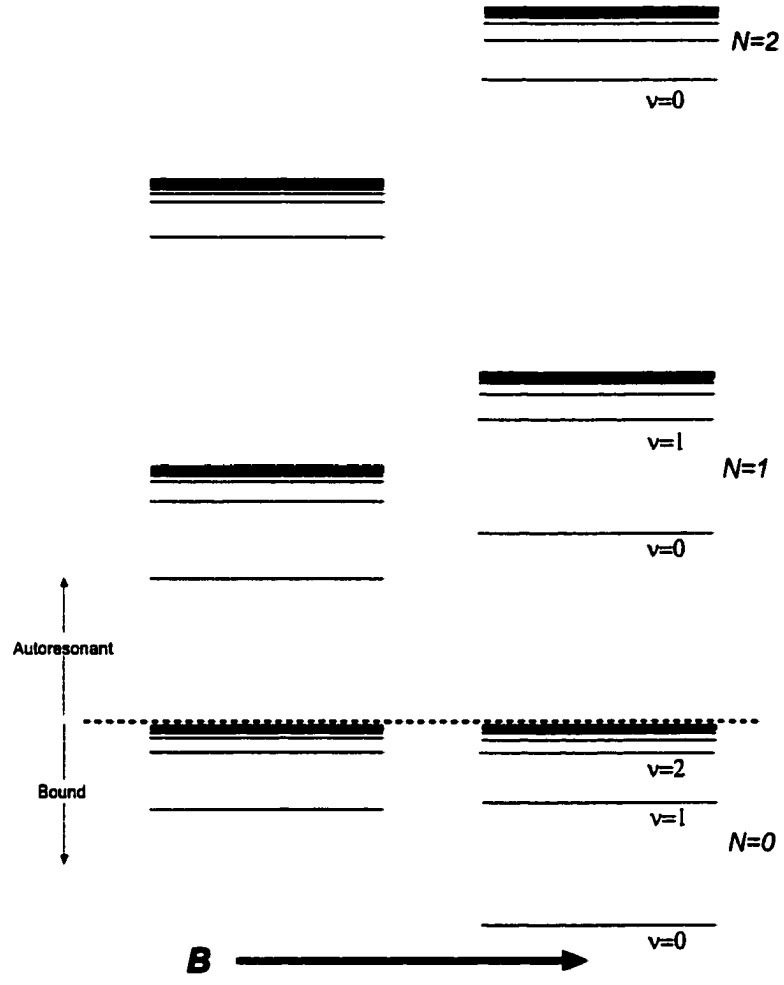

Figure 2.10: Schematic of the large-field energy spectrum of diamagnetic hydrogen at two unspecified values of the magnetic field strength. The vertical axis represents the energy, to no particular scale. Here, we concentrate on a particular subspace of $|m|$ and parity. Notice that the excited Landau levels ($N \geq 1$) rise uniformly as B increases since these threshold energies are directly proportional to B. On the other hand, the ground state Landau level threshold is not a function of B. As explained in Sec. 2.2.1.3, the hydrogenic levels line up under each Landau threshold, with energy levels associated with large principal quantum numbers ν lying highest in energy.

in the wave equation in Eq. (2.18) is singular at $z = 0$, so a careful analysis of the eigensolutions is required. A rough sketch of the wave functions can be made by considering the qualitative solutions to the modified potential $\breve{V}(z)$ in Fig. 2.11. Since the following arguments are qualitative, we will not concern ourselves with the exact functional dependence of $\breve{V}(z)$. Note that the parameter a determines how singular the potential energy is at the origin, with $a \to 0$ corresponding to the true Coulombic limit, which coincides with the one-dimensional hydrogenic atom with the potential energy in Eq. (2.28). Here, we will observe the evolution of the wave function as a is reduced to 0. [From here on, those variables denoted with a *breve* accent "$\breve{}$" will correspond to properties associated with the modified potential $\breve{V}(z)$].

Since we do not know the mathematical form of $\breve{V}(z)$ we simply write the Schroedinger equation as

$$\frac{\partial^2 \breve{R}}{\partial z^2} = \left[\breve{V} - \breve{E}\right] \breve{R}(z), \tag{2.29}$$

where we use $\breve{R}(z)$ to denote the wave function corresponding to motion along the z-axis. The modified potential, $\breve{V}(z)$, has the same symmetry as $V(z)$ but is everywhere finite and continuous, so we can expect the bound energy levels to correspond to even-parity and odd-parity solutions and be finite and continuous everywhere.

We now consider the situations where the wave function has even-parity and odd-parity separately.

Even-parity solutions

First, we consider the case where the even-parity solution to the modified potential does *not* have a node at $z = 0$. If this is the case then $[\breve{V}(0) - \breve{E}]\breve{R}(0)$, where $\breve{R}(0) \neq 0$, so that as $\breve{V}(0) \to -\infty$ the kinetic term $d^2\breve{R}/dz^2$ diverges. The Coulombic wave function $R(z)$ in this case must therefore have a discontinuity at the origin.

Suppose instead that the even-parity state *does* have a node at the origin. If the wave function is smooth, then the slope at the origin must be 0, given that the state we are

considering has even parity. If the potential energy is finite at the origin, which is the case for the modified potential, then not only are $R(0)$ and $dR(0)/dz$ equal to 0, but so are all higher-order derivatives. In this case, the Coulombic wave function remains zero (flat) as it propagates past $z = 0$ in either direction, which means that the wave function is 0 at all points — a completely unphysical result. Since we are concerned here with a physical system, which cannot truly have a singularity at the origin, then regardless of the value of $R(0)$, *the even-parity wave functions of the one-dimensional hydrogenic atom must have a discontinuity in their slopes at the origin.*[93]

Odd-parity solutions

The requirement that $\breve{R}(0) = 0$ for odd-parity states means that no matter how negative $\breve{V}(0)$ becomes, the quantity $[\breve{V}(0) - \breve{E}]\breve{R}(0)$ on the right-hand side (and hence $d^2\breve{R}/dz^2$) always remains finite. Therefore odd-parity states are smooth throughout the full range of z, even in the limit $a \rightarrow 0$.

As a is reduced the average depth of the potential energy across all values of z lowers, so we can expect the energy levels to be correspondingly lower. This effect will be more dramatic for even-parity wave functions because for these states the electron is more localized at $z = 0$, the location of the largest decrease in potential energy. Therefore we expect even-parity energy levels to lower more than odd-parity energy levels as a decreases. In fact, as we approach the Coulombic limit, any given even-parity energy level will eventually coincide with the odd-parity energy level that was once directly below it on the energy scale.[94] *Therefore, a one-dimensional hydrogenic atom is two-fold degenerate.* (This is also shown in Fig. 2.11) This rule does not include the ground state, which will be treated at the end of this section and in Appendix C.

In the Coulombic limit the degenerate even-parity and odd-parity wave functions at a given energy level will take on the same form, albeit of different parity[94]. (By "same form" I mean that the probability density associated with the two wave functions are identical, but the wave functions alone have opposite parity. See Fig. 2.11.) The inner nodes

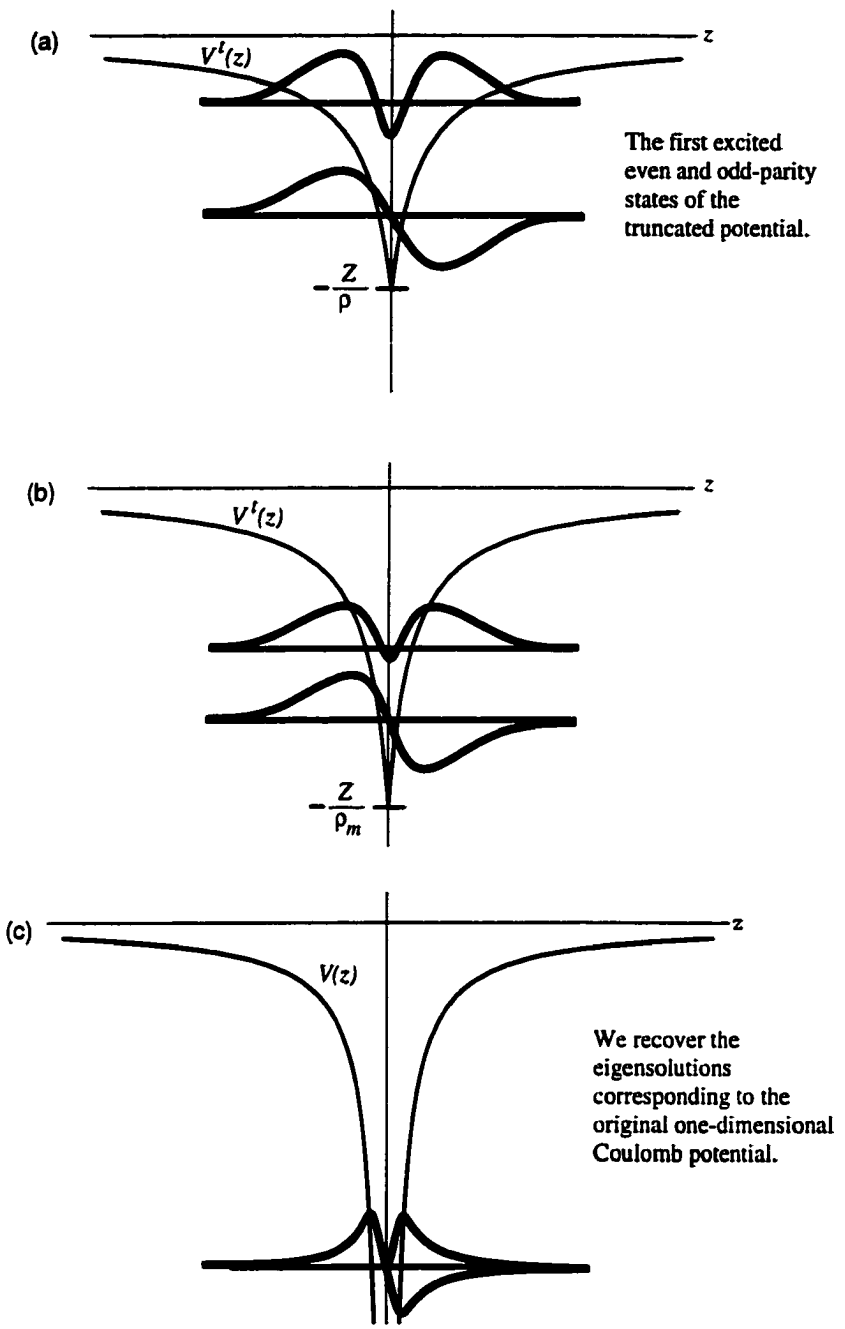

Figure 2.11: The role the modified potential $V^t(z)$ (denoted $\breve{V}(z)$ in the text) plays in modeling the one-dimensional hydrogen atom. (Here $V'(z)$ is simply a qualitative sketch and has no specified functional dependence. Similarly, the wave functions are hand drawn, not results of exact computation.) As $a \to 0$ the even-parity and odd-parity wave functions tend towards degeneracy and take the same shape (albeit of opposite degeneracy.)

(the two closest to $z = 0$) of the even-parity state eventually combine to form a double node at the origin. As a consequence, the probability density $|R(z)|^2$ for degenerate even-parity and odd-parity states are identical for a one-dimensional hydrogenic atom.

More interestingly, in the Coulombic limit the ground state ceases to be observable[95, 96], as is shown in Appendix C.

To summarize, as the bottom of the well in the modified potential energy $\breve{V}(z)$ drops to $-\infty$ (thus reproducing the one-dimensional Coulomb potential):

1. The energy levels all lower until the even-parity energy levels (except the ground state) fall to the same level as the odd-parity levels directly below them. Therefore, the energy levels become two-fold degenerate.

2. The even-parity wave functions tend to the "same form" as their degenerate odd-parity partners, only of opposite parity. The probability density of the two degenerate states become identical.

3. The original ground state ceases being an observable, although this is of no consequence to this research, as the $B \to \infty$ limit is inherently unphysical.

We can now go back and investigate the solutions to the pure Coulombic Schroedinger equation in Eq. (2.18). It is convenient to make the substitutions

$$E = -\frac{Z^2}{2\nu^2}, \qquad x = \frac{2z}{\nu}, \tag{2.30}$$

where ν is a dimensionless quantity.[97] The Schroedinger equation, which is now

$$\frac{\partial^2 R}{\partial x^2} + \frac{\nu}{|x|}R(x) - \frac{1}{4}R(x) = 0, \tag{2.31}$$

admits solutions[94] only if ν is a positive integer; that is, $\nu = 1, 2, 3, \ldots$. The eigenfunctions are

$$\text{(odd parity)} \quad R_\nu(z) = Aze^{-|z|/\nu}L_\nu^1(2|z|/\nu), \tag{2.32}$$

$$\text{(even parity)} \quad R_\nu(z) = A|z|e^{-|z|/\nu}L_\nu^1(2|z|/\nu), \tag{2.33}$$

where $A = \sqrt{2/[\nu^5(\nu!)^2]}$ is a normalization constant and $L_i^j(z)$ are associated Laguerre polynomials. We can readily see that $R(z)$ has the same form for both odd-parity and even-parity states, except that z in the odd state is replaced by $|z|$ in the even state. This reaffirms that the odd-parity and even-parity wave functions have the same form, but opposite parity.

The energy eigenvalues

$$E = -\frac{Z^2}{2\nu^2}, \qquad \nu = 1, 2, 3, \ldots \tag{2.34}$$

are not only quantized but are identical in value to those of the three-dimensional hydrogenic atom. Therefore, one-dimensional Coulomb eigenvalues form a Rydberg series, with their own continuum threshold at $E = 0$. The principal quantum number ν denotes the excitation level for motion along the $\hat{\mathbf{z}}$ axis and counts the number of nodes in the eigenfunctions in Eqs. (2.32) and (2.33).

The methodology above for finding the solutions to the Schroedinger equation does not include the ground state,[94]

$$R_{\nu\to 0}(z) = \lim_{\nu\to 0} \frac{e^{-|z|}}{\sqrt{\nu}}. \tag{2.35}$$

But as previously stated, the ground state is unphysical in the limit $B \to \infty$, although this is of little concern since infinite magnetic field strengths are likewise unphysical. For a detailed analysis of the ground state see Appendix C.

2.2.2 The strong (but finite) field limit

The eigenfunctions $\Omega_{N,m}(\rho)$ in Eq. (2.17) are the so-called *Landau eigenstates* and are functions of the magnetic field strength. (Their exact form is given in Appendix D.) For

large B it is practical to solve the Schroedinger equation in Eq. (2.1) by expanding $\Phi(\rho, z)$ in the Landau eigenbasis:

$$\Phi(\rho, z) = \sum_{N=0}^{\infty} \Omega_{N,m}(\rho)\Xi_N(z), \tag{2.36}$$

where we call $\Xi_N(z)$ the *Landau channel wave functions.*

By substituting our expansion into the Schroedinger equation we find

$$\left[-\frac{1}{2}\left(\frac{\partial^2}{\partial\rho^2}+\frac{\partial^2}{\partial z^2}\right)+\frac{4m^2-1}{8\rho^2}+\frac{B^2}{8}\rho^2-\frac{Z}{\sqrt{\rho^2+z^2}}\right]\sum_N \Omega_{N,m}(\rho)\Xi_N(z) = E\sum_N \Omega_{N,m}(\rho)\Xi_N(z), \tag{2.37}$$

which becomes

$$\left[-\frac{1}{2}\frac{\partial}{\partial z^2}+E_{N,m}-\frac{Z}{\sqrt{\rho^2+z^2}}\right]\sum_N \Omega_{N,m}(\rho)\Xi_N(z) = E\sum_N \Omega_{N,m}(\rho)\Xi_N(z). \tag{2.38}$$

Multiplying by $\Omega^*_{N',m}(\rho)$, integrating over all radial space, and taking advantage of the orthonormal nature of the Landau eigenbasis produces

$$\left[-\frac{1}{2}\frac{\partial^2\Xi_N}{\partial z^2}+E_{N,m}-Z\sum_N \Xi_N(z)\int_0^\infty \frac{\Omega^*_{N',m}(\rho)\Omega_{N,m}(\rho)}{\sqrt{\rho^2+z^2}}\,\rho\,d\rho\right] = E\,\Xi_N(z). \tag{2.39}$$

We then define $V^m_{N,N'}(z)$ so that

$$\left[-\frac{1}{2}\frac{\partial^2\Xi_N}{\partial z^2}+Z\sum_N V^m_{N,N'}(z)\Xi_N(z)\right] = (E-E_{N,m})\,\Xi_N(z), \tag{2.40}$$

where

$$V^m_{N,N'}(z) = -\int_0^\infty \frac{\Omega^*_{N',m}(\rho)\Omega_{N,m}(\rho)}{\sqrt{\rho^2+z^2}}\,\rho\,d\rho. \tag{2.41}$$

In Appendix D we show that in the limit of large $|z|$ the coupling potential $V^m_{N,N'}(z)$ becomes roughly diagonal, approaching that of a one-dimensional Coulombic potential, that is,

$$V^m_{N,N'}(z) \approx V^m_{N,N}(z) = -\frac{1}{|z|}\left(1 - \frac{2}{B^2 z^2}E_{N,m}\right), \tag{2.42}$$

where $E_{N,m}$ is the Landau energy. The second order correction to Eq. (2.42) above is proportional to the Landau energy, but this correction falls off by a factor of $1/B^2$, so that in the limit of large field strengths the Coulomb potential $V(r)$ becomes increasingly modeled by a one-dimensional hydrogenic atom. It is straightforward to show from the results in Appendix D that the higher-order terms in $V^m_{N,N}$ are inversely related to even larger powers of B, and therefore fall off even faster as B is increased.

The appearance of the coupling potential $V^m_{N,N'}(z)$ in Eq. (2.40) means that for any given value of $|m|$ the energy levels corresponding to the $\hat{\rho}$ and $\hat{\mathbf{z}}$ degrees of freedom are directly coupled. As a result, a state excited to (say) $N = 1$ can de-excite by transferring energy into motion along the z-axis, thus allowing the possibility of pushing the electron into the continuum if this transferred energy is great enough to overcome the Coulombic interaction. It is well-known that any Landau channel de-excitation satisfies this condition for a sufficiently strong B-field.[98] Therefore the threshold energy E_T for finite fields requires that $N = 0$ in Eq. (2.27), so that

$$E_T = E_{0,m} = \frac{B}{2}(|m| + 1) \tag{2.43}$$

is the true threshold energy for a hydrogen atom in a strong (but finite) magnetic field.

As we previously stated, for a given $|m|$ subspace the $N = 0$ energy levels are ordered below the continuum threshold and are truly bound states. (See Fig. 2.10.) The higher energy levels are still ordered below $E_{N,m}$, but we have learned that for finite field strengths these levels correspond to resonant states, that is, they tend to autoionize,[98] *and this autoionization is due solely to presence of the two coupled degrees of freedom.*

2.2.2.1 Motion along the $\hat{z}$ axis in the strong field limit

For large B the electron is highly localized at a radial distance ρ_m so we can, for all practical purposes, consider the radial variable ρ in the Coulomb potential to be constant.

$$V(\rho, z) = \frac{-Z}{\sqrt{z^2+\rho^2}} \approx \frac{-Z}{\sqrt{z^2+\rho_m^2}}. \quad (\rho_m = \text{ constant}) \tag{2.44}$$

If ρ_m is sufficiently small (B is sufficiently large) then the radical

$$\sqrt{z^2+\rho_m^2} = \sqrt{(|z|+\rho_m)^2[1-2|z|\rho_m/(|z|+\rho_m)^2]} \approx |z|+\rho_m, \tag{2.45}$$

since $2|z|\rho_m$ falls off faster than $(|z|+\rho_m)^2$ as ρ_m becomes small. Therefore,

$$V(\rho_m, z) = \frac{-Z}{\sqrt{z^2+\rho_m^2}} \approx \frac{-Z}{|z|+\rho_m}, \tag{2.46}$$

which is of the form of a one dimensional hydrogenic atom but with the potential truncated to a finite depth of $-Z/\rho_m$ at the origin, as shown in Fig. 2.11. The description of the eigensolutions for this potential is similar to the modified Coulomb potential described earlier. The larger the magnetic field strength, the smaller the value of ρ_m and the more the potential resembles the one-dimensional Coulomb potential.

The energy levels of the truncated potential,

$$E_{\nu'} = \frac{-Z^2}{2\nu'^2}, \tag{2.47}$$

still form a Rydberg-like series, except that the nonintegral principal quantum number ν' is slightly larger than the corresponding quantum number ν. We call the difference between ν' and the integral quantum number ν for the true Coulomb potential the *quantum defect* δ_ν. Thus $\delta_\nu = \nu' - \nu$, with $\delta_\nu > 0$. Naturally, $\delta_\nu \to 0$ as $\rho_m \to 0$ (and hence $B \to \infty$).

As long as B is finite there exists a physically meaningful ground state solution[96] to the truncated potential,

$$E_{\nu'\approx 0} = -4Z^2 \ln^2[(Z\rho_m)^{-1}], \tag{2.48}$$

where $\rho_m = \sqrt{ZB(2|m|+1)/2}$. In the Coulombic limit, this energy level drops to $E_{\nu'\to 0} \to -\infty$ and becomes unphysical, as previously discussed.

2.3 The intermediate field region

The region between the weak-field and strong-field region has always been difficult to understand because the wave functions of the system undergo rapid changes as the field strength is adiabatically swept through the many avoided crossings that appear throughout this region. More specifically, the physical characteristics of the wave functions, which denote the state of the system, re-organize when the field strength is swept past an avoided crossing, thus interchanging the nodal structures between the plane perpendicular to the field and the z-axis. This can be seen in Fig. 2.12, where nodes that originally appeared along the x, y-plane for low field strengths begin to appear mainly along the z-axis.

> Caveat: When we speak of "sweeping the magnetic field" we are specifically talking about changing the field strength *adiabatically*, that is, infinitely-slowly. In this sense, we are not really changing the magnetic field by any finite rate, but rather independently solving the *time-independent* Schrödinger equation for the system at every possible value of B. Otherwise, we would have to consider the possibility of transitions between energy levels as the field is swept through the avoided crossing region. This situation is discussed in Appendix E.

In the region of dense avoided crossings, the states of the system become linear superpositions of many eigenstates and are impossible to label with any sort of meaningful quantum numbers. However, the nodal structure in the two limits of field strength can be correlated, regardless of what takes place between these two regions. To understand how,

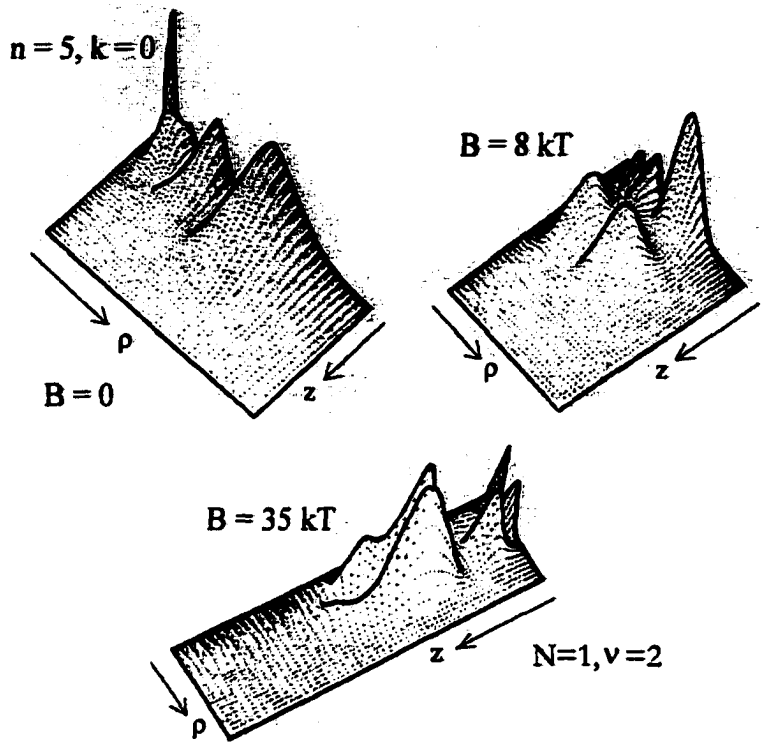

Figure 2.12: Transformation of the even-parity nodal structure of diamagnetic hydrogen as a function of field strength. Here, $m = 1$ and the vertical axis is $\rho|\Psi(\rho, z)|^2$. (a) Zero-field limit, where $n = 5$ and $k = 0$ (rotator state). (b) $B = 8$ kT. (c) $B = 35$ kT. In this last case the state is in an autoresonant state, as described in Sec. 2. From Ref. [4].

we now consider a low-lying section of the energy spectrum. For simplicity, we will focus on the even-parity, $m = 0$ subspace.

2.3.0.2 The correlation between quantum numbers in the low and high-field regions.

In Fig. 2.13 we show a schematic representation of the behavior of the three lowest energy levels of diamagnetic hydrogen. The nodal structure of the ground state ($n = 1$) energy level does not change as the field strength changes because this state does not undergo any avoided crossings with other states, so we instead concentrate on the $n = 2$ and $n = 3$ energy levels.

At low fields, the $n = 2$ subspace only has one k-level, $k = 0$ (remember that k only takes on values from 0 to $n - m - 1$, which means that k can only be 0). This is a rotator

state, so the nodal structure is distinctly laid out on the x, y-plane. As B is increased, this level rises in energy. The $n = 3$ subspace above it has two levels, $k = 0$ and $k = 2$ (we are ignoring the $k = 1$ level, since it belongs to the odd-parity subspace). The $k = 0$ (rotator) level rises with increasing field strength to undergo avoided crossings with levels originating above it. The $n = 3, k = 2$ vibrator level drops in energy until it encounters the $n = 2, k = 0$ level directly below it, upon which an avoided crossing between the two levels occurs (circled region in Fig. 2.13.

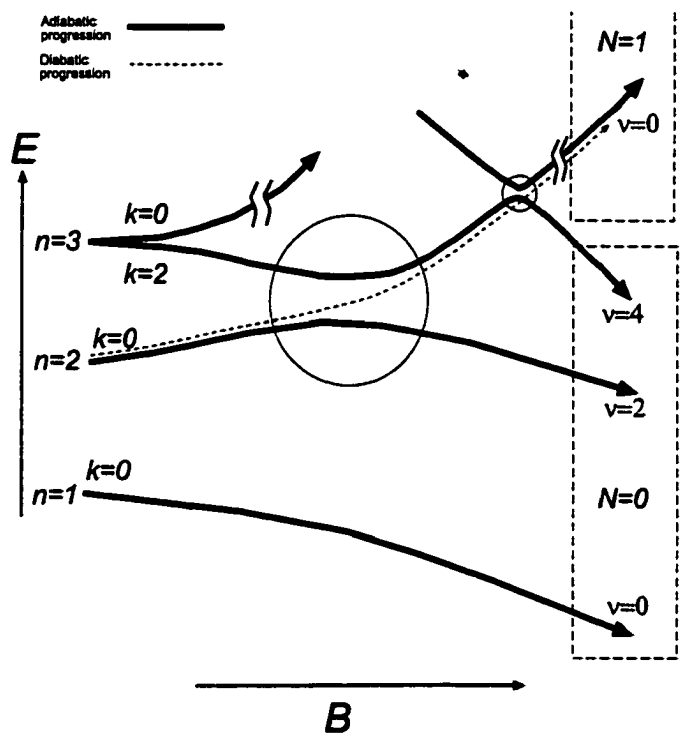

Figure 2.13: Evolution of a few low-lying states as the field strength is swept through the intermediate region. The broadness of the $\Delta k = 2$ avoided crossing (large circle) is greatly understated, since this avoided crossing is so broad as to be hard to distinguish (that is, a *hidden* avoided crossing). The boxed regions group Landau levels having the same N. Note that the nodal structure is preserved if we follow the dotted line (the *diabatic* curve) from the low-field region to the high field region. This would require changing the field strength at an infinite rate, as explained in Appendix E. The roughness of the lines owes to the unsteady hand of the graphics artist[101].

Since the two levels have relatively little nodal overlap (one is a vibrator state, the other a rotator state), it would be tempting to think that the avoided crossing between these two levels would be narrow. However, for this interaction, $\Delta k = 2$, and we saw in Sec. 2.1.1 that this avoided crossing is an exception — the avoided crossing between these two levels is actually very broad, so broad in fact that the avoided crossing is an example of a hidden avoided crossing. In the region of the avoided crossing the nodal structures of the two levels interchange, so that the nodes that originally appeared on the x, y-plane at low field strengths transfer to the z-axis at some point in the avoided crossing region. What was once a rotator state is now largely a vibrator state, being doubly excited ($\nu = 2$) along the z-axis at some point in the avoided crossing region. And since the excitation is now along the z-axis, the energy lowers with increasing field strength and the state becomes completely bound (because in this case $N = 0$).

The lowest-lying $n = 3$ state, on the other hand, has its excitation along the z-axis transferred to the x, y-plane upon passing through the avoided crossing. It will not maintain this nodal structure, however, because now its energy will rise with increasing field strength where it will undergo yet another avoided crossing with a state directly above it in energy (small circle in the figure), switching nodal characteristics yet again. When it finally reaches the large-field limit, after passing through these two avoided crossings, it will end up forming the next-highest excited ($\nu = 4$) state in the $N = 0$ subspace. The energy level that it interacted with in the last avoided crossing will now have a nodal structure much like the original $n = 2$ low-field state, which means its excitation is along the x, y-plane. After passing through an infinite number of avoided crossings, it goes on to form the lowest-lying *excited* Landau level, denoted $N = 1, \nu = 0$.[102]

In Fig. 2.13 the *diabatic* energy level is indicated with a dotted line. This would be the progression of the energy level if we were to sweep the magnetic field infinitely fast so that the probability of tunneling through the barrier between the two energy levels was unity. In

this case, the nodal structure of the state would be maintained throughout the entire range of field strength.

The example above is as simple as it gets in the intermediate field-strength region. We can see that trying to track the nodal structure of higher-lying energy levels is going to be exceptionally difficult, especially if we consider that not all avoided crossings in the energy spectrum are going to be discernible. *However, dimensional perturbation theory provides a systematic means of tracking the energy levels of diamagnetic hydrogen through the intermediate-field strength region and determining when, and where, avoided crossings must occur, even when hidden.* So in the next chapter we turn our attention to the theoreticla basis of dimensional perturbation theory. From there we begin Part II, our discussion of the original research in this dissertation.

Chapter 3

Dimensional Perturbation Theory and its Application to Diamagnetic Hydrogen

To analyze the avoided crossings appearing in the energy spectrum of diamagnetic hydrogen we use dimensional perturbation theory[103], which in the system we are considering is equivalent to angular-momentum ($|m|$) perturbation theory[54]. However, unlike angular-momentum perturbation theory this method is applicable to a wider range of more complex problems. To date dimensional perturbation theory has been applied to such diverse fields as statistical mechanics, nuclear and particle physics, quantum optics, and atomic and molecular physics[103, 104, 105, 106]. In atomic and molecular physics alone, dimensional perturbation theory has been applied to the atomic Zeeman and Stark effects[103, 106, 107], van der Waals coefficients[108], the hydrogen atom in parallel electric and magnetic fields[109, 110], two-electron and many-electron atoms, ions and molecules[103, 111], quasistationary states[106, 109, 112], potential scattering problems[107, 113], and density functional theory,[114], to name just a few. Furthermore, projects are currently underway using this theory to compute the rotational spectra of molecules[115] and virial coefficients and phase transitions in the electronic structure of atoms and molecules[116].

Dimensional perturbation theory is not only a potent method for calculating energies and other properties of many quantum-mechanical systems[103, 117], but it also provides a natural way of examining avoided crossings in diamagnetic hydrogen energy levels.

With this method, the magnetic field and Coulomb potential are both incorporated into the Hamiltonian at zeroth-order to such an extent that we can directly associate avoided crossings appearing in the E-versus-B spectrum with degeneracies arising at zeroth order.

> Therefore, this method establishes an orderly means of examining the complicated energy spectrum of diamagnetic hydrogen.

Also, all angular momentum-dependence of the problem is contained within the perturbation parameter, which we denote in this research as δ. Changing m merely amounts to resumming the energy series at a different value of δ, which is *considerably* easier than a new calculation required by other methods. This greatly simplifies examining energy levels as a function of angular momentum.

3.1 Formulation of the dimensional perturbation theory

The basic steps involved in all dimensional scaling methods, including dimensional perturbation theory, is to generalize the system to D spatial dimensions and subsequently scale the physical variables to remove the leading D-dependence[103]. In the case of dimensional perturbation theory the scaled Schrödinger equation is expanded in a perturbation series about a value of D; this expansion allows an analytic solution. With diamagnetic hydrogen (as for many systems) the infinite-dimensional limit serves this purpose well. To find the energy corresponding to the three-dimensional system the perturbation series is simply summed at the value $D = 3$ because all D-dependence is incorporated into the perturbation parameter.

The generalization of the Schrödinger equation describing a hydrogenic atom in a constant magnetic field B to D dimensions is[103]

$$\left\{-\frac{1}{2}\left(\frac{\partial^2}{\partial\rho^2}+\frac{\partial^2}{\partial z^2}\right)+\frac{\kappa^2-4\kappa+3}{8\rho^2}+\frac{B^2\rho^2}{8}-\frac{Z}{r}\right\}\Phi(\rho,z)=E(\rho,z)\Phi(\rho,z), \quad (3.1)$$

$$\kappa \equiv D+2|m|-1, \quad (3.2)$$

where the time-independent wave function $\Psi(\rho, z)$ is dimensionally scaled as $\Phi(\rho, z) = \rho^{\frac{\kappa-1}{2}}\Psi(\rho, z)$. Here, ρ and z are the D-dimensional generalization of the usual cylindrical coordinates, and the remaining $D-2$ angular coordinates have been factored out to yield the ρ^{-2} centrifugal potential term. Note that D and $|m|$ only enter the Schrödinger equation through κ.

To obtain a useful infinite-dimensional limit some of the physical quantities must be dimensionally scaled:

$$\widetilde{\rho} = \frac{\rho}{\kappa^2}, \quad \widetilde{z} = \frac{z}{\kappa^2}, \quad \widetilde{E} = \kappa^2 E, \quad \widetilde{B} = \kappa^3 B. \tag{3.3}$$

Note that the conversion between B and $\widetilde{B}$ in three dimensions is[118]

$$B(\text{tesla}) \approx \frac{29\,375 \cdot \widetilde{B}}{(1+|m|)^3}. \tag{3.4}$$

For example, 100 scaled units roughly equates to 75 T in three dimensions when $|m| = 33$.

With these scaled quantities the Schrödinger equation has the form $\mathcal{H}\Phi = \widetilde{E}\Phi$, where

$$\mathcal{H} = -\frac{1}{2}\delta^2\left(\frac{\partial^2}{\partial\widetilde{\rho}^2} + \frac{\partial^2}{\partial\widetilde{z}^2}\right) + \widetilde{V}_{eff}, \tag{3.5}$$

$$\widetilde{V}_{eff} = \frac{1-4\delta+3\delta^2}{8\widetilde{\rho}^2} + \frac{\widetilde{B}^2\widetilde{\rho}^2}{8} - \frac{Z}{\sqrt{\widetilde{\rho}^2+\widetilde{z}^2}}. \tag{3.6}$$

Note that we introduced the perturbation parameter

$$\delta \equiv \frac{1}{\kappa} = \frac{1}{D+2|m|-1} \tag{3.7}$$

into the Hamiltonian. It is important to note that, as with κ, all D- and m-dependence is accounted for in δ.

As $\kappa \to \infty$ ($\delta \to 0$) all derivative terms in the Hamiltonian vanish, producing an "electrostatic" problem; the electron settles to the minimum of the $\lim_{\delta\to 0}\widetilde{V}_{eff}(\widetilde{\rho}, \widetilde{z})$ located at $(\widetilde{\rho}, \widetilde{z}) = (\rho_m, z_m = 0)$. We denote the energy in the large κ limit, i.e. $\lim_{\delta\to 0}\widetilde{V}_{eff}(\rho_m, z_m)$,

by $\widetilde{E}_\infty$. Therefore, in the large κ limit (large D and/or $|m|$ limit) the electron of energy $\widetilde{E}_\infty$ is constrained to a hypercircle of radius $\widetilde{\rho}=\rho_m$ perpendicular to the $\hat{z}$ axis.

Using dimensionally-scaled displacements, x_1 and x_2, the origin is shifted to this minimum by means of the relations

$$\widetilde{\rho} = \rho_m + \delta^{\frac{1}{2}} x_1 , \qquad \widetilde{z} = \delta^{\frac{1}{2}} x_2 . \tag{3.8}$$

The Schrödinger equation is then expanded in powers of $\delta^{\frac{1}{2}}$,

$$\widetilde{E} = \widetilde{E}_\infty + \sum_{i=0}^{\infty} \widetilde{E}_{2i} \delta^{i+1} , \tag{3.9}$$

$$\mathcal{H}(\widetilde{\rho}, \widetilde{z}) = \widetilde{E}_\infty + \sum_{i=0}^{\infty} \mathcal{H}_i(x_1, x_2) \delta^{\frac{i}{2}+1} , \tag{3.10}$$

$$\Phi(\widetilde{\rho}, \widetilde{z}) = \Phi_0(x_1, x_2) + \sum_{i=1}^{\infty} \Phi_i(x_1, x_2) \delta^{\frac{i}{2}} . \tag{3.11}$$

By equating powers of $\delta^{\frac{1}{2}}$ we obtain an infinite set of coupled differential equations,

$$\sum_{j=0}^{p} (\mathcal{H}_j - \widetilde{E}_j) \Phi_{p-j} = 0, \quad \widetilde{E}_{2i+1} = 0 , \quad p = 0, 1, 2, \ldots . \tag{3.12}$$

The general form of $\mathcal{H}_j$ is given in Refs. [105, 119]. Equations (3.9)–(3.12) can then be solved for the expansion coefficients $\widetilde{E}_i$ and $\Phi_i(x_1, x_2)$. Of immediate importance is the solution for zeroth-order (harmonic) wave functions. When $p=0$ in Eq. (3.12) we obtain $(\mathcal{H}_0 - \widetilde{E}_0)\Phi_0 = 0$, where

$$\mathcal{H}_0 = -\frac{1}{2}\left(\frac{\partial^2}{\partial x_1^2} + \frac{\partial^2}{\partial x_2^2}\right) + \frac{1}{2}\omega_1^2 x_1^2 + \frac{1}{2}\omega_2^2 x_2^2 - \frac{1}{2\rho_m^2} \tag{3.13}$$

has been put into the same form as a two-dimensional simple harmonic oscillator (SHO) by defining the so-called Langmuir oscillation frequencies

$$\omega_1^2 = \frac{3}{4\rho_m^4} - \frac{2Z}{\rho_m^3} + \frac{\widetilde{B}^2}{4} , \qquad \omega_2^2 = \frac{Z}{\rho_m^3} . \tag{3.14}$$

Both the large-κ limit ($\rho = \rho_m$, $z = z_m$) and the harmonic zeroth-order wave functions Φ_0 (which describe quantum fluctuations about the large-κ limit) not only automatically adapt as B changes, but they adapt in a way that is sensitive to the interplay between the Coulombic and diamagnetic potentials. Therefore, dimensional perturbation theory is applicable to the entire range of magnetic field strengths, not just to the high- or low-field regions.

Since Eq. (3.12) for $p=0$ is a two-dimensional SHO equation for $\Phi_0(x_1, x_2)$, then to this harmonic order the energy is simply

$$\widetilde{E} \approx \widetilde{E}_\infty + \delta \widetilde{E}_0 \,, \tag{3.15}$$

where

$$E_0 = \widetilde{E}_\infty + \delta\left[\left(\nu_1 + \frac{1}{2}\right)\omega_1 + \left(\nu_2 + \frac{1}{2}\right)\omega_2 - \frac{1}{2\rho_m^2}\right]. \tag{3.16}$$

We assign the ket

$$|\nu_1 \nu_2\rangle \equiv \Phi_0(x_1, x_2) = h_{\nu_1}(\sqrt{\omega_1}\, x_1)\, h_{\nu_2}(\sqrt{\omega_2}\, x_2) \tag{3.17}$$

to represent the "unperturbed" harmonic basis, where the ν_i are the quantum numbers of the SHO eigenfunctions $h_{\nu_i}(x)$. The quantum numbers ν_1 and ν_2 are the number of nodal lines in the $\hat{z}$ direction and nodes in the $\hat{\rho}$ direction, respectively. The basic topology of nodal lines is preserved at finite κ with the provision that states are traced diabatically across avoided crossings. (Tracing the energy levels diabatically means following the dotted line in Fig. 2.13.) Therefore we use the quantum numbers ν_1 and ν_2 to label the *nodal structure* of the state corresponding to a particular energy level.

We are now in a position to meaningfully assign quantum numbers that describe the nodal structure of diamagnetic hydrogen in both limits of field strength. In the low-field limit:

- The principle quantum number $n = \nu_1 + k + |m| + 1$.
- In terms of ν_1, we have therefore $\nu_1 = n - k - |m| - 1$.
- $\nu_2 = k$.
- Therefore, ν_2 determines the parity of the system, $\pi_z = (-1)^{\nu_2}$, with even values of ν_2 corresponding to even-parity, and so on.
- For circular states, $n = |m| + 1$, so in this case $\nu_1 = \nu_2 = 0$. Therefore, for a given m subspace the circular state will always be labeled $|\nu_1, \nu_2\rangle = |0, 0\rangle$. (This is true in both limits.)

In the $B \rightarrow \infty$ limit,

- The Landau channel number N is simply $N = \nu_1$.
- The Coulomb quantum number ν is given by $\nu = \text{INT}[\frac{\nu_2+1}{2}]$, where INT[$x$] denotes the integer part of x, rounded down.
- Note that taking only the integer part will guarantee that that the odd-parity and even-parity wave functions of the one-dimensional hydrogen problem have the same nodal structure because ν counts the number of nodes along the z-axis. For example, both the $\nu_2 = 3$ and $\nu_2 = 4$ states correspond to $\nu = 2$, and thus have one node along the z-axis. (See Fig. 2.11.)

The correlation between the low-field and high-field states of diamagnetic hydrogen is summarized in Fig. 3.1.

Therefore, the quantum numbers ν_1 and ν_2 of the harmonic-order, dimensional perturbation theory Hamiltonian provide meaningful labels of the wave functions of diamagnetic hydrogen in both limits of field strength.

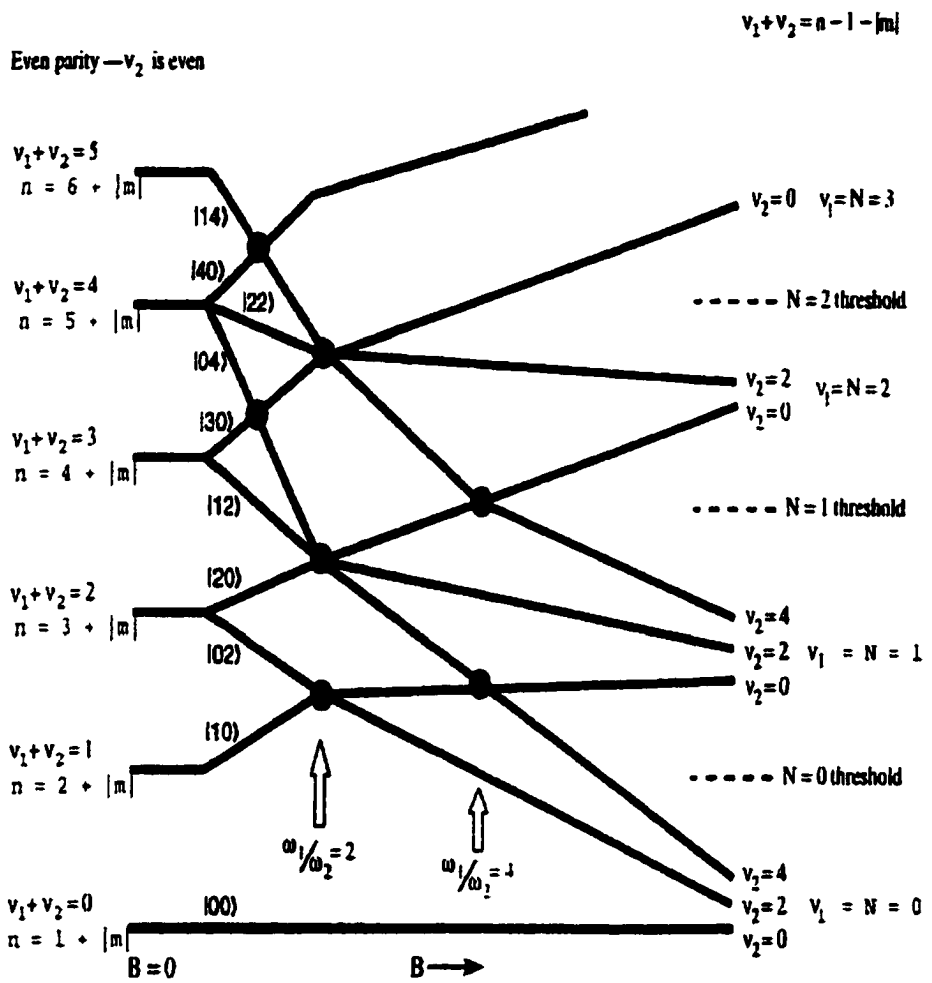

Figure 3.1: A correlation diagram, which we originally published in Ref. [135], that demonstrates how the quantum numbers ν_1 and ν_2 order the energy at the two extremes of field strength. The upward arrows point to level crossings that correspond to Fermi resonances, as discussed in Chap. 4.

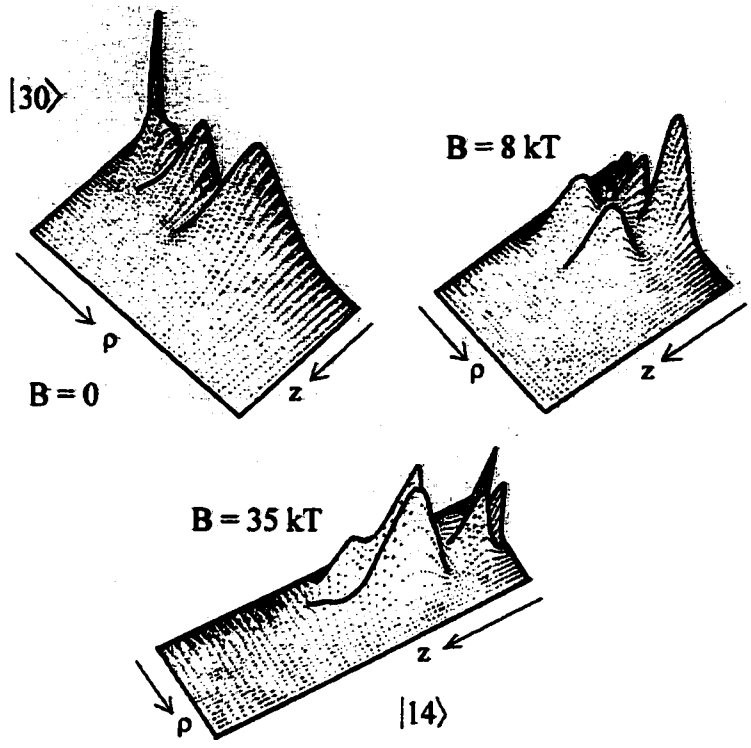

Figure 3.2: Same as Fig. 2.12 but labeled instead with the ν_1 and ν_2 quantum numbers of dimensional perturbation theory. Again, $m = 1$, with even-parity. (a) Zero-field limit, where $n = 5$, $k = 0$. Using the prescription in this chapter for defining ν_1 and ν_2 we have $\nu_1 = n - k - |m| - 1 = 3$ and $\nu_2 = k = 0$, therefore this state is the $|\nu_1, \nu_2\rangle = |3, 0\rangle$ state. (b) $B = 8$ kT. This is the region of intermediate field strength, and assigning meaningful quantum numbers is impossible. (c) $B = 35$ kT. This is the high-field limit. By examining Fig. 3.1 and following the $|30\rangle$ state *adiabatically* we find that this situation corresponds to the $|14\rangle$ state, signifying one node in the radial direction and four nodes in the z-direction.

In Fig. 3.2 we show an example of how the quantum numbers ν_1 and ν_2 count the nodes in the ρ and z directions.

The system parity π_z, which refers to reflection in the z coordinate, is determined by the value of ν_2 — *even* parity states correspond to *even* values of ν_2; likewise for odd parity states. Although we largely limit the following discussion to odd parity states, the response of the system described by Eq. (3.1) to adiabatic changes in $\widetilde{B}$, most importantly the energy spectra and branch-point trajectories as functions of $\widetilde{B}$, are qualitatively the same no matter which parity we choose to consider.

In the next section we discover a one-to-one correspondence between the avoided crossings in the E-versus-B and the E-versus-$|m|$ spectra. To illustrate this relationship, we only need to look at a couple of avoided crossings in each of the E-versus-B and E-versus-$|m|$ spectra in detail. Because the perturbation parameter δ in Eq. (3.7) is especially small when $|m|$ is large, dimensional perturbation theory is particularly easy to apply to circular Rydberg states[119]. For that reason, we now apply dimensional perturbation theory to circular and near-circular states of diamagnetic hydrogen[120] and see how the system energy $E(\widetilde{B}, |m|)$ responds as both the magnetic field strength $\widetilde{B}$ (Sec. 4.2) and angular momentum $|m|$ (Sec. 4.3) independently change.

Part II

Singularity Structure and Its Relation to Avoided Crossings of Diamagnetic Hydrogen

Chapter 4

Avoided Crossings of Diamagnetic Hydrogen as Functions of Magnetic Field Strength and Angular Momentum

The material in this chapter is largely derived from J.R. Walkup, M. Dunn, D.K. Watson, and T.C. Germann, *Physical Review A* **58**, 4668-4682 (1998).

We have shown that the coupling between the two degrees of freedom in the diamagnetic hydrogen problem creates a markedly different energy ordering in two important extremes of B: For $B = 0$ the energy spectrum is hydrogenic, while at sufficiently large B the energy levels divide into a series of Landau channels. These channels are supported by the same radial wave functions which describe motion perpendicular to a magnetic field as found with a free electron in a magnetic field. Between these two limits of B the interplay between the Coulombic and diamagnetic contributions creates a complicated, often highly irregular, energy spectrum. Each energy level is perturbed from above and below by adjacent levels as the system evolves from the hydrogenic to Landau limits so the response of the system as B is increased is necessarily quite complex. Even for very low B the diamagnetic term generates ℓ-mixing in each hydrogenic n-manifold.

The most distinctive feature of the response of the energy spectrum to adiabatic changes in the B-field is an intricate array of avoided crossings, which provide the mechanism for state reordering with energy E as B is changed. By this we mean that the nodal structures of the states exchange diabatically as the system is taken through the avoided crossings by varying the external magnetic field.[121] However, the appearance of avoided crossings is not restricted merely to variations in B. In the particular system we have chosen to study,

the magnetic quantum number m is a conserved quantity because of the separability of the azimuthal degree of freedom. We show that avoided crossings also appear in the energy spectrum as m of the system is incremented in value. (Actually, m is treated in this research as a continuous real parameter, interpolated between integer values.) As when B is varied for fixed m, the nodal structures of the states diabatically exchange across the avoided crossings [122].

Avoided crossings are not always easy to distinguish. Some are so narrow that energy levels superficially appear to actually cross. (Energy levels with the same parity and m cannot cross because of the Wigner-von Neumann non-crossing rule[123]). On the other hand, some avoided crossings are so broad that they are not easily discernible. These are termed *hidden* avoided crossings[124, 125]. Regardless of whether they are hidden or not, the nodal structure of the states still exchange diabatically across the avoided crossings. Because of this very important physical effect, it is important to have a strategy to predict the existence of avoided crossings and where they occur, hidden or not. In this chapter we offer such a strategy, which relies on understanding the mathematical structure resulting from degeneracies between energy levels. Furthermore, we can use the *same* mechanism that explains the appearance of avoided crossings in the E-versus-B spectrum to understand those appearing in the E-versus-$|m|$ spectrum. Therefore, this mechanism directly relates the response of the energy to independent changes in B and $|m|$.

In this chapter we examine the degeneracies of diamagnetic hydrogen for two characteristic energy-level interactions, and from this information we explain the existence and locations of some low-lying avoided crossings appearing in its energy spectrum. In Sec. 4.1 we consider a simple example in which a system parameter is varied adiabatically. We then explain how the resulting avoided crossing in the energy spectrum is related to square-root branch-point degeneracies appearing in the complex parameter-plane. Using the resulting energy series, in Sec. 4.2 we plot energy levels as functions of magnetic field strengths at two different orders in dimensional perturbation theory — harmonic (zeroth) order, which

corresponds to Eq. (3.13), and higher (28th) order, which corresponds to $p = 28$ in Eq. (3.12). We show that we can relate the avoided crossings appearing in the energy spectrum to energy degeneracies appearing at harmonic order, as expected.

In Sec. 4.3 we instead fix B and plot energy levels as the *angular momentum* $|m|$ is changed. We show that the avoided crossings appearing in this situation are directly related to those appearing in the E-versus-B spectrum. As demonstrated in this chapter, this relationship is illuminated by examining the anatomy of the branch-point degeneracies connecting the two energy levels in question. We use this anatomy in Sec. 4.4 to predict the appearance of avoided crossings in both types of spectra.

We expect the analysis in Sec. 4.4 to apply to all avoided crossings appearing throughout the energy spectra (both E-versus-B and E-versus-m) of diamagnetic hydrogen. However, there is one small subset of avoided crossings that demands expanded treatment, and we consider this subset of avoided crossings in Sec. 4.5.

This chapter focuses solely on examining the odd-parity states of diamagnetic hydrogen. As we explain in Sec. 4.6, all results apply to the even-parity states equally well.

4.1 Energy degeneracies and avoided crossings

To illustrate the relationship between energy degeneracies and avoided crossings, we use an example much like the one discussed by Bender and Orszag[126]. Consider the time-independent Schrödinger equation of a simple two-level system,

$$\mathcal{H}\Psi_{\pm} = E^{\pm}\Psi_{\pm}, \tag{4.1}$$

where

$$\mathcal{H} = \begin{pmatrix} b & c \\ c & d \end{pmatrix}. \tag{4.2}$$

Here we consider b as a parameter that we will vary continuously while keeping all other parameters fixed in value. (In this sense, b is analagous to $\widetilde{B}$ or $|m|$ in this research, depending on which parameter is varied while the other one is held fixed.) Equations (4.1) and (4.2) model a general quantum mechanical problem in those regions where only two states interact strongly enough to warrant consideration. If $d = -b$, then these equations model a well-known Landau-Zener problem, where b is associated with a linearly-varying, time-dependent magnetic field, and c measures the splitting between energy levels caused by a constant magnetic field oriented perpendicular to the first. (See Appendix E and references therein.) The energy eigenvalues as functions of b are plotted in Fig. 4.1 which shows an avoided crossing centered about $b = d$. As $b \rightarrow \pm\infty$, the energies E^+ and E^- and the eigenstates Ψ_+ and Ψ_- limit to the $c = 0$ solutions,

$$\phi_1 = \begin{pmatrix} 1 \\ 0 \end{pmatrix} \tag{4.3}$$

with energy $E_1 = b$ and

$$\phi_2 = \begin{pmatrix} 0 \\ 1 \end{pmatrix} \tag{4.4}$$

with energy $E_2 = d$. Thus when b is sufficiently far from the avoided crossing, the energies and eigenstates are approximated by the $c = 0$ energies and eigenstates. We use ϕ_1 and ϕ_2 to label the physical characteristics of the finite b eigenstates away from the avoided crossings. Since the energy ordering of the $c = 0$ eigenstates ϕ_1 and ϕ_2 is different from one extreme value of b to the other, the states must exchange physical characteristics diabatically somewhere in the spectrum — across the avoided crossing. If the physical characteristic of the state defined by ϕ_2 is associated with the *upper* energy level E^- when $b \ll d$, then ϕ_1 will be associated with the *lower* level E^+. However, this ordering of states reverses for $b \gg d$, so the physical characteristics of both energy levels exchange across the avoided crossing.

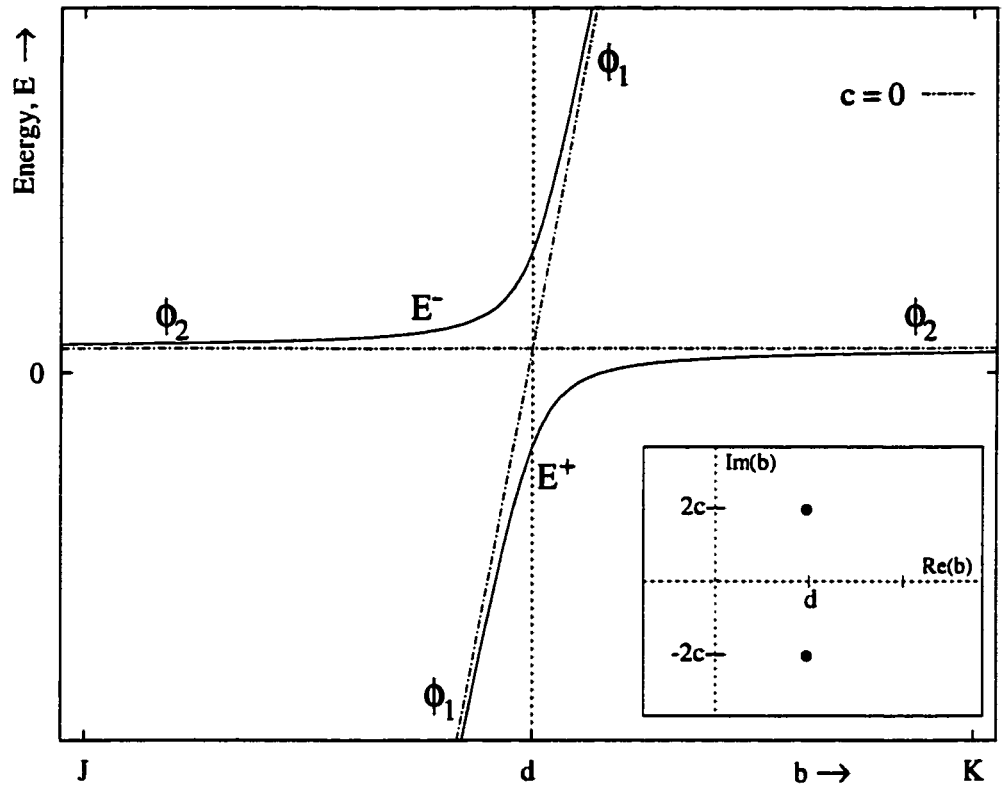

Figure 4.1: Energy levels E^+ (lower level) and E^- (upper level) arising from Eq. (4.1), with b treated as a parameter. Note that the physical characteristics of the states, defined as either ϕ_1 or ϕ_2, exchange diabatically as the system progresses through the avoided crossing. In other words, if we (infinitely slowly) increase b from J to K, the state corresponding to the E^+ level would transform from ϕ_1 to ϕ_2 in the avoided crossing region. For $c=0$ the system becomes separable, so at this limit the energy levels (shown by dot-dashed lines) cross at $b=d$. The inset shows the square-root branch points lying in the complex-b plane that connect the two energy levels.

In this example the avoided crossing is clearly visible in the energy spectrum, but as we stated previously such is not always the case. Yet the existence of hidden avoided crossings remains physically important since the physical characteristic of each interacting energy level exchanges when the system passes through the avoided crossing. Therefore, it is important to find a distinguishing characteristic of the system that signifies the locations of avoided crossings, whether they are hidden or not.

From Eqs. (4.1) and (4.2) we can write the secular equation in the form

$$(E - E^+)(E - E^-) = E^2 - (E^+ + E^-)E + E^+E^- = 0, \tag{4.5}$$

where

$$E^+ + E^- = b + d \quad \text{and} \quad E^+E^- = bd - c^2. \tag{4.6}$$

The avoided crossing occurs when the parameter b, restricted to the real line, passes closest to the complex value of b where the two eigenenergies are degenerate. According to Eqs. (4.6), in order for $E^+ = E^-$ the parameter b must satisfy $b^2 - 2db + 4c^2 + d^2 = 0$, that is

$$b^{\pm} = d \pm 2ic. \tag{4.7}$$

Note that the degeneracies occur at complex values of b; physical (real-valued) energies cannot cross as b is held on the real line and swept past the degeneracy points. (The Schwarz Reflection Principle[127] ensures that degeneracies occur at complex-*conjugate* values of b.) Rather, as shown in Fig. 4.1, we see an avoided crossing centered about $b = d$ because the energies come closest to degeneracy when b is closest to d.

The analytic solutions for the eigenenergies are

$$E_{\pm} = \frac{1}{2}\left[b + d \pm \sqrt{b^2 - 2db + 4c^2 + d^2}\right], \tag{4.8}$$

thus we find square-root branch-point singularities at the points where the energies are degenerate[128]. In other words, *the two square-root branch points provide a signature for the appearance of avoided crossings.* (See the inset in Fig. 4.1.)

A square root appeared in Eq. (4.8) because we considered an interaction between only two levels. When three levels interact, one might think that the degeneracies would be marked by both cube-root as well as square-root branch points. However, as explained by Bender and Orszag, higher-order, three-state degeneracies at which cube-root singularities can occur are extremely unlikely[126]. This reasoning applies to degeneracies and higher-order singularities involving more than three states as well. Therefore, as a general rule avoided crossings will be marked by the nearby presence of *square-root* branch points no matter how many states effectively interact[129].

Naturally, we cannot properly describe diamagnetic hydrogen with a simple 2×2 matrix equation; rather we require an infinite-dimensional matrix equation, limited to finite dimensions for practicality. Dimensional perturbation theory, when formulated in the matrix method[105] (the method used for large-order calculations in this research), automatically furnishes matrix equations of finite dimension at finite order. But as we increase the rank of the matrix equation it is natural to question what happens to the square-root branch-point structure of the system. There are at least four possibilities[126]:

1. The square-root branch points stabilize and
   (a) remain well separated from each other or
   (b) form a sequence that becomes denser and denser towards some limiting point.
2. The square-root branch points coalesce to form more complex singularities in the limit of infinite-dimensional matrices.
3. The square-root branch points move to infinity.
4. A square root branch point present when the matrix equation is of a certain dimensionality is not present at other dimensionalities.

We are only interested in avoided crossings which stabilize as the dimension of the matrix equation is increased, and thus we rule out square-root branch points which behave as in items 3 and 4. As we shall see, for the energy level interactions considered in this research the nearby square-root branch-point degeneracies behave as in item 1a.

Finally, we note that for simple two-level systems Eq. (4.7) requires that real-valued branch points must exist at the same location on the real axis.[130] However, for higher ranking matrix equations this requirement no longer applies — real-valued branch points can exist at two different points on the real line.

4.2 Energy as a function of magnetic field strength

We saw in Chap. 3 that in the harmonic limit the Hamiltonian of the diamagnetic hydrogen atom reduces to

$$\mathcal{H}_0 = -\frac{1}{2}\left(\frac{\partial^2}{\partial x_1^2} + \frac{\partial^2}{\partial x_2^2}\right) + \frac{1}{2}\omega_1^2 x_1^2 + \frac{1}{2}\omega_2^2 x_2^2 - \frac{1}{2\rho_m^2}\,. \tag{4.9}$$

This harmonic limit (that is, the limit corresponding to the zeroth-order Hamiltonian $\mathcal{H}_0$) is not only mathematically useful but incorporates many features of the three-dimensional system. In fact, the harmonic Hamiltonian incorporates the effects of $\widetilde{B}$ to such an extent that the ordering of states, with respect to energy, correlates exactly with that in three dimensions in both the small-$\widetilde{B}$ and $\widetilde{B} \to \infty$ limits. This is a key result, because if the harmonic energy spectrum has the same basic structure as the exact spectrum, then we maintain the same energy-level ordering as higher-order corrections are incorporated, making the spectrum easier to examine. This is a major advantage of dimensional perturbation theory over many traditional methods.

The harmonic Hamiltonian $\mathcal{H}_0$ is also completely separable in $\hat{\rho}$ and $\hat{z}$, that is the $\hat{\rho}$ and $\hat{z}$ degrees of freedom are uncoupled. This has important consequences for the harmonic energy spectrum which results from Eq. (3.13). As shown in Fig. 4.2 (for odd-parity states):

1. The harmonic energy levels do not interact and actually cross.

2. The most distinct characteristics of the harmonic spectrum are the numerous *Fermi resonances*[131, 132] (degeneracies), that appear at certain values of $\widetilde{B}$, some of which we indicate with vertical lines in the figure. (See also Fig. 3.1 in Chap. 2.) These values of $\widetilde{B}$ are determined by the Fermi resonance condition $\ell\omega_1 = k\omega_2$, where ℓ and k are any two integers[124]. For example, as highlighted in the figure, the $|11\rangle$ and $|05\rangle$ states are degenerate at harmonic order near $\widetilde{B} = 320$, where the ratio $\omega_1/\omega_2 = 4$. Therefore, we say that these two states, even at converged orders, are related through a 4:1 Fermi resonance (see below). To determine which states coincide with a given Fermi resonance, consider two states $|a\,b\rangle$ and $|c\,d\rangle$ (the variables b, c, and d here are unrelated to the same variables in the previous section). The harmonic energy levels of these two states cross at the X:Y Fermi resonance provided that $Xa+Yb=Xc+Yd$. For example, the $|15\rangle$ and $|41\rangle$ harmonic levels cross at the 4:3 Fermi resonance, since $4\cdot 1+3\cdot 5=4\cdot 4+3\cdot 1$. We show more examples in Table 4.1. In Figs. 4.2 and 3.1 we highlight energy-level crossings at two particular Fermi resonances — a 2:1 Fermi resonance ($\omega_1 = 2\omega_2$) between the $|03\rangle$ and $|11\rangle$ states, and a 4:1 Fermi resonance ($\omega_1 = 4\omega_2$) between the $|05\rangle$ and $|11\rangle$ states. Although the $|11\rangle$ and $|03\rangle$ states are not the only states that interact through a 2:1 Fermi resonance, we will only consider these two states when we discuss this particular Fermi resonance. Along the same lines, we will only discuss the interaction between the $|11\rangle$ and $|05\rangle$ states when we focus on the 4:1 Fermi resonance.

At finite $|m|$, terms in the Hamiltonian which couple the $\hat{\rho}$ and $\hat{z}$ degrees of freedom are no longer negligible. Therefore level crossings become forbidden by the von Neumann-Wigner non-crossing rule and are replaced by avoided crossings. The avoided crossing center at finite $|m|$ is displaced from the harmonic crossing because of the $|m|$-dependence of the energy levels. As an example, in Fig. 4.3 the 4:1 crossing highlighted in Fig. 4.2 is displaced from $\widetilde{B} = 320.8$ (the harmonic *level* crossing) to $\widetilde{B} = 138.4$ (the *avoided*

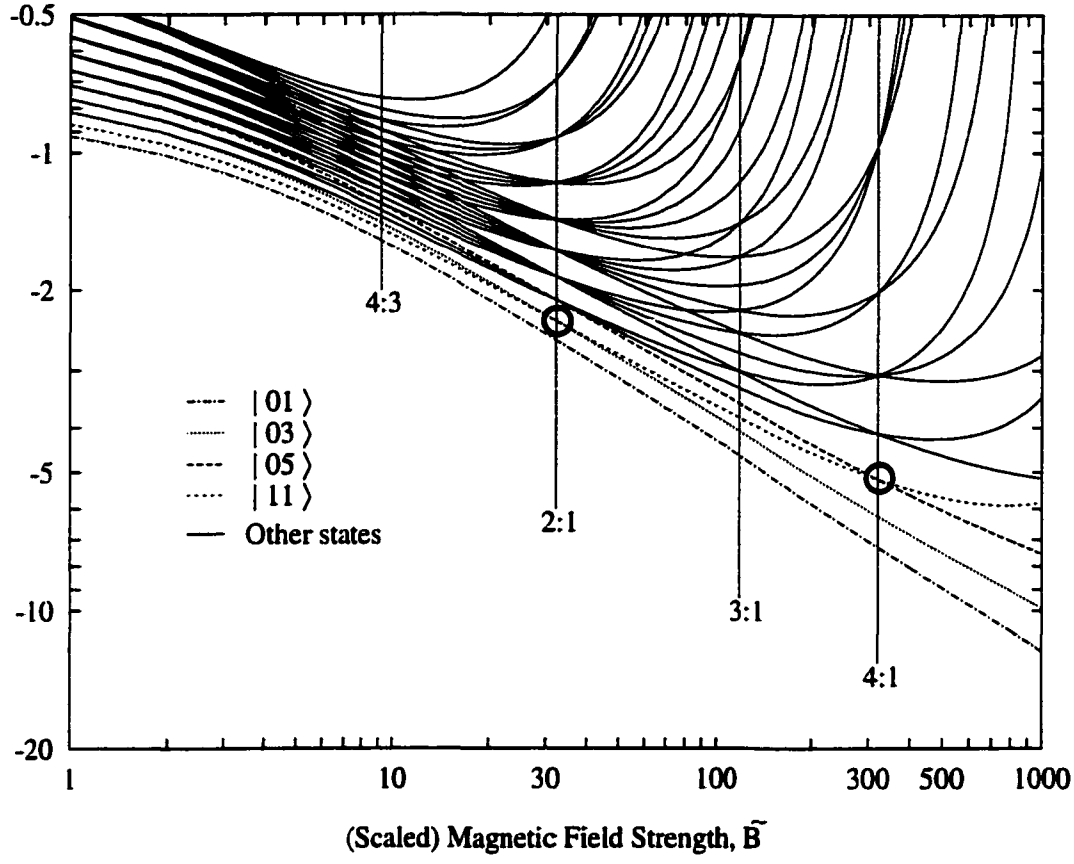

Figure 4.2: Harmonic (zeroth-order) energy levels as functions of $\widetilde{B}$ for diamagnetic hydrogen. The vertical axis measures binding energy in mRyd for $|m| = 33$. The vertical lines denote some prominent degeneracies (Fermi resonances) appearing in the spectrum. The crossings explicitly discussed the most in this chapter are highlighted in bold circles; one associated with a 4:1 Fermi resonance at $\widetilde{B} = 320.8$ and the other with a 2:1 Fermi resonance at $\widetilde{B} = 32.1$. Only levels corresponding to the ten lowest hydrogenic ($\widetilde{B} = 0$) shells are shown.

Table 4.1: Fermi resonances and corresponding interacting states appearing in the harmonic-order energy spectrum in Fig. 4.2, with the lowest energy interactions appearing highest in the table. The (scaled) magnetic field strength at which each resonance appears is given in parentheses, rounded to the nearest whole number. Each entry corresponds to an individual interaction, many of which involve more than two states. Any even-parity states that are degenerate to those listed were omitted. Also, some of the higher-lying Fermi resonances in Fig. 4.2 were omitted for brevity.

8:7 (5)	6:5 (6)	4:3 (9)	3:2 (13)	8:5 (16)	12:1 (32)	8:3 (79)	3:1 (118)	4:1 (321)
$\|09\rangle\|71\rangle$	$\|07\rangle\|51\rangle$	$\|05\rangle\|31\rangle$	$\|07\rangle\|41\rangle$	$\|09\rangle\|51\rangle$	$\|03\rangle\|11\rangle$	$\|09\rangle\|31\rangle$	$\|07\rangle\|21\rangle$	$\|05\rangle\|11\rangle$
$\|19\rangle\|81\rangle$	$\|17\rangle\|61\rangle$	$\|15\rangle\|41\rangle$	$\|17\rangle\|51\rangle$	$\|19\rangle\|61\rangle$	$\|05\rangle\|21\rangle$	$\|19\rangle\|41\rangle$	$\|09\rangle\|23\rangle$	$\|07\rangle\|13\rangle$
	$\|09\rangle\|53\rangle$	$\|07\rangle\|33\rangle$	$\|09\rangle\|43\rangle$		$\|07\rangle\|15\rangle$		$\|17\rangle\|31\rangle$	$\|09\rangle$
					$\|23\rangle\|31\rangle$			$\|15\rangle\|21\rangle$
	$\|27\rangle\|71\rangle$	$\|25\rangle\|51\rangle$	$\|27\rangle\|61\rangle$		$\|09\rangle\|17\rangle$		$\|19\rangle\|33\rangle$	$\|17\rangle\|23\rangle$
					$\|25\rangle\|33\rangle\|41\rangle$			
	$\|19\rangle\|63\rangle$	$\|17\rangle\|43\rangle$	$\|19\rangle\|53\rangle$		$\|19\rangle\|27\rangle$		$\|27\rangle\|41\rangle$	$\|19\rangle$
					$\|35\rangle\|43\rangle\|51\rangle$			$\|25\rangle\|31\rangle$

crossing). In Fig. 4.4 we show the avoided crossing in Fig. 4.3 in more detail. We can see that the two energy levels do not cross. Despite this shift in location, we can still associate the avoided crossing with the 4:1 Fermi resonance because the location of the avoided crossing gradually shifts to the location of the level crossing (associated with the 4:1 Fermi resonance) as $|m| \to \infty$.

> *Therefore, even though the spectrum of diamagnetic hydrogen contains a complex arrangement of avoided crossings, we can use the harmonic energy spectrum to assign each avoided crossing to a particular Fermi resonance.*

We now turn our attention to the avoided crossings that appear between two energy levels when we plot the energy as a function of *angular momentum*. We show that not only is there a clear relationship between the E-versus-B and the E-versus-$|m|$ spectra, but that we can understand this relationship by examining the branch points that connect the two energy levels.

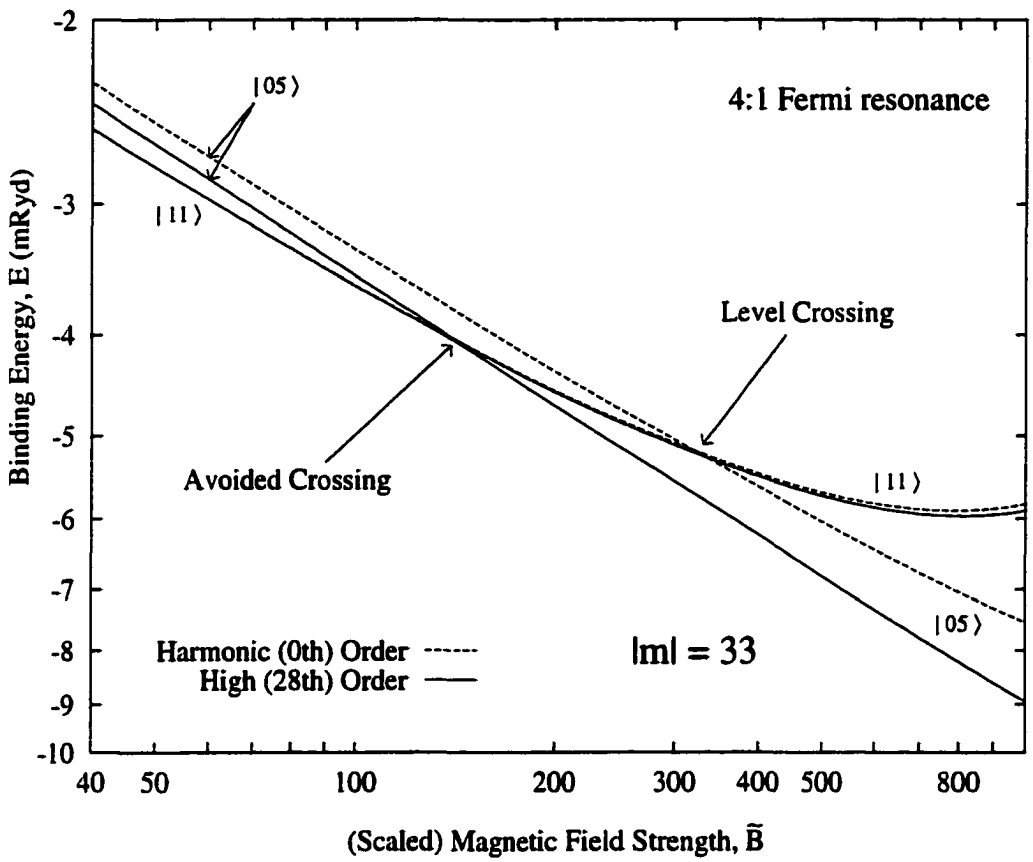

Figure 4.3: Harmonic ($p = 0$) and convergent ($p = 28$) energy levels of the $|m| = 33$ $|05\rangle$ and $|11\rangle$ states related to the 4:1 Fermi resonance degeneracy highlighted in Fig. 4.2. Note the shift of the minimum energy separation to lower $\tilde{B}$ in the convergent spectrum.

4.3 Energy as a function of angular momentum

In Fig. 4.4 an avoided crossing in the E-versus-$\widetilde{B}$ spectrum appears[133] at $\widetilde{B}=138.4$ when the angular momentum is fixed at $|m|=33$. From Eq. (3.4) this corresponds to $B=103.4$ tesla.[134] We now consider $|m|$ as a continuous real parameter and see how the system energy responds as B is held fixed at 103.4 tesla and $|m|$ is changed.

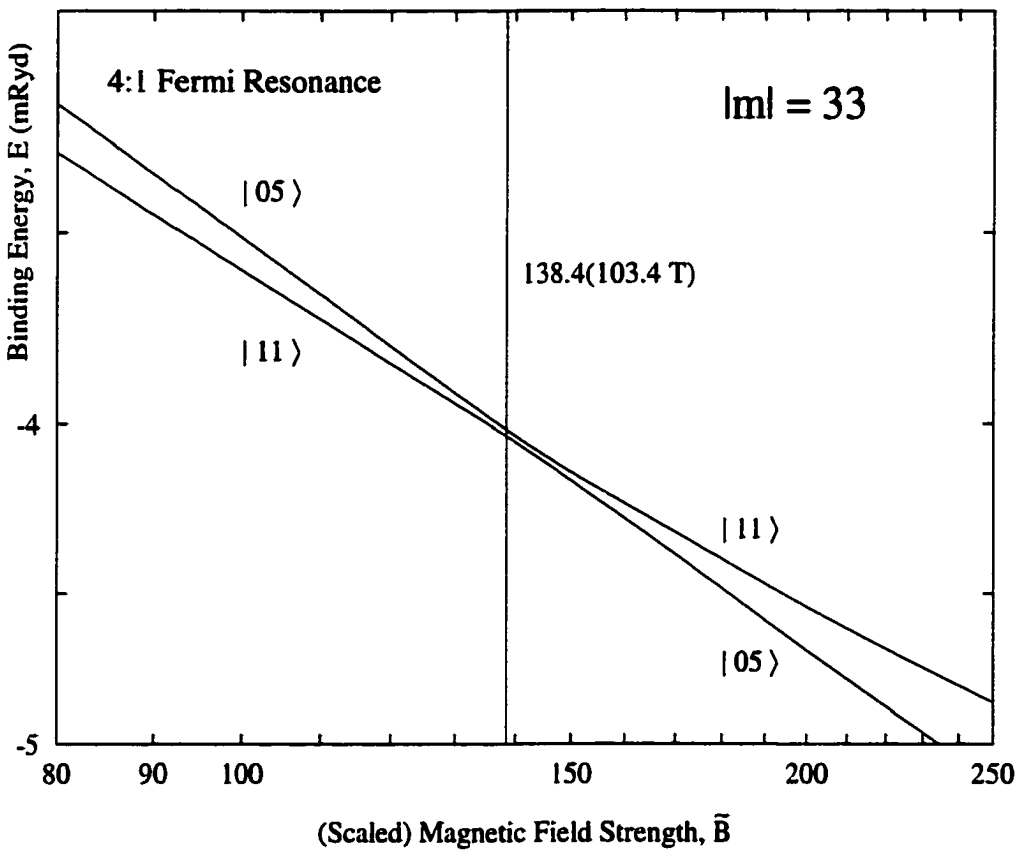

Figure 4.4: Detail of the converged ($p=28$) energy levels shown in Fig. 4.3. The nodal structure of the wave function, which is represented by $|\nu_1\nu_2\rangle$, is exchanged diabatically as the magnetic field sweeps past the avoided crossing. Note the avoided crossing center occurs at $\widetilde{B}=138.4$, which is equivalent in this case ($|m|=33$) to $B=103.4$ tesla (noted in parentheses).

Consider Fig. 4.5, which shows the same two energy levels for the 4:1 Fermi resonance as $|m|$ is changed. With $B=103.4$ tesla, the avoided crossing occurs near $|m| \equiv |m_0| = 33$, rounded to the nearest integer. Therefore, there is a strong correspondence between avoided

crossings appearing in the E-versus-B spectra and those appearing in the E-versus-$|m|$ spectra — if $|m|$ is fixed at $|m_0|$ while B is swept, an avoided crossing appears at some value $B \equiv B_0$. Correspondingly, if B is fixed at B_0 while $|m|$ is swept, an avoided crossing appears at (or very near) $|m_0|$. This correlation between the avoided crossings in the E-versus-B and the E-versus-$|m|$ spectra points to the existence of nearby degeneracies which cause an avoided crossing whether we sweep B or $|m|$. We discuss this in detail in the next two sections.

Before moving on, we should note that the avoided crossings that appear in the E-versus-$|m|$ spectrum are harder to find than those appearing in the E-versus-B spectrum. One reason for this is the leading $\widetilde{E}_\infty$ in Eq. (3.9) which does not affect the dynamics of the problem (that is, which state is associated with each energy level), but because of its $|m|$-dependence tends to mask the appearance of the avoided crossing. Therefore subtracting this term from the energy series does not affect where an avoided crossing appears, but rather makes the avoided crossing more visible. The subsequent energy series has a leading δ that is also a function of $|m|$ but, as in $\widetilde{E}_\infty$, does not affect the dynamics of the problem. Therefore, we factor this term out of the series as well. The result is a rescaling of the series as $\widetilde{E}(\text{Rescaled}) = (\widetilde{E} - \widetilde{E}_\infty)/\delta$ whenever we calculate the energy with respect to changes in $|m|$. Also, for these cases we use total energies, not binding energies. Therefore, the vertical axes on such plots change accordingly.

4.4 Energy level characterization and avoided crossings

In the next chapter we argue that the behavior of the branch points as functions of $\widetilde{B}$ for both the 4:1 and 2:1 Fermi resonance indicates that the energy levels of a two-state Fermi resonance has the following analytic form:

$$E_\pm(\delta, \widetilde{B}) = \widetilde{E}_a(\delta, \widetilde{B}) \pm \widetilde{E}_b(\delta, \widetilde{B}) \sqrt{\delta - \tilde{\delta}_+(\widetilde{B})} \sqrt{\delta - \tilde{\delta}_-(\widetilde{B})}\,. \tag{4.10}$$

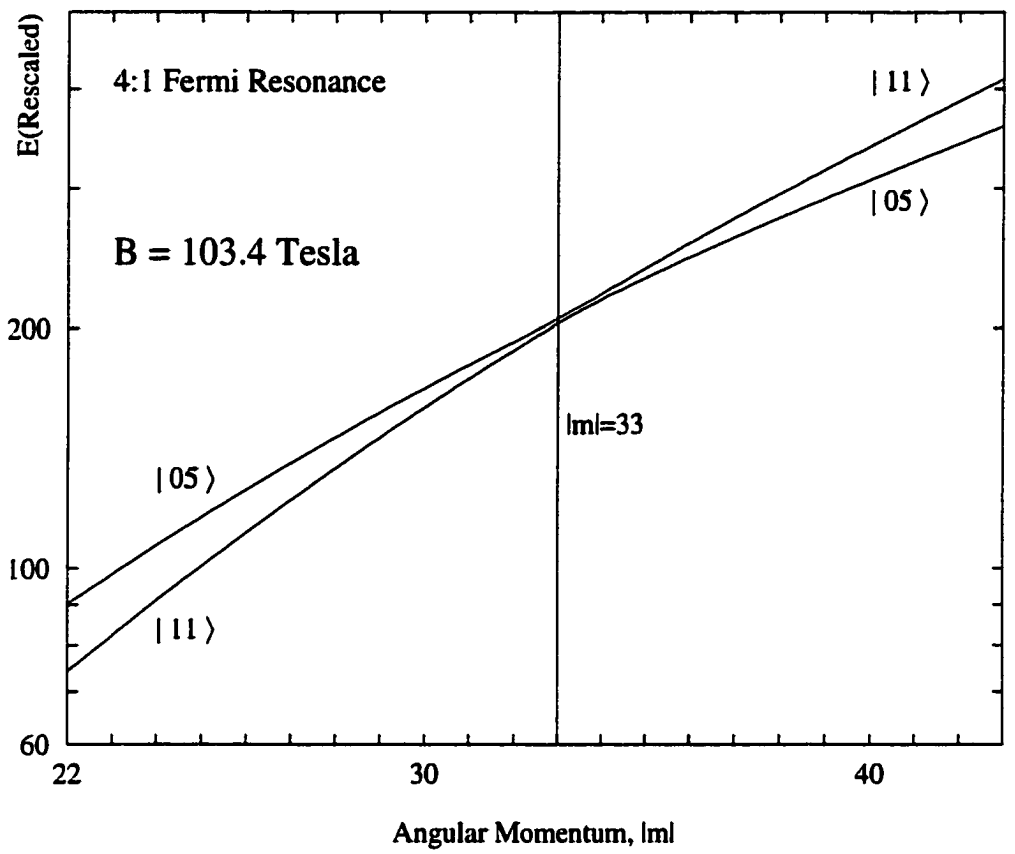

Figure 4.5: In contrast to Fig. 4.4, here we plot E as a function of $|m|$, not $\widetilde{B}$, with B held fixed at 103.4 tesla. Note that the avoided crossing is centered about $|m| = 33$ (rounded to the nearest integer). Note the change in scaling for the vertical axis.

For the rest of this discussion keep in mind that δ is directly related to $|m|$ in three dimensions through the relation $\delta = 1/(2+2|m|)$. The branch-point locations $\tilde{\delta}_+(\tilde{B})$ and $\tilde{\delta}_-(\tilde{B})$ are solutions of the equation

$$\Delta E(\delta, \tilde{B}) \equiv E_+(\delta, \tilde{B}) - E_-(\delta, \tilde{B}) = 0 \tag{4.11}$$

for fixed $\tilde{B}$. (See Sec. 4.1.)

The branch-point trajectories in the complex δ-plane are shown for a 4:1 and a 2:1 Fermi resonance in Figs. 4.6 and 4.7, respectively. Notice that the branch points for the 4:1 Fermi resonance in Fig. 4.6 are initially complex conjugates of one another and approach the origin as $\tilde{B}$ increases towards the value $\tilde{B} = 320.8$. (This is the same value of $\tilde{B}$ which corresponds to the 4:1 Fermi resonance.) As $\tilde{B}$ increases beyond this value the branch points form on the negative real axis and head towards $-\infty$, although at slightly different rates.

The branch-point structure of the 2:1 Fermi resonance in Fig. 4.7 looks more complicated. Here, the branch points are complex-conjugate until $\tilde{B} \approx 25.1$, at which point they coalesce onto the negative real axis. As $\tilde{B}$ further increases one of the branch points will head towards $-\infty$ while the other will head towards the origin, reaching that point at $\tilde{B} \approx 32.1$. (This value of $\tilde{B}$ corresponds to the 2:1 Fermi resonance.) From there the latter branch point reverses direction and both branch points will then be moving towards $-\infty$.

As required, when δ equals either $\tilde{\delta}_+(\tilde{B})$ or $\tilde{\delta}_-(\tilde{B})$ the energies E_+ and E_- become equal (degenerate). Note that $\tilde{\delta}_- = (\tilde{\delta}_+)^*$ unless the branch points lie on the real axis (again, a consequence of the Schwarz Reflection Principle.) Thus when δ lies on the real axis (the physically relevant situation) and the branch points lie off the real axis in the complex plane, δ is symmetrically placed between the complex conjugate pair of branch points and the term $\sqrt{\delta - \tilde{\delta}_+(\tilde{B})}\sqrt{\delta - \tilde{\delta}_-(\tilde{B})}$ in Eq. (4.10) is just the distance in the complex plane from the point δ to either of the two branch points.

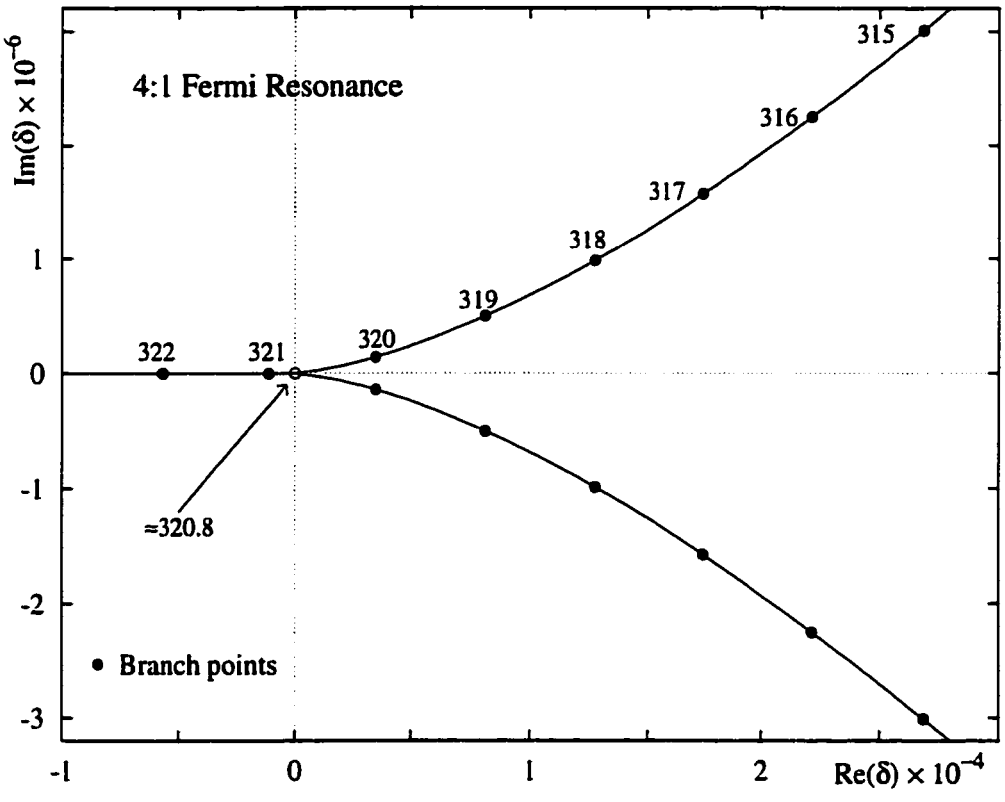

Figure 4.6: Branch-point structure of diamagnetic hydrogen in the complex δ-plane relating to the 4:1 Fermi resonance involving the $|11\rangle$ and $|05\rangle$ states[7]. The numbers near each branch point refer to the corresponding value of $\widetilde{B}$. Note that the locations of the branch points are particular to a given value of $\widetilde{B}$, and that they move to the left as $\widetilde{B}$ increases. Due to the scaling of the axes, the branch points on the negative real axis appear to be located at the same point. They are however separated, and this separation increases for increasing $\widetilde{B}$.

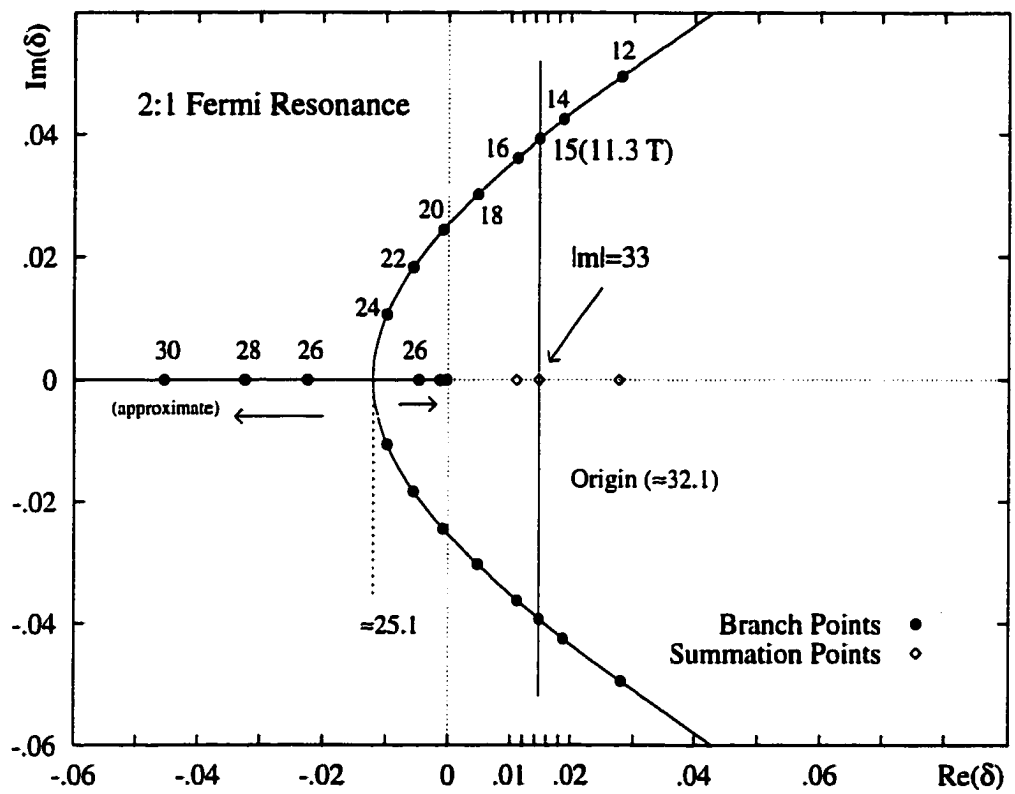

Figure 4.7: Branch-point structure of diamagnetic hydrogen relating to a 2:1 Fermi resonance involving the $|11\rangle$ and $|03\rangle$ states, for field strengths up to $\widetilde{B} = 30$. As in Fig. 4.6, the numbers near each branch point refer to $\widetilde{B}$. The number in the parentheses refers to the corresponding value of B in tesla for $|m| = 33$ and $D = 3$. The arrows on the real axis indicate the direction the branch points move with increasing magnetic field strength. The arrow closest to the origin will reverse direction once that branch point reaches the origin (at $\widetilde{B} \approx 32.1$). The unmarked branch points close to the origin correspond to (from left to right) $\widetilde{B} = 28$ and $\widetilde{B} = 30$. The points on the real axis correspond to (from left to right) $|m| = 44$, $|m| = 33$, and $|m| = 17$, and are referenced in Table 4.3.

In Sec. 4.1 we argued that avoided crossings will occur close to complex-conjugate, square-root branch-point degeneracies present in the complex parameter-plane. We will now use the energy level characterization in Eq. (4.10) to sharpen our understanding of the relationship between the locations of avoided crossings and the branch-point structure of diamagnetic hydrogen. First we consider in Sec. 4.4.1.1 avoided crossings as $|m|$ is swept while the magnetic field strength is fixed. Dimensional perturbation theory is naturally formulated in terms of the scaled field strength $\widetilde{B}$ and so automatically provides results for fixed $\widetilde{B}$. From an experimental point of view, investigating the response of the system to changes in $|m|$ for fixed $\widetilde{B}$ would appear to be quite feasible, although obviously $|m|$ is limited to integer values. As $|m|$ is changed, the unscaled field strength will have to be appropriately altered [see Eq. (3.4)].

In Sect. 4.4.1.2 we also consider the case of avoided crossings as $|m|$ is swept while the *unscaled* field strength B is held constant.

4.4.1 The 4:1 Fermi resonance: Avoided crossings as $|m|$ is swept

4.4.1.1 Scaled field strengths held constant

We define the center of the avoided crossing ${}^{\text{AC}}\widetilde{\delta}(\widetilde{B})$ to be the value of δ where ΔE is a minimum. While there is no reason to believe that the $\widetilde{E}_b$ term in Eq. (4.10) should remain constant over any appreciable range of angular momentum or magnetic field strengths, the avoided crossing for the 4:1 Fermi resonance is so narrow in both spectra that we can expect $\widetilde{E}_b$ not to vary significantly from one side of the avoided crossing to the other. (We will see that this assumption fails for the broad avoided crossings of the 2:1 Fermi resonance.) Therefore, the center of the avoided crossing occurs when the distance from the *summation point* δ (that is, the value of δ at which we are evaluating the perturbation series) to the branch points is a minimum, that is

$$ {}^{\text{AC}}\widetilde{\delta}(\widetilde{B}) = \Re e(\bar{\delta}_{\pm}(\widetilde{B}))\,. \tag{4.12}$$

Therefore, as long as the branch point is held fixed (that is, when $\widetilde{B}$ is held fixed) and $|m|$ is swept, we can state the following:

> Since $\widetilde{E}_b$ is roughly constant over the avoided crossing region, the avoided crossing appears whenever the summation point δ reaches the vicinity of ${}^{AC}\delta(\widetilde{B})$, the real component of the branch-point locations on the complex-δ plane.

We now use this result to predict the locations of avoided crossings appearing in the E-versus-$|m|$ spectrum. In Fig. 4.8 the energy levels of the $|11\rangle$ and $|05\rangle$ states are plotted as functions of $|m|$, but this time for fixed $\widetilde{B}$, not B. Now consider the summation point P in Fig. 4.9, which corresponds to $|m| = 26$ in three dimensions. (Figure 4.9 is the same as Fig. 4.6, but for lower values of $\widetilde{B}$.) If we sum the energy series about this point, we determine the resulting energies by referring to the energy levels in Fig. 4.8 that intersect line P. In fact, with the use of Eq. (4.12) we can understand the entire dependence of E on $|m|$ by fixing $\widetilde{B}$ and sweeping the summation point δ (therefore sweeping $|m|$) along the real axis in the complex δ-plane. For example, suppose we fix $\widetilde{B} = 140$, therefore fixing the branch-point locations at points C in Fig. 4.9, and sweep $|m|$ from point P to point R. An avoided crossing occurs when we reach point Q, because at that point $\Re e(\bar{\delta}_{\pm})$ coincides with the summation point δ. We can verify this result by referring to Fig. 4.8.

4.4.1.2 Unscaled field strengths held constant

As stated earlier, the locations on the complex δ-plane of the branch points that connect the two energy levels are purely functions of $\widetilde{B}$. However, since the relationship between $\widetilde{B}$ and B in Eq. (3.4) involves $|m|$, the branch points cannot be fixed in location in the complex δ-plane while $|m|$ (that is, δ) is swept with B constant.

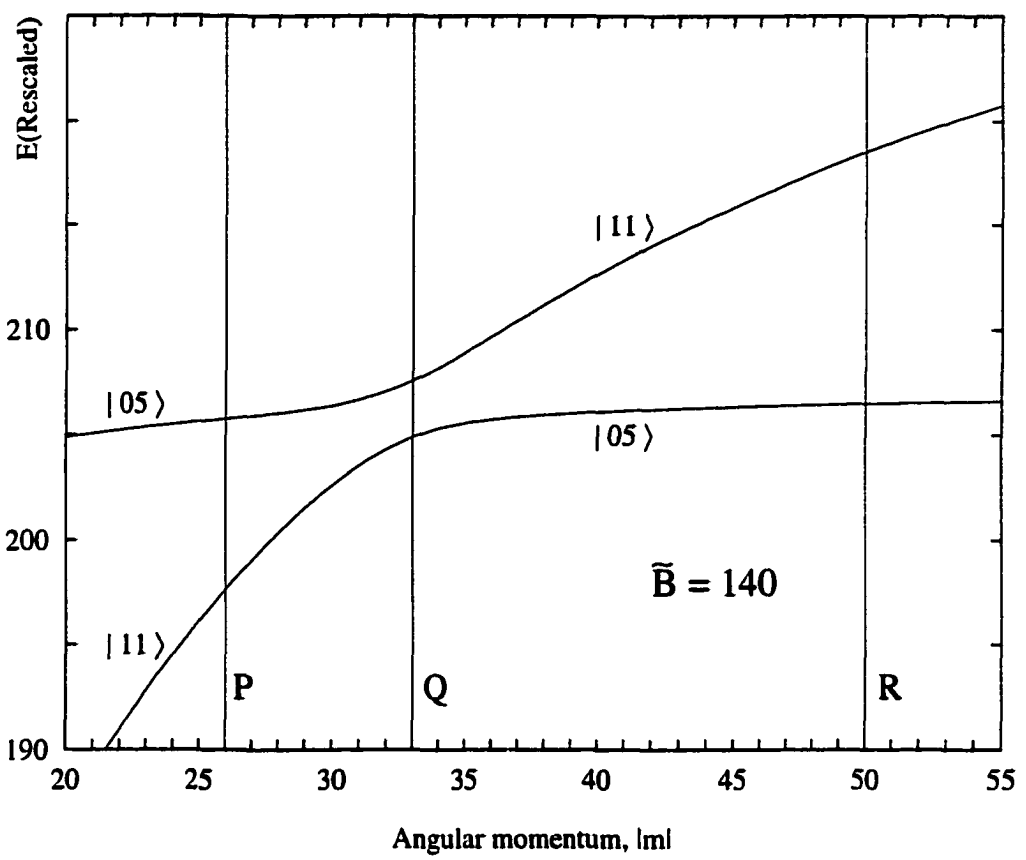

Figure 4.8: Energy as a function of angular momentum for the 4:1 Fermi resonance. Here, instead of fixing B, as in Fig. 4.5, we fix $\widetilde{B}$ instead. As in Fig. 4.5 we rescaled the vertical axis.

However, it turns out that Eq. (4.12) also applies when the *unscaled* field strength B, is held fixed, with $\widetilde{B}$ replaced by B in the equation. To see this, Eq. (4.10) needs to be re-expressed in terms of B (rather than $\widetilde{B}$), and the solutions $\delta_{\pm}(B)$ of the equation

$$\Delta E(\delta, B) = 0 \tag{4.13}$$

calculated for fixed B [rather than the $\tilde{\delta}_{\pm}(\widetilde{B})$, the solutions of Eq. (4.11) for fixed $\widetilde{B}$]. This is done in Appendix F with the result

$$E_{\pm}(\delta, B) = E_a(\delta, B) \pm E_b(\delta, B)\sqrt{\delta - \delta_+(B)}\,\sqrt{\delta - \delta_-(B)}\,. \tag{4.14}$$

Compare this with Eq. (4.10). Analogously to Eq. (4.10), when δ lies on the real axis and the branch points lie off the real axis in the complex plane, the term $\sqrt{\delta - \delta_+(B)}\,\sqrt{\delta - \delta_-(B)}$ in Eq. (4.14) is just the distance in the complex plane from the point δ to either of the two branch points with B held fixed.

Thus assuming that $E_b(\delta, B)$ in Eq. (4.14) is constant under changes in $|m|$ throughout the region spanning the avoided crossing, then the center of the avoided crossing occurs when the distance from the point δ to the branch points $\delta_{\pm}(B)$ is a minimum, that is

$$^{\mathrm{AC}}\delta(B) = \Re e(\delta_{\pm}(B))\,. \tag{4.15}$$

Therefore, as long as the branch point is held fixed (B is held fixed) and $|m|$ is swept, we can make the following assertion:

> *If E_b is roughly constant, the avoided crossing appears whenever the summation point δ reaches the vicinity of $^{\mathrm{AC}}\delta(B)$, the real component of the branch-point locations on the complex-δ plane. [See Eq. (4.12).]*

A good approximation for $\Re e(\delta_{\pm}(B))$, the real part of the solutions of Eq. (4.13) for fixed B, may be obtained from the positions of the branch points in the complex

Table 4.2: Avoided crossing locations in the E-versus-B spectrum for the 4:1 Fermi resonance. The summation points corresponding to $|m| = 26$, 33, and 50 are illustrated in Fig. 4.9. The $\Re e(\delta^{\pm})$ that corresponds to each $|m|$ assumes $D = 3$.

4:1 Fermi Resonance					
$\|m\|$	$\Re e(\delta^{\pm})$	$\widetilde{B}$ [a]	B(T) [a]	$\widetilde{B}$ [b]	B(T) [b]
26	0.019	120	179	116.7	174.1
33	0.015	140	105	138.4	103.4
50	0.010	180	40	180.0	39.9

[a] Predicted value from scanning Fig. 4.6.

[b] Computed value from Padé summing Eq. (3.9) for the two energy levels.

plane for fixed $\widetilde{B}$, the solutions $\tilde{\delta}_{\pm}(\widetilde{B})$ of Eq. (4.11). In Appendix F we show that since $|\Re e(\tilde{\delta}_{\pm}(\widetilde{B}))| \gg |\Im m(\tilde{\delta}_{\pm}(\widetilde{B}))|$, Eq. (4.15) implies the approximate relationship

$$^{AC}\delta\left(\left[\Re e(\tilde{\delta}_{\pm}(\widetilde{B}))\right]^3 \widetilde{B}\right) \approx \Re e(\tilde{\delta}_{\pm}(\widetilde{B}))\,, \tag{4.16}$$

where we remind the reader that $B = \delta^3\widetilde{B}$. *Therefore, we can predict the locations of avoided crossings in the E-versus-$|m|$ spectrum for fixed B by merely glancing at the branch-point structure connecting the two energy levels in the complex δ-plane for fixed $\widetilde{B}$.* For example, in Fig. 4.9 we see that the real part of the branch-point locations corresponding to $\widetilde{B} = 140$ is at roughly the same location as the summation point corresponding to $|m| = 33$. At this value of $|m|$ and $\widetilde{B}$, the physical field strength is $B = 107.6$ tesla. Therefore we would expect an avoided crossing to appear at $B = 107.6$ tesla when $|m|$ is fixed at 33. This is close to where the avoided crossing appears in Fig. 4.5, at $B = 103.4$ tesla.

Next we consider avoided crossings as the magnetic field strength, either scaled or unscaled, is swept while $|m|$ is unchanged.

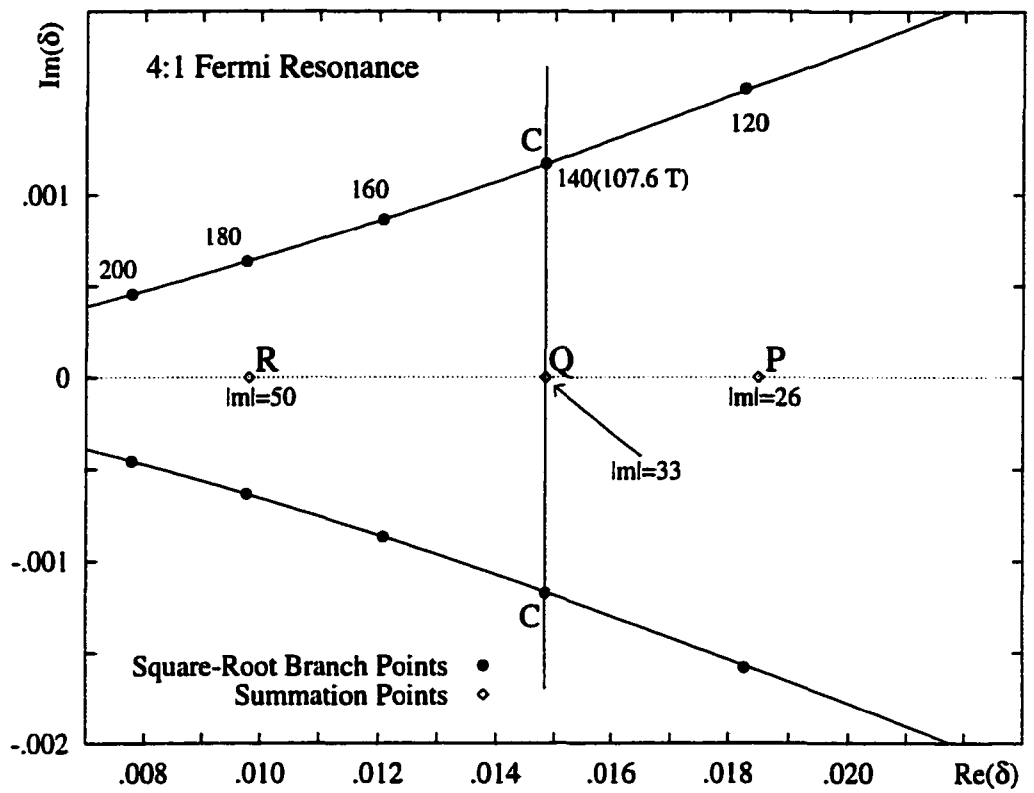

Figure 4.9: Another view of the data in Fig. 4.6, the branch-point structure of the 4:1 Fermi resonance, plotted at lower values of $\widetilde{B}$. The values of $|m|$ shown correspond to $D=3$ and are referenced in Table 4.2 and the text. The numbers near each branch point refer to the corresponding values of $\widetilde{B}$. The number in parentheses refers to the magnetic field strength B in tesla for $|m|=33$. The vertical line at $|m|=33$ is referred to in the text.

4.4.2 The 4:1 Fermi resonance: Avoided crossings as the magnetic field strength is swept

Let us hold $|m|$ (or equivalently δ) constant on the real line and sweep $\widetilde{B}$. An avoided crossing appears at that value of $\widetilde{B}$ for which $\Delta E(\delta, \widetilde{B})$ is a minimum. Suppose $\widetilde{E}_b$ in Eq. (4.10) is constant under changes in $\widetilde{B}$ throughout the region spanning the avoided crossing.

> *Thus from Eq. (4.10) the avoided crossing occurs when the branch-point trajectories in the complex plane pass closest to the summation point δ.*

By examining the horizontal and vertical scaling in Figs. 4.6 and 4.9 we see that the gradient of the branch-point trajectories remains quite small, so to a good approximation the point of closest approach occurs when

$$\Re e(\tilde{\delta}_{\pm}(\widetilde{B})) = \delta\,. \tag{4.17}$$

Therefore if $\widetilde{E}_b$ is roughly constant over the avoided crossing and the slope of the branch-point trajectories to the real line is small, $\left|\Re e(\tilde{\delta}_{\pm}(\widetilde{B}))\right| \gg \left|\Im m(\tilde{\delta}_{\pm}(\widetilde{B}))\right|$, then when the real part of the branch points, $\Re e(\tilde{\delta}_{\pm}(\widetilde{B}))$, reaches the summation point δ the separation between the two energy levels is close to a minimum. To a good approximation we can say that the center of the avoided crossing has been reached. For example, if we fix $|m| = 33$ (point Q in Fig. 4.9) and sweep $\widetilde{B}$, we should get an avoided crossing near $\widetilde{B} = 140$. The crossing actually occurs at $\widetilde{B} = 138.7$, as we saw in Fig. 4.4.

As seen in Eq. (3.3), any result for which $|m|$ is held fixed equally applies to either sweeping $\widetilde{B}$ or B, since B and $\widetilde{B}$ are then directly proportional.

In Table 4.2, we predict the locations of avoided crossings for both scaled and physical magnetic field strengths for three different fixed values of $|m|$. From this table we see that the branch-point structure of the 4:1 Fermi resonance provides a convenient way of accurately determining such avoided crossing locations.

To conclude:

It is possible to predict the locations of avoided crossings in the E-versus-$|m|$ spectrum for fixed B (or $\widetilde{B}$) and the E-versus-$\widetilde{B}$ (or B) spectra for fixed $|m|$ by merely glancing at the branch-point structure connecting the two energy levels in the complex δ-plane.

4.5 The 2:1 Fermi resonance

Having established the relationship between avoided crossings and branch-point structure by focusing on the 4:1 Fermi resonance, we now direct our attention to the 2:1 Fermi resonance. By examining Figs. 4.10 and 4.11 we can see that the same correspondence between the two spectra that exists for the 4:1 Fermi resonance applies to the 2:1 Fermi resonance as well: (1) An avoided crossing appears at $B = 14.0$ T for $|m|$ fixed at $|m| = 33$. (2) With B fixed at $B = 14.0$ T an avoided crossing appears at $|m| = 34$. Notice that since the avoided crossing appears at $|m| = 34$ and not $|m| = 33$, the correspondence between the two plots is not as precise as it was for the 4:1 Fermi resonance. More on this below.

The repulsion between the $|11\rangle$ and $|03\rangle$ states is quite strong, therefore the avoided crossing is actually spread out over a large region of magnetic field strength. Therefore we should not expect $\widetilde{E}_b$ in Eq. (4.10) to remain nearly constant throughout the avoided crossing region. However, our previous discussion relied on a roughly constant $\widetilde{E}_b$, so we now see how our results apply to the 2:1 Fermi resonance.

4.5.1 Avoided crossings as $|m|$ is swept

4.5.1.1 Scaled field strengths held constant

In Fig. 4.12 energy is plotted as a function of $|m|$, with the scaled magnetic field strength fixed to $\widetilde{B} = 15$. According to the argument in the previous section, an avoided crossing should appear when the summation point reaches the real part of the branch points corresponding to $\widetilde{B} = 15$. According to Fig. 4.7, this should be near $|m| = 33$ (note the vertical line that runs through the $|m| = 33$ summation point and the branch point corresponding to

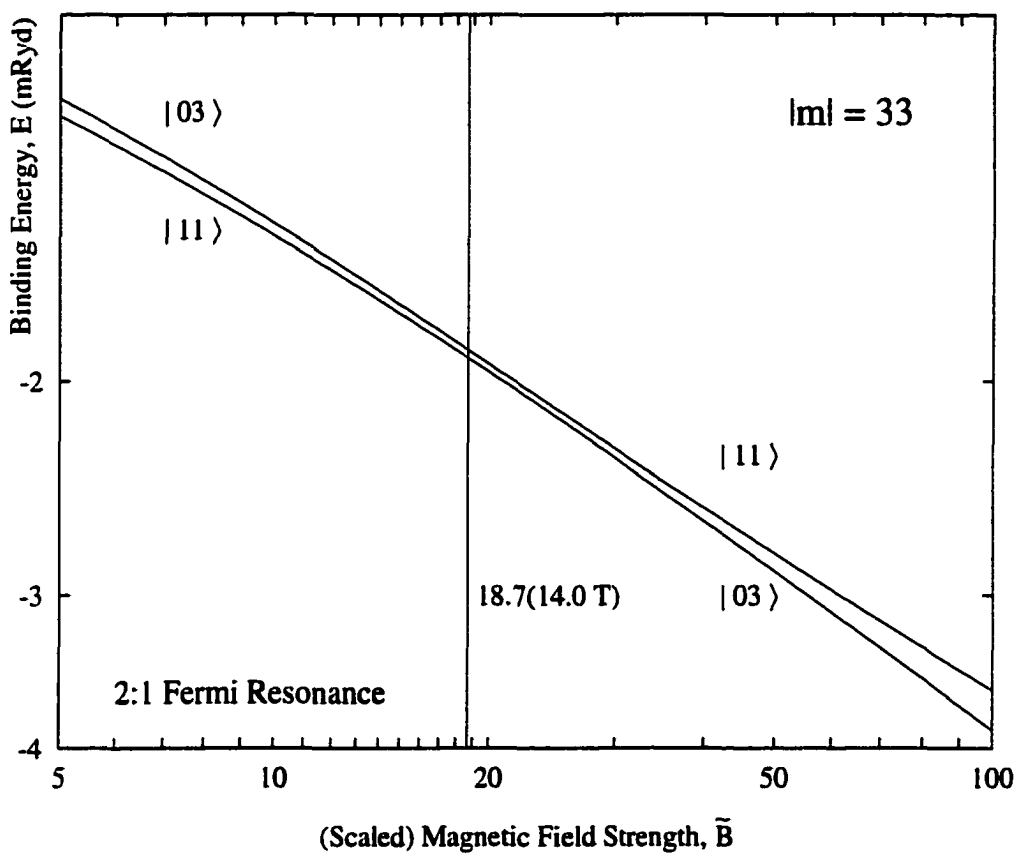

Figure 4.10: Detail of the interaction between the $|03\rangle$ and $|11\rangle$ states, associated with a 2:1 Fermi resonance, at higher order ($p=28$) in perturbation theory. As in Fig. 4.4, the number in parentheses refers to the magnetic field strength in tesla when $|m|=33$.

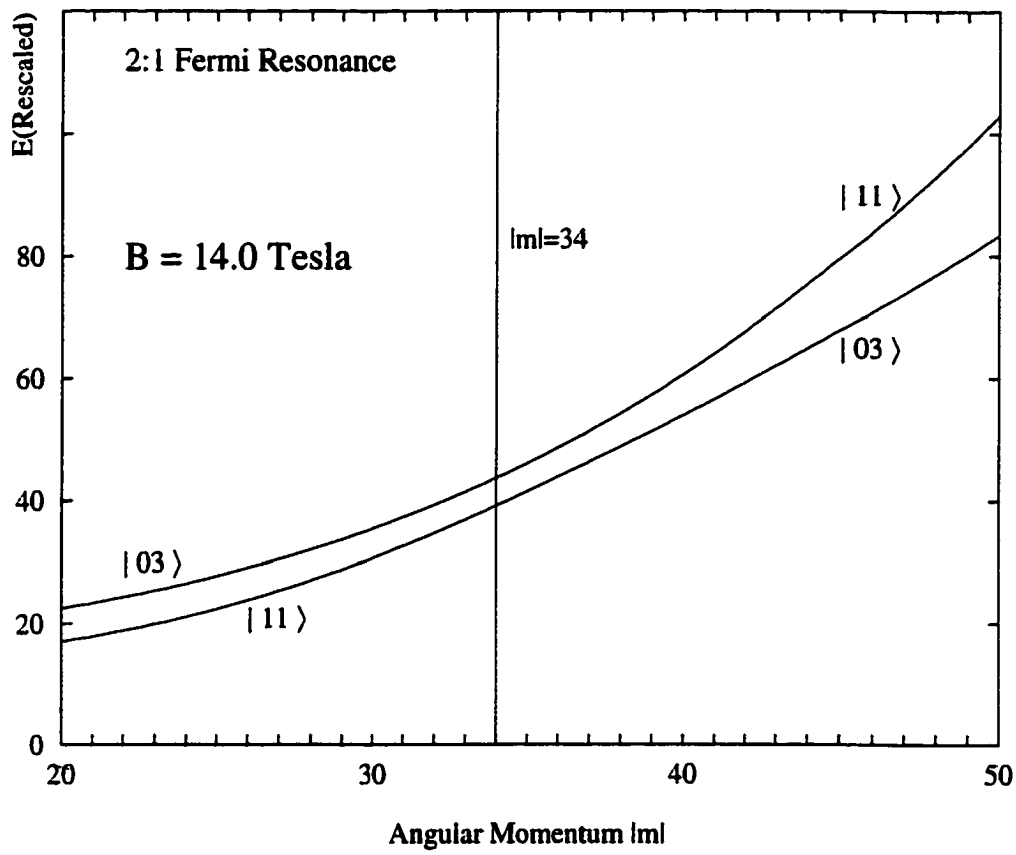

Figure 4.11: Same as Fig. 4.5, except for a 2:1 Fermi resonance. Here we fix $B = 14.0$ tesla. The avoided crossing here is close to $|m| = 34$, rounded to the nearest integer. As in Fig. 4.5, we rescaled the vertical axis.

$\widetilde{B} = 15$). However, Fig. 4.12 shows that the avoided crossing appears at $|m| = 19.0$. The only approximation that went into Eq. (4.12) was that $\widetilde{E}_b$ was nearly constant, so at this point we can conclude that for the 2:1 Fermi resonance $\widetilde{E}_b$ changes significantly over the region of the avoided crossing. This means that the first term

$$\frac{\partial(\Delta E)}{\partial \delta} = 2\frac{\partial \widetilde{E}_b}{\partial \delta}\sqrt{\delta^2 - (\delta_+ + \delta_-)\delta + \delta_+\delta_-} + \frac{\widetilde{E}_b(2\delta - (\delta_+ + \delta_-))}{\sqrt{\delta^2 - (\delta_+ + \delta_-)\delta + \delta_+\delta_-}}. \quad (4.18)$$

is appreciable in comparison to the second.

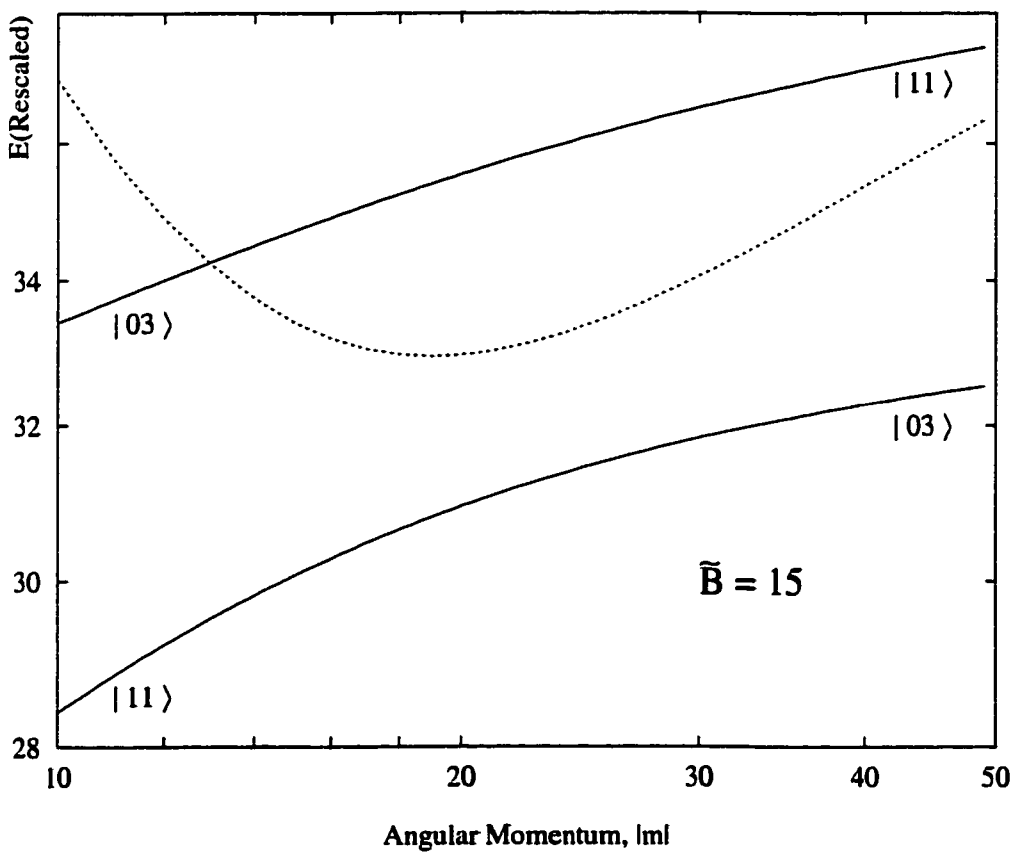

Figure 4.12: Energy levels corresponding to a 2:1 Fermi resonance as $|m|$ is swept. Here we hold the scaled magnetic field $\widetilde{B}$ fixed. The dashed line is the difference between the two energies, scaled to fit on the same plot. The minimum (avoided crossing) occurs at $|m| = 19.0$. Note that even though the vertical axis has been rescaled, this avoided crossing is still very hard to distinguish.

For $\widetilde{B}=15$ the fact that $\widetilde{E}_b$ varies significantly over the avoided crossing region is easily shown. From a plot of $\widetilde{E}_b$ as a function of δ (that is, $|m|$) over the avoided crossing region (see Fig. 4.13) we see that $\widetilde{E}_b$ roughly has the form

$$\widetilde{E}_b = -C_1\delta + C_2, \tag{4.19}$$

where $C_1 \approx 344$ and $C_2 \approx 65.3$. Substituting this expression into Eq. (4.18) and noting that $\delta_\pm \approx .0147 \pm .0393$ for $\widetilde{B}=15$, we find that the ratio of the first term to the second term in Eq. (4.18) lies roughly anywhere between .25 and 1 from one end of the avoided crossing to the other. Therefore the first term in Eq. (4.18) containing $\partial\widetilde{E}_b/\partial\delta$ cannot be ignored, so $\widetilde{E}_b$ is not sufficiently constant throughout the avoided crossing region.

With the linear approximation of Eq. (4.19), the relationship in Eq. (4.18) shows that $\partial(\Delta E)/\partial\delta = 0$ places the avoided crossing center at $|m| \approx 19.3$, which is very close to the exact value of $|m| = 19.0$ (see Fig. 4.12). Therefore by merely taking into account the next term of the Taylor series expansion of $\widetilde{E}_b$ with respect to δ, we accurately obtain the position of the avoided crossing at the 2:1 Fermi resonance.

4.5.1.2 Unscaled field strengths held constant

In the previous section we found that the same relationship for predicting the appearance of avoided crossings for fixed *scaled* field strength also applied to fixed *unscaled* field strength because the approximation $|\Re e(\tilde{\delta}_\pm(\widetilde{B}))| \gg |\Im m(\tilde{\delta}_\pm(\widetilde{B}))|$ applied. In Fig. 4.7 we can see that such an approximation does not apply to the 2:1 Fermi resonance.

4.5.2 Avoided crossings as the magnetic field strength is swept

When sweeping the magnetic field strength (scaled or unscaled) for the 4:1 Fermi resonance we simplified the predictions of avoided crossings by noting that the trajectories of the branch points were nearly parallel to the real axis. Therefore, for this interaction the closest distance between the branch point and the summation point simply coincided with the

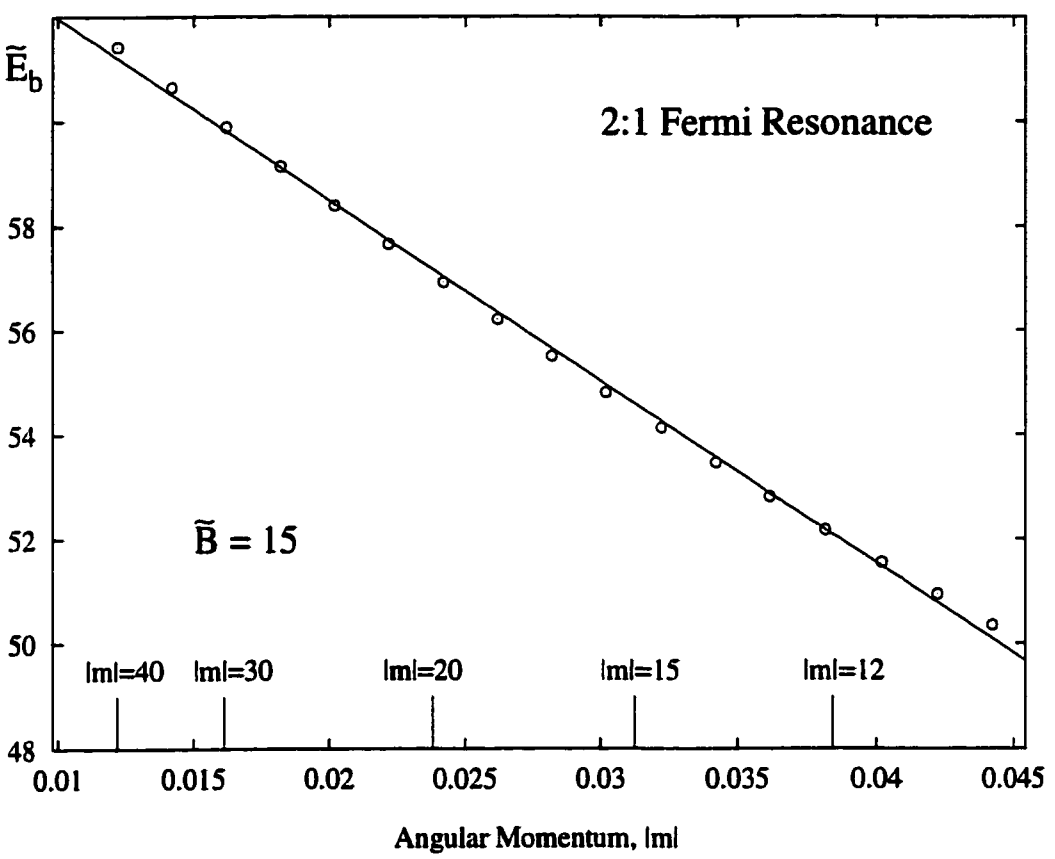

Figure 4.13: The $\widetilde{E}_b$ term in Eq. (4.10) plotted as a function of δ over the range of the avoided crossing in Fig. 4.12. The corresponding values of $|m|$ are shown for reference ($D = 3$). The extreme left of the plot corresponds to $|m| = 50$, whereas the extreme right corresponds to $|m| = 10$.

summation point located at the real part of the branch point. A glance at Fig. 4.7 shows that this simplification will not hold for the 2:1 Fermi resonance. However, finding the branch point that is closest to the summation point from a plot of the branch-point trajectory is not too difficult as long as the real and imaginary axes are scaled the same, as in the figure. Here we can see that for $|m| = 33$ the branch point coinciding with $\widetilde{B} \approx 23$ is closest to the summation point, so we expect to find an avoided crossing at roughly $\widetilde{B} = 23$ if we fix $|m| = 33$. However, Fig. 4.10 shows that the avoided crossing actually appears at $\widetilde{B} = 18.7$. By plotting $\widetilde{E}_b$ as a function of $\widetilde{B}$ in Fig. 4.14, and noting that $\widetilde{E}_b$ increases by roughly a factor of 4 over the range of the avoided crossing, we can verify that $\widetilde{E}_b$ varies considerably over the region of the avoided crossing for this interaction, so such a discrepancy is not unexpected.

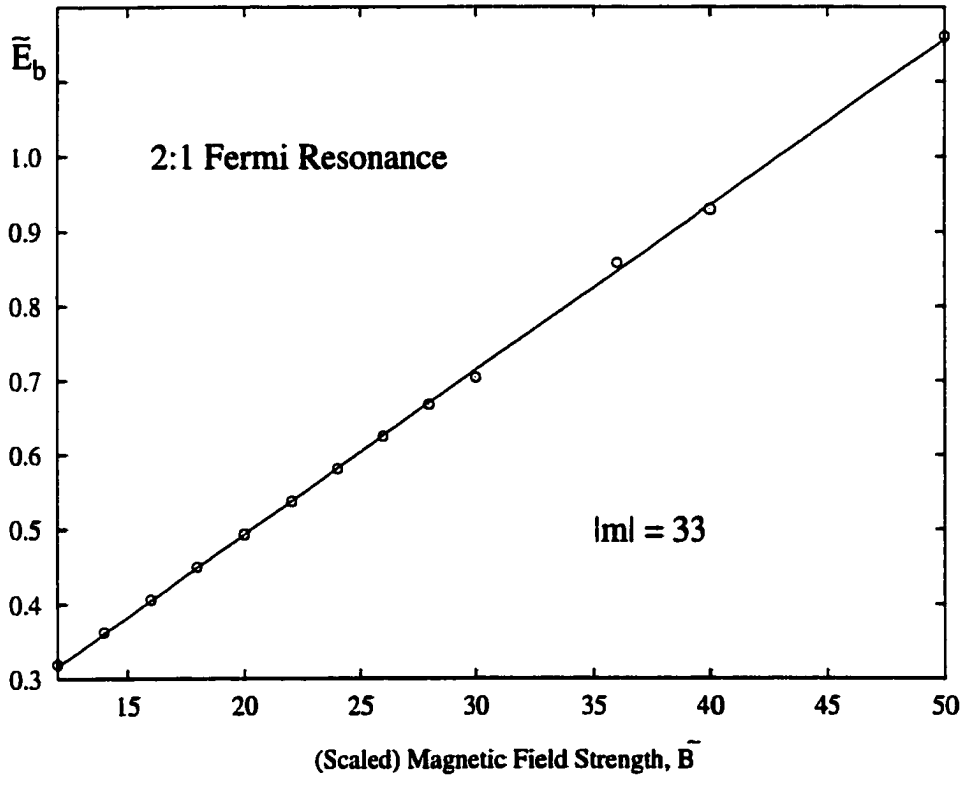

Figure 4.14: The $\widetilde{E}_b$ term in Eq. (4.10) plotted as a function of $\widetilde{B}$ over the range of the avoided crossing in Fig. 4.10. Clearly $\widetilde{E}_b$ is not constant over this range of field strengths.

Table 4.3: Avoided crossing locations in the E-versus-B spectrum for the 2:1 Fermi resonance. The summation points corresponding to $|m| = 17$, 33, and 44 are illustrated in Fig. 4.7. The $\Re e(\delta^{\pm})$ that corresponds to each $|m|$ assumes $D = 3$.

2:1 Fermi Resonance					
$\|m\|$	$\Re e(\delta^{\pm})$	$\widetilde{B}$ [a]	B(T) [a]	$\widetilde{B}$ [b]	B(T) [b]
17	0.028	19	96	13.0	65.5
33	0.015	23	17	18.7	14.0
44	0.011	25	8	21.6	7.0

[a] Predicted value from scanning Fig. 4.7.

[b] Computed value from Padé summing Eq. (3.9) for the two energy levels.

Just as for the 4:1 Fermi resonance between the $|11\rangle$ and $|05\rangle$ states, we summarize in Table 4.3 comparisons between expected and calculated results corresponding to those summation points shown in Fig. 4.7, the branch-point structure of the 2:1 Fermi resonance between the $|11\rangle$ and $|03\rangle$ states. Despite the discrepancy in assuming a constant $\widetilde{E}_b$, the predicted values are still fairly close to those found by our computer calculations (by summing the energy series with the matrix method) for a wide range of $|m|$.

4.6 Even parity states

All calculations in this chapter focused on odd-parity states. However, even-parity energy levels and branch-point trajectories are essentially the same as for odd-parity states. As examples we show the *even-parity* branch-point structure of a 4:1 and 2:1 Fermi resonance in Figs. 4.15 and 4.16. Comparing these figures to Figs. 4.6 and 4.7 it appears that, except for slight shifts in locations, the branch-point structures are essentially the same. Therefore, the energy level characterization in Eq. (4.10) applies to both even- and odd-parity states.

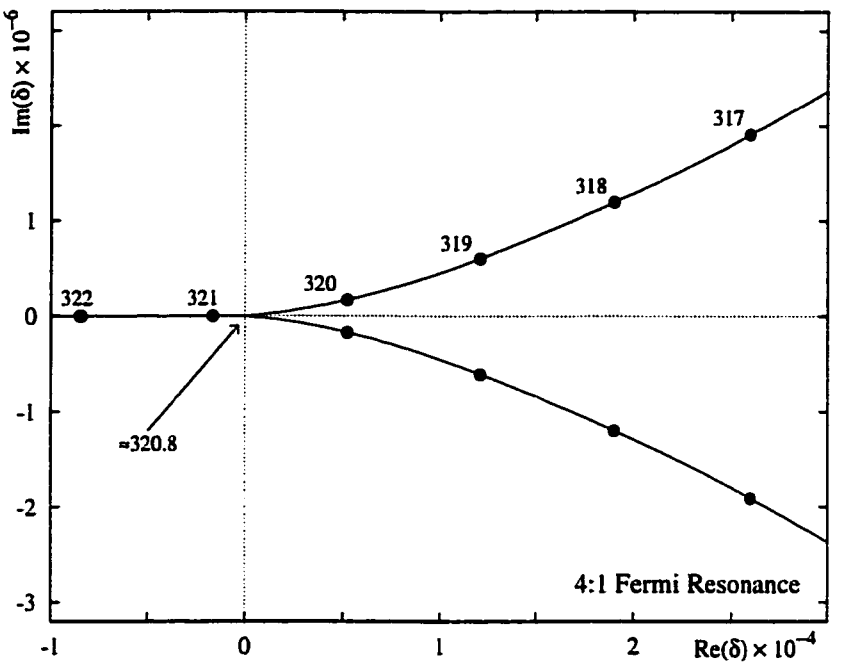

Figure 4.15: Same as Fig. 4.6, except this time we show the *even*-parity branch-point structure involving the $|10\rangle$ and $|04\rangle$ states.

This is not surprising, since dimensional perturbation theory shows that at harmonic (zeroth) order the location of the Fermi resonances, which determines the location of degeneracy at higher order and thus the location of branch points, is the same for either parity. (Watson *et al.* include a plot of the harmonic-order even-parity energy levels as a function of $\widetilde{B}$, although at a different value of $|m|$[135]). Because of this similarity in the harmonic-order spectra between the two parities, the even-parity energy levels share the same qualitative features as their odd-parity counterparts. Some examples of even-parity counterparts to the odd-parity E-versus-B spectra are shown in Watson *et al.*, again for a different value of $|m|$.

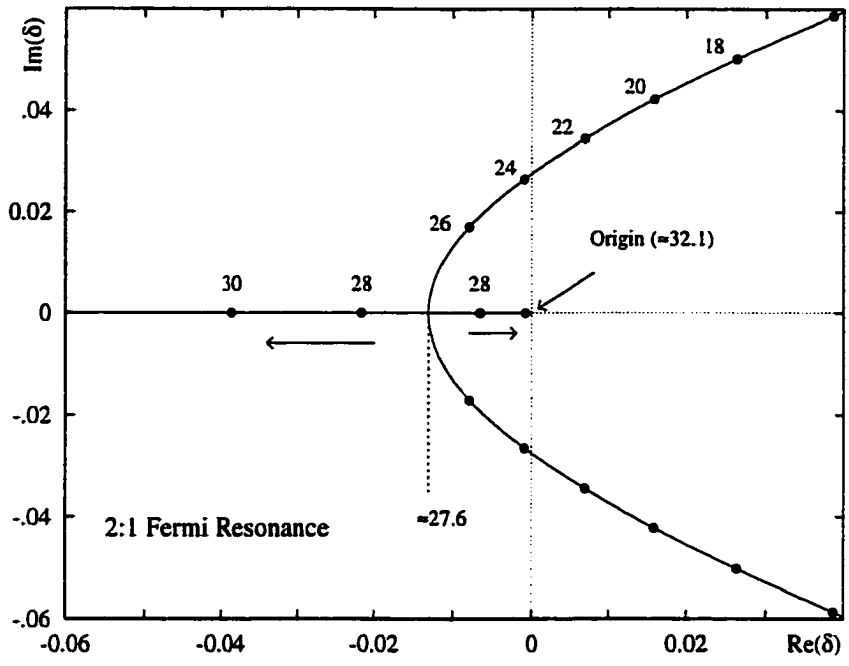

Figure 4.16: Same as Fig. 4.7, except this time we show the *even*-parity branch-point structure involving the $|10\rangle$ and $|02\rangle$ states. The branch points close to the origin and lying on the negative real axis correspond to (from left to right) $\widetilde{B}=28$ and $\widetilde{B}=30$.

4.7 Discussion

Although we have explicitly analyzed only the situation involving two strongly interacting states (two-state Fermi resonances), Table 4.1 shows that three and more strongly interacting states (three- and more-state Fermi resonances) are common in the eigenvalue spectrum of diamagnetic hydrogen. Heiss and Steeb[136] have studied the analytic characterization of branch points of the eigenvalues associated with avoided crossings of three and more strongly interacting states in finite-dimensional matrix eigenvalue problems. They find that in this case Eq. (4.10) correctly characterizes the branch-point structure of the eigenvalues in the neighborhoods of the branch points. Thus although infinite-dimensional matrix equations can in principle involve more complex branch-point characterizations involving

states with complex energies (resonances)[137], we expect that Eq. (4.10) will still correctly parameterize the energy involving three and more strongly interacting states in the neighborhood of branch points that will produce avoided crossings. Therefore the analysis performed in this chapter should apply to all avoided crossings of diamagnetic hydrogen.

The ability to predict and understand the appearance of avoided crossings is aided by the assumption that the $\widetilde{E}_b$ term in Eq. (4.10) is constant over the range of the avoided crossing. The avoided crossing pertaining to the 4:1 Fermi resonance was sufficiently narrow to satisfy this assumption, but we saw that because of the broad avoided crossing in the 2:1 Fermi resonance this condition failed. Therefore, predicting the positions of the avoided crossings for the 2:1 Fermi resonance is somewhat involved. However, the broadness of the 2:1 Fermi resonance is the exception rather than the rule. The quantum numbers ν_1 and ν_2, denoting the nodal structure of the states, are related to the low-field quantum numbers n and k by $|\nu_1, \nu_2\rangle = |n - k - |m| - 1, k\rangle$, where k orders the states with respect to energy in each n hydrogenic manifold in the low B-field limit. As we stated in Sec. 2.1, Wintgen and Friedrich[15, 4, 61] find that only states with k ($= \nu_2$) quanta that differ by 2 can exhibit a broad avoided crossing. In this case the Fermi resonance condition associated with these avoided crossings implies that, for the X:Y Fermi resonance, the ratio $2X/Y$ must be an integer. Since X must be larger than Y (ω_1 must be larger than ω_2), the only allowed Fermi resonance[138] that satisfies the $|\Delta k| = 2$ condition is the 2:1 Fermi resonance. Note from Table 4.1 that not even all 2:1 Fermi resonances satisfy this condition. Therefore, not all 2:1 Fermi resonances are expected to be broad. Furthermore only avoided crossings involving two vibrational states (large k) are broad; this condition further reduces the number of broad avoided crossings of the 2:1 Fermi resonance. Therefore the ability to predict the locations of avoided crossings based only on examining the positions of the branch points that connect the two levels should have broad applicability throughout the spectra of diamagnetic hydrogen.

Chapter 5

Branch-Point Structure of Diamagnetic Hydrogen

Largely derived from J.R. Walkup, M. Dunn, D.K. Watson, J. Math. Phys. **41**, 218-239 (2000).

Until now we have been mostly concerned with the avoided crossings that appear in the energy spectrum of diamagnetic hydrogen. But avoided crossings in energy level spectra as system parameters are adiabatically varied are prevalent in all areas of quantum physics. They are often viewed as the result of a residual interaction which couples states which would otherwise cross. When the interaction is introduced, the degeneracies move off the real line into the complex parameter-plane. Therefore, as the parameter is varied along the real line, a near-degeneracy occurs in the vicinity of these degeneracies in the complex plane; that is, an avoided crossing appears. Nevertheless, the states diabatically exchange physical characteristics across an avoided crossing, so the ordering of the states with respect to their physical characteristics still follows the pattern set when the residual interaction is turned off.

Near an avoided crossing, if we can ignore the perturbing influence of all other states on the two states involved in the crossing, the problem reduces to a two-dimensional, matrix eigenvalue equation. This naturally produces a square-root branch-point structure in the eigenvalue at the degeneracy points; that is, the energy is a two-branched function of the parameter, with the physical energies lying on the real axis of a two-sheeted Riemann surface. Analytic continuation of the system parameter by 2π around a square-root branch point takes one onto the other sheet. If one starts on the real axis of one of the sheets, the

physical energy of one of the states transforms in a continuous fashion into the energy of the other state — the energies interchange.[136, 124] Since the eigenvalue determines the eigenvectors, the wave functions also interchange under the transformation. As more distant states are included, the size of the matrix-eigenvalue problem increases, so the order of the secular equation increases as well. This raises the possibility that higher-order branch-points/degeneracies may appear. However, Bender, Happ, and Svetitsky[139] demonstrated that this is extremely unlikely. Therefore, as a general rule avoided crossings are signaled by square-root branch points.

Hidden avoided crossings[124, 125, 140, 141, 142, 143, 144] are nearly impossible to spot in the energy spectrum, yet the physical characteristics of the states still exchange diabatically across these avoided crossings.[124] However, hidden crossings are easily identified by the presence of nearby branch-point degeneracies in the energy function for complex values of the system parameter. Therefore, important information is obtained by studying the branch-point degeneracies for complex values of the system parameter — examples include the works of Solov'ev, Ovchinnikov, and others in low-energy heavy-ion collisions[125, 145]). This information could be missed or more difficult to obtain through other approaches.

5.0.1 Distribution of branch points on the complex parameter-plane

With the energy real-valued for real values of the system parameter, the Schwartz reflection principle[127] has an important consequence for the branch-point distribution of the *single-parameter* system: Branch-point degeneracies must appear as complex-conjugate pairs. Therefore, avoided crossings in single-parameter problems result from nearby *complex-conjugate*, square-root branch-point degeneracies.

If a system has more than one parameter, however, the extra degrees of freedom in the combined parameter space make it possible to find specific *real* values for all parameters (a conical section) for which neighboring states are degenerate for real energy. However,

this seldom occurs. If one of the parameters does not correspond to one of these specific values, then at least one parameter must be complex-valued for neighboring states to be degenerate (albeit at a complex energy).

Consider the situation where one parameter is varied while the others are held constant. Furthermore, consider u as a parameter that has been continued off the real axis into the complex plane. Regarding the avoided crossings caused by these degeneracies:

1. If u is the parameter being adiabatically varied, then the situation is the same as the one-parameter problem discussed above.

2. If a different parameter v is being varied, then the degeneracies in the complex u-plane move in response to adiabatic changes in v. When they pass close to the point on the real axis at which u has been fixed, then the nearby degeneracy causes a near-degeneracy to appear in the energy levels for real values of all parameters. In other words, at this value of v an avoided crossing between energy levels appears at real values of all system parameters.

In Chap. 4 we showed specific examples where both situations occur.

The avoided crossings as one parameter is varied depend on the values of the other parameters, which are held constant. Since avoided crossings are the result of nearby degeneracies for complex values of the parameter, we can study this dependence by examining the trajectories of the degeneracies, with the other parameters held to physical (real) values. These degeneracies have a square-root branch-point structure for the same reasons as the single-parameter problem considered above.[146]

5.0.2 Emergence of an alternative branch-point structure

Heiss and Steeb determined the square-root branch-point structure of the symmetric-matrix eigenvalue problem, which only permits real eigenvalues.[136] The analytic form of the square-root branch points uncovered by Heiss and Steeb conforms to this requirement, in

that the branch points only connect states with real energy to other states with real energy when the branch points are *off* the real axis. However, this same analytic form of the symmetric-matrix eigenvalue problem permits the square-root branch points to connect states with real energies to those with complex energies, but only when the branch points are *on* the real axis (which does not occur with real-valued, symmetric-matrix, eigenvalue problems). This situation corresponds to a bound state in a short-range potential crossing into the continuum to become a resonant state as the parameter u is varied along the real axis around a branch point at the continuum threshold.[147] This does not correspond to the case of interest here where two branch points are complex-valued, causing avoided crossings between two bound states.

The existence of complex energies for the "infinite-dimensional" problem, and the possibility that square-root branch points connect states with real energy to states with complex energy opens up another possibility for the analytic structure of the energy that is not present for the finite-dimensional problem limited to real eigenvalues. It represents an additional analytic structure that the "infinite-dimensional" problem can have over the finite-dimensional problem, and as we will see in Sec. 5.1, the branch points which connect states with real energies to states with complex energies can also cause avoided crossings between two states with real energies.

We derive the two analytic structures in the next section and determine which is present in a particular quantum-mechanical problem in Sec. 5.4. This is explored through our example of a dimensional perturbation treatment of diamagnetic hydrogen. Given the two possible analytic structures for the general quantum-mechanical problem, one way to see which is correct is to traverse a path around a branch point that is away from the real u-axis by 2π, beginning and ending on the real u-axis. If, starting with a real energy, we obtain a complex energy, then this alternative analytic structure must be present near the square-root branch point. That such an alternative branch-point structure connecting states with real energies to states with complex energies exists within quantum mechanics is demonstrated

by the example of the H_2^+ problem in the Born-Oppenheimer approximation, as studied by Solov'ev, Ochinnikov, and others.[145] Defining the distance between the two hydrogen nuclei as R, they found that taking a path in the complex R-plane around the branch point at the ends of the S-series of branch points in the complex R-plane does indeed take one from states with real energy to states with complex energy.

However, one is not always in a position to traverse such a path in the Riemann sheet structure of the problem. An example occurs with perturbation theory in the parameter u. The analytic structure does not immediately emerge from a power series, since partial sums of the series are single-valued functions of u, and may not converge even if they are asymptotic series. Asymptotic series are often "summable" with Padé approximates, but they too are single-valued functions and "sum" multi-valued functions by limiting themselves to a single branch through the introduction of branch cut discontinuities.[124] Furthermore, to sum a perturbation series with maximum accuracy and/or for all branches of the original function one needs to know the analytic structure of the original function beforehand so that one can choose an approximate that possesses the same analytic structure.

In Sec. 5.4 we use quadratic Padè approximates and analytical methods to determine from a perturbation series which of the two analytic structures is present in a given problem.

5.1 Analytic structure of degeneracies

Consider an atomic system whose energy E is a function of at least two variables u and v, where u is the parameter that is continued off the real axis and v is the external, real-valued, parameter. (Note that this is exactly Situation 2 in Sec. 5, with the same nomenclature.) We define the branch points to be located at values $u_1(v)$ and $u_2(v)$ on the complex u-plane. Near the branch point u_1 we expand and resum the energy series about u_1 as

$$E(u,v) = \sum_{k=0}^{\infty} c_k(v)\,(u-u_1)^{k/2} = a + b\sqrt{u-u_1}\,, \tag{5.1}$$

where a and b are sums over even and odd powers of $c_k(u-u_1)^k$, respectively, and u is a function of v. One branch point is paired with another, so expanding a and b about $u_2(v)$ and resumming the series we obtain

$$E(u,v) = A + C\sqrt{u-u_1} + F\sqrt{u-u_2} + G\sqrt{u-u_1}\sqrt{u-u_2}\,, \tag{5.2}$$

where the coefficients A, C, F, and G are functions of u and v.

This function has four branches connected by square-root branch points, so here the energy is defined on a u-domain consisting of a four-sheeted Riemann surface. Near the avoided crossing caused by the branch points at u_1 and u_2, the energies of the states are real on the positive, real u-axis. Therefore, if Eq. (5.2) is to represent the functional form of the energy of the two states involved in an avoided crossing, then on at least two of the four sheets the energy must be real on the positive, real u-axis. Note that $\sqrt{u-u_1}\sqrt{u-u_2}$ is real-valued when u is on the positive, real axis and when the branch points are either complex conjugate or both lie on the negative real axis. Therefore the first and last terms are real on the positive, real u-axis of all four sheets if A and G are real on the positive, real u-axis. The sum of the second and third terms is real on the positive, real u-axis of two of the four sheets, with

$$F(u,v) = C^*(u,v) \tag{5.3}$$

when u_1 and u_2 are complex conjugate[148] and with C and F real when the branch points lie on the negative real axis. Given these criteria, we obtain the *general energy structure*

$$E^{\pm}(u,v) = A \pm \left[C\sqrt{u-u_1} + F\sqrt{u-u_2}\right] + G\sqrt{u-u_1}\sqrt{u-u_2}\,. \tag{5.4}$$

The energies on the other two branches are complex for positive, real u and complex-conjugate values of u_1 and u_2.

An exception to the four-sheeted structure outlined above occurs if $C(u,v)$ and $F(u,v)$ were identically 0. Then Eq. (5.2) defines a two-sheeted energy function. The energies of the two interacting states are then given by the *reduced energy structure*

$$E^{\pm}(u,v) = A \pm G\sqrt{u-u_1}\sqrt{u-u_2}, \tag{5.5}$$

evaluated on the positive, real u-axis. This has the analytic form we expect from a finite-matrix problem. With a Hamiltonian that is self-adjoint for real u, the eigenenergies must be real for positive, real u. As discussed in the introduction, avoided crossings arise from the proximity of nearby branch points at which the two states are degenerate in energy. However, for the *general energy structure*, Eq. (5.4), the branch points represent degeneracies between two states, but only one of which has a real energy on the positive, real u-axis. Despite this, the *general energy structure* can also feature avoided crossing-like structures near the branch points,[149] as shown by the solid lines in Fig. 5.1.

It is important to note that a high-order examination of the perturbation series will not differentiate between the two analytic structures because both structures have the same high-order behavior.[150]

We have shown that there are two different possible analytic structures of the energy near an avoided crossing in "infinite-dimensional" matrix problems. The functional forms of both structures provide a means of determining which structure is correct for a given avoided crossing:

1. If Eq. (5.4) is correct, then $E^+ + E^-$ is a function with two branches and two branch points. On the other hand, if Eq. (5.5) is correct then $E^+ + E^-$ is a function with only one branch and *no* branch points.

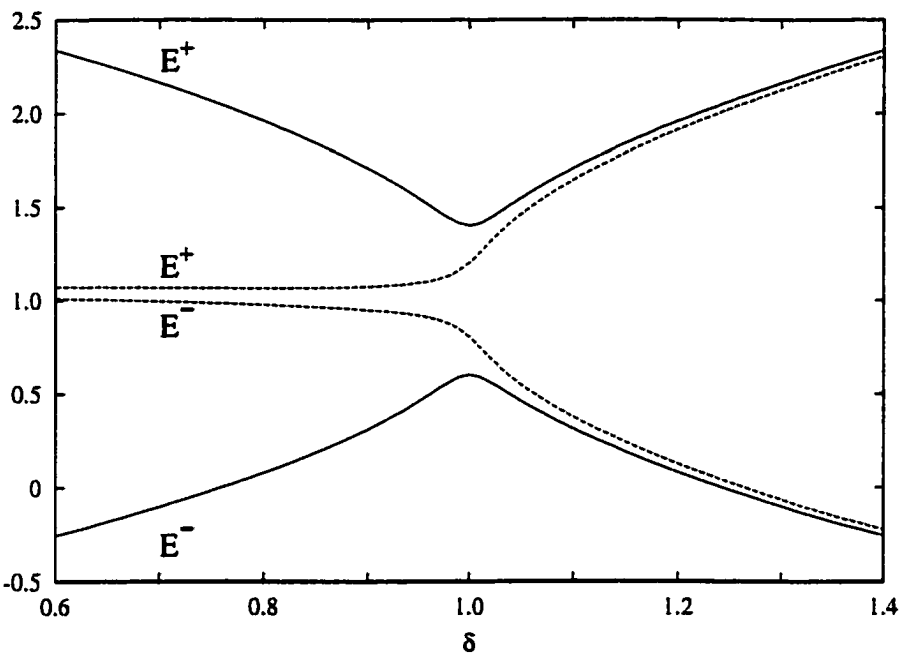

Figure 5.1: Avoided crossings occurring between energy levels resulting from the *general energy structure*, Eq. (5.4), for $A = 1$, $G = 0.1$, and $\delta^{\pm} = 1.0 \pm 0.02i$. The solid lines correspond to $C = 1+i$ and $F = 1-i$, whereas the dashed lines correspond to $C = F = 1$.

2. One characteristic feature of Eq. (5.5) is that at the *coalescence point* v_c, where the two branch points are at the same location (that is, the point v_c where $u_1(v_c) = u_2(v_c) \equiv u_c$), the energy reduces to

$$E^{\pm}(u, v_c) = A(u, v_c) \pm G(u, v_c)\,(u - u_c)\,. \tag{5.6}$$

Therefore, we lose the square-root nature of the energy function; the two branch points annihilate at v_c. In Eq. (5.4), however, square-root branch points at v_c remain in the second and third terms. Therefore, we can also distinguish between these two possibilities by the presence or absence of branch-point annihilation at the coalescence point.

To see how this may be implemented in a specific example, we now reconsider our dimensional perturbation treatment of the diamagnetic hydrogen problem.

5.2 Diamagnetic hydrogen

In a recent paper[124] we examined some branch-point degeneracy trajectories for the Barbanis Hamiltonian, which has two nontrivial parameters.[151] In Chap. 4 we examined in detail a similar situation with the diamagnetic hydrogen problem. With Z held constant this is not normally regarded as a two-parameter problem. However, in dimensional perturbation theory (see Chap. 3) the dimensionality of space is regarded as a continuous parameter.[119, 103, 107, 152] For two-particle problems, dimensionality and angular momentum enter the problem in equivalent and interchangeable ways. Therefore we can consider the diamagnetic hydrogen problem as a function of two parameters, the external (scaled) magnetic field $\widetilde{B}$ and the magnetic quantum number $|m|$.

In dimensional perturbation theory, the magnetic field and Coulomb potential are both incorporated into the zeroth-order Hamiltonian to such an extent that we can directly associate avoided crossings appearing in the E-versus-B spectrum with degeneracies arising at

zeroth order (Sec. 5.3). Therefore, this method establishes an orderly means of examining the complicated energy spectrum of diamagnetic hydrogen.

In Chap. 4 we used the positions of the branch points in the complex m-plane,[153] together with the analytic structure imparted by the branch points to the energy function in the complex m-plane, to determine the position of the avoided crossings, whether hidden or not. One purpose of this chapter is to establish this analytic structure.[154]

As with the Barbanis system, the branch-point trajectories in the complex m-plane as a function of field strength exhibit nonanalytic behavior where the branch points coalesce onto the real axis (Sec. 5.5). (Here, m is the parameter continued off the real line, whereas the field strength is the parameter *not* continued off the real line.) A second purpose of this chapter, once we have determined the analytic form of the energy in the complex m-plane, is to find a smooth parameterization underlying the nonanalytic behavior of the branch points (Sec. 5.6), that is, to uncover the nature of the singularity in the trajectory of the branch points as a function of field strength. As we will see in Sec. 5.6, the singular behavior of the branch-point trajectories in the complex m-plane as a function of field strength arises quite naturally from the analytic form of the energy in the complex m-plane. There is no need to further invoke any additional singular behavior. Despite the common singularity at the coalescence points, the branch-point trajectories and their behaviors through the coalescence points can be markedly different. In Sec. 5.7 we study this dissimilarity by deriving analytic expressions for the motion of branch points as a function of field strength near the coalescence points. For the two branch-point-pair trajectories studied in detail in this chapter, we show that, despite the differences in their trajectories, they share a common structure.

5.3 Avoided crossings and Fermi resonances

At small δ (which is the same as large D and large $|m|$) the Coulombic, diamagnetic, and kinetic terms of the Hamiltonian all contribute, so the small-δ solution is sensitive to the

interplay between these terms as $\widetilde{B}$ is changed. Therefore, we can understand much of the basic structure of the avoided crossings from the behavior of the small-δ solution, as we will see shortly. Note that much of the following has been discussed in more detail in Chap. 4.

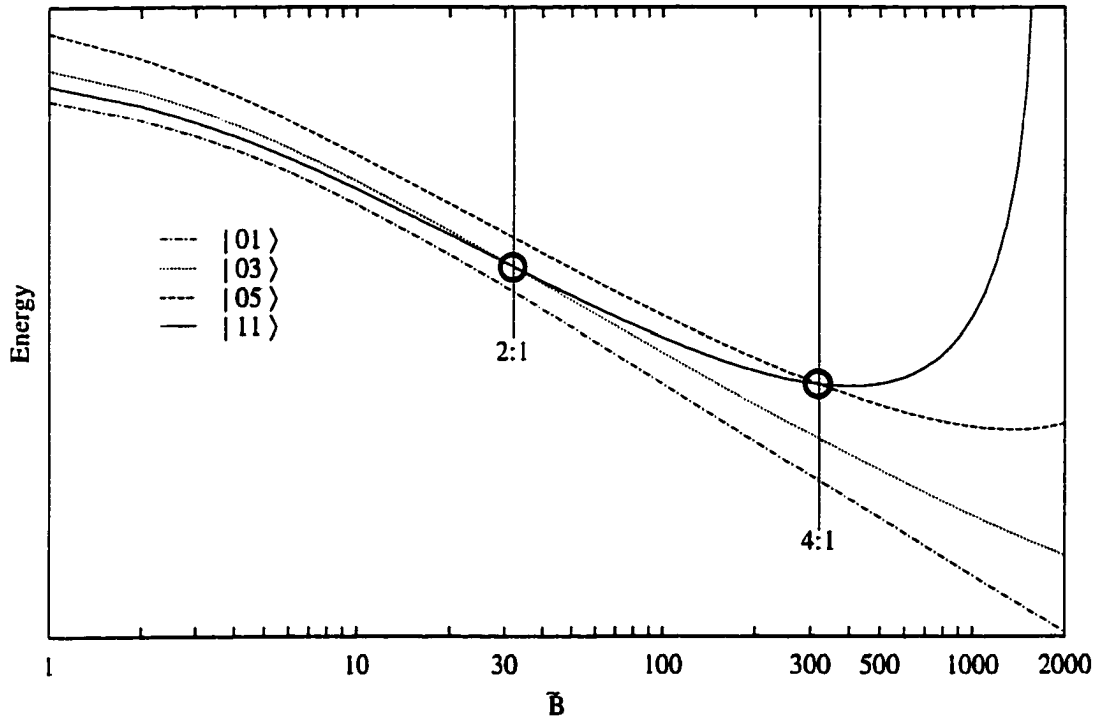

Figure 5.2: Harmonic-order energy levels of diamagnetic hydrogen. Note that the 2:1 and 4:1 Fermi-resonance degeneracies involving the $|11\rangle$ state, extensively discussed in this chapter, are circled. For clarity, we only show the lowest-lying states. The $|11\rangle$ energy level (solid line) crosses even more higher-lying energy levels (at 6:1, 8:1, ... Fermi resonances) as it rises toward the continuum. For a more complete spectrum, see Fig. 4.2 in Chap. 4.

As we stated in Chap. 4, there is a clear relationship between the E-versus-B and E-versus-$|m|$ spectra. Consider the situation where $\widetilde{B}$ is held constant at some value $\widetilde{B}_0$. As δ is adiabatically varied the avoided crossing occurs at some value $\delta \equiv \delta_0$. Now if δ is held constant at δ_0 while $\widetilde{B}$ is adiabatically varied, the avoided crossing will occur at roughly $\widetilde{B}_0$. This relationship was explained in Chap. 4 from the analytic structure of the branch

points and the positions of the branch points in the complex δ-plane. In the next section we establish the analytic structure of these branch points. We focus on the same two avoided crossings that we focused exclusively on in Chap. 4 (see Fig. 5.2):

- The 4:1 Fermi resonance ($\omega_2 = 4\,\omega_1$) between the $|05\rangle$ and $|11\rangle$ states near $\widetilde{B} = 320.8$.
- The 2:1 Fermi resonance ($\omega_2 = 2\,\omega_1$) between the $|03\rangle$ and $|11\rangle$ states near $\widetilde{B} = 32.1$.

Both are the lowest-lying crossings for their respective field strengths. These are also the first two crossings that the $|11\rangle$ state encounters as it rises toward the continuum as $\widetilde{B}$ increases. They are markedly dissimilar. The avoided crossing for the 2:1 Fermi resonance is a good example of a hidden avoided crossing, whereas the 4:1 avoided crossing is so narrow as to look almost like a *level* crossing. Furthermore, we already know that although both avoided crossings have different branch-point structures, underlying their branch-point structures is a common characterization between the branch-point trajectories as functions of field strength and the resulting avoided crossings.

5.4 Analytic Energy structure of diamagnetic hydrogen

In Sec. 5.1 we derived two basic criteria for determining the analytic energy structure of an avoided crossing. We now apply these criteria to determine whether the *general energy structure* or the *reduced energy structure* applies to the avoided crossings of diamagnetic hydrogen we consider in this chapter. At this point, we remind the reader that the parameters δ and $\widetilde{B}$ of the diamagnetic hydrogen problem correspond to the parameters u and v in Sec. 5.1, respectively.

5.4.1 Quadratic Padé analysis of the 2:1 and 4:1 Fermi resonances

We can use quadratic Padé approximants, which can naturally approximate functions with one or two branches[155] (see Appendix G) to distinguish which of Eqs. (5.4) or (5.5) is correct. Like linear Padé approximants, quadratic Padé approximants are more accurate

when the branch points are closer to the origin, so to ensure that the quadratic Padés pick up any branch points that may be present in $E^+(\delta, \widetilde{B}) + E^-(\delta, \widetilde{B})$ one should look for these branch points when $\widetilde{B}$ is such that they are close to the origin. As shown in Appendix H, at least one of the branch points is close to the origin when $\widetilde{B}$ is close to the Fermi resonance. However, after examining the quadratic Padé approximants for the $E^+(0, \widetilde{B}) + E^-(0, \widetilde{B})$ series near both Fermi resonances, we find *no* branch points which converge on the origin as the Fermi resonance condition is approached. Therefore, according to Criterion 1 in Sec. 5.1, this indicates that the *reduced*, and not the *general*, energy structure correctly parameterizes the energies of the states involved in both the 2:1 and 4:1 Fermi resonances.

5.4.2 Analytic investigation of the energy structure of the 4:1 Fermi resonance

Upon applying degenerate perturbation theory to the 2:1 Fermi resonance states at exact degeneracy in Appendix H, we obtain a series in powers of $\delta^{1/2}$; this leads us to conclude that the energies have a square-root branch point at the origin. Naively, we would expect the same result and conclusion to hold for the 4:1 Fermi resonance. In Appendix I, however, we show that this is not so, since the zeroth-order states turn out *not* to be a superposition of the $|11\rangle$ and $|05\rangle$ harmonic states, but rather either the $|11\rangle$ or the $|05\rangle$ harmonic state *individually*. Therefore, in this case the coefficients of the odd powers of $\delta^{1/2}$ in the energy series are 0, just as the coefficients of the odd powers of $\delta^{1/2}$ in the energy series derived from nondegenerate perturbation theory are 0 (see the text following Eqs. (3.9) and (3.11)).

Although the coefficients of the nondegenerate energy series rise without bound, indicating that at least one branch point is converging onto the origin at exact resonance (see Sec. 5.4.1 above, as well as Sec. 5.5.2 below), using degenerate perturbation theory we find no branch points at the origin at exact degeneracy. The two branch points must therefore annihilate at the origin, as in Eq. (5.6). Therefore, according to Criterion 2 in Sec. 5.1, this rules out Eq. (5.4) for the energies of the 4:1 states.

Hence the independent arguments of Secs. 5.4.1 and 5.4.2 both agree and we conclude that the *reduced energy structure*, Eq. (5.5), rather than the *general energy structure*, Eq. (5.4), correctly describes the analytic energy structure of the states for both Fermi resonances.

5.5 Branch-point trajectories of diamagnetic hydrogen

We determined that Eq. (5.5) correctly characterizes the branch-point structure of the energies of the 2:1 and 4:1 Fermi resonances states. Now we apply quadratic Padé approximants, which naturally approximate functions with two branch points connecting two branches (see Appendix G), to determine the branch-point trajectories of this energy structure in the complex δ-plane as we adiabatically vary $\widetilde{B}$ along the real axis.

5.5.1 2:1 Fermi resonance

In Fig. 4.7 we show the branch-point trajectories of the 2:1 Fermi resonance involving the $|11\rangle$ and $|03\rangle$ states. (We denote the branch points as $\delta^{\pm}$.) Here, the branch points are complex conjugate until $\widetilde{B}$ reaches roughly 25.1, at which point the branch points coalesce onto the negative real axis. From there one branch point travels toward $-\infty$, while the other travels toward the origin. In Sec. 5.4.1 and Appendix I we demonstrated through degenerate perturbation theory the existence of a branch point at the origin at the 2:1 Fermi-resonance degeneracy. The branch point that travels toward the origin from the coalescence point reaches the origin at $\widetilde{B} = 32.1$, the value of $\widetilde{B}$ at the 2:1 Fermi-resonance degeneracy. Once we increase $\widetilde{B}$ beyond this value both points travel toward $-\infty$ (this last step is not demonstrated in Fig. 4.7).

5.5.2 4:1 Fermi resonance

In Fig. 4.6 we show the branch points that connect the $|11\rangle$ and $|05\rangle$ states, associated with a 4:1 Fermi resonance, for various values of $\widetilde{B}$. If we start out with $\widetilde{B} < 320.8$, we see

that the branch points initially are complex conjugate and lie in the positive half-plane of the complex δ-plane. As we increase $\widetilde{B}$, the branch points sweep toward the left in the complex plane until they simultaneously reach the origin at roughly $\widetilde{B} = 320.8$; this value of $\widetilde{B}$ corresponds to the 4:1 Fermi-resonance degeneracy. As we saw in Sec. 5.4.2, there are no branch points at the origin at the exact 4:1 Fermi resonance condition, so the branch points annihilate when they reach this point (denoted by an open square in the figure). This means that the two energy levels at the 4:1 Fermi-resonance degeneracy are *not* actually connected by square-root branch points. For $\widetilde{B} > 320.8$ the branch points reappear and separate on the negative real axis, all the while traveling toward $-\infty$ as we increase $\widetilde{B}$.

5.6 Smooth parameterization of the branch-point trajectories through the coalescence points

Section 5.5 clearly shows that the branch-point trajectories display nonanalytic behavior at the coalescence points. In this section we identify a parameterization of the energy function which is smooth and apparently analytic through these coalescence points; this in turn provides a smooth parameterization for the branch-point trajectories and makes explicit the nature of the singularity in the branch-point trajectories.

5.6.1 The parameterization

If we define two functions

$$\beta(\widetilde{B}) = -\frac{\tilde{\delta}^{+}(\widetilde{B}) + \tilde{\delta}^{-}(\widetilde{B})}{2}, \qquad \gamma(\widetilde{B}) = \sqrt{\tilde{\delta}^{+}(\widetilde{B})\,\tilde{\delta}^{-}(\widetilde{B})}, \tag{5.7}$$

we can re-express Eq. (5.5) as

$$E^{\pm}(\delta, \widetilde{B}) = A \pm G\sqrt{\delta^2 + 2\beta\delta + \gamma^2}, \tag{5.8}$$

where the coefficients A and G are functions of δ and $\widetilde{B}$.

A priori there is no more reason to expect β and γ to be smooth — or even *analytic* — functions of $\widetilde{B}$ than there is for the branch-point locations $\tilde{\delta}^{\pm}(\widetilde{B})$; we saw that $\tilde{\delta}^{\pm}(\widetilde{B})$ are indeed nonanalytic at the coalescence point. However, we plot $\beta(\widetilde{B})$ and $\gamma(\widetilde{B})$ in Figs. 5.3 and 5.4 and we see that, for both the 4:1 *and* 2:1 Fermi resonances, both functions are smooth, apparently analytic, functions of $\widetilde{B}$ *even as the branch points move through the coalescence point and Fermi-resonance degeneracy.* This means that the branch-point positions in the complex δ-plane are given by the roots of the quadratic equation

$$\delta^2 + 2\beta\,\delta + \gamma^2 = 0\,, \tag{5.9}$$

where the nonanalytic behavior of the roots with $\widetilde{B}$ is solely determined by the quadratic nature of the equation rather than any nonanalytic behavior of the parameters in Eq. (5.9). Therefore, Eq. (5.5) automatically determines the positions of the branch points from the last term of the *reduced energy structure*, Eq. (5.9); that is, the nonanalytic behavior of the branch points at the coalescence points is naturally explained from the analytic structure of the energy in the complex δ-plane in terms of smooth, apparently analytic, functions β and γ. The analytic structure of the energy in the complex δ-plane *alone* determines the nonanalytic behavior of the branch points as a function of $\widetilde{B}$!

Note that if the *general energy structure*, Eq. (5.4), correctly parameterized the analytic structure of the energy, then the above economy of explanation would not hold since the terms in the brackets on the right side of Eq. (5.4) could not be expressed in terms of β and γ without the introduction of additional singularities.

5.6.2 Determining branch-point trajectories by the smooth parameterization of the energy

The solutions of Eq. (5.9),

$$\tilde{\delta}^{\pm}(\widetilde{B}) = -\beta(\widetilde{B}) \pm \sqrt{[\beta(\widetilde{B})]^2 - [\gamma(\widetilde{B})]^2}\,, \tag{5.10}$$

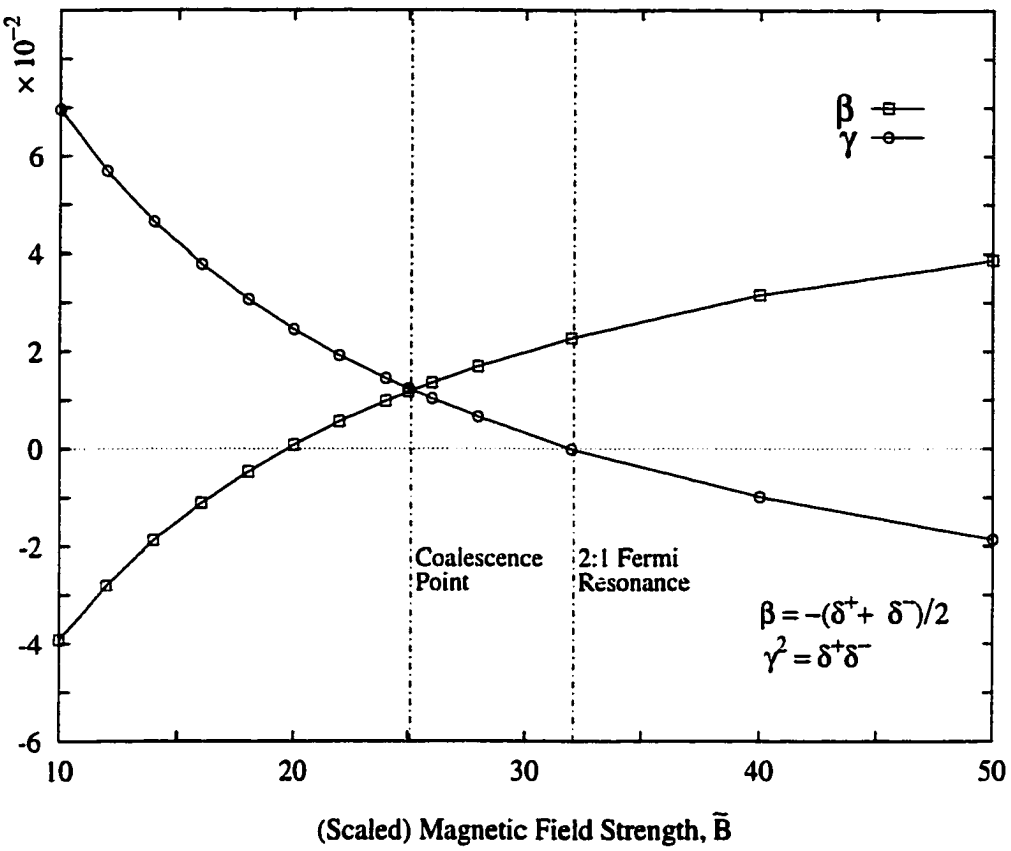

Figure 5.3: Branch-point parameters $\beta = -(\delta^+ + \delta^-)/2$ and $\gamma = \pm\sqrt{\delta^+\delta^-}$, where $\delta^\pm$ are the branch points in Fig. 4.7, plotted as functions of $\widetilde{B}$ for the 2:1 Fermi resonance. Note the smooth trajectories of both parameters through the coalescence point and the Fermi resonance.

allow us to understand the trajectories of the branch points in Figs. 4.7 and 4.6 in Chap. 4 from the behavior of the smooth parameters $\beta(\widetilde{B})$ and $\gamma(\widetilde{B})$ in Figs. 5.3 and 5.4. Since both β and γ are real, the branch points $\delta^\pm$ either both lie on the real axis or are complex conjugate. This also means that γ^2 and β^2 are always positive, regardless of the field strength. The field strength $\widetilde{B}_c$ at which the branch points coalesce onto the real axis corresponds to $\beta^2 = \gamma^2$. Across the branch-point singularity in Eq. (5.10) at $\widetilde{B}_c$, the branch points $\tilde{\delta}^\pm$ discontinuously change their behavior as $\beta^2 - \gamma^2$ changes sign. Therefore, for the purposes of this analysis it is convenient to divide the branch-point trajectories into two separate regions of field strength: $\widetilde{B} \leq \widetilde{B}_c$ and $\widetilde{B} > \widetilde{B}_c$.

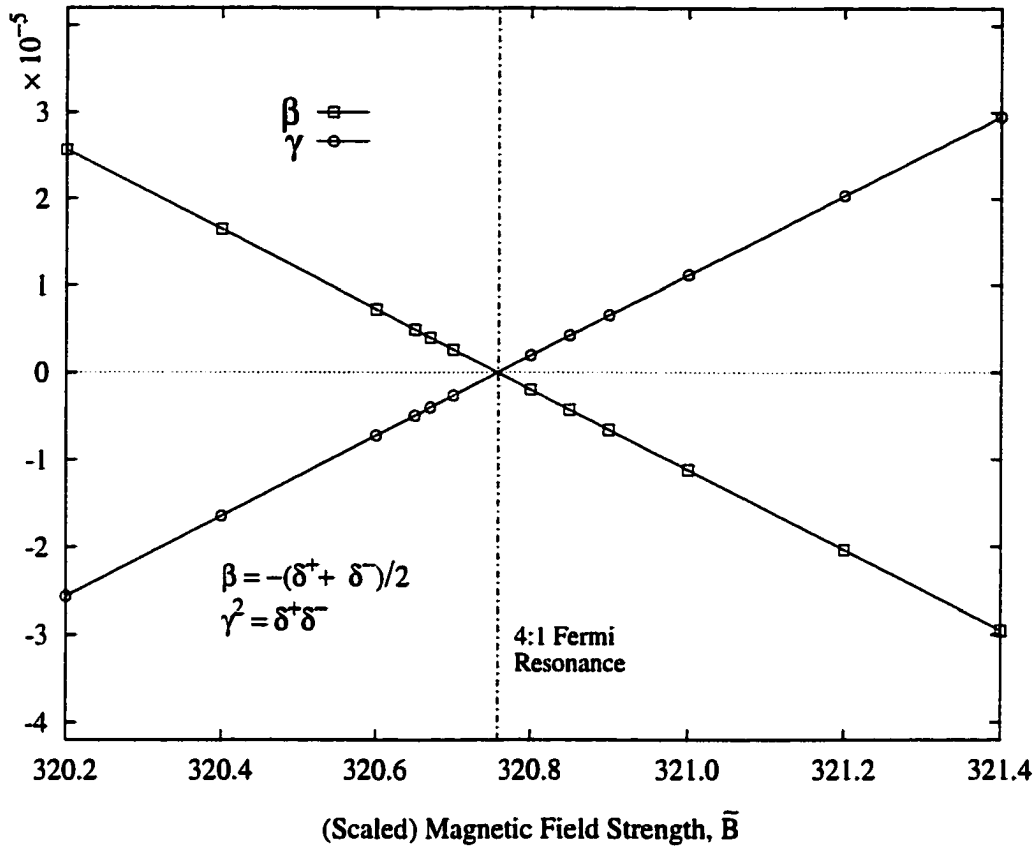

Figure 5.4: Same as Fig. 5.3, except for the 4:1 Fermi resonance. As in Fig. 5.3, both parameters are smooth functions of $\widetilde{B}$, even through the Fermi resonance (which coincides with the coalescence point for this interaction).

We initially consider $\widetilde{B} < \widetilde{B}_c$ and allow it to increase adiabatically. For the 2:1 Fermi resonance in Fig. 4.7, $\beta^2 \leq \gamma^2$ when $\widetilde{B} < \widetilde{B}_c$. Therefore, the branch points form complex-conjugate pairs straddling the positive real axis. Initially, $\beta < 0$, so the branch points lie in the positive half-plane. As β increases to 0 as we increase $\widetilde{B}$, the value of $\beta^2 - \gamma^2$ approaches 0 but remains negative. Therefore, the branch points approach the imaginary axis with a falling imaginary component, crossing the axis when $\beta = 0$. The parameter β becomes increasingly positive as we increase $\widetilde{B}$, while γ continues to fall, so the branch points continue to sweep toward the left in the negative half-plane. During this time the imaginary component continues to shrink until $\beta^2 = \gamma^2$ at $\widetilde{B}_c$, at which point they coalesce onto the negative real axis.

When $\widetilde{B} > \widetilde{B}_c$ the quantity $\beta^2 - \gamma^2 > 0$, so from Eq. (5.10) the branch points $\delta^{\pm}$ lie on the real axis. Since $\beta \geq \sqrt{\beta^2 - \gamma^2}$, both branch points must be negative. The parameter γ continues to fall as $\widetilde{B}$ increases past $\widetilde{B}_c$, so $\sqrt{\beta^2 - \gamma^2}$ rises in value faster than β. Therefore, while δ^- travels in the negative direction from the coalescence point, δ^+ initially travels toward the origin. However, γ^2 has a minimum value of 0 at the Fermi resonance, so δ^+ bounces off the origin at the Fermi resonance and then follows δ^- in the negative direction.

The nonanalytic behavior of the 4:1 Fermi-resonance, branch-point trajectories of Fig. 4.6 is similarly explained from the plots of $\beta(\widetilde{B})$ and $\gamma(\widetilde{B})$ in Fig. 5.4. In this case the coalescence point, $\beta = \gamma$, coincides with the Fermi resonance, $\gamma = 0$. The parameters β and γ are almost straight lines passing through the origin with opposite gradient, so $\beta^2 - \gamma^2 = (\beta - \gamma)(\beta + \gamma)$ in the radical of Eq. (5.10) is not readily determined from Fig. 5.4. The quantity $(\beta - \gamma)$ is close to a straight line, but with twice the gradient of β. Therefore $(\beta - \gamma) < 0$ for $\widetilde{B} < \widetilde{B}_c$, whereas $(\beta - \gamma) > 0$ for $\widetilde{B} > \widetilde{B}_c$. The quantity $(\beta + \gamma) \geq 0$, with a minimum of 0 at the coalescence points (see Fig. 5.5). Therefore, since $\beta^2 - \gamma^2 < 0$ for $\widetilde{B} < \widetilde{B}_c$, the branch points of the 4:1 Fermi resonance, as for the 2:1 Fermi resonance, are complex conjugate in the complex δ-plane for these values of $\widetilde{B}$. Because $\beta^2 - \gamma^2 > 0$ when $\widetilde{B} > \widetilde{B}_c$, both branch points of the 4:1 Fermi resonance lie on the negative real axis for these values of $\widetilde{B}$. Since $(\beta + \gamma) \ll \beta$, both branch points travel in the negative direction more or less as a pair centered around the point $-\beta$.

5.7 Analytic behavior of the branch points at the coalescence points

Although we found a common singularity structure in the branch-point trajectories of both the 2:1 and 4:1 Fermi resonances, the trajectories of Figs. 4.7 and 4.6 differ significantly. Given the above smooth parameterization we can investigate this further and determine

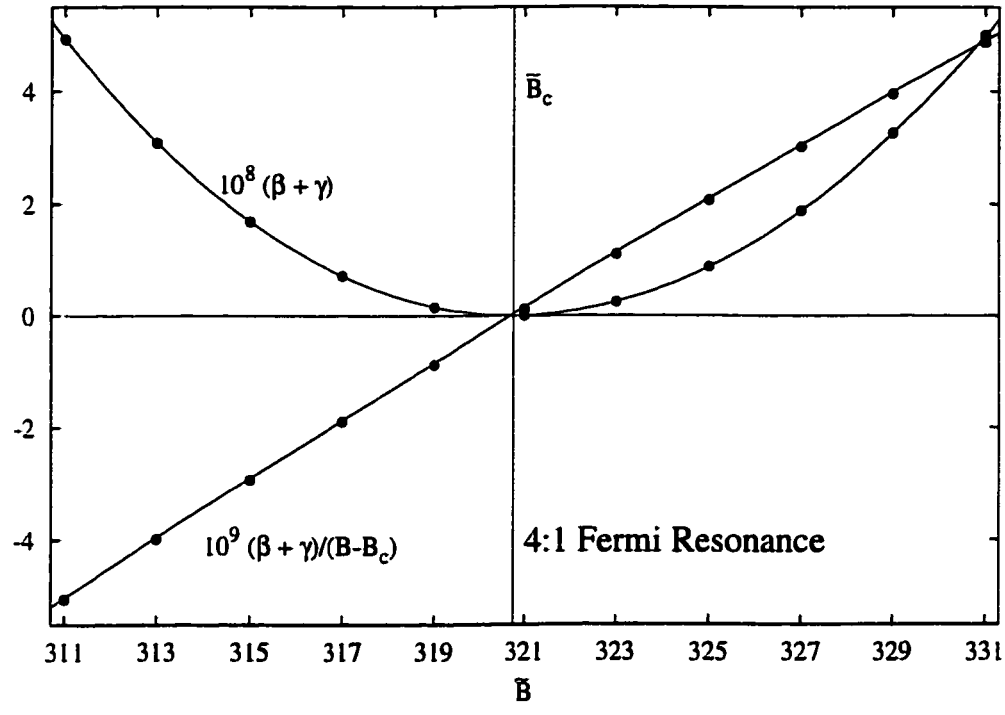

Figure 5.5: Plot of the sums $\beta+\gamma$ and $(\beta+\gamma)/(\tilde{B}-\tilde{B})$ as functions of $\tilde{B}$ for the 4:1 Fermi resonance.

from Eq. (5.10) the precise nonanalytic behavior of the branch points through the coalescence points. At the coalescence point $\tilde{B} \equiv \tilde{B}_c$ and $\beta(\tilde{B}_c) = \gamma(\tilde{B}_c) = a$, so we can expand β and γ as

$$\beta = a + b(\Delta\tilde{B}) + c(\Delta\tilde{B})^2 + \cdots, \qquad \gamma = a - e(\Delta\tilde{B}) + f(\Delta\tilde{B})^2 + \cdots, \tag{5.11}$$

where $\Delta\tilde{B} \equiv \tilde{B} - \tilde{B}_c$. Substituting β and γ into Eq. (5.10) we find to lowest order that

$$\tilde{\delta}^{\pm} = -a - b(\Delta\tilde{B}) - c(\Delta\tilde{B})^2 \pm (\Delta\tilde{B})^{1/2}\Big\{2a[(b+e) + (c-f)(\Delta\tilde{B})] + (\Delta\tilde{B})[(b^2-e^2) + 2(bc+ef)(\Delta\tilde{B})]\Big\}^{1/2}. \tag{5.12}$$

Therefore to second order in $(\Delta\widetilde{B})^{1/2}$ the branch points of the 2:1 Fermi resonance in the neighborhood of the coalescence point behave as

$$\tilde{\delta}^{\pm} = -a - b(\Delta\widetilde{B}) \pm (\Delta\widetilde{B})^{1/2}\sqrt{2a(b+e)}. \tag{5.13}$$

Now we consider the 4:1 Fermi resonance. Figure 5.4 shows that $a = 0$. From Eqs. (5.11) we get

$$\frac{\beta+\gamma}{\Delta\widetilde{B}} = (b-e) + (c+f)(\Delta\widetilde{B}) + \cdots, \tag{5.14}$$

from which Fig. 5.5 shows that $b = e$. Therefore, to fourth order in $(\Delta\widetilde{B})^{1/2}$ Eq. (5.12) becomes

$$\tilde{\delta}^{\pm} = (\Delta\widetilde{B})\left[-b - c(\Delta\widetilde{B}) \pm (\Delta\widetilde{B})^{1/2}\sqrt{2b(c+f)}\right] \tag{5.15}$$

for the 4:1 Fermi resonance in the neighborhood of the coalescence point/Fermi resonance.

Equations (5.13) and (5.15) reveal the square-root branch-point singularities which account for the nonanalytic behavior at $\widetilde{B}_c$ of the branch-point trajectories in the complex δ-plane for the 2:1 and 4:1 Fermi resonances, respectively. They also make it clear where the differences in the branch-point trajectories develop. Surprisingly, the right side of Eq. (5.15) has the same form as the right side of Eq. (5.13) except that it is multiplied by $\Delta\widetilde{B} = (\widetilde{B} - \widetilde{B}_c)$. Hence the plot of $\tilde{\delta}^{\pm}(\widetilde{B})/(\widetilde{B} - \widetilde{B}_c)$ for the 4:1 Fermi resonance should look similar in structure to the plot of $\tilde{\delta}^{\pm}(\widetilde{B})$ for the 2:1 Fermi resonance. Comparing Figs. 5.6 and 4.7 we see that this is indeed the case; the branch points travel in opposite directions along the real axis as $\widetilde{B}$ is raised past the coalescence points. The branch point traveling in the negative direction then reverses direction and follows the other branch point in the positive direction.[156]

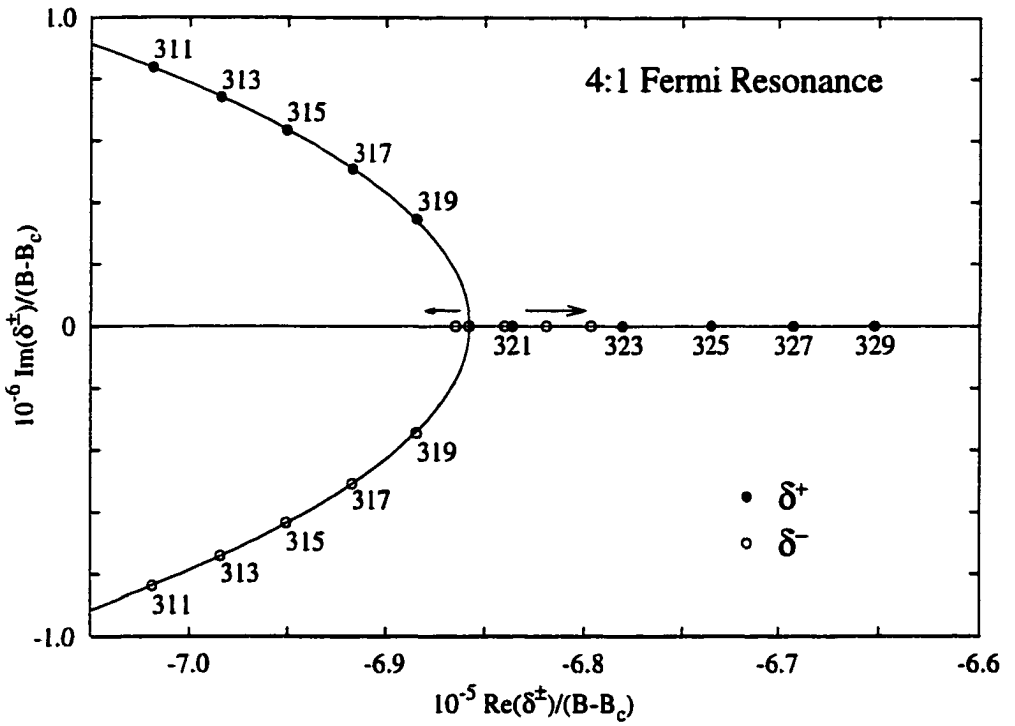

Figure 5.6: Plot of $\delta^{\pm}(\widetilde{B})/(\widetilde{B}-\widetilde{B}_c)$ for the 4:1 Fermi resonance, for field strengths up to $\widetilde{B}=329$. The coalescence point here occurs at the 4:1 Fermi resonance, which occurs roughly at $\widetilde{B}=320.8$. The unmarked branch-point locations for δ^- (open circles) on the real axis are, from left to right, $\widetilde{B}=323$, 321, 325, 327, 329. Note that at $\widetilde{B}=321$ the branch point δ^- lies practically on top of the coalescence point, whereas the other branch point has already moved a significant distance to the right. Once the field is strengthened beyond $\widetilde{B}_c$, the δ^- branch point initially travels toward the left, subsequently reversing its direction and traveling in the same direction as δ^+. Compare to Fig. 4.7 and note the similarity in the branch-point trajectories.

Part III

Local Optimization of the Summation of Divergent Power Series: A New Approach in Applied Numerical Analysis

Chapter 6

Local Optimization of Economized Rational Approximants

Until now this dissertation has focused mainly on states of large $|m|$, and one question remaining is whether dimensional perturbation theory can produce meaningful calculations of energy at much lower $|m|$ for a given *scaled* field strength $\widetilde{B}$. Upon further investigation, simple Padé summation proves effective in summing the energy series of diamagnetic hydrogen, but for some states and field strengths this summation diverges. The attempt to find a better approximant resulted in an entirely new technique in applied numerical analysis. This new technique not only sums the perturbation series of diamagnetic hydrogen in many instances where Padé summation fails, but its effectiveness transcends our scope of research in atomic physics to include general problems in numerical analysis.

This chapter describes the problem of summing divergent perturbation series, and how this new technique often can overcome this problem. In the next chapter, we will see how this technique was successfully applied to the perturbation series in this research.

6.1 The problem of summing a divergent power series

The bulk of the following was accepted for publication in *Journal of Mathematical Physics* and will appear in the July or August, 2000 issue.

The divergence of perturbation series is an important hindrance to progress in many fields of physics. Fortunately, there are many methods[126, 157, 158, 159] available that can often transform perturbation series into approximants that converge to accurate results.

Padé approximants[160] can incorporate singularities into their structure that the original perturbation series cannot, and for this reason have long been a favored method of approximation. They tend to have remarkable short-range accuracy (that is, when the distance from the origin to the point of evaluation is small), but somewhat poorer long-range accuracy. Therefore, although they almost always yield better results than directly summing the perturbation series and often converge when direct summation completely fails, we will see shortly that they can still produce frustratingly poor or meaningless results at larger distances away from the origin. An example is discussed in detail later in this chapter, namely the exponential function $f(x) = 1/(1 + e^x)$ evaluated at $x = 6000$. In this case, not only are the Padé approximants inaccurate, they do not even appear to converge to the correct value. (We will see how this research rectifies this situation later.)

Various extrapolation methods can extract accurate results from poorly converging sequences by extrapolating the sequence out to infinity,[126] but these frequently fail with poorly convergent Padé sequences since they tend to be quite irregular in their convergence. Other rational polynomial approximants[157] can perform significantly better than Padé approximants, but rarely share their rugged versatility.

In the field of applied computing one is usually interested in evaluating a function repeatedly within a certain range of the independent variable x. Because computers can only add, subtract, multiply and divide, rational functions of polynomials are the most complex functions which can be directly evaluated on a computer.[162] Therefore computers use rational polynomial approximants to approximate more complex functions to a high degree of accuracy. The Padé approximant, being one example, is hampered by its relatively poor long-range accuracy. Fortunately, there are methods that transform Padé approximants by sacrificing their superior short-range accuracy so as to lower the maximum error over the entire evaluation range. One such method is *economization*. Padé approximants can be

economized[162, 163] to produce an approximant, called an economized rational approximant (ERA), that guarantees a lower maximum error throughout a specific range of the independent variable.

With perturbation theory, however, one is usually more concerned with evaluating the perturbation series at a particular value of x which is known beforehand. In such cases it is beneficial to minimize the error at that specific value of x, rather than to minimize the maximum error over the entire range. In this chapter, we introduce a method for optimizing ERAs[164] to minimize the error *at a specific value* of the independent variable. We chose to optimize ERAs because:

1. They are capable of providing a more accurate summation of the perturbation series than Padé approximants when the point of evaluation is far from the origin.

2. They contain a parameter that allows one to change the convergence of the resulting sequence in a continuous fashion.

In Sec. 6.2 we review the economization of power series and in Sec. 6.3 we briefly review the process of economization of Padé approximants. In Sec. 6.4 we demonstrate how to optimize ERAs to produce a convergent sequence which reduces the error at a specific value of the independent variable, even when the original Padé sequence behaves erratically. We then test this method on six basic functions in Sec. 6.5. Finally, in Sec. 6.6 we discuss various details of the numerical procedure used in optimization and suggest an explanation for its success.

6.2 Economization of a power series

In approximation theory one often derives an approximate representation of a function (an approximant), specified by $N+1$ parameters, that have been derived from the first $N+1$ coefficients of the power series. Such a representation may be, for example, the original power series truncated at the Nth order, S_N, or a Padé approximant $P_{m,k}(x)$, where m and

k are the respective orders of the numerator and denominator polynomials and $m+k=N$. Economization involves finding an alternative representation for the function containing $N+1$ parameters that possesses the same functional form as the initial approximant, but also incorporates information present in the higher orders of the original power series to minimize the maximum error of the new approximant over a specified range of x. In other words, one has an economy of representation: An accuracy is obtained which would otherwise be achieved by taking the original approximant to higher order, which would require more than $N+1$ parameters to specify.

In this section we consider the economization of a power series representation. This may be achieved by subtracting from S_{N+1} (the original power series truncated at order $N+1$) a suitable polynomial $\mathcal{P}_{N+1}$ of the same order such that the leading orders cancel. In other words,

$$S_{N+1} \equiv \sum_{i=0}^{N+1} c_i x^i \quad \Longrightarrow \quad S_{N+1} - \mathcal{P}_{N+1} = \sum_{i=0}^{N} c_i' x^i, \tag{6.1}$$

where c_i' denotes the resulting expansion coefficient of x^i. Naturally, the goal is to pick $\mathcal{P}_{N+1}$ so that the maximum error of the new Nth order series representation over a specified range x is significantly reduced. We can satisfy this requirement with the Chebyshev polynomial T_{N+1} such that[161, 162, 163]

$$\mathcal{P}_{N+1} = 2c_{N+1}\frac{\alpha^{N+1}}{2^{N+1}}T_{N+1}, \qquad T_{N+1}(x/\alpha) = \frac{2^{N+1}}{2}\left(\frac{x}{\alpha}\right)^{N+1} + p_N(x/\alpha), \tag{6.2}$$

where $p_N(x/\alpha)$ is a polynomial of order N and α is an arbitrary scaling parameter.[165] If we apply the transformation

$$\begin{aligned} S_{N+1} \equiv \sum_{i=0}^{N+1} c_i x^i \quad \Longrightarrow \quad C_N &\equiv S_{N+1} - 2c_{N+1}\frac{\alpha^{N+1}}{2^{N+1}}T_{N+1}(x/\alpha) \\ &= \sum_{i=0}^{N} c_i x^i - p_N(x/\alpha) = \sum_{i=0}^{N} c_i' x^i, \end{aligned} \tag{6.3}$$

we produce an economized power series representation C_N of order N provided α is chosen sufficiently small and x lies within the region $-\alpha \leq x \leq \alpha$. When $\alpha = 0$ we recover the original representation S_{N+1}.

The maximum error of this new Nth-order polynomial, C_N, for finite α is nearly the same as the maximum error of the $(N+1)$th order polynomial S_{N+1} and considerably less than S_N. In Fig. 6.1(a) the errors for the power series and economized power series expansion of $f(x) = e^x$ are shown for values throughout the range $-1 \leq x \leq 1$. Here we have set $\alpha = 1$, which guarantees that the economization principle will apply throughout the range shown in the figure.[162] As we can see, the maximum error of C_3 is only slightly larger than S_4, but is considerably smaller than S_3. However, we emphasize that in certain regions, especially near the origin, even S_N provides a better representation of the function. Again, the errors we discussed previously correspond to *maximum* errors throughout a specified range, and do not indicate in any way how the errors will compare at a specific value of x. Economizing the power series represents a trade-off; the error will be larger in some regions, but there is a guarantee that the maximum error of the entire region will be lower.

For those interested in finding an analytic approximation for a function in power series form that is valid for a specific range of the independent variable x and is as economic in its expression as possible, insuring that the maximum error is as small as possible is essential. However, in most applications of perturbation theory it is desirable to minimize the error *at a particular value of the independent variable* x, irrespective of the effects this has on the maximum error throughout the range. We will denote this value x_0. *The fact that the parameter* α *is arbitrary and continuous allows us, in principle, to raise* α *from 0 until it reaches a value that minimizes the error at* x_0. This is illustrated in Fig. 6.1(b), which is a closeup of Fig. 6.1(a) near $x_0 = 0.42$. At this x_0 the error in C_3 for $\alpha = 1$ is significantly larger than S_4. However, if we had instead increased α to the value $\alpha = 0.61$, the resulting error in C_3 would have been considerably lower than S_4.

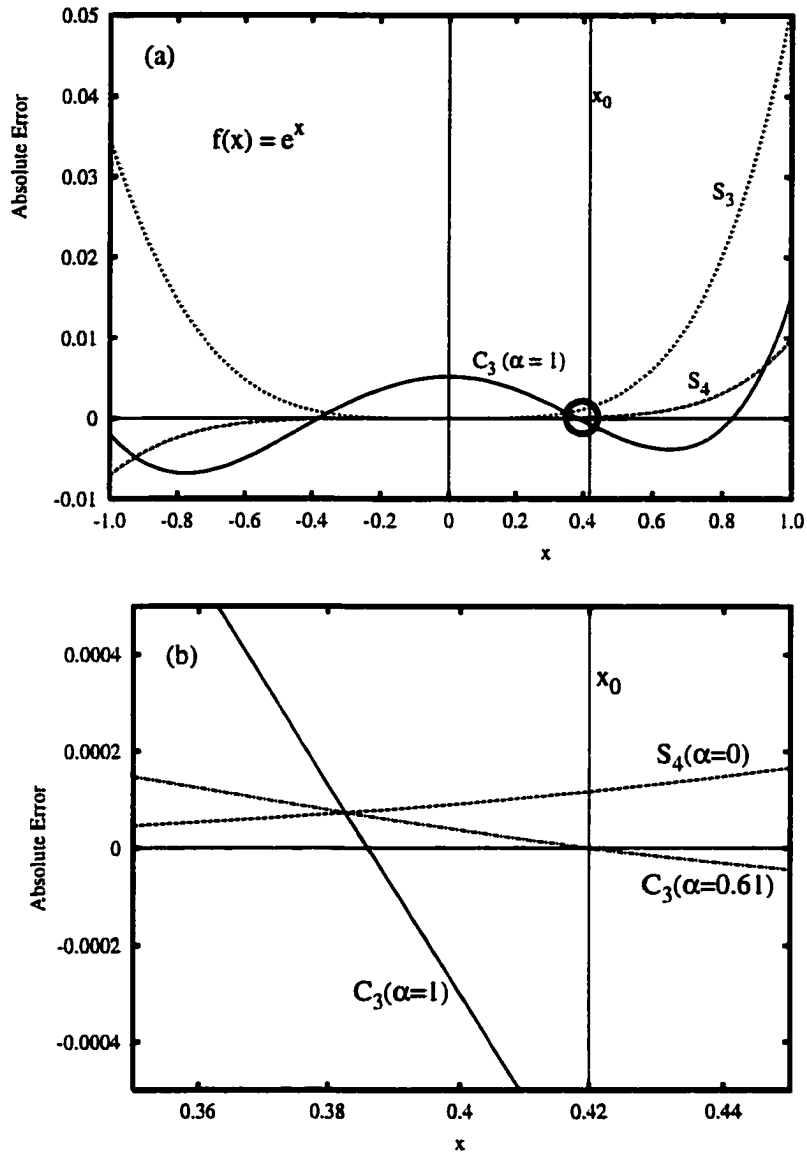

Figure 6.1: (a) Comparison between the error of the third and fourth order power series expansions, S_3 and S_4, and the third order economized representation C_3 for the function $f(x) = e^x$, where we have highlighted a specific value of the independent variable x_0 at $x = 0.42$. The maximum error of C_3 is considerably lower than S_3, and compares favorably with S_4. However, the error is larger in some regions of x, especially near the origin. (b) A closeup of the circled region in the first figure. When α_0 approaches 0.61 we see that the error of $C_3(x)$ reduces dramatically at x_0. Notice that increasing α further to $\alpha = 1$ leads to considerable error at x_0. (S_3 not shown.)

From here on, we designate the value of α that reduces the error at x_0 to a minimum as α_0. Finding α_0 when the original function is not known is the goal of this research, but we first describe how the process of economization is applied to problems where the function is approximated by a Padé approximant.

6.3 Padé and economized rational approximants

When the original power series S_N diverges it is often beneficial to replace it with a more suitable representation such as a Padé approximant:

$$S_N(x) \quad \Longrightarrow \quad P_{m,k}(x) \equiv \frac{P_m(x)}{Q_k(x)} = \frac{a_0 + a_1 x + a_2 + \cdots + a_m x^m}{1 + b_1 x + b_2 x^2 + b_3 x^3 + \cdots + b_k x^k}, \tag{6.4}$$

where the order $N = m + k$. The coefficients are chosen so that the Padé approximant and its first N derivatives coincide with those of the original power series representation at the origin. We can economize the Padé approximant in much the same way as we economized the power series in the previous section. The corresponding economized rational approximant $C_{m,k}$ is[162]

$$S_{N+1}(x) \quad \Longrightarrow \quad C_{m,k}(x) = \frac{P_m(x) + \sum_{j=0}^{N-1} \gamma_{j+1} P_i(x) + \gamma_0}{Q_k(x) + \sum_{j=0}^{N-1} \gamma_{j+1} Q_{j-i}(x)}, \tag{6.5}$$

where

$$\gamma_{j+1} = \frac{d_{N+1}}{d_{j+1}} \frac{\alpha^{N-j}}{2^N} t_{j+1}, \qquad \gamma_0 = -\frac{d_{N+1} \alpha^{N+1} t_0}{2^N}, \qquad (j = 0, 1, \ldots, N-1), \tag{6.6}$$

and t_i is the Chebyshev coefficient of x^i. The coefficients $\{d_i\}$ are given by

$$d_i = \sum_{j=0}^{k} c_{i-j} b_j, \tag{6.7}$$

where $\{c_i\}$ are simply the expansion coefficients of the original power series and k is the power of the leading coefficient of Q_k. As for the Padé approximants $P_{m,k}(x)$, m and k are the orders of the polynomials of the numerator and denominator respectively and $m+k=N$. To calculate the ERA from Eq. (6.5) Padé approximant of the form in Eq. (6.4) must be chosen and generated, producing the terms P_i, Q_i, and b_i. From the coefficients $\{b_i\}$ we can determine the coefficients[166] $\{d_i\}$ and, therefore, calculate the parameters γ_0 and γ_{j+1}.

Like Padé approximants $P_{m,k}$, the ERAs $C_{m,k}$ are specified by $(m+1)+k=N+1$ parameters. When α is reduced to 0, the ERA $C_{m,k}$ is identical to the Padé approximant $P_{m,k}$. The ERAs are economized in the same sense as for the economized power series C_N of Section 6.2. For the Padé approximants $P_{m,k}$, these $N+1$ parameters are derived from the first $N+1$ coefficients of the power series; however, the $N+1$ parameters specifying $C_{m,k}$ are derived from the first $N+2$ coefficients of the power series so that the maximum error over $-\alpha \leq x \leq \alpha$ is minimized. The $(N+2)$th coefficient, c_{N+1}, of the power series is needed to calculate the γ_i. (A proof that $C_{m,k}$ economizes the Padé approximant $P_{m,k}$ for sufficiently small α is given in Ralston[162].)

In Fig. 6.2 we compare the error between a Padé approximant and the corresponding ERA for the function $f(x)=\log(1+x)$ when $\alpha=1$. As expected, the ERA has a lower maximum error throughout the range $-1 \leq x \leq 1$, and for some values is significantly more accurate.

As in Section 6.2, instead of using ERAs to minimizing the maximum error over a range of x specified by α, we can use ERAs to minimize the error at some specific value x_0 of the independent variable x by choosing a suitable value for α. We now turn our attention to finding the appropriate value of α.

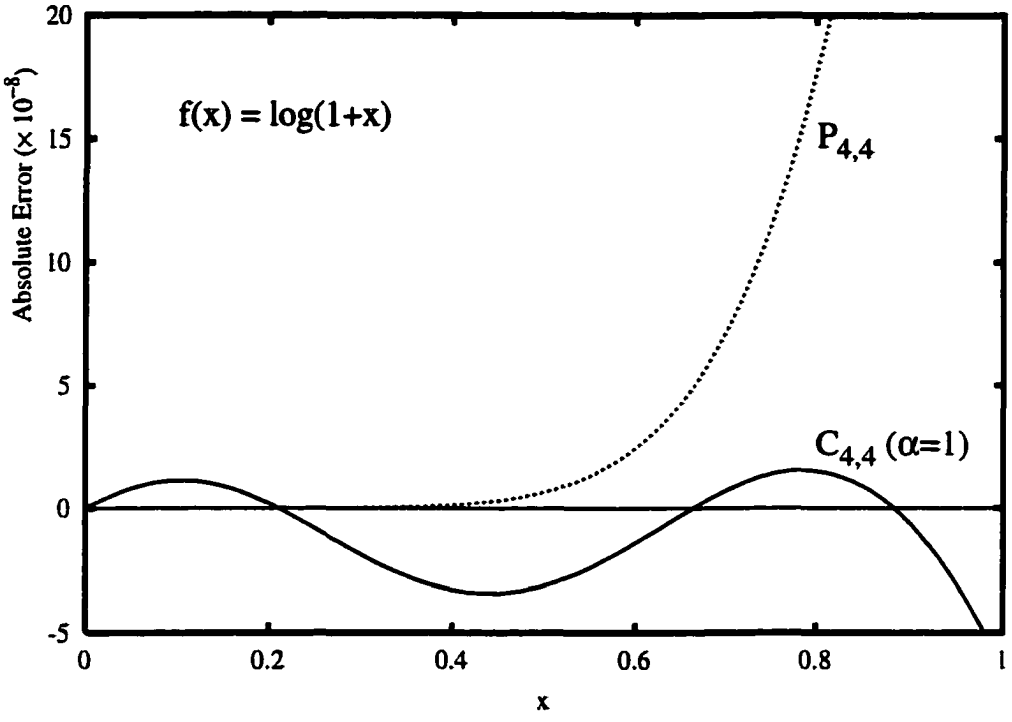

Figure 6.2: The error of the Padé approximant $P_{4,4}(x)$ and the corresponding economized Padé approximant (ERA) $C_{4,4}(x)$ for the function $f(x) = \log(1+x)$. Here, $\alpha = 1$. Notice that the overall maximum error of $C_{4,4}$ is much lower than $P_{4,4}$, at least over the interval shown. Outside this interval the error in $C_{4,4}(x)$ diverges as well.

6.4 Optimizing the scaling parameter

There appears to be no definitive prescription in the literature for determining the optimal value of α, which we denote $\alpha^{\alpha_0}_{m,k}$ of an ERA, that minimizes the error at a point x_0. We based our method for finding $\alpha_0(m,k)$ on three assumptions:

1. If the optimized ERA provides a good representation of the original function at a particular point, then, for sufficiently large N, the value of the optimized ERA will converge smoothly towards the correct value as the order is increased towards the maximum order, N, of the power series. Therefore the values of the sequence of optimized ERAs will fit closely to the function of the form $\mathcal{G}_A(N) \equiv A(1 - e^{-g(N)})$,

where $g(N)$ is a smooth function such that $g(N) \rightarrow \infty$ as $N \rightarrow \infty$ and A is the fully converged ($N \rightarrow \infty$) value of the summed power series.

2. We also require that $\lim_{N\rightarrow\infty} \exp[-\nu N]\, g(N) = 0$ for all $\nu > 0$. Therefore, in the vicinity of $N = N_0$ we can expand $g(N)$ in a Taylor series about N_0 and write

$$\begin{aligned} \mathcal{G}_A(N) &= A\left(1-e^{-g(N_0)} \exp[-g'(N)|_{N_0}\Delta N\{1+[g''(N)/(2g'(N))]_{N_0}\Delta N+\ldots\}]\right) \\ &\approx A(1-e^{-sN}B)\,, \end{aligned} \tag{6.8}$$

where $\Delta N \equiv N - N_0$, $B = \exp[N_0 g'(N)|_{N_0} - g(N_0)]$, $s = g'(N)|_{N_0}$, and the approximation holds when N_0 is sufficiently large and N is in the vicinity of N_0. Hence we determine the value of $\alpha = \alpha_0(m', k')$ which optimizes the accuracy of each $C_{m',k'}$ in a sequence of approximants $m' = (m+i), k' = (k+i)$, where i is an integer, as follows. We require that the values of a sequence of optimized ERAs at large $N = m' + k'$ locally fit close to a function of the form

$$\mathcal{F}_{A,B,s}(N) \equiv A(1 - e^{-sN}B)\,, \tag{6.9}$$

where A, B, and s are arbitrary fitting parameters, regardless of the nature of the original series (convergent, or divergent).

3. If α for the $[m,k]$ approximant is optimized when $\alpha = \alpha_0(m,k)$, then the optimal value of α for all approximants $[(m+i),(k+i)]$ of the same sequence near $[m,k]$, where i can be positive or negative and not too far from zero, will be close to $\alpha_0(m,k)$. Therefore, when locally fitting a sequence to a function of the form $\mathcal{F}_{A,B,s}(N)$, each approximant may be assumed to have the same value of α.

The basis for optimizing α can now be easily summarized:

The optimal value of α is that which produces the closest fit to the function of the form $\mathcal{F}_{A,B,s}(N)$ where A, B and $s \geq 0$ are determined by the fit.

Since the functional form $\mathcal{F}_{A,B,s}(N)$ for the optimal convergence emerges locally at large orders, $\mathcal{F}_{A,B,s}(N)$ should be fitted to the last available terms of the sequence where this behavior is most strongly manifested. Four terms of the sequence are the minimum necessary to determine the four quantities α_0, A, B and s specifying the optimal fit. At this point we can detail an algorithm for optimizing α:

1. Select a sequence of ERAs specified by the integer p, where $p = m - k$, for some initial value of α.

2. For this value of α find the value of A, B and s which maximizes the fit of $\mathcal{F}_{A,B,s}(N)$ to the last four terms of the ERA sequence.

3. Choose a new value for α and repeat Step 2.

The value of α which maximizes the fit is designated α_0, from which the last and most accurate approximant in the sequence is generated. In the rest of the chapter we refer to this last approximant of an optimized sequence as the optimized ERA and denote it by $C^{\alpha_0}_{m,k}$.

In practice we perform step 2 through a least-squares fit to the last four terms of the sequence by minimizing $\sum_{i=0}^{3}[C^{\alpha}_{m-i,k-i} - (A - e^{-s(N-2i)}B')]^2$ with respect to the linear parameters A and B',where $B' = AB$. We use the coefficient of determination R^2 to quantify the accuracy of the fit, where R^2 is the square of the multiple correlation coefficient R, and is given by

$$R^2 \equiv \frac{\sum_{i=0}^{3}(A - e^{-s(N-2i)}B')^2}{\sum_{i=0}^{3}(C^{\alpha}_{(m-i),(k-i)})^2} = 1 - \frac{\sum_{i=0}^{3}[C^{\alpha}_{(m-i),(k-i)} - (A - e^{-s(N-2i)}B')]^2}{\sum_{i=0}^{3}(C^{\alpha}_{(m-i),(k-i)})^2}. \quad (6.10)$$

The coefficient of determination R^2 clearly runs between 0 and 1, and a perfect fit corresponds to $R^2 = 1$. The maximizing of the fit with respect to the non-linear parameter s is achieved by maximizing R^2 with respect to s. The optimal parameter α_0 is that value of α for which the maximum value of R^2 with respect to s, is maximized.[167] In Appendix J, I provide the source code (written in *Mathematia*) for the optimization process.

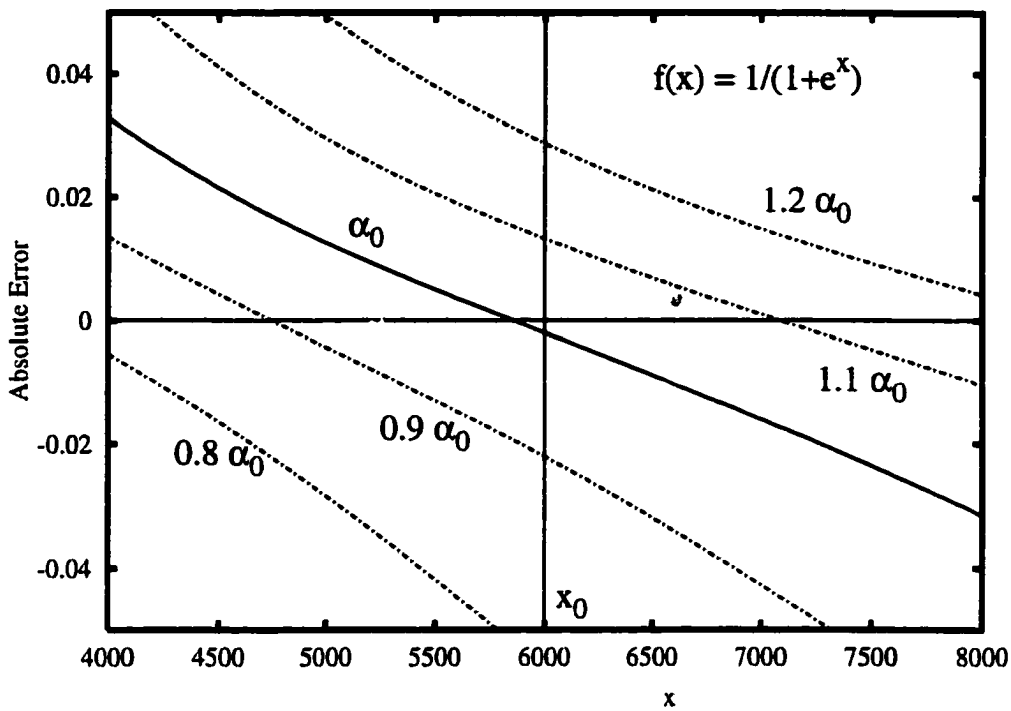

Figure 6.3: The role optimization plays in reducing the error of an ERA to a minimum. The function here is $f(x) = 1/(1+e^x)$ in the asymptotic region. As α is swept across α_0 we see that the error reduces to a minimum at a value very close to α_0. This minimization of error occurs in much the same way as choosing an optimal value for α reduces the error of a power series, as we found by comparing Figs. 6.1(a) and 6.1(b).

As in Fig. 6.1 and the discussion in Sec. 6.2, we can see in Fig. 6.3 [in this case, for $f(x) = 1/(1+e^x)$] how optimization reduces the error of the ERAs: As α is swept from 0, the error reduces until it reaches a (near) minimum at α_0, corresponding to a sequence having the closest fit to an exponential function. Beyond α_0 the error begins to increase.

This procedure is illustrated in Figs. 6.4(a)–(d) for $f(x) = \tanh(x)$. At $\alpha = 0$ (the Padé sequence) the highest-ordered term appears to be reasonably accurate, but the lower-ordered terms do not converge towards the correct value in a smooth fashion. As α is increased, the lower-ordered terms begin to drop in value so as to create a monotonic sequence that ultimately fits very closely to an exponential line. Finally, at some value of α

the terms line up very precisely to the exponential line. Once this point is reached the corresponding value for α is designated α_0 and we can then determine whether this (optimized) ERA is more accurate than the original Padé approximant.

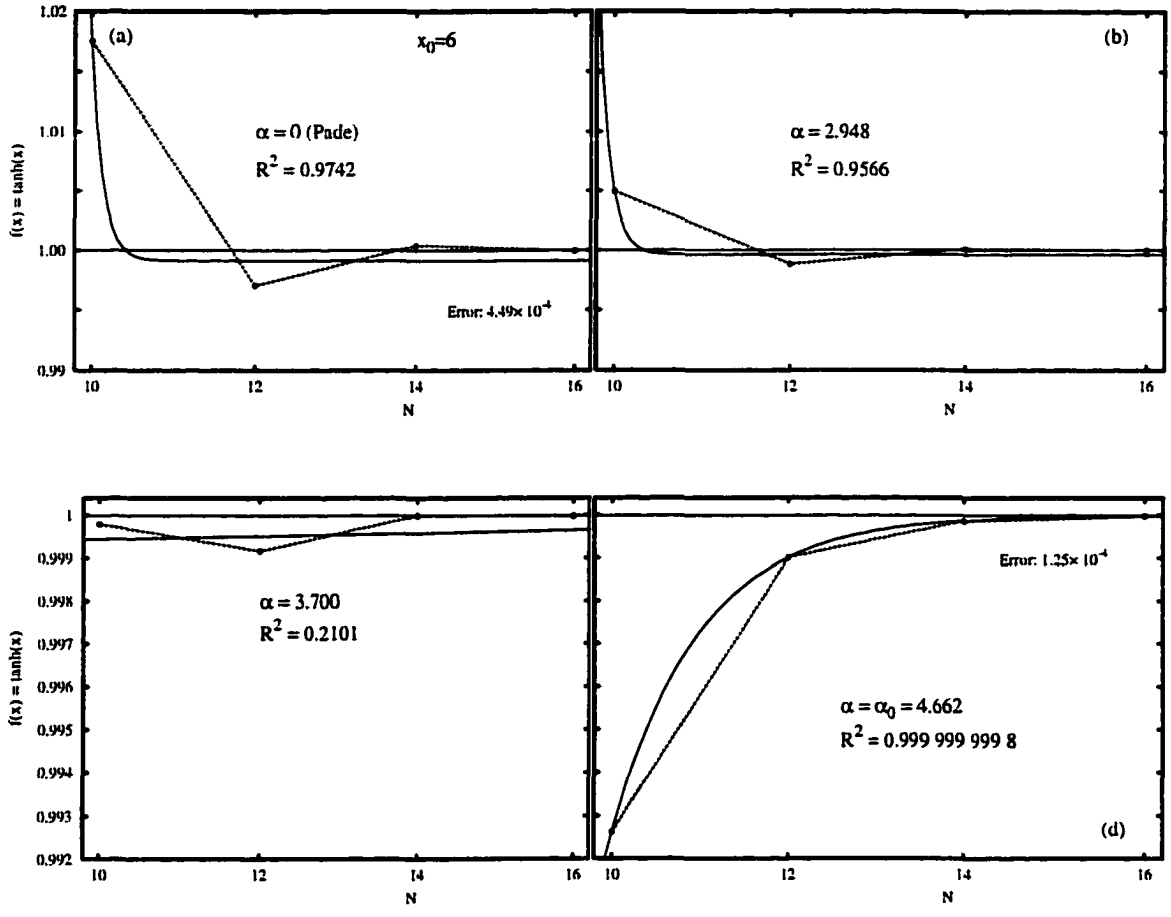

Figure 6.4: (a)–(d) Economized rational sequences as the parameter α is varied from 0 (equivalent to the Padé sequence) to 4.662 (corresponding to the optimized economized rational sequence). Note the change and refinement of the vertical axis. The function being approximated here is $f(x) = \tanh(x)$ at $x_0 = 6$, with the actual value represented by the horizontal solid line. For each α, the second solid line corresponds to the best exponential fit $\mathcal{F}_{A,B,s}(N)$. The coefficient of determination, R^2, is maximized at α_0.

Before we summarize our results in the next section, we should note that ERAs which originally (that is, when $\alpha = 0$) have oscillatory convergence do indeed tend towards

monotonic convergence as α is increased towards its optimal value. This can be seen in Figs. 6.4(a)–(d). (For a discussion of similar behavior, see Ref. [168].)

6.5 Results

We tested this method for determining α_0 on the Padé approximants generated from power series of six known functions:

$$f(x) = 1/(1+e^x)\,; \tag{6.11}$$

$$f(x) = \frac{(e\,x)^{1/x}}{\sqrt{2\,\pi\,x}}\,\Gamma(1/x)\,; \tag{6.12}$$

$$f(x) = e^x\,; \tag{6.13}$$

$$f(x) = \log(1+x)\,; \tag{6.14}$$

$$f(x) = \arctan(x)\,; \tag{6.15}$$

$$f(x) = \tanh(x)\,. \tag{6.16}$$

The power series of the second function is an asymptotic series. We now summarize the results.

1. *Enhanced accuracy and convergence.* The most dramatic improvement over Padé approximants involved the test function $f(x) = 1/(1+e^x)$, which has a radius of convergence of π (there are poles at $x = \pm i\pi$). At $x_0 = 6000$ *the optimized ERAs were more accurate at 2nd order ($m = k = 1$) than the Padé approximants at 16th order.* From the results shown in Fig. 6.5 and the right-hand columns of Table 6.1, the Padé approximants do not even appear to be converging to the correct value. The optimization of the asymptotic series in Eq. (6.12) improved the accuracy to nearly the same extent, as shown in Table 6.2 and Fig. 6.6. As we see in Table 6.3 and Fig. 6.7, improvement in convergence of $f(x) = e^x$ at $x_0 = 8$ — where the low-order Padé approximants are essentially worthless — was also remarkable. Even at 16th order (Table 6.4 and Fig. 6.8, for $x_0 = 10$) optimization produces an ERA with an absolute

error of only 5×10^{-3}, compared to the Padé approximant error of 1837. Even more noteworthy in the table and figure is the improvement over dual-parameterized Euler transformations, considered to be highly effective for summing the power series of this function.[169] We also show in Tables 6.5 and 6.7 the optimization results for the functions $f(x) = \log(1 + x)$ and $f(x) = \arctan(x)$, respectively. In these cases the improvement over Padé approximants is less dramatic, but nonetheless significant.

2. *Precision.* Nearly all the fits were very precise, larger than $R^2 = 0.999\,999\,999\,9$ in some cases. (The coefficient of determination, R^2, is noted in each table.)

3. *Transformation of alternating sequences towards monotonic sequences.* We already saw in Figs. 6.4(a)–(d) how the optimization process transforms an alternating Padé sequence into a monotonic sequence. Analogous behavior was noticed by Le Guillou and Zinn-Justin when they optimized (using a different method) sequences of Borel-Leroy transformations.[168] In each case where the Padé approximants were alternatingly convergent, the optimization process found a value for α_0 which coincided with a monotonically convergent sequence. For example, the Padé sequence for $f(x) = \arctan(x)$ converges alternatingly towards the correct value. Yet there exists a value α_0 that not only produces a sequence that is monotonically convergent, but as seen in Table 6.7 and Fig. 6.9 the error of each approximant is significantly lower than the Padé approximant at all orders. This behavior was repeated for the test functions $f(x) = e^x$ (Table 6.3) and $f(x) = \tanh(x)$ (Table 6.6).

4. *Stability with respect to the point of evaluation.* The optimization method appears to offer significant improvement no matter which value of x_0 is chosen, up to the point where both Padé approximants and optimized ERAs fail to converge. Table 6.1 shows that in some cases the improvement in accuracy (as measured by the number of additional decimal places of accuracy), in comparison to the original Padé approximant, actually increases for larger x_0.

5. *Stability with respect to order.* It is important that this optimization method not be confined to a few select (and subjective) choices of order. In each test the optimized ERAs provided significant improvement over Padé approximants no matter which maximum order is chosen. An example is found by comparing the data in Table 6.3 for $f(x) = e^x$, as well as Table 6.4 for the same function. Upon individually optimizing each ERA for each order near N, the resulting values converge *smoothly* to the correct value, as seen in Table 6.8 and Fig. 6.10 for the $\tanh(x)$ function and in Fig. 6.11 for the asymptotic series generated from Eq. (6.12). This indicates that optimizing the ERAs at each order produces a sequence that reflects the global behavior of the fit. Table 6.8 clearly shows how the parameters of the local fitting functions $\mathcal{F}_{A,B,s}(N)$ adjust to provide a local approximation to $\mathcal{G}_A(N)$ for different values of N. This characteristic is especially evident when examining the optimized sequence of the atomic perturbation series in the next section.

Table 6.1: Dramatic improvement in low order convergence and accuracy of a Padé approximant $P_{m,k}$ by optimizing the corresponding economized rational approximant (ERA) $C_{m,k}^{\alpha_0}$. The function here is $f(x) = 1/(1+e^x)$, evaluated at the two points, $x_0 = 6$ and $x_0 = 6000$. (See also Fig. 6.5.) The last row in the table designates the error of the highest ordered approximant.

$x_0 = 6$;	Exact Value: 0.002472623157		$x_0 = 6000$;	Exact Value: $\approx 10^{-2606}$	
$[m/k]$	$P_{m,k}$	$C_{m,k}^{\alpha_0}$ [a]	$[m/k]$	$P_{m,k}$	$C_{m,k}^{\alpha_0}$ [b]
[1/1]	−1.0000000	0.24105856	[1/1]	−1499.5	0.41447
[2/2]	0.12500000	0.021910077	[2/2]	0.49950	0.26411
[3/3]	−0.021739130	0.0011931096	[3/3]	−249.50	0.11724
[4/4]	0.0050761421	0.0024686256	[4/4]	0.49833	0.035395
[5/5]	0.0022727273	0.0024781024	[5/5]	−99.501	0.0076689
[6/6]	0.0024837600	0.0024726212	[6/6]	0.49650	0.0012793
[7/7]	0.0024721536	0.0024726186	[7/7]	−53.073	0.00015866
[8/8]	0.0024726386	0.0024726231	[8/8]	0.49400	0.000025680
Error	−1.54602(−8)	1.68212(−12)		−0.49400029	−0.000025680

[a] α_0=8.757, R^2=0.999 999 5, $\mathcal{F}_{A,B,s}(N)$=0.0024726209+0.1049650717 exp($-sN$), s=9.860.

[b] α_0=529.71, R^2=0.999 96, $\mathcal{F}_{A,B,s}(N)$=−0.000030701+0.045665 exp($-sN$), s=1.78.

Table 6.2: Padé and ERA values for the asymptotic power series generated from Eq. (6.12) at $x_0 = 5$. The errors are plotted in Fig. 6.6, and in Fig. 6.11 we show the results when the Padé approximants are optimized individually at each successive order. Note that a partial sum of the asymptotic series is optimally truncated at the zeroth order term, and so is unity.

Exact Value: 1.380290405		
$[m/k]$	$P_{m,k}$	$C_{m,k}^{\alpha_0}$ [a]
[5/5]	1.4354227	1.3865357
[6/6]	1.3220338	1.3753524
[7/7]	1.4236428	1.3794838
[8/8]	1.3335364	1.3786878
[9/9]	1.4163588	1.3789340
[10/10]	1.3409803	1.3790855
[11/11]	1.4113652	1.3791569
[12/12]	1.3462210	1.3792392
[13/13]	1.4077065	1.3793082
[14/14]	1.3501264	1.3793661
Error	0.030164	0.00092430

[a] α_0=1.089, R^2=0.999 999 99, $\mathcal{F}_{A,B,s}(N)$=1.3796669−0.0006082153 exp($-sN$), s=0.176.

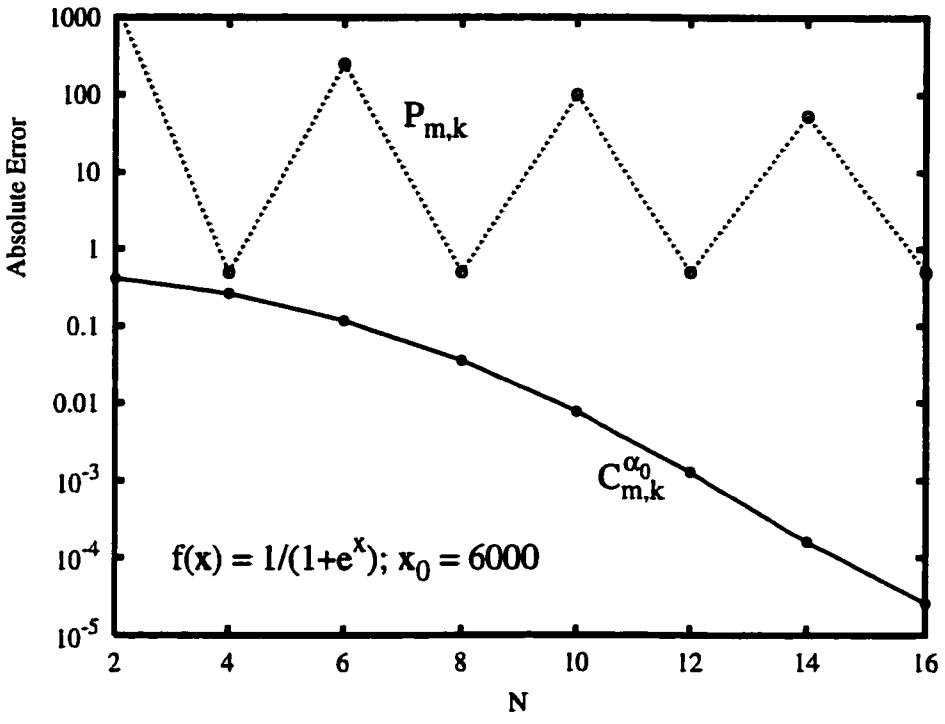

Figure 6.5: Errors of the Padé approximants $P_{m,k}$ and optimized ERAs $C^{\alpha_0}_{m,k}$ for the asymptotic region of $f(x) = 1/(1+e^x)$ derived from Table 6.1. The vertical axis is log scaled, so the differences in error are enormous. The conversion from an alternating sequence to a monotonic sequence is very clear. Note that the Padé approximants do not appear to be even converging to the correct value.

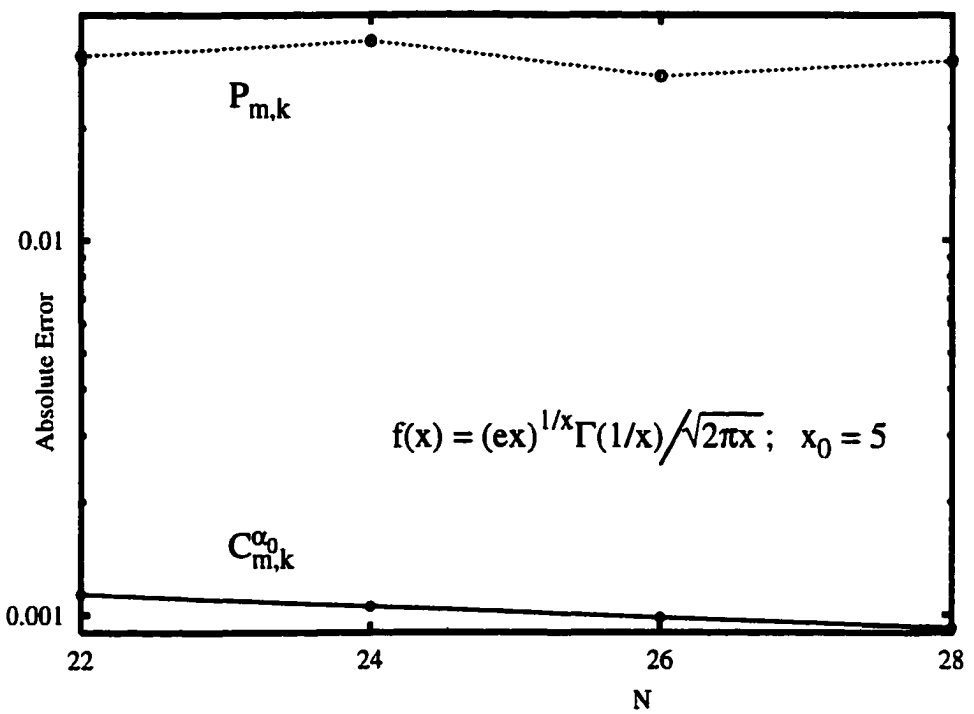

Figure 6.6: Same as Fig. 6.5, except for the asymptotic series generated by the Gamma function in Eq. (6.12) at $x_0 = 5$. Again, the vertical axis is log scaled, so the differences in error are considerable. These error results were calculated from the data in Table 6.2.

Table 6.3: Another comparison between Padé approximants and optimized ERAs. Here, $f(x) = e^x$ at $x_0 = 8$ and both the diagonal and off-diagonal sequences are tabulated. The errors for the diagonal sequence are plotted in Fig. 6.7.

Exact Value: 2980.957987					
$[m/k]$	$P_{m,k}$	$C_{m,k}^{\alpha_0\,a}$	$[m/k]$	$P_{m,k}$	$C_{m,k}^{\alpha_0\,b}$
[0/0]	1.00000	1.00000	[1/0]	9.00000	25.5324
[1/1]	−1.66667	8.12615	[2/1]	−10.2000	241.537
[2/2]	4.44286	192.552	[3/2]	23.9333	1603.42
[3/3]	−18.0769	2988.20	[4/3]	−99.3871	2982.66
[4/4]	101.952	2995.58	[5/4]	486.046	2985.83
[5/5]	−1212.05	2979.09	[6/5]	7444.92	2980.62
Error	4193.01	1.87293		−4463.96	0.334190

[a] α_0=8.123, R^2=0.999 97, $\mathcal{F}_{A,B,s}(N)$=2987.62−3.36136×10^9 exp(−sN), s=14.

[b] α_0=8.132, R^2=0.999 99, $\mathcal{F}_{A,B,s}(N)$=2983.23−3.33404×10^6 exp(−sN), s=7.790.

Table 6.4: Same as Table 6.3, except at higher order and at $x_0 = 10$. (See Fig. 6.8.) Since α_0 here differs somewhat from that in Table 6.3, the resulting sequence at all orders differ as well. Yet, the error remains significantly lower at nearly all orders than the Padé approximants, demonstrating that the optimization method is stable with respect to order. Here, we include the results from applying a dual-parameterized Euler transformation (PET).

Exact Value: 22026.46579						
N	S_N	$[N,N+2]$	PET[a]	$[m/k]$	$P_{m,k}$	$C_{m,k}^{\alpha_0\,b}$
2	61.000000	[2, 4]	−32.750000	[1/1]	−1.5000000	5.2913740
4	644.33333	[4, 6]	(complex)	[2/2]	3.3076923	91.029420
6	2866.5556	[6, 8]	(complex)	[3/3]	−10.428571	8427.3527
8	7330.8413	[8, 10]	201718.49	[4/4]	45.375000	19093.040
10	12842.305	[10, 12]	29468.144	[5/5]	−269.64516	22106.611
12	17435.192	[12, 14]	23450.497	[6/6]	1866.0847	22026.513
14	20188.171	[14, 16]	22325.434	[7/7]	−205032.75	22026.360
16	21430.835	[16, 18]	22085.476	[8/8]	20189.229	22026.471
Error	595.631		59.010		1837.2370	−4.908(−3)

[a] Computed from the algorithm discussed in Appendix K.

[b] α_0=10.064, R^2=0.999 998, $\mathcal{F}_{A,B,s}(N)$=22026.415+65608.939 exp(−sN), s=6.707.

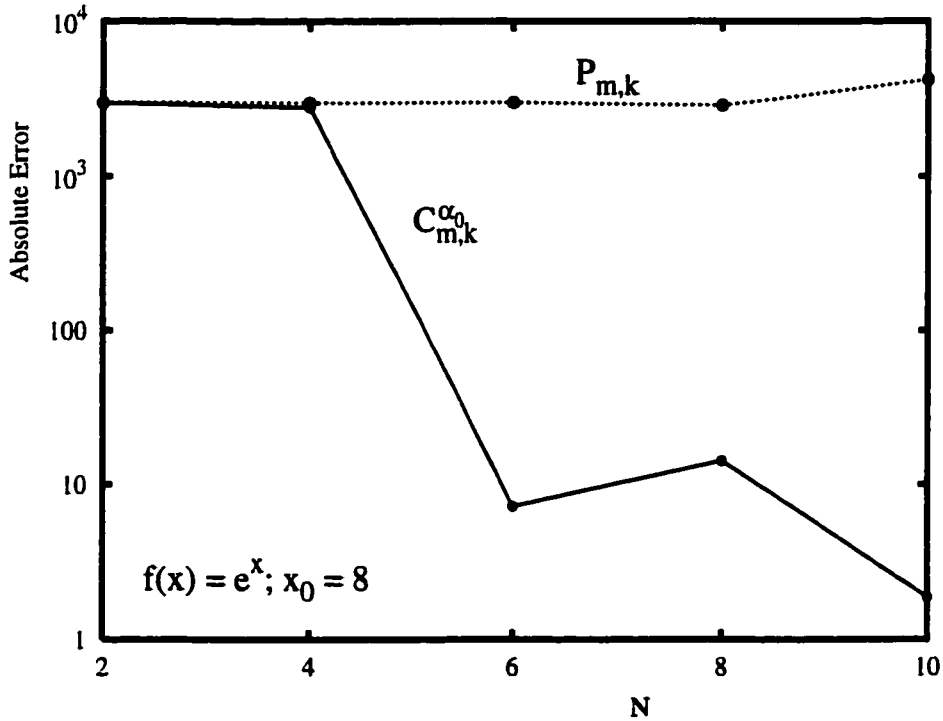

Figure 6.7: Errors for $f(x) = e^x$ at $x_0 = 8$ (see Table 6.3. In this example, the best exponential fit of the ERA sequence is not completely monotonic, which explains the rise in error (exaggerated by the vertical log scaling) at $N = 8$. Again, the vertical axis is log scaled so the difference in accuracy between the two approximates is considerable.

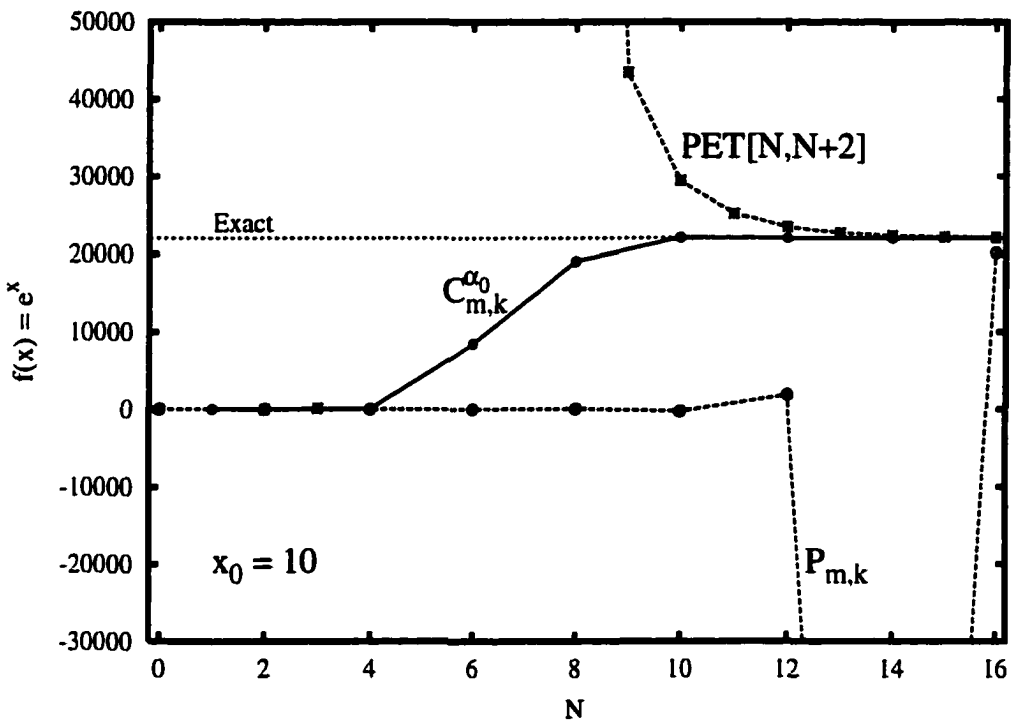

Figure 6.8: A comparison of the dual-parameter Euler transformation (PET[N,N+2]), Padé approximants, and optimized ERAs for $f(x) = e^x$ at $x_0 = 10$. The horizontal line corresponds to the exact value of $f(x)$. Notice that if $P_{7,7}$ were taken to be the converged result (a seemingly converged result at low orders) the error would be considerable. On the other hand, the optimized ERAs are significantly more accurate for nearly all orders, even when compared to PETs. See Table 6.4.

Table 6.5: Here, $f(x) = \log(1+x)$ at $x_0 = 5$. The error is halved.

Exact Value: 1.791759469		
$[m/k]$	$P_{m,k}$	$C_{m,k}^{\alpha_0\ a}$
[1/1]	1.4285714	1.5060643
[2/2]	1.7213115	1.7404539
[3/3]	1.7787115	1.7829493
[4/4]	1.7893952	1.7902805
[5/5]	1.7913354	1.7917137
[6/6]	1.7916838	1.7917189
[7/7]	1.7917460	1.7917528
[8/8]	1.7917571	1.7917594
Error	2.3912(−6)	1.0988(−6)

[a] α_0=1.141, R^2=0.999 999 996, $\mathcal{F}_{A,B,s}(N)$=1.7917595−0.0014867123 exp($-sN$), s=1.800

Table 6.6: The function $\tanh(x)$ at $x_0 = 6$. Note the precise fit, which is surprising given the low-order erratic behavior of the original Padé approximants.

Exact Value: 0.99998772		
$[m/k]$	$P_{m,k}$	$C_{m,k}^{\alpha_0\ a}$
[1/1]	6.000000	−10.524225
[2/2]	0.4615384	0.57148464
[3/3]	1.3246753	0.87461628
[4/4]	0.9235352	0.96829300
[5/5]	1.0174904	0.99718535
Error	−0.0175028	0.0028023

[a] α_0=4.065, R^2=0.999 999 993, $\mathcal{F}_{A,B,s}(N)$=1.0101293−1.4199726 exp($-sN$), s=1.1747.

Table 6.7: Here, $f(x) = \arctan(x)$ at $x_0 = 4$. Notice that optimizing $C_{m,k}$ again transforms the alternating Padé sequence into a monotonic sequence, which is apparent when examining the errors in this data in Fig. 6.9.

Exact Value: 1.3258177		
$[m/k]$	$P_{m,k}$	$C_{m,k}^{\alpha_0}$ [a]
[1/1]	4.0000000	2.3315173
[2/2]	0.6315789	0.9129322
[3/3]	1.9874214	1.2911074
[4/4]	1.0236425	1.2023396
[5/5]	1.5443095	1.2721575
[6/6]	1.2058444	1.2873382
[7/7]	1.4038412	1.3008169
[8/8]	1.2800401	1.3126944
Error	0.045777579	0.013123226

[a] α_0=1.582, R^2=0.999 999 4, $\mathcal{F}_{A,B,s}(N)$=1.4040869−0.14911241 exp(−sN), s=0.1224.

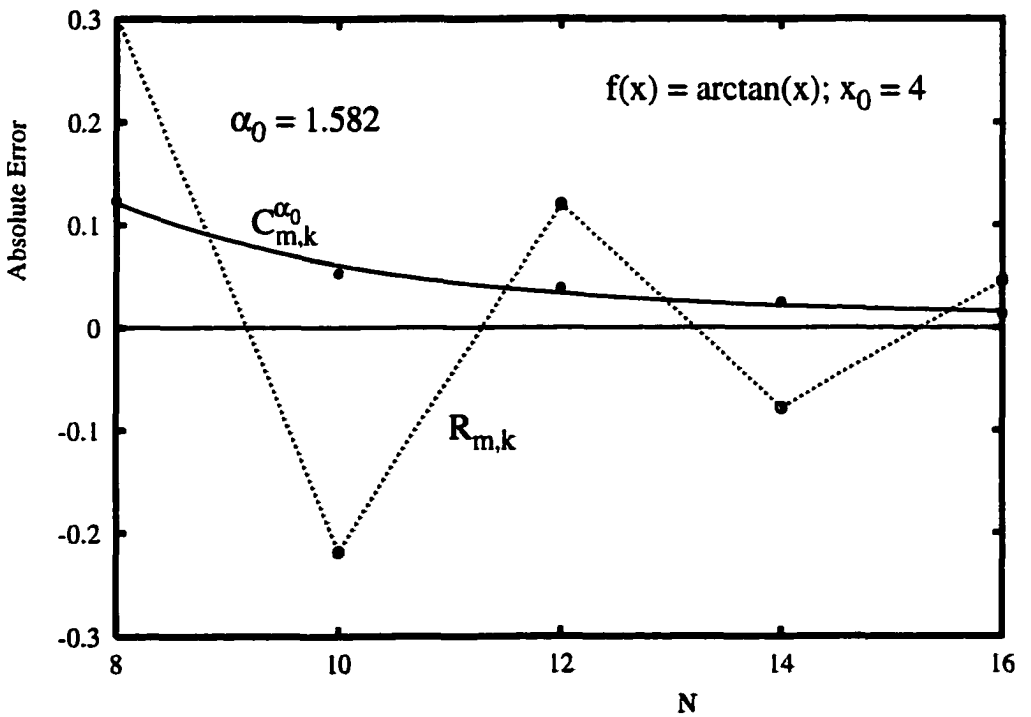

Figure 6.9: Error comparison between Padé approximants and optimized ERAs for $f(x) = \arctan(x)$ at $x_0 = 4$. The conversion from alternating to monotonic convergence here is very apparent. The relevant data is tabulated in Table 6.7.

Table 6.8: A comparison of the convergence of the optimized ERAs as the parameter α is individually optimized at each order, for $f(x) = \tanh(x)$ at $x_0 = 6$. Notice that α_0, s (the exponential fitting parameter), and R^2 are roughly the same at all orders, and that the values of the resulting approximants converge asymptotically towards the correct value, suggesting that this method of optimizing the ERAs is stable with respect to order. This data is plotted in Fig. 6.10. The errors for the Padé approximants at each order are also tabulated. The numbers in parentheses correspond to powers of 10.

Exact Value: 0.99998772							
$[m/k]$	$C^{\alpha_0}_{m,k}$	A	B	s	R^2	Error($P_{m,k}$)	Error($C^{\alpha_0}_{m,k}$)
[5/5]	0.9971854	1.010129	−1.42033	1.175	0.999 999 987 2	−1.8(−2)	2.8(−3)
[6/6]	0.9991068	1.000052	−1.23328	1.793	0.999 999 998 8	3.0(−3)	8.8(−4)
[7/7]	0.9998925	1.000050	−0.205655	1.795	0.999 999 999 5	−4.0(−4)	9.5(−5)
[8/8]	0.9999752	0.9999930	−0.0549783	2.010	0.999 999 999 1	4.5(−5)	1.2(−5)
[9/9]	0.9999869	0.9999880	−0.00798239	2.189	0.999 999 998 4	−4.1(−6)	9.1(−7)

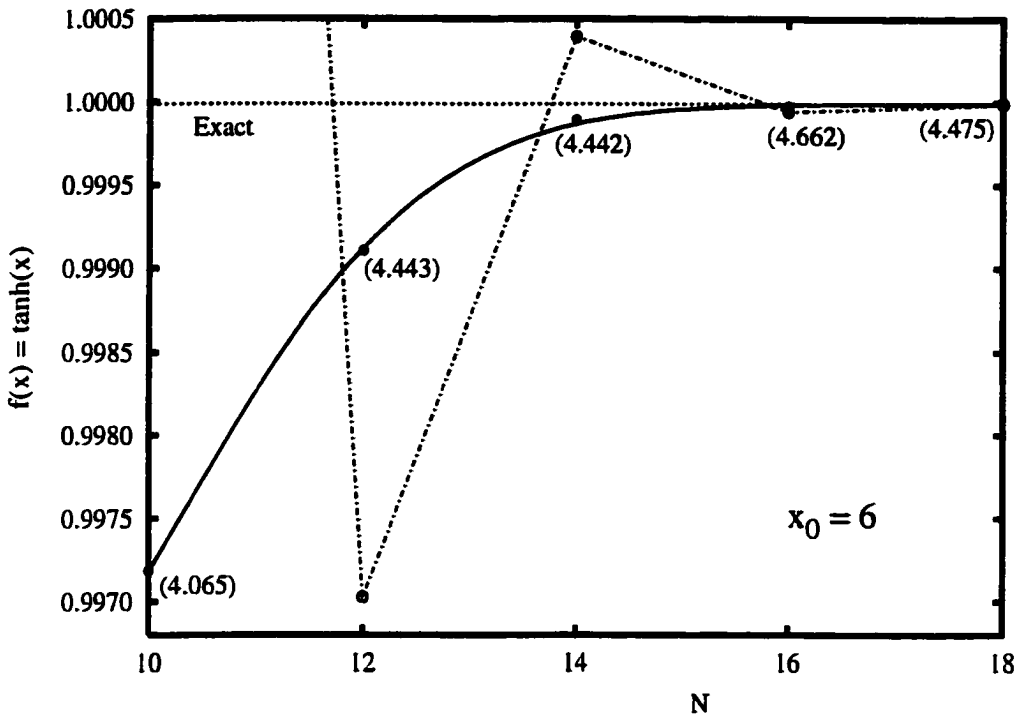

Figure 6.10: A comparison of the convergence of the optimized economized rational approximant s (solid circles) with Padé approximants (open circles) for $f(x) = \tanh(x)$ at $x_0 = 6$. Here, each term of the optimized economized rational approximant sequence has been optimized individually (see item 5 of Sec. 6.5). The value of α_0 corresponding to each order is shown in parentheses, The exact value of $f(x)$ is shown by the horizontal line. The data appears in Table 6.8.

6.6 Discussion

One means of determining whether a result is likely to be accurate is to examine the convergence of the sequence of approximants as the order is increased to its maximum value. Erratic behavior in convergence is a good indication that the highest-ordered approximant may not be a satisfactory representation of the function at the point it is being evaluated. In this case, accurate results could merely be the fortunate result of a numerical artifact.

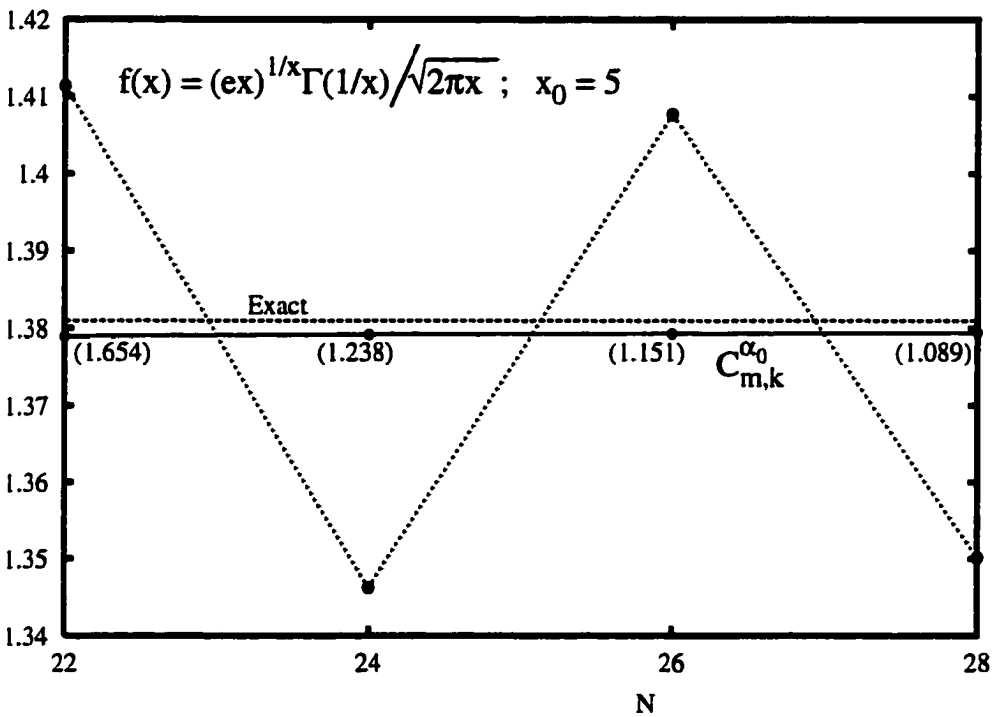

Figure 6.11: Another example of individual optimization, but for the asymptotic series generated by the Gamma function [see Eq. (6.12)]. Again, the numbers in parentheses correspond to the α_0 for each particular order. In this case, the exponential fit is not only precise locally, but also appears to apply globally as well. The equation of the line shown is given by $1.37942898 - 0.0008876041 \exp[-0.641N]$.

In optimizing the economized rational approximants (ERAs), the resulting sequence is required to be almost smooth and monotonically convergent, which raises confidence that the optimized ERA is providing a satisfactory representation of the system.

A few remarks on the numerical process are in order. We used the minimum number of points needed to determine A, B, s and α. As can be seen from Fig. 7.2 in Chap. 7 we can sometimes take many more than four points and still provide an accurate exponential fit. Generally though, the more terms that are included, the lower R^2 and the less accurate are the results at the relatively low orders considered in this chapter. This is to be expected since in general, as we noted above, the fitting function $\mathcal{F}_{A,B,s}(N)$ will be valid only locally, not globally, around $N = N_0$. Since the least-squares fit used in this chapter weights all points equally, any additional terms of the sequence used in the fit could lower R^2 and result in a less than optimal α for the last approximant of the sequence. Even if the fitting function happens to be globally appropriate [as appears to be the case for the $\log(1+x)$ function], there is the possibility that the earlier terms of a sequence have non-negligible finite-N corrections to the large-N exponential behavior of the error. Again since the least-squares fit weights all points equally, any additional earlier terms of the sequence used in the fit could lower R^2. Keeping the number of terms of the sequence used in the fitting to the minimum number of four guards against these errors.

In general, the fitting parameter A [that is, $\lim_{N\to\infty} \mathcal{F}_{A,B,s}(N)$] will not be the converged value of the sequence since $\mathcal{F}_{A,B,s}(N)$ is valid only locally, not globally. However, if R^2 is exceptionally large as with the function $f(x) = \log(1+x)$ (see Table 6.5), A can be more accurate than the last approximate, implying that the fitting function, $\mathcal{F}_{A,B,s}(N)$, may well be globally valid for this function.

As α is increased there will usually be multiple regions of α where the last four approximants line up close to an exponential line. As an example, in Table 6.9 we tabulate the values of the diagonal optimized ERAs for the function $f(x) = \exp(x)$ at the next and slightly larger value of α at which this occurs. Again, the optimized ERAs converge to the

correct answer, somewhat more slowly than at the smaller value of α (see Table 6.3), but still significantly better than the performance of the Padé approximants. We have found that the smallest value of α for which the last four points line up close to an exponential line yields the largest value of R^2 and the most accurate results. This is perhaps to be expected since ERAs "spread the error" without systematic favor in the region from the origin to $x \approx \alpha$. The larger the value of α, the larger the region the error is "spread" over, so the larger the average error becomes for $x \leq \alpha$. Therefore one would expect the best results to be obtained for the smallest value for which the last four points line up close to an exponential line. However, as the above discussion makes clear, this smallest value of α cannot be much smaller than the value of x at which the series is being summed. As Padé approximants sometimes appear to converge to the wrong value (an example appears in Fig. 6.5) it would not be surprising if this were true of optimized ERAs as well. Indeed, if one chooses an "optimal" value of α which is too large, even though the last four points are lining up around an exponential line, the sequence of ERAs appear to converge to the wrong result.

In order to further understand what is taking place during the optimization process we examined the effects the optimization process has on the singularity structure of the ERAs. As seen in Fig. 6.12 for the entire function $f(x) = e^x$, at α_0 the poles appear to be located such that the distance of the closest pole to the point of summation is roughly maximized. Since e^x has no singularities except at infinity, the poles mark isolated regions at which the ERAs locally fail. Therefore the optimization process moves the poles so that they are, as a whole, sufficiently far from the point of evaluation that their disturbing effects are minimized. If α is chosen large enough, then the poles in Fig. 6.12 move far to the right of the summation point and we might imagine that yet better results would be obtained. However, as we have noted above, the overall error at the summation point, x_0, of an ERA generally becomes very large when $\alpha \gg x_0$, and this works against the reduction of the error resulting from moving the poles well away from the summation point.

Table 6.9: Diagonal Padé approximants and optimized ERAs for the function $f(x) = e^x$ at $x_0 = 8$. However, here the next largest value of α which optimizes the convergence is used. This table should be compared with the results of Table 6.3 and Fig. 6.7 where the smaller and most optimized value of α is used. Note that the convergence, though still better than for Padé approximants, is significantly worse than for the optimized ERAs at the smallest value of α at which the last four terms of the sequence line up close to an exponential line.

Exact Value: 2980.957987		
$[m/k]$	$P_{m,k}$	$C_{m,k}^{\alpha_0\ a}$
[0/0]	1.00000	1.00000
[1/1]	−1.66667	3.97462
[2/2]	4.44286	97.3388
[3/3]	−18.0769	1877.56
[4/4]	101.952	2658.54
[5/5]	−1212.05	2999.70
Error	4193.01	−18.7424

[a] α_0=9.541, R^2=0.999 999 92, $\mathcal{F}_{A,B,s}(N)$=3266.61−7232.74 exp($-sN$), s=0.8251.

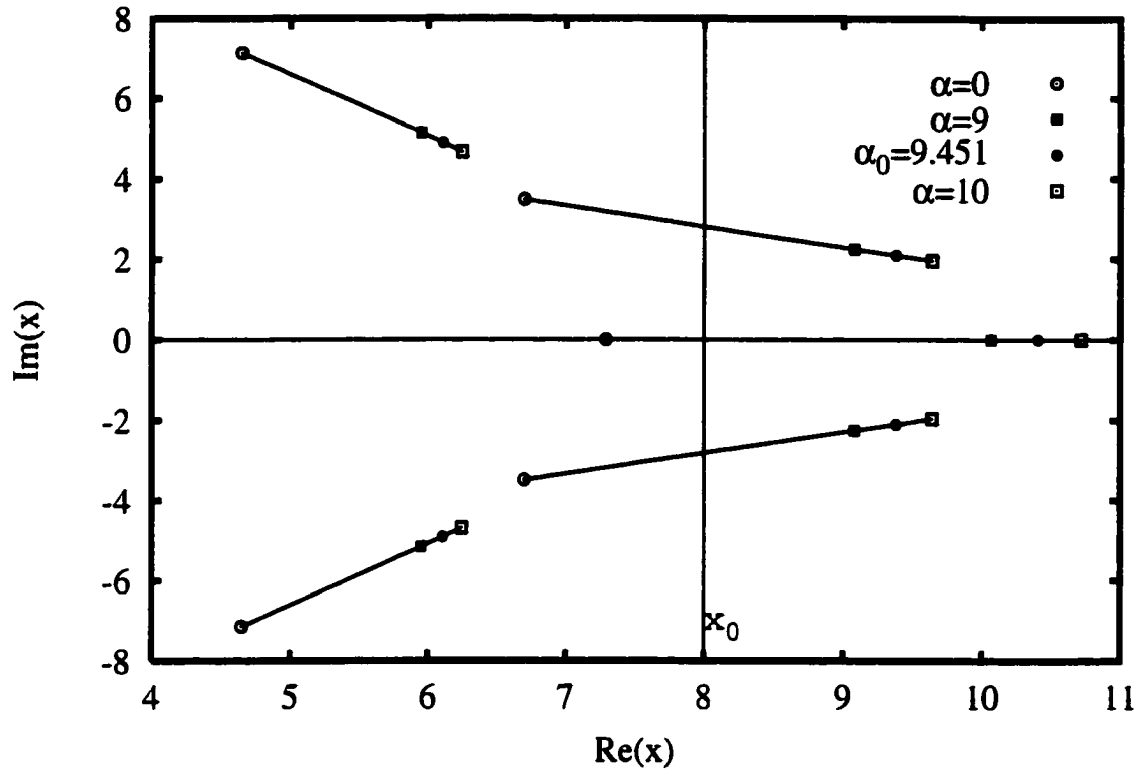

Figure 6.12: The [5/5] poles of the Padé and economized rational approximants. Those poles joined by common movement as α is changed are joined by a solid line. The zeroes of the approximants all lie in the negative half-plane and have been omitted. The function $f(x) = e^x$ was chosen here since it is an entire function for which the optimization process is especially effective. As we can see, as α increases from 0 the poles sweep towards the right. In this case, it seems as if α_0 corresponds to the instance when the poles are, on average, the farthest distance from the point at which we are evaluating the series.

Chapter 7

Physical Application: Summing the Dimensional Perturbation Energy Series of Diamagnetic Hydrogen at Low $|m|$

We now demonstrate the effectiveness of the procedure as it pertains to a physical problem, when the original function is not known beforehand. The majority of the following results were submitted for publication by J. R. Walkup, M. Dunn, and D. K. Watson and accepted for publication by *Physical Review A*.

At the beginning of this dissertation I mentioned that circular Rydberg states of diamagnetic hydrogen are useful because they provide insight into the theoretical framework of Rydberg atoms at *laboratory-accessible* values of B. Dimensional perturbation theory has been shown[135, 170] to be highly effective for calculating energy levels of circular Rydberg states in this region of B. Since all m-dependence for a given $\widetilde{B}$ is incorporated into a perturbation parameter that varies inversely with $|m|$, we would expect dimensional perturbation theory to be especially effective for large values of $|m|$. However, this principle only applies when comparing states having the same *scaled* field strength $\widetilde{B}$. For a fixed *physical* field strength B the perturbation series coefficients corresponding to a lower value of $|m|$ are, in general, smaller than those corresponding to larger values of $|m|$. Therefore, despite the fact that the perturbation parameter is larger for small values of $|m|$, the smaller coefficients may result in better convergence. After all, for a given state, the perturbation series coefficients are purely functions of $\widetilde{B}$, and not $|m|$. However, fixing the physical

Table 7.1: Strong convergence of partial sums S_N and Padé approximants $P_{m,k}$ for the ground state and lowest-lying $m = -2$ state ($3d_{-2}$) energies (in a.u.) of diamagnetic hydrogen at $B = 470$ T. All four states were chosen because they are examples of circular states. The Padé approximants belong to the diagonal sequence, so $m = k = N/2$. The energy values $E_{\rm R}$ of Ruder *et al.* [8] are tabulated at the bottom.

	$m = 0$ ($1s$)		$m = -2$ ($3d$)		$m = -4$ ($5g$)		$m = -24$ ($n = 25$)	
N	S_N	$P_{m,k}$	S_N	$P_{m,k}$	S_N	$P_{m,k}$	S_N	$P_{m,k}$
0	1.001 999	1.001 998	0.1170 302	0.1170 032	0.049 3843	0.049 2663	0.0130 7608	0.0130 7608
1	1.001 998	—	0.1170 032	—	0.049 2652	—	0.0127 3243	—
2	1.001 998	1.001 998	0.1170 033	0.1170 033	0.049 2663	0.049 2663	0.0127 4333	0.0127 4300
3	1.001 998	—	0.1170 033	—	0.049 2663	—	0.0127 4298	—
4	1.001 998	1.001 998	0.1170 033	0.1170 033	0.049 2663	0.049 2663	0.0127 4299	0.0127 4299
$E_{\rm R}$	1.001 998		0.1170 033		0.049 2663		(none given)	

field strength B and varying $|m|$ requires varying $\widetilde{B}$. [See Eq. (3.3).] Therefore, for a given fixed value of B these coefficients become functions of $|m|$.

In Table 7.1 we show that not only does dimensional perturbation theory remain effective as m is reduced for fixed B, *but that its effectiveness slightly improves.* For example, at this field strength the partial sums and Padé approximants for the $1s_0$ and $3d_{-2}$ states actually converge to 12 significant figures by second order. (!) For the same field strength the convergence at $|m| = 24$ was roughly seven digits by fourth order.

Large n states are "more elliptical" when m is small, so we would expect dimensional perturbation theory to be effective for a smaller number of states at low values of $|m|$. However, in Table 7.2 we show that, even for $|m| = 0$, at sufficiently low field strengths dimensional perturbation theory remains effective for highly noncircular states. Note from Fig. A1.2a in Ref. [6] that the field strength represented in the table is just below the region of significant n-mixing of states.

In Table 7.3 we show that the perturbation series for diamagnetic hydrogen can be summed quite effectively for $m = 0$ for most values of B, especially for smaller field strengths.[171] In the large field region, the perturbation series often fails to converge

Table 7.2: The first six excited states of the $m = 0$ manifold. Again, $B = 470$ T. Since the partial sums diverge for these states, only the Padé approximants $P_{m,k}$ are listed.

$[m/k]$	$2s_0$	$3d_0$	$3s_0$	$4d_0$	$4s_0$	$5g_0$
[0/0]	1.0019 990	1.0019 990	1.0019 990	1.0019 9900	1.0019 9900	1.0019 9900
[1/1]	0.2019 918	0.0019 949	0.0009 891	−0.0889 1664	−0.0889 2133	−0.1408 6285
[2/2]	0.2519 807	0.1130 958	0.1130 690	0.0644 7038	0.0644 4002	0.0419 7663
[3/3]	0.2519 729	0.1130 406	0.1122 709	0.0648 3287	0.0646 8243	0.0420 5545
[4/4]	0.2519 720	0.1130 710	0.1129 648	0.0643 6796	0.0641 7057	0.0418 8974
[5/5]	0.2519 720	0.1130 697	0.1129 545	0.0643 5124	0.0639 6809	0.0417 5191
[6/6]	0.2519 720	0.1130 698	0.1129 548	0.0643 5178	0.0639 8137	0.0417 7365
[7/7]	0.2519 720	0.1130 698	0.1129 547	0.0643 5189	0.0639 8127	0.0417 7746
[8/8]	0.2519 720	0.1130 698	0.1129 547	0.0643 5167	0.0639 8170	0.0417 7553
E_R	0.2519 720	0.1130 698	0.1129 547	0.0643 5166	0.0639 8170	0.0417 7604

even using Padé approximants. However, the sequence of Padé approximants can be economized[162, 163] into a new sequence of approximants (economized rational approximants, hereafter denoted ERAs) which can be *optimized* by adjusting a parameter to minimize the error for particular values of the physical parameters B and $|m|$. As seen in Table 7.3 and Figs. 7.1 and 7.2, the values of these *optimized ERAs* provide reasonably accurate energy values, even when the original Padé approximants fail to converge. (See Chap. 6.1 and Ref. [172].)

Finally, we note that the precision of the Padé approximants in Table 7.3 is defined by the number of digits that agree with the next lowest-ordered approximant, whereas the precision of the optimized ERAs depends largely on the fit of the ERA sequence to an exponential line (as explained in Chap. 6.1). It is difficult, therefore, to compare the precisions of these two methods, so the results found using optimized ERAs were expressed using seven significant figures in all cases.

Table 7.3: Energy levels for $|m| = 0$ at various field strengths. Here, $\beta = 1$ corresponds to 4.7×10^5 T. The energies of Ruder, *et al.* are given in parentheses. To the left of each value the summation method is noted, with partial summation denoted S_N, Padé summation $P_{m,k}$, and optimized economized rational approximants $C^{\alpha_0}_{m,k}$, where α_0 and the optimization method is described in Chap. 6.1. The indices indicate the minimum order at which convergence was achieved. Padé summation was used once partial summation failed to converge to seven significant figures by 50th order (quadruple precision). Similarly, the optimization method was used once Padé summation failed to converge to seven significant figures by the same order. (For practical reasons optimization was always performed using the largest-ordered economized rational approximant available, in this case $C_{25,25}$, given the limited number of power series coefficients at hand.) For a discussion of the precision of the results found using optimized ERAs, see Sec. III.

β		$1s_0/\|000\rangle$[a]		$2s_0/\|002\rangle$		$3d_0^b/\|004\rangle$
5(−4)	S_1	1.001000(1.000999)	$P_{4,4}$	0.2509930 (0.2509930)	$P_{5,5}$	0.1121008 (0.1121008)
5(−3)	S_2	1.009950(1.009950)	$P_{6,6}$	0.2593031 (0.2593031)	$P_{9,9}$	0.1200958 (0.1200958)
5(−2)	S_5	1.095053(1.095053)	$P_{12,12}$	0.2961494 (0.2961783)	$C^{(0.0407)}_{25,25}$	0.1500983 (0.1498760)
5(−1)	$P_{4,4}$	1.662338(1.662338)	—	(Not found) (0.3209379)	—	(Not found)[c] (0.13202)
5	$P_{10,10}$	3.495594(3.495594)	$C^{(0.059)}_{25,25}$	0.4178979 (0.41777)	—	(Not found)[c] (0.154286)
50	$P_{16,16}$	7.579610(7.5781)	$C^{(0.051)}_{25,25}$	0.5120457 (0.512339)	$C^{(0.0387)}_{25,25}$	0.1749461 (0.1737679)
500	$P_{21,21}$	15.32482(15.3241)	$C^{(0.041)}_{25,25}$	0.5772800 (0.5917099)	$C^{(0.0498)}_{25,25}$	0.1975335 (0.1887047)

[a] The asymptotic large-field state has the form $|nm\nu\rangle$, where n and m are the principle and magnetic quantum numbers and ν counts the number of nodes along the field axis. See Ref. [8], Sec. 3.1.2.

[b] For this state, Ruder *et al.* used a linear combination of the $3d_0$ and $3s_0$ states as their initial state. On the other hand, all initial states in this research were pure states.

[c] At this field strength neither Padé approximants or optimized ERAs successfully converge. This does not appear to be due to a limitation of optimized ERAs, but rather due to a limitation of the non-degenerate perturbation series evaluated at a finite number of decimal places. We think that the method of *almost-degenerate* perturbation theory will greatly improve the results. This is an avenue of future investigation.

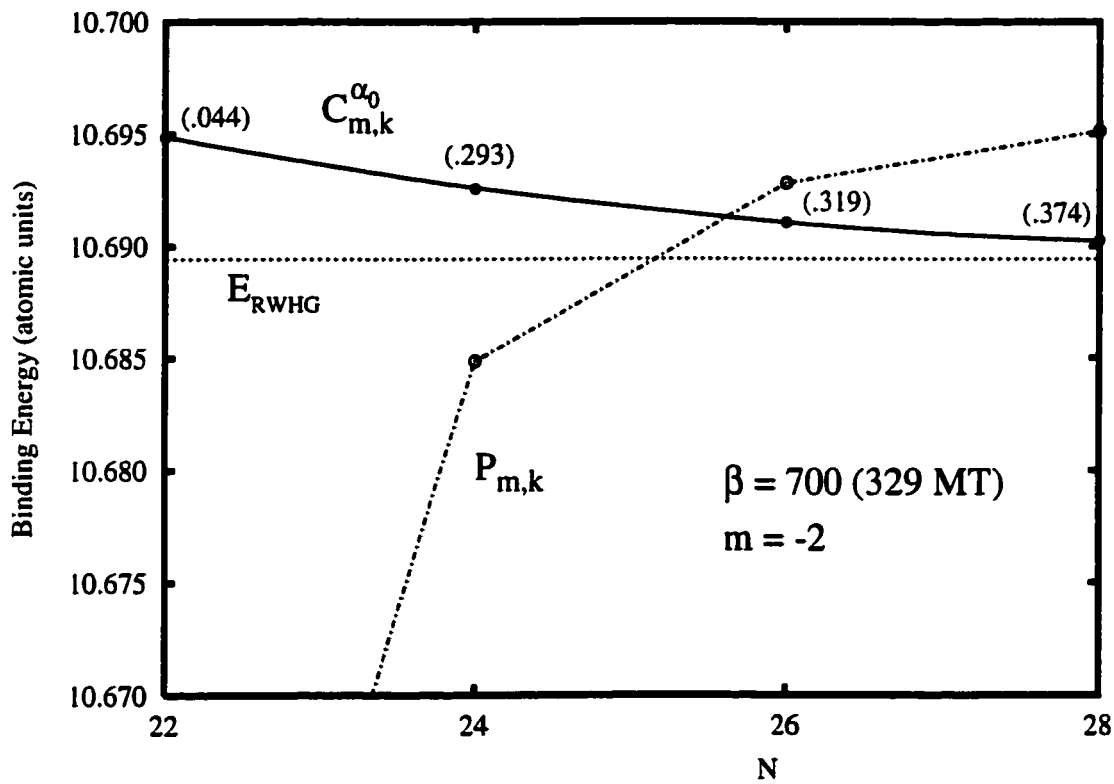

Figure 7.1: The energy of the lowest-lying $m = -2$ state of diamagnetic hydrogen for $B = 329$ MT. The horizontal line corresponds to the multi-configurational Hartree-Fock calculation of Ruder (Ref. [17]). Note that the ERAs have been optimized individually.

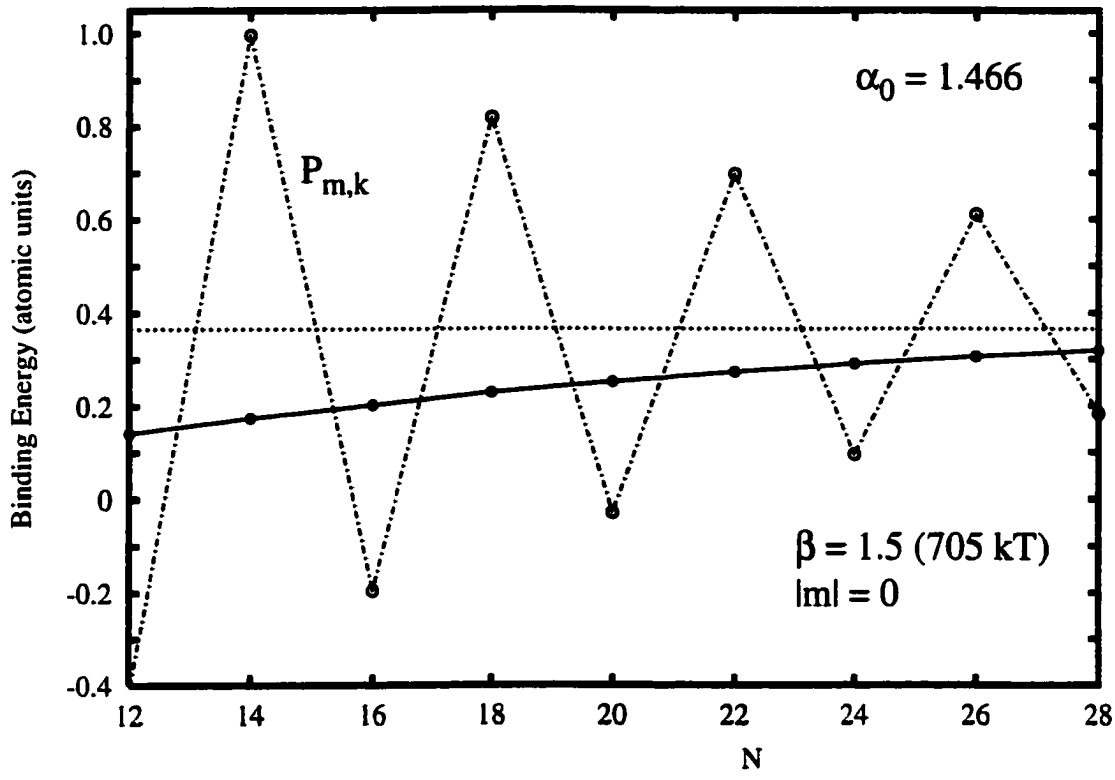

Figure 7.2: Same as Fig. 7.1, but for the ground state at $B = 705$ kT. Here we show that we can often incorporate many elements of the sequence into the optimization process. The horizontal line corresponds to the energy calculated by Ruder, *et al.* As in the other figures, the optimized ERAs are shown by solid dots, with the best-fitting exponential fit shown by a solid line.

Part IV

Epilogue

7.1 Summary

In the largest part of our research we examined two types of spectra. In one, the magnetic quantum number $|m|$ was held constant while the *magnetic field* B changed adiabatically, and in the other the magnetic field was held constant while the *angular momentum* changed adiabatically. We found that the location of the avoided crossings appearing in the E-versus-B spectra are directly related to the locations of those appearing in the E-versus-$|m|$ spectra, and that this correspondence points to a degeneracy in the energy levels that provides the mechanism for the appearance of avoided crossings in both spectra.

The branch points that connect the energy levels are the mathematical basis of such a mechanism[129], and by understanding this basis we have found it possible to predict the locations of avoided crossings in both spectra. By successfully characterizing the energy levels in terms of these branch points through Eq. (4.10), a simple relationship that merely requires visually examining the branch-point trajectories of the system as functions of B was found that could be used to predict the locations of avoided crossings in both spectra.

The new technique for summing divergent power series developed in this research was found to improve upon Padé approximants in every test case considered. In many instances the improvements over Padé approximants was dramatic. We have shown that such improvements appear when summing the perturbation series of physical systems (in this case, diamagnetic hydrogen) as well.

7.2 Future endeavors

My dissertation research is just the start.

Probability transitions of diamagnetic hydrogen for time-dependent fields

My first goal is to extend my research on diamagnetic hydrogen to compute transition probabilities when the external field B varies with time across an avoided crossing. Such

research is largely unexplored, so the ability to calculate such transition probabilities would be a significant step in research involving diamagnetic hydrogen, which has numerous applications in such fields as solid-state physics and astrophysics. Using a semi-classical treatment, Landau and Lifshitz[173] proposed a useful way of making such calculations when the field strength varies sufficiently slow in comparison to the classical period of the electron. This method requires integrating around the square-root branch point on the complex B plane at which the two interacting energy levels are degenerate. (See Appendix E for a more detailed discussion.)

Dimensional perturbation theory should be ideal for making such calculations. First, using dimensional perturbation theory we have an analytic means of precisely determining the locations of such avoided crossings, even when their approaches are so shallow as to make the crossings imperceptible. Dimensional perturbation theory also provides a simple way to find the exact locations of these square-root branch points on the complex B plane. Furthermore, since all m-dependence is incorporated in the perturbation parameter, where m is the magnetic quantum number, transition probabilities for a given value of m can be easily extended to other value of m — the energy series for a given field strength are the same, changing m only requires summing the series at a different value of the perturbation parameter.

I have already made progress in performing these calculations, and the remaining work appears to be straightforward.

Avoided crossings in the Stark spectrum of Rydberg atoms

Another goal is to examine the avoided crossings that appear in the Stark effect for Rydberg atoms when the excited electron interacts with the core electrons. With diamagnetic hydrogen we were able to establish a correlation diagram that allows one to track a particular energy level as it is adiabatically swept from very low to very high field strengths, even through the complicated tangle of avoided crossings in the intermediate field region.

Dimensional perturbation theory, which has been successfully applied to the Stark effect, should prove useful in finding a similar correlation diagram for the Stark effect as well. Such a correlation diagram can help establish the location of hidden avoided crossings in the energy spectrum.

7.2.1 Approximation theory

Initially, I would like to build multi-point Padé approximants of a perturbation series by minimizing the error at many values of the independent variable. If successful, this will create a Padé-type approximant having reasonably small errors for an extensive range of the independent variable. Then I would like to apply the same optimization technique that we found to be successful with Padé approximants to other types of approximants that employ "arbitrary convergence parameters," such as Borel-Leroy transformations. Finally, I would like to investigate the role such optimization plays when summing asymptotic series. For the asymptotic series we considered in this research, this optimization technique provided dramatic improvement over Padé approximants. (In fact, the Padé approximants appeared to be converging to the wrong value, whereas the optimized ERAs not only converged to the correct value but also very strongly.) Neither research project should employ formidable mathematics, so students of either physics or mathematics may be able to take the lead in such research.

Reference List

[1] D. Koester, "White dwarfs for physicists," in Ref. [8], p. 1; S. Jordan, "Magnetic white dwarfs: observations in cosmic laboratories," in Ref. [8], p. 9; G. Chanmugam, Ann. Rev. Astr. P. **30**, 143 (1992); S. L. Shapiro, S. A. Teukolsky, *Black Holes, White Dwarfs, and Neutron Stars* (Wiley, NY, 1983).

[2] G. Pavlov, "Neutron star atmospheres," in Ref. [8], p. 37; A. Y. Potekhin, "Hydrogen atoms in neutron star atmospheres: analytical approximations for binding energies," in Ref. [8], p. 49.

[3] These pictures do not necessarily have much to do with this research. I just thought they were so cool looking that I just *had* to put them in somewhere. From Ref. [6].

[4] D. Wintgen and H. Friedrich, J. Phys. B **19**, 991 (1986).

[5] D. Kleppner, M. G. Littman, and L. Zimmerman in Ref. [36], pp. 73–116.

[6] H. Ruder, G. Wunner, H. Herold, F. Geyer, *Atoms in Strong Magnetic Fields*, (Springer-Verlag, Berlin, 1994).

[7] We used *quadratic* Padé summation to find the square-root branch points shown in the figures. See Ref. [124] and references therein.

[8] P. Schmelcher and W. Schweizer, *Atoms and Molecules in Strong External Fields, Proceedings of the 172nd WE-Heraeus-Seminar on Atoms and Molecules in Strong External Fields* (Plenum Press, NY, 1998).

[9] R. H. Garstang, Rep. Progr. Phys. **40**, 105 (1977), and references therein.

[10] G. Wunner, H. Ruder, and H. Herold, J. Phys. B **247**, 374 (1981).

[11] J. C. Gay, J. Phys. B **247**, 145 (1991).

[12] D. Wintgen and H. Friedrich, *Phys. Rev. A* **36**, 131 (1987).

[13] D. Delande and J. C. Gay, Comments At. Mol. Phys. **19**, 35 (1986).

[14] C. Iu, G. R. Welch, M. M. Kash, D. Kleppner, D. Delande, and J. C. Gay, Phys. Rev. Lett. **66**, 145 (1991).

[15] H. Friedrich and D. Wintgen, Phys. Rep. **183**, 37 (1989).

[16] The rules of thumb for defining weak and strong fields in this research do not really apply to the ground state, which does not undergo avoided crossings with higher-lying states, as seen in Fig. 1.1.

[17] C. Angelié and C. Deutsch, Phys. Lett. A **67**, 357 (1978).

[18] I have been unable to find a more precise definition of the strong field limit.

[19] An early discussion of the generation of high magnetic fields is found in *High Magnetic Fields: Proceedings of the International Conference on High Magnetic Fields, 1961*, edited by H. Kolm, B. Lax, F. Bitter, and R. Mills (M.I.T. Press and Wiley, NY, 1962).

[20] A more recent description of modern magnetic field technology is found in J. E. Crow, J. R. Sabin, and N. S. Sullivan, "The National High Magnetic Field Laboratory – *a Precis*" in Ref. [8], p. 77. The laboratory's website at http://www.magnet.fsu.edu is also very informative.

[21] M. Robnik, J. Phys. A **14**, 105 (1977); J. L. Greenstein and J. B. Oke, Astrophys. J. **252**, 285 (1982).

[22] C. M. Dai and D. S. Chu, Physica B **172**, 445 (1991); A. K. Ramdas and S. Rodriguez, Rep. Prog. Phys. **44**, 1297 (1981); J. G. Mavroides, *Optical Properties of Solids*, edited by F. Abeles (North-Holland, Amsterdam, 1972); G. E. Stillman, D. M. Larsen, C. M. Wolfe, and R. C. Brandt, Solid State Commun. **9**, 2245 (1971); H. Hasegawa, *Physics of Solids in Intense Magnetic Fields* (Plenum Press, New York, 1969).

[23] H. S. Brandi, Phys. Rev. A **11**, 1835 (1975);

[24] T. O. Claassen, J. L. Dunn, and C. A. Bates, "Shallow Donor States in a Magnetic Field," in Ref. [8], p. 291.

[25] D. Cabib, E. Fabri, and G. Fiorio, Nuevo Cimento **10**, 185 (1972).

[26] D. Delande and J .C. Gay, Europhys. Lett. **5**, 303 (1988);

[27] L. Chen, M. Cheret, F. Roussel and G. Spiess, *J. Phs. B* **26**, L437 (1993).

[28] J. Liang, M. Gross, P. Goy, and S. Haroche, Phys. Rev. A **33**, 4437 (1986); R. G. Hulet and D. Kleppner, Phys. Rev. Lett. **51**, 1430 (1983).

[29] P. Fassbinder and W. Schweizer, Phys. Rev. A **53**, 2135 (1996).

[30] D. Delande and J. C. Gay, Phys. Rev. Lett. **66**, 3237 (1991).

[31] S. Friedrich, P. Fassbinder, I. Seipp, and W. Schwiezer, "Hydrogen in strong electric and magnetic fields and its application to magnetic white dwarfs," in Ref. [8], p. 19; Regarding Rydberg atoms in parallel fields see L. Cacciani, S. Liberman, E. Luc-Koenig, J. Pinard, and C. Thomas, J. Phys. B **21**, 3473 (1988); **21**, 3499 (1988); **21**, 3523 (1988).

[32] J. Trümper, W. Pietsch, C. Reppin, B. Sacco, E. Kendziorra, and R. Staubert, Ann. N.Y. Acad. Sci. **302**, 538 (1977).

[33] W. E. Lamb, Phys. Rev. **85**, 259 (1952).

[34] Much of the interest in studying hydrogen atoms in crossed electric and magnetic fields is concerned with the transition from quantum to classical mechanics. See E. Flothmann and K. H. Welge, Phys. Rev. A **54**, 1884 (1996); R. C. Hilborn, Am. J. Phys. **63**, 330 (1995); V. S. Melezhik, Phys. Rev. A **48**, 4528 (1993). Special attention has been paid to Rydberg states of atoms in such fields, as discussed in T. van der Veldt, W. Vassen, and W. Hogervorst, J. Phys. B **26**, 1945 (1993); Phys. Rev. A **21**, 903 (1993).

[35] S. Watanabe and H. Komine, Phys. Rev. Lett. **67**, 3227 (1991); J. Main, G. Wiebush, A. Holle and K. H. Welge, Phys. Rev. Lett. **56**, 2594 (1986).

[36] *Rydberg States of Atoms and Molecules*, edited by R. F. Stebbings and F. B. Dunning (Cambridge University Press, Cambridge, 1983).

[37] J. C. Gay and D. Delande, *Atomic Excitation and Recombination in External Fields*, edited by M. H. Nayfeh and C. W. Clark (Gordon and Breach, New York, 1985);

[38] F. A. Jenkins and E. Segre, Phys. Rev. **55**, 59 (1939).

[39] Semi-classical wave functions are typically generated by building coherent states of a given system. See R. J. Glauber, Phys. Rev. Lett. **10**, 84 (1963); Phys. Rev. **130**, 2529 (1963).

[40] H. Carlsen and O. Goscinski, Phys. Rev. A **59**, 1063 (1998); L. S. Brown, Am. J. Phys. **41**, 525 (1973).

[41] Z. D. Gaeta, M. W. Noel, and C. R. Stroud, Jr., Phys. Rev. Lett. **73**, 636 (1994).

[42] G. A. Kohring, A. E. Wetmore, and R. E. Olson, Phys. Rev. A **28**, 2526 (1983).

[43] E. de Prunelé, Phys. Rev. A **31**, 3593 (1985).

[44] E. Schrödinger, Naturwissenschaften **14**, 664 (1926). This problem is worked out in great detail in C. Cohen-Tannoudji, B. Diu, and F. LaLoë, *Quantum Mechanics* (Wiley, New York, 1977) Vol. I, Complement G_V.

[45] P. Ehrenfest, Z. Physik **45**, 455 (1927). This theorem is discussed in many basic quantum textbooks. See, for example, L. Schiff, *Quantum Mechanics* (McGraw-Hill, New York, 1985), p. 29.

[46] Z. D. Gaeta and C. R. Stroud Jr., Phys. Rev. A **42**, 6308 (1990).

[47] L. I. Schiff and H. Snyder, Phys. Rev. **55**, 59 (1939).

[48] E. R. Smith, R. J. W. Henry, G. L. Surmelian, and R. F. O'Connell, Astrophys. J. **179**, 659 (1973); **182**, 651 (1973).

[49] H. C. Praddaude, Phys. Rev. A **6**, 1321 (1972).

[50] E. P. Pokatilov and M. M. Rusanov, Sov. Phys. Solid State **10**, 2458 (1969).

[51] V. Canuto and D. C. Kelly, Astrophys. Space Sci. **17**, 277 (1972).

[52] A. R. P. Rau and J. Spruch, Astrphys. J. **207**, 671 (1976).

[53] Y. Yafet, R. W. Keyes, and E. N. Adams, J. Phys. Chem. Solids **1**, 137 (1956).

[54] C. M. Bender, L. D. Mlodinow and N. Papanicolaou, Phys. Rev. A **25**, 1305 (1982).

[55] M. A. DuVernois, J. L. Boorstein, and T. Uzer, Phys. Rev. A **47**, 53 (1993).

[56] A. F. Starace and G. L. Webster, *Phys. Rev. A*, **19**, 1629 (1979).

[57] C. R. Liu and A. F. Starace, *Phys. Rev. A*, **35**, 647 (1987).

[58] J. Shertzer, *Phys. Rev. A* **39**, 3833 (1989).

[59] J. Shertzer, L. R. Ram-Mohan and D. Dossa, *Phys. Rev. A*, **40**, 4777 (1989).

[60] P. Falsaperla and G. Fonte, Phys. Rev. A **47**, 4143 (1993); **50**, 3051 (1994).

[61] D. Wintgen and H. Friedrich, J. Phys. B **19**, 1261 (1986).

[62] M. L. Zimmerman, M. M. Kash, and D. Kleppner, Phys. Rev. Lett. **45**, 1092 (1980).

[63] C. W. Clark and K. T. Taylor, J. Phys. B **13**, L737 (1980).

[64] D. Delande and J. C. Gay, Phys. Lett. A **82**, 393 (1981).

[65] E. A. Solov'ev, JETP Lett. **34**, 265 (1982) [Pis'ma Zh. Eksp. Teor. Fiz. **34**, 278 (1981)].

[66] D. R. Herrick, Phys. Rev. A **26**, 323 (1982).

[67] J. C. Gay, D. Delande, F. Biraben, and F. Penent, J. Phys. B **16**, L693 (1983).

[68] D. Delande and J. C. Gay, J. Phys. B **17**, L335 (1984).

[69] W. Rösner, G. Wunner, H. Herold, and H. Ruder, J. Phys. B **17**, 29 (1984).

[70] G. Wunner, H. Ruder, and H. Herold, Phys. Lett. **85A**, 430 (1981).

[71] H. Ruder, G. Wunner, H. Herold, and M. Reinecke, J. Phys. B **14**, L45 (1981).

[72] H. Herold, H. Ruder, and G. Wunner, J. Phys. B **14**, 751 (1981).

[73] W. Rösner, H. Herold, G. Wunner, and H. Ruder, Phys. Rev. A **28**, 2071 (1983).

[74] G. Wunner, M. Kost, and H. Ruder, Phys. Rev. A **33**, 1444 (1986).

[75] G. Wunner, W. Rösner, H. Herold, and H. Ruder, Astron. Astrophys. **149**, 102 (1985).

[76] G. Wunner and H. Ruder, Astrophys. J. **242**, 828 (1980).

[77] G. Wunner and H. Ruder, Astron. Astrophys. **95**, 204 (1981).

[78] G. Wunner, W. Rösner, H. Ruder, and H. Herold, Astrophys. J. **262**, 407 (1982).

[79] J. E. Bayfield, Phys. Rep. **51**, 317 (1979).

[80] H. Friedrich, *Theoretical Atomic Physics* (Springer-Verlag, Berlin, 1991), Sec. 5.3.4.

[81] T. F. Gallagher, *Rydberg Atoms* (Cambridge University Press, Cambridge, 1994).

[82] D. Baye and M. Vincke, "Center-of-mass effects on atoms in magnetic fields," in Ref. [8], p. 141.

[83] J. E. Avron, I. B. Herbst, and B. Simon, Ann. Phys. (NY) **114**, 431 (1978).

[84] P. Schmelcher, J. Phys. B **25**, 2697 (1992).

[85] D. Baye and M. Vincke, J. Phys. B **19**, 4051 (1986).

[86] K. A. U. Lindgren and J. T. Virtamo, J. Phys. B **12**, 3465 (1979).

[87] In SI units the diamagentic hydrogen Hamiltonian is given by

$$H = -\frac{\hbar^2}{2\mu}\nabla^2 - \frac{ke^2}{r} + \frac{e^2B^2}{8\mu c^2}\rho^2, \tag{7.1}$$

where k is the Boltzmann constant and μ is the reduced mass of the electron. (We have omitted the linear Zeeman term since it does not affect the dynamics of the problem.) To write the expression for the Schrödinger equation in Eq. (2.1) we simply scale the spatial coordinates in units of the Bohr radius. In other words, $\nabla^2 \rightarrow \nabla^2/a_0^2$, $\rho^2 \rightarrow a_0^2\rho^2$, and $r \rightarrow a_0 r$. The field strength B is scaled in units of $\mu^2e^3c/\hbar^3 \approx 2.35 \times 10^5$ tesla, which means $B = 1$ in Eq. (2.1) corresponds to 2.35×10^5 T, which is the threshold field strength at which the Lorentz force on the electron of mass μ produces an orbital radius that matches the Bohr radius of the atom. (The scaled field strength is often denoted β in the literature.)

[88] More precisely, the diamagnetic term mixes states of $\Delta\ell = \pm 2$, as shown by the corresponding matrix elements of the diamagnetic term in the hydrogenic basis,

$$\langle n\ell m|\rho^2|n'(\ell+2)m\rangle \propto f(\ell,m)\langle n\ell|r^2|n'(\ell+2)\rangle. \tag{7.2}$$

[89] See Ref. [81], pp. 146–147.

[90] This was first noted by Zimmerman, *et al.* in Ref. [62] and confirmed theoretically by Delande and Gay in Ref. [64]. See also Refs. [4] and [61].

[91] C. Cohen-Tannoudji, B. Diu, and F. LaLoë, *Quantum Mechanics* (Wiley, New York, 1977), Complement D_{VI}.

[92] We remind the reader that the bound state energy levels in Eq. (2.26) are derived by demanding that the wave function (and hence the probability amplitude) vanish as $\rho \rightarrow \infty$. Therefore the electron is completely bound all the way to $E \rightarrow \infty$ and there can be no continuum levels.

[93] Here we argue from a physical standpoint. From a purely theoretical standpoint, where the potential energy diverges at the origin, there has been considerable debate about the behavior of the energy levels and the physical characteristics of the wave functions. See Refs. [95] and [96].

[94] R. Loudon, Am. J. Phys. **27**, 649 (1959).

[95] L. K. Haines and D. H. Roberts, Am. J. Phys. **37**, 1145 (1969).

[96] M. Andrews, Am. J. Phys. **34**, 1194 (1966).

[97] We use ν to represent this quantity rather than the traditional k to avoid confusion since k is used as an (approximate) quantum number in the low-field limit.

[98] H. Friedrich and M. Chu, Phys. Rev. A **28**, 1423 (1983).

[99] R. F. O'Connel, Phys. Lett. **70A**, 389 (1979).

[100] G. Wunner, H. Ruder, and H. Herold, Phys. Lett. **79A**, 159 (1980);

[101] Me.

[102] For each N subspace, there are an infinite number of Rydberg (hydrogenic) levels, since ν is unbounded. Each of these levels must diabatically cross the level that will form the $N = 1, \nu = 0$ high-field level.

[103] *Dimensional Scaling in Chemical Physics*, edited by D. R. Herschbach, J. Avery, and O. Goscinski (Kluwer, Dordrecht, 1992).

[104] Y. Y. Goldschmidt, Nucl. Phys. B **393**, 507 (1993); J. Rudnick and G. Gaspari, Science **237**, 384 (1987); R. A. Ferrell and D. J. Scalapino, *Phys. Rev. A* **9**, 846 (1974); A. J. Bray, J. Phys. A **7**, 2144 (1974); H. E. Stanley, Phys. Rev. **176**, 718 (1968); T. H. Berlin and M. Kac, Phys. Rev. **86**, 821 (1952).

[105] M. Dunn, T. C. Germann, D. Z. Goodson, C. A. Traynor, J. D. Morgan III, D. K. Watson, D. R. Herschbach J. Chem. Phys. **101**, 5987 (1994).

[106] V. S. Popov, V. D. Mur, A. V. Sergeev, and V. M. Weinberg, Phys. Lett. **149A**, 418 (1990); V. S. Popov, V. D. Mur, and A. V. Sergeev, Phys. Lett. **149A**, 425 (1990); V. S. Popov, V. D. Mur, A. V. Shcheblykin, and V. M. Weinberg, Phys. Lett. **124A**, 77 (1987).

[107] A. Chatterjee, Phys. Repts. **186**, 249 (1990).

[108] A. A. Belov, Yu. E. Lozovik and V. A. Mandelshtam, Zh. Eksp. Teor. Fiz. **98**, 25 (1990) [Sov. Phys. JETP **71**, 12 (1990)].

[109] V. S. Popov and A. V. Sergeev, Phys. Lett. **193A**, 165 (1994).

[110] V. M. Vaĭnberg, V. S. Popov and A. V. Sergeev, Zh. Eksp. Teor. Fiz. **98**, 847 (1990) [Sov. Phys. JETP **71**, 470 (1990)];

[111] *New Methods in Quantum Theory*, edited by C. A. Tsipis, V. S. Popov, D. R. Herschbach and J. Avery, NATO Conference Book, Vol. 8 (Kluwer Academic, Dordrecht, Holland, 1996).

[112] T. C. Germann and S. Kais, J. Chem. Phys. **99**, 7739 (1993).

[113] L. J. Boya and R. Murray, Phys. Rev. A **50**, 4397 (1994); S. Kais and G. Beltrame, J. Phys. Chem. **97**, 2453 (1993); U. P. Sukhatme, B. M. Lauer and T. D. Imbo, Phys. Rev. D **33**, 1166 (1986); R. S. Gangyopadhyay, R. Dutt and Y. P. Varshni, Phys. Rev. D **32**, 3312 (1985); D. Bollé and F. Gesztesy, Phys. Rev. A **30**, 1279 (1984); M. Sinha-Roy, R. S. Gangyopadhyay and B. Dutta-Roy, J. Phys. A **17**, L687 (1984).

[114] S. M. Valone, Int. J. Quantum Chem. **49**, 591 (1994); S. Kais, D. R. Herschbach, N. C. Handy, C. W. Marray and G. J. Laming, J. Phys. Chem. **99**, 417 (1993); G. F. Kventsel and J. Katriel, Phys. Rev. A **24**, 2299 (1981); N.H. March, Phys. Rev. A **30**, 2936 (1984); Phys. Rev. A **34**, 5106 (1986); J. Math. Phys. **26**, 554 (1985).

[115] A. A. Suvernev and D. Z. Goodson, Chem. Phys. Lett. **269**, 177 (1997); J. Chem. Phys. **107**, 4099 (1997).

[116] P. Serra and S. Kais, Phys. Rev. A **55**, 238 (1997); J. Phys. A **30**, 1483 (1997); Chem. Phys. Lett. **275**, 211 (1997); Phys. Rev. Lett. **77**, 466 (1996); J. P. Neirotti, P. Serra, and S. Kais, Phys. Rev. Lett. **79**, 3142 (1997); Chem. Phys. Lett. **260**, 302 (1996).

[117] T. C. Germann, D. R. Herschbach, and B. M. Boghosian, *Comput. Phys.* **8**, 712 (1994).

[118] This equation follows from the scaling and the fact that the magnetic field strength is measured in units of $B_0 = \mu^2 e^3 c/\hbar^3 \approx 2.35 \times 10^5$ tesla, where μ is the reduced mass of the electron. In other words,

$$\frac{B(tesla)}{B_0} = \delta^3 \widetilde{B} \quad \Longrightarrow \quad B(tesla) \approx \frac{2.35 \times 10^5 \widetilde{B}}{8(1+|m|)^3} = \frac{29\,375 \cdot \widetilde{B}}{(1+|m|)^3}. \tag{7.3}$$

See also my comments in Ref. [87].

[119] T. C. Germann, D. R. Herschbach, M. Dunn, and D. K. Watson, *Phys. Rev. Lett.* **74**, 658 (1995).

[120] The algorithm of choice for calculating circular Rydberg states using dimensional perturbation theory is the matrix method[105]. Twentieth-order calculations using the matrix method only take about three minutes to compute on a SparcStation 20 workstation.

[121] The intermediate field region for large values of n is much harder to describe, since avoided crossings are so close together that assigning a well-defined nodal structure to each energy level becomes impossible.

[122] It is technically incorrect to say that the physical characteristics of the wave functions exchange *at* the avoided crossing, because the states close to the avoided crossing are actually made up of a superposition of the states that are used to label each energy level.

[123] L. D. Landau and E. M. Lifshitz, *Quantum Mechanics* (Pergamon, Oxford, 1977), Sec. 79.

[124] M. Dunn, D. K. Watson, J. R. Walkup, and T. C. Germann, J. Chem. Phys. **104**, 9870 (1996).

[125] E. A. Solov'ev, Zh. Eksp. Teor. Fiz. **81**, 1681 (1981) [Sov. Phys. JETP **54**, 893 (1981)]; S. Yu. Ovchinnikov and E. A. Solov'ev, Comments At. Mol. Phys. **22**, 69 (1988).

[126] C. M. Bender and S. A. Orszag, *Advanced Mathematical Methods for Scientists and Engineers* (McGraw-Hill, New York, 1978), Chap. 8.

[127] G. Arfken, *Mathematical Methods for Physicists* (Academic Press, San Diego, 1985), pp. 377–378.

[128] These branch points are not only the values of the parameter b where $E_+ = E_-$; the energy functions $E_+(b)$ and $E_-(b)$ actually share this point. This may be shown by following a path which takes $b \rightarrow b$ and encloses one of the branch points. From Eq. (4.8) this path takes $E_\pm$ into $E_\mp$. Thus by letting the distance of the path to the branch point tend to zero while ensuring the path continues to enclose the branch point we see that the branch point is common to both E_+ and E_-. (For a more detailed discussion see, for example, Ref. [124].)

[129] W. D. Heiss and A. L. Sannino [J. Phys. A **23**, 1167 (1990)] have related the distribution of square-root branch points in matrix Hamiltonian problems to the appearance of quantum chaos in these systems. See also A. A. Kotze and W. D. Heiss [J. Phys. A **27**, 3059 (1994)]

[130] Although the two-level system we chose in our example was real-valued, we note that complex-valued two-level systems also require that real-valued branch points exist at the same location as long as the Hamiltonian is Hermitian.

[131] A. V. Sergeev (private communication).

[132] E. Fermi, Z. Physik **71**, 250 (1931); G. Herzberg, *Molecular Spectra and Molecular Structure* (Van Norstrand Reinhold, New York, 1945), Vol. II, p. 215.

[133] Because we use a log scale on both axes, the avoided crossing center is slightly displaced from where the narrowest approach of energy levels appears in the figures.

[134] The reader may be curious as to why "tesla" is spelled out rather than abbreviated. This chapter can be confusing since there is regular switching from physical field strengths (measured in tesla) and scaled field strengths (unitless). I think that spelling out the units makes it less likely that the reader will mistake which parameter a particular quoted value refers.

[135] D. K. Watson, M. Dunn, T. C. Germann, D. R. Herschbach, D. Z. Goodson, and J. R. Walkup, "Dimensional Expansions for Atomic Systems," in Ref. [111].

[136] W. D. Heiss and W. -H. Steeb, J. Math Phys. **32**, 3003 (1991).

[137] A. Bohm, *Quantum Mechanics: Foundations and Applications* (Springer-Verlag, New York, 1986), Sect. I.7 and Chapter XXI.

[138] That is, other than the hydrogenic 1:1 Fermi resonance which occurs at $B = 0$, not relevant to this discussion.

[139] C. M. Bender, H. J. Happ, and B. Svetitsky, Phys. Rev. D **9**, 2324 (1974).

[140] E. A. Solov'ev, Usp. Fiz. Nauk **157**, 437 (1989) [Sov. Phys. Usp. **32**, 228 (1989)]; T. P. Grozdanov and E. A. Solov'ev, Phys. Rev. A **51**, 2630 (1995); R. K. Janev, J. Pop-Jordanov, and E. A. Solov'ev, J. Phys. B **30**, L353, (1997).

[141] M. Pieksma and S. Yu. Ovchinnikov, J. Phys. B **24**, 2699 (1991).

[142] D. Jakimovski, V. I. Savichev, and E. A. Solov'ev, Phys. Rev. A **54**, 2962 (1996).

[143] S. J. Ward, J. H. Macek, and S. Yu. Ovchinnikov, Nucl. Inst. Meth. in Phys. Res. B **143**, 175 (1998).

[144] J. R. Walkup, M. Dunn, D. K. Watson, and T. C. Phys. Rev. A **58**, 4688 (1999).

[145] E. A. Solov'ev, Zh. Eksp. Teor. Fiz. **90**, 1165 (1986) [Sov. Phys. JETP **63**, 678 (1986); **91**, 477 (1986) [Sov. Phys. JETP **64**, 280 (1987)].

[146] Bender, Happ, and Svetitsky in Ref. [139] consider a finite $N \times N$ matrix approximation to the full Schrödinger equation and show that, although we can expect square-root branch points, we must view the presence of higher-order branch points as quite fortuitous. In the context of the multivariable problem, it means that with any change of the parameters not continued off the real axis, a higher-order-root branch point in the complex plane of the parameter continued off the real axis disappears. Therefore, in Situation 1 the parameter continued off the real axis is the same as the parameter which is being adiabatically varied. Except for possible isolated values of the parameters held along the real axis, higher-order branch points play no role in the avoided crossings of the system. In Situation 2, the parameter continued into the

complex plane is different from the parameter which is adiabatically varied. A higher-order branch point may momentarily appear as we scan the adiabatic variable, but the higher-order branch point would have to be sufficiently close to the real axis, and the summation point close to the place where it momentarily appears, for it to have any effect on the energies of states.

[147] V. I. Kukulin, V. M. Krasnopol'sky, and J. Horáček, *Theory of Resonances: Principles and Applications* (Kluwer Academic Press, Dordrecht, 1989), Sec. 2.2 and Chap. 5.

[148] Note that $C^*(\delta, \widetilde{B}) = \left[C(\delta^*, \widetilde{B}^*)\right]^*$, not $C^*(\delta, \widetilde{B}) = \left[C(\delta, \widetilde{B})\right]^*$. Therefore Eq. (5.3) does not imply that the sum of the second and third terms in Eq. (5.2) on the two sheets, for which the energy is real on the positive, real δ-axis, is real off the real axis.

[149] We find the energies close together near the branch-point degeneracies because the branch points connect to states which are complex on the positive, real δ-axis, These states, in turn, connect with other states having real energy on the positive, real δ-axis by branch points in the same positions. Therefore, near the branch points, the minimum path length in the four-sheeted Riemann surface connecting the two states having real energies $E^{\pm}(\delta, \widetilde{B})$ on the positive, real δ-axis is a minimum. Therefore, we would also expect the separation in energy to be small as well.

[150] D. Z. Goodson, M. Lòpez-Cabrera, and D. R. Herschbach, J. Chem. Phys. **97**, 8481 (1992).

[151] The Barbanis Hamiltonian models many molecular systems containing Fermi resonances, such as the CO_2 stretch-bend resonance and certain near-resonances of symmetric ABA triatomic molecules.

[152] E. Witten, Phys. Today **33**, 38 (1980).

[153] Rather than studying the energy as a function of complex m, we actually study it as a function of complex $\delta = 1/(2[|m| + 1])$. This is the natural parameter in dimensional perturbation theory, the method used in this research. The results we obtain in the complex δ-plane apply equally well in the complex $|m|$-plane. In particular, a square-root branch point in the complex δ-plane is a square-root branch point in the complex $|m|$-plane since by expanding $\delta(|m|)$ about the branch-point position $\delta_{bp} = \delta(|m|_{bp})$ mapped into the complex $|m|$-plane we obtain $\sqrt{\delta - \delta_{bp}} = g(|m|)\sqrt{|m| - |m|_{bp}}$, where $g(|m|)$ is not singular at $|m|_{bp}$.

[154] Dimensional perturbation theory provides a natural way to study the above discrete avoided crossings as we vary m. The physical states of the system were found for integer values of the continuous parameter m, so by restricting ourselves to these values a discrete version of avoided crossings appeared, complete with a diabatic nodal-structure exchange across the avoided crossings.

[155] We are not saying that quadratic Padés cannot approximate more complex multisheeted functions. After all, conventional linear Padés, which are single-sheeted rational-polynomial functions, model multisheeted functions by stringing poles and zeros of the rational polynomial along a line to approximate a branch cut. Therefore linear Padés approximate multisheeted functions on a single cut sheet of the original function. Rather, we avoid such discussion of approximating a four-sheeted function with quadratic Padés by instead examining $E^{+}(\delta, \widetilde{B}) + E^{-}(\delta, \widetilde{B})$, which is either either a single-sheeted function or a two-sheeted function with the same analytic form as the two-sheeted quadratic Padé approximant of Eq. (G.1).

[156] Note that since $(\widetilde{B} - \widetilde{B}_c)$ is an odd function about $\widetilde{B}_c$, the plot of $\tilde{\delta}^{\pm}(\widetilde{B})/(\widetilde{B} - \widetilde{B}_c)$ for the 4:1 Fermi resonance is reflected about the imaginary axis through $(\widetilde{B} - \widetilde{B}_c)$ compared to the plot of $\tilde{\delta}^{\pm}(\widetilde{B})$ for the 2:1 Fermi resonance. Also note that the coalescence point in Fig. 5.6 occurs at the 4:1 Fermi resonance, unlike in Fig. 4.7 where it occurs for $\widetilde{B}$ less than the Fermi resonance.

[157] E. J. Weniger, Comput. Phys. Rep. **10**, 189 (1989); Phys. Rev. A **56**, 5165 (1997).

[158] *Current Physics Sources and Comments, Vol.7: Large-Order Behavior of Perturbation Theory*, edited by J. C. Le Guillou and J. Zinn-Justin, (North Holland, Amsterdam, 1990).

[159] R. B. Dingle, *Asymptotic Expansions: Their Derivation and Interpretation* (Academic Press, New York, 1973).

[160] There are many excellent introductions to Padé summation, such as G. Baker and P. Graves-Morris, *Padé Approximants*, Vol. 59 of *Encyclopedia of Mathematics and its Applications* (Cambridge University Press, 1996); Ref. [126], Sec. 8.3, and V. O. Kukulin, V. M. Krasnopol'sky, and J. Horáček, *Theory of Resonances* (Kluwer Academic Publishers, Dordrecht, 1989), Sec. 1.2.

[161] The Chebyshev polynomial is *guaranteed* to satisfy this requirement. There may be other polynomials that satisfy this requirement as well.

[162] A. Ralston, *A First Course in Numeral Analysis* (McGraw-Hill, New York, 1965), Sec. 7.7-2.

[163] C-E. Fröberg, *Numerical Mathematics: Theory and Computer Applications* (Addison-Wesley, Reading, MA, 1985), p. 262.

[164] Do not confuse the optimized economized rational approximants discussed here with optimal rational approximants, a completely different approximation. See M. A. Snyder, *Chebyshev Methods in Numerical Approximation* (Prentice-Hall, Inc., Englewood Cliffs, NJ, 1966), Sec. 4.1.

[165] The fact that the Chebyshev polynomial satisfies this requirement is proven in Ref. [162], p. 265.

[166] Note that the values of d_i for any i depend on which sequence is chosen. For this reason superscripts are sometimes added to the coefficients $\{d_i\}$ and to the Padé approximant polynomials P_i and Q_i. To reduce clutter we omitted the superscripts.

[167] Before running the curve-fitting routine, we initially narrowed the search over α by "eye-balling" the convergence of the ERAs for the value of α at which the convergence qualitatively began to look smooth and exponential.

[168] J. C. Le Guillou and J. Zinn-Justin, Phys. Rev. B **21**, 531 (1979). Also Ref. [158], p. 531.

[169] K. Bhattacharyya, Int. J. Quant. Chem. **22**, 307 (1982). See also J. N. Silverman, Phys. Rev. A **28**, 498 (1983).

[170] T. C. Germann, Ph.D. thesis, Harvard University, 1995.

[171] This was partially demonstrated earlier by T. C. Germann, *et al.* in Ref. [117]

[172] "Local optimization of the summation of divergent power series." Accepted for publication by *Journal of Mathematical Physics.*

[173] See Ref. [123], Sec. 52.

[174] See for example B. H. Bransden and C. J. Joachain, *Physics of Atoms and Molecules* (Longman Group Ltd., London, 1983) and M. A. Morrison, T. L. Estle, and N. F. Lane, *Quantum States of Atoms, Molecules, and Solids* (Prentice-Hall, Englewood Cliffs, NJ, 1976).

[175] There are a number of good group theory books available. For the special case of diamagnetic hydrogen I especially relied on M. J. Englefield, *Group Theory and the Coulomb Problem* (Wiley-Interscience, NY, 1972) as well as M. Samuals, *Group Theory Made Easy for Scientists and Engineers* (Wiley, NY, 1979). A very readable introduction to group theory is A. P. Cracknell, *Applied Group Theory*, (Pergamon Press, London, 1968). Also recommended is B. G. Wybourne, *Classical Groups for Physicists* (Wiley, NY, 1974). Probably the most commonly used texts on group theory are M. Hamermesh, *Group Theory and its Application to Physical Problems* (Dover, Mineola, NY, 1962) and H. Weyl, *The Theory of Groups and Quantum Mechanics* (Dover, Mineola, NY, 1950).

[176] We say that the $SO(2,2)$ Lie algebra is a *spectrum generating* algebra because it contains raising and lowering operators that allow one to step up and down the energy spectrum (that is, raise and lower the principle quantum number n) while preserving m.

[177] M. Gourdin, *Unitary Symmetries and their Application to High Energy Physics* (Wiley-Interscience, NY, 1967), p. 198.

[178] M. J. Englefield in Ref. [175], p. 2.

[179] It is beyond the scope of this review to discuss the definition of a semi-simple Lie algebra. Those interested in such basic issues of group theory will likely find the discussions in Ref. [175] sufficient.

[180] Schur's Lemma: A matrix which commutes with all the members of an irreducible representation is a constant matrix (that is, a multiple of the unit matrix. From A. P. Cracknell, Ref. [175], p. 34.

[181] W. J. Thompson, *Angular Momentum: An Illustrated Guide to Rotational Symmeties for Physical Systems* (Wiley, NY, 1994).

[182] See Ref. [91], p. 705.

[183] J. Simola and J. Virtamo, J. Phys. B **11**, 3309 (1978).

[184] B. H. Bransden and C. J. Joachain, *Physics of Atoms and Molecules* (Longman Group Ltd., London, 1983), pp. 147–8.

[185] M. N. Padé, *Sur la rèprésentation approchée d'une fontion par des fractions rationelles*, Ann. Sci. Ecole Norm. Sup. 9 (1892), Supplement, pp. 1-8; R. E. Shafer, SIAM J. Numer. Anal. **11**, 447 (1972); S. Paszkowski, J. Comput. Appl. Math. **32**, 229 (1990).

[186] See for example G. F. Carrier, M. Krook, and C. E. Pearson, *Functions of a Complex Variable* (McGraw-Hill, New York, 1966).

[187] P. Fong, *Elementary Quantum Mechanics* (Addison-Wesley, Reading, MA, 1962), Chap. 10, Sec. 2.

[188] In terms of fundamental constants, $\mu = \frac{g\beta}{\hbar}$, where g (the spin g-factor) and $\beta = e\hbar/(2m_e c)$ (the Bohr magneton) are both positive.

[189] Note that I did not say that we would plot $E_\uparrow$ *as a function of* $B_\parallel$, since that could imply that the magnetic field was considered continuously changing. In this system, with only one magnetic field, such a distinction is not needed. However, we will see why such a distinction is made later when we incorporate a second magnetic field into the system.

[190] At least, not for any physical (real) values of $B_\parallel$.

[191] K. Mullen, E. Ben-Jacob, Y. Gefen, and Z. Schuss, *Phys. Rev. Letters.* **62**, 2543 (1989).

[192] C. Zener, *Proc. R. Soc. London A* **137**, 696 (1932).

[193] G. Wannier, *Physics.* **1**, 251 (1965).

[194] It would seem that starting the system out at a negative time would be more natural. However, the asymptotic solutions we are going to rely on are typically expressed in the literature (Whittaker and Watson,[195] for example) for positive t, so finding the solution which corresponds to the correct boundary conditions will be easier if we choose our initial time as positive. Since we are varying only one parameter, the result is the same no matter which direction of time we choose. If we were varying more than one parameter the Berry phase problem would have to be considered. [See M. V. Berry, Proc. Roc. Soc. London, Ser. A **392**, 45 (1984).] In other words, we are starting the system at roughly pt. D in Fig. E.3.

[195] E.T. Whittaker and G.N. Watson, *A Course of Modern Analysis* (Cambridge Univ. Press, Cambridge, 1952), p. 348.

[196] D. Lubin, Y. Gefen, and I. Goldhirsch, *Physica A.* **168**, 456 (1990).

[197] Again, in regards to the Berry phase, we are only varying one parameter in this treatment. See Ref. [194] and the literature citation therein.

[198] L. Schiff, *Quantum Mechanics* (McGraw-Hill, New York, 1985), pp. 290–291.

[199] R. Eisberg and R. Resnick, *Quantum Physics of Atoms, Molecules, Solids, Nuclei, and Particles* (John Wiley & Sons, New York, 1985), pp. 276–277.

[200] J. R. Rubbmark, M. M. Kash, M. G. Littman, and D. Kleppner, *Phys. Rev. A.* **23**, 3107 (1981).

[201] S. Brundobler, and V. Elser, *J. Phys. A: Math. Gen.* **26**, 1211 (1993).

[202] S. Fishman, K. Mullen, E. Ben-Jacob, *Phys. Rev. A.* **42**, 5181 (1990).

Appendix A

A Brief Review of Important Quantum-Mechanical Corrections to the Energy Spectrum of Hydrogen

When discussing such effects as fine structure, the anomalous Zeeman effect, and so on, few textbooks provide calculations for large values of the quantum numbers. The purpose of this appendix is to provide the reader an understanding of how these effects compare in magnitude for the values of quantum numbers used in this research and to understand at which values the field strengths become dominant. Many of our calculations involve circular Rydberg states having $|m| = 33$, so in this appendix we will consider the cases where $n = 34$, $\ell = 33$, and $m = \pm 33$, as well as many of the quantum numbers associated with low-lying states. However, we will not discuss how these energy shifts are derived, since many textbooks do so in quite adequately.[174]

We must keep in mind that the following does not incorporate the effects of an enormously strong magnetic field. For field strengths of the order 10^{10} T the Dirac equation for diamagnetic hydrogen must be solved numerically, as discussed in Sec. 1.2.2. In the weak-field region, the following serve as a rough guide for the energy corrections due to these effects.

A.1 Fine Structure

The fine structure is composed of three effects, the first of which is the relativistic correction to the kinetic energy,

$$\mathcal{H}'_{\mathrm{KE}} = -\frac{p^4}{8m_e^3c^2}, \tag{A.1}$$

where p and m_e are the momentum and mass of the electron and c is the speed of light. The correction (in eV),

$$(\Delta E)_{\mathrm{KE}} = 13.6\frac{Z^4\alpha^2}{n^4}\left(\frac{3}{4} - \frac{n}{\ell+\frac{1}{2}}\right);(\mathrm{eV}), \tag{A.2}$$

always lowers the energy by a small amount (it can never be 0). Its greatest contribution occurs when n is small and Z is large.

The Darwin term

$$(\mathcal{H})'_{\mathrm{D}} = \frac{\pi\hbar^2}{2m_e^2c^2}\left(\frac{Ze^2}{4\pi\epsilon_0}\right)\delta(\mathbf{r});(\mathrm{eV}), \tag{A.3}$$

only shifts the energy when the atom is in a $\ell = 0$ state. This energy shift is given by (in eV)

$$(\Delta E)_{\mathrm{D}} = 13.6\frac{Z^4\alpha^2}{n^3};(\mathrm{eV}). \tag{A.4}$$

If nonzero, this term always shifts the energy up.

The spin-orbit coupling is now calculated independently because its relative strength in comparison to the Zeeman effect determines the field region at which the anomalous Zeeman effect becomes dominated by the Paschen-Back effect. (There is little point in tabulating the energy shifts for the other two interactions, since they are never much larger in magnitude than the spin-orbit coupling, whereas the spin-orbit coupling can dominate for those atoms that feature strong coupling between the two angular momenta.)

Table A.1: Energy corrections due to spin-orbit coupling. The asterisk denotes the maximum shift possible for *any* set of quantum numbers. Energies are measured in electron-Volts, with wavenumbers (cm^{-1}) in parentheses.

n	ℓ	m_ℓ	j	$(\Delta E)_{so}$
1	0	0	1/2	$^*1.5 \times 10^{-5}(0.122)$
34	0	0	1/2	$3 \times 10^{-9}(2 \times 10^{-5})$
34	33	33	67/2	$8 \times 10^{-12}(7 \times 10^{-8})$

A.1.1 Spin-orbit coupling

The third relativistic effect we consider is the spin-orbit coupling term,

$$(\mathcal{H})'_{SO} = \xi(r)\mathbf{L}\cdot\mathbf{S}\,, \xi(r) \equiv \frac{1}{2r}\frac{dV}{dr}\,, \tag{A.5}$$

which shifts the energy by

$$(\Delta E)_{SO} = 13.6\frac{Z^4\alpha^2}{2n^3(\ell+\frac{1}{2})(\ell+1)} \tag{A.6}$$

for $j = \ell + \frac{1}{2}$ and

$$\Delta E = -13.6\frac{Z^4\alpha^2(\ell+1)}{2n\ell(\ell+\frac{1}{2})(\ell+1)} \tag{A.7}$$

for $j = \ell - \frac{1}{2}$. Notice that depending on the value of j, this energy shift can go either up or down.

The energy shifts for various quanta are tabulated for the spin-orbit coupling in Table (A.1).

A.1.2 The relative importance of the spin-orbit effect

If the field strength is much weaker than the spin-orbit coupling term in Eq. (A.5) then the Zeeman effect can be treated as a perturbation. In Table A.2 the field strengths at which threshold is crossed (denoted $B_{(a)}$ in Fig. 1.2) are tabulated for various quantum numbers of interest. Note that even the largest threshold field strength possible is far below the field

Table A.2: The field strength at which the effects of the external magnetic field become stronger than spin-orbit coupling. The data in this table determine the value of (a) in Fig. 1.2. For the lowest lying ($n \geq 3$) states and the states of special interest in this research ($n = 34$) only those quantum numbers are shown that produce the smallest and largest values of $B_{(a)}$.

n	ℓ	m_j	$B_{(a)}$(T)
2	1	1/2	[a]0.0624
3	2	5/2	[b]0.0008
34	1	1/2	[a]6.4×10^{-6}
34	33	65/2	[b]3.5×10^{-12}

[a] $j = \ell + \frac{1}{2}$.
[b] $j = \ell - \frac{1}{2}$.

strengths of interest in this research, showing that for our purposes spin-orbit coupling is completely negligible. This especially applies to circular Rydberg (large n, maximal $|m|$) states.

Appendix B

Lie Algebra and Group Theory of the Hydrogenic Atom

The low-field energy spectrum we are attempting to understand pertains to fixed $|m|$. Unfortunately, although it does commute with the Hamiltonian and therefore preserves n under all operations, the SO(4) Lie algebra does not conserve m under all operations because not all the operators contained within this algebra commute with L_z. There is, however, a different Lie algebra that *does* conserve m under all operations, the SO(2, 2) Lie algebra. Unfortunately, the SO(2, 2) Lie algebra does not conserve the principle quantum number n under all operations because it contains operators that do not commute with the Hamiltonian.[176] However, there exists in both algebras a subset of operators that preserve both n and m, and there is an isomorphism between these two subsets of operators. As we will see, this isomorphism allows us to express the perturbation Hamiltonian $H' \propto \rho^2$ as a first-order invariant operator which is diagonal in each n-subspace.

B.1 Lie algebra

If we consider elements A, B, and C of a vector space we can denote a "product" between these two elements as $[A \odot B]$. In general, a *Lie algebra* of a vector space containing elements A, B, and C is defined according to the following conditions[177]:

1. If we define $D \equiv [A \odot B]$, then D is also a member of the same vector space,
2. $[(aA + bB) \odot C] = a[A \odot C] + b[B \odot C]$ for any constants a and b,

3. $[A \odot A] = 0$,

4. $[A \odot [B \odot C]] + [B \odot [C \odot A]] + [C \odot [A \odot B]] = 0$.

In this appendix the elements A, B, and C will be quantum-mechanical *operators*, and therefore these elements do not necessarily commute. Therefore, we now define the product $[A \odot B]$ to be the commutator of the operators A and B,

$$[A, B] \equiv AB - BA. \tag{B.1}$$

Note that we do not have to worry about items 2, 3, and 4 any longer since they are automatically satisfied when the product $[A \odot B]$ is defined as the commutator $[A, B]$.

B.2 The SO(4) Lie algebra

A Lie algebra is defined according to the commutator relationships obeyed by the operators that form the basis of the algebra. The most important for our purposes is the SO(4) Lie algebra. The operators that comprise the basis of an SO(4) Lie algebra are given as[178]

$$D_{jk} = -x_j \partial x_k + x_k \partial x_j \ (j < k = 1, 2, 3, 4, 5, 6), \tag{B.2}$$

where $\partial x_j \equiv \partial / \partial x_j$, so that we can define

$$\Gamma_1 \equiv D_{23} = -x_2 \partial x_3 + x_3 \partial x_2 , \tag{B.3}$$

$$-\Gamma_2 \equiv D_{13} = -x_1 \partial x_3 + x_3 \partial x_1 , \tag{B.4}$$

$$\Gamma_3 \equiv D_{12} = -x_1 \partial x_2 + x_2 \partial x_1 , \tag{B.5}$$

$$-\Xi_1 \equiv D_{14} = -x_1 \partial x_4 + x_4 \partial x_1 , \tag{B.6}$$

$$-\Xi_2 \equiv D_{24} = -x_2 \partial x_4 + x_4 \partial x_2 , \tag{B.7}$$

$$-\Xi_3 \equiv D_{34} = -x_3 \partial x_4 + x_4 \partial x_3 . \tag{B.8}$$

(The numerical subscripts and negative signs above are assigned to make the following as simple to follow as possible.) We can show that these operators form a basis for a Lie algebra by applying the conditions in Sec. B.1. Our work is simplified because we now generate a rule that can be applied to nearly all possible commutator relationships formed by the operators Γ_i and Ξ_i defined above (those that it cannot are clearly 0 by inspection). We begin with

$$\begin{aligned}[D_{AB}, D_{AC}] &= [-x_A\partial x_B + x_B\partial x_A, -x_A\partial x_C + x_C\partial x_A]\, f \\ &= [x_A\partial x_B, x_A\partial x_C]\, f + [x_C\partial x_A, x_A\partial x_B]\, f \\ &\quad + [x_A\partial x_C, x_B\partial x_A]\, f + [x_B\partial x_A, x_C\partial x_A]\, f, \end{aligned} \tag{B.9}$$

where $f = f(x_A, x_B, x_C)$. The first and last terms in Eq. (B.9) are 0. For the first nonvanishing term we get

$$\begin{aligned}[x_C\partial x_A, x_A\partial x_B]\, f &= x_C\,[\partial x_A, x_A\partial x_B]\, f + [x_C, x_A\partial x_B]\,\partial x_A f \\ &= -x_C\,[x_A\partial x_B, \partial x_A]\, f - [x_A\partial x_B, \partial x_C]\,\partial x_A f \\ &= -x_C x_A\,[\partial x_B, \partial x_A]\, f - x_C\,[x_A, \partial x_A]\,\partial x_B f. \end{aligned} \tag{B.10}$$

For the second nonvanishing term in Eq. (B.9) we get (using similar operations) $x_C\partial x_B - x_B\partial x_C$. Therefore, we now have a general rule that will prove very convenient for computing the commutation relationships satisfied by the operators in Eqs. (B.3)–(B.8):

$$[D_{AB}, D_{AC}] = -x_B\partial x_C + x_C\partial x_B. \tag{B.11}$$

The above rule defines the nontrivial part of the Lie algebra. It is not a general rule for all Lie algebras, only the Lie algebra pertaining to Eqs. (B.8).

Using Eq. (B.11) we can immediately write down the commutation relations

$$[\Gamma_1, \Gamma_2] = \Gamma_3\,, \quad [\Gamma_2, \Gamma_3] = \Gamma_1\,, \quad [\Gamma_3, \Gamma_1] = \Gamma_2\,, \tag{B.12}$$

$$[\Xi_1, \Xi_2] = \Gamma_3\,, \quad [\Xi_2, \Xi_3] = \Gamma_1\,, \quad [\Xi_3, \Xi_1] = \Gamma_2\,, \tag{B.13}$$

$$[\Gamma_1, \Xi_2] = -\Xi_3\,, \quad [\Gamma_2, \Xi_3] = -\Xi_1\,, \quad [\Gamma_3, \Xi_1] = -\Xi_2\,, \tag{B.14}$$

$$[\Xi_1, \Gamma_2] = \Xi_3\,, \quad [\Xi_2, \Gamma_3] = \Xi_1\,, \quad [\Xi_3, \Gamma_1] = \Xi_2\,. \tag{B.15}$$

Note that there was no real need to write down the commutation relations in Eq. (B.15) since they are a direct result of those in Eq. (B.14). Those commutation relationships that do not have the pattern of subscripts in Eq. (B.11) can be deduced by mere inspection of the subscripts in the commutation relationships:

$$[\Gamma_1, \Xi_1] = 0\,, \quad [\Gamma_2, \Xi_2] = 0\,, \quad [\Gamma_3, \Xi_3] = 0\,. \tag{B.16}$$

Clearly, unless an index is repeated on the left-hand side of Eq. (B.11), the commutator will be 0. We can represent the above commutators in terms of the Levi-Cevita tensor ϵ_{ijk} and, therefore, cross products:

$$[\Gamma_i, \Gamma_j] = \epsilon_{ijk}\Gamma_k\,, \quad \boldsymbol{\Gamma} \times \boldsymbol{\Gamma} = \boldsymbol{\Gamma}\,; \tag{B.17}$$

$$[\Xi_i, \Xi_j] = \epsilon_{ijk}\Gamma_k\,, \quad \boldsymbol{\Xi} \times \boldsymbol{\Xi} = \boldsymbol{\Gamma}\,; \tag{B.18}$$

$$[\Xi_i, \Gamma_j] = \epsilon_{ijk}\Xi_k\,, \quad \boldsymbol{\Xi} \times \boldsymbol{\Gamma} = \boldsymbol{\Xi}\,. \tag{B.19}$$

Finally

$$[\Gamma_i, \Xi_i] = 0\,, \quad \boldsymbol{\Gamma} \cdot \boldsymbol{\Xi} = \mathbf{0}\,, \tag{B.20}$$

which can be deduced by inspection.

We can see from Eqs. (B.12)–(B.16) that the set of operators Ξ and Γ satisfy the first condition for a Lie algebra in Sec. B.1, and therefore provide a basis for an SO(4) Lie algebra as well. We will later see that the hydrogenic problem, under certain limitations which we will discuss, contains the appropriate generators to produce operators that satisfy the above commutation relations and, therefore, provide a basis for an SO(4) Lie algebra.

B.3 The Casimir operator

All semi-simple[179] Lie algebras, which include all the Lie algebras considered in this appendix, contain one or more Casimir operators, which commute with all other operators in the Lie algebra. Casimir operators are important because they are guaranteed, according to Schur's lemma[180], to have a fixed numerical value in a given Lie algebra. Even more importantly, the set of Casimir operators of a Lie algebra completely characterize the Lie algebra. For the Lie algebra above the Casimir operators are $\Gamma \cdot \Xi$ and Γ^2.

B.4 The direct-sum representation of the SO(4) Lie algebra

By a quick look at the commutation relations in Eq. (B.12) we can verify that the set of operators Γ_i form an SO(3) algebra of their own (a *subalgebra*) because the product of any two members of Γ produces a member of Γ (remember, that "product" here is defined as the commutator). However, by examining the commutators in Eq. (B.13) it is clear that, based on the same condition, the operators Ξ do *not* form a Lie subalgebra. However, we can recast the operators Γ and Ξ to produce a new set of operators Λ and Υ that form individual SO(3) subalgebras and the *direct sum* of these subalgebras form an SO(4) Lie algebra.

Consider the operators

$$\Lambda_1 \equiv \tfrac{1}{2}\left(\Gamma_1 + \Xi_1 + i\Gamma_2 + i\,\Xi_2\right) , \tag{B.21}$$

$$\Lambda_2 \equiv \tfrac{1}{2}\left(\Gamma_1 + \Xi_1 - i\Gamma_2 - i\,\Xi_2\right) , \tag{B.22}$$

$$\Lambda_3 \equiv \tfrac{1}{2}\left(\Gamma_3 + \Xi_3\right) , \tag{B.23}$$

$$\Upsilon_1 \equiv \tfrac{1}{2}\left(\Gamma_1 - \Xi_1 + i\Gamma_2 - i\,\Xi_2\right) , \tag{B.24}$$

$$\Upsilon_2 \equiv \tfrac{1}{2}\left(\Gamma_1 - \Xi_1 - i\Gamma_2 + i\,\Xi_2\right) , \tag{B.25}$$

$$\Upsilon_3 \equiv \tfrac{1}{2}\left(\Gamma_3 - \Xi_3\right) . \tag{B.26}$$

The commutation relations involving Λ_i are

$$[\Lambda_3, \Lambda_1] = \Lambda_1\,, \quad [\Lambda_2, \Lambda_3] = \Lambda_2\,, \quad [\Lambda_1, \Lambda_2] = 2\Lambda_3\,. \tag{B.27}$$

so that the operators Λ_i clearly form an SO(3) Lie algebra which we denote A_Λ, which is a subalgebra of the SO(4) Lie algebra. Furthermore,

$$[\Upsilon_3, \Upsilon_1] = \Upsilon_1\,, \quad [\Upsilon_2, \Upsilon_3] = \Upsilon_2\,, \quad [\Upsilon_1, \Upsilon_2] = 2\Upsilon_3\,. \tag{B.28}$$

so the operators Υ_i also form another SO(3) subalgebra of SO(4), which we call A_Υ. More importantly, since

$$[\Lambda_i, \Upsilon_j] = 0 \text{ for all possible } i \text{ and } j \tag{B.29}$$

then the two subalgebras A_Λ and A_Υ are completely independent of each other. In this situation, we say that the two subalgebras directly sum to produce an SO(4) Lie algebra:

$$A_\Lambda \oplus A_\Upsilon = \mathrm{SO}(4). \tag{B.30}$$

Note, however, that neither set of operators Λ_i nor Υ_i are angular momenta, that is, they do not obey angular momentum-like commutation relationships.

> Note: In this disseration I define an angular momentum operator as any Hermitian operator, generally denoted **J**, that obeys the commutator relationships defined by $\mathbf{J} \times \mathbf{J} = \mathbf{J}$. The physical (that is, orbital) angular momentum operator is usually denoted **L** and satisfies the relationship $\mathbf{L} \times \mathbf{L} = i\mathbf{L}$. Notice the sudden appearance of the imaginary number i. For a more detailed discussion of what constitutes angular momentum see Ref. [181].

B.5 The hydrogenic problem

It is well-known to students of quantum physics that the hydrogenic Halmiltonian (with $\hbar$ and the reduced mass of the electron μ set equal to 1)

$$H = -\frac{p^2}{2} + Z/r \tag{B.31}$$

commutes with the orbital angular momentum operators L_x, L_y, L_z. What is not as widely known is that H also commutes with the three components of the Runge-Lenz vector of Eq. (2.4),

$$\mathbf{A} = (-2E)^{-1/2}\left[\frac{1}{2}(\mathbf{L}\times\mathbf{p} - \mathbf{p}\times\mathbf{L}) + Z\hat{\mathbf{r}}\right] \tag{B.32}$$

Note that we are using the dilated (energy-scaled) Runge-Lenz vector. Many authors, such as Englefield[178], do not include this energy dependence because they are interested in deriving the energy eigenvalues of hydrogen that force the operators that form the basis of the Lie algebra to obey the commutator relationships of angular momenta. That is not the aim here, so by applying the knowledge that the zero-field energy of hydrogen is $E = -1/(2n^2)$ and scaling the Runge-Lenz vector accordingly, we will produce a basis of the SO(4) Lie algebra that consists of angular momentum operators.

In quantum mechanics **A** is a (Hermitian) *vector* operator because it satisfies the commutation relations

$$[J_i, A_j] = iA_k \tag{B.33}$$

with any angular momentum operator **J**, which for our specific purposes is the orbital angular momentum operator **L**:

$$[L_i, \mathbf{A}_i] = 0\,, \tag{B.34}$$

$$[L_i, \mathbf{A}_j] = iA_k\,, \tag{B.35}$$

$$[A_i, A_j] = iL_k\,. \tag{B.36}$$

(A complete derivation of this commutator is given in Englefield[178], Appendix A.) We know that $\mathbf{L}$ satisfies $[L_i, L_j] = iL_k$ so $\mathbf{L}$ is analogous to Γ in Sec. B.2. From Eqs. (B.13)–(B.15) it is clear that $\mathbf{A}$ is analogous to Ξ.

From our earlier discussion we should be able to form operators from $\mathbf{L}$ and $\mathbf{A}$ that are analogous to Λ and Υ and that form SO(3) subalgebras of SO(4). However, we can go one step further and derive two Hermitian operators, which we call $\mathbf{F}$ and $\mathbf{G}$, that not only form SO(3) subalgebras of SO(4), but also individually satisfy the commutation relations of angular momentum operators.

First let us assume (using hindsight) that $\mathbf{F}$ and $\mathbf{G}$ have the basic form

$$\mathbf{F} = \tfrac{1}{2}(\mathbf{L} + \mathbf{A}), \quad \mathbf{G} = \tfrac{1}{2}(\mathbf{L} - \mathbf{A}). \tag{B.37}$$

We can start with the commutator

$$\begin{aligned}
[F_x, F_y] &= [\tfrac{1}{2}L_x + \tfrac{1}{2}A_x, \tfrac{1}{2}L_y + \tfrac{1}{2}A_y] \\
&= \frac{1}{4}\left([L_x, L_y] + [L_x, A_y] - [L_y, A_x] + [A_x, A_y]\right) \\
&= \frac{i}{2}(L_z + A_z) \\
&= iF_z.
\end{aligned} \tag{B.38}$$

Performing the same operations on the other compenents of $\mathbf{F}$ leads to the general relation

$$\mathbf{F} \times \mathbf{F} = i\mathbf{F}. \tag{B.39}$$

The same relationship as Eq. (B.39) holds for $\mathbf{G}$ as well. Therefore, the components of $\mathbf{F}$ are generators of an SO(3) Lie algebra.

Therefore, the components of $\mathbf{F}$ and $\mathbf{G}$ are generators of an SO(3) Lie algebra. Most importantly, $\mathbf{F}$ and $\mathbf{G}$ are both angular momenta, so we know beforehand that the Casimir operators of each subalgebra are $\mathbf{F}^2$ and $\mathbf{G}^2$, respectively.

It is straightforward to show that

$$[F_i, G_i] = 0\,, \quad [F_i, G_j] = 0. \tag{B.40}$$

Therefore, all elements of **F** commute with all elements of **G**, so the subalgebras of **F** and **G** directly sum to an SO(4) Lie algebra of the hydrogenic atom:

$$\mathrm{SO}(3)_F \oplus \mathrm{SO}(3)_G = \mathrm{SO}(4). \tag{B.41}$$

We mentioned earlier that although this SO(4) Lie algebra does not preserve the magnetic quantum number m, it does preserve the principal quantum number n. It should then be possible to construct a set of raising and lowering operators that allow one to step up and down in m while, at the same time, keeping the quantum number n fixed. Since **F** and **G** are angular momenta, they have the same form of raising and lowering operators as **L**, that is,

$$F^{\pm} = (F_x \pm F_y)\,, \quad G^{\pm} = (G_x \pm G_y)\,. \tag{B.42}$$

Note that $F^{\pm}$ and $G^{\pm}$ commute with the Hamiltonian, which coincides with our statement that when acting on a state of the system all four operators preserve n.

We are also in a position to now establish the relationship between the two quantum numbers of interest, n and m, and the generators of the SO(4) Lie algebra. Since **F** is an angular momentum, the corresponding Casimir operator $\mathbf{F}^2$ has an eigenvalue $f(f+1)$ [in the same way that the eigenvalue of $\mathbf{L}^2$ is $\ell(\ell+1)$]. Furthermore,

$$\begin{aligned} \mathbf{F}^2 &= (\mathbf{L}^2 + \mathbf{A}^2) = -\frac{1}{4}\left(\frac{1}{2E} - 1\right) \\ &= (n^2 - 1) = f(f+1). \end{aligned} \tag{B.43}$$

Clearly, the same relationship applies for $\mathbf{G}^2$. So we now have a prescription for relating the principle quantum number n with the operators of the SO(4) Lie algebra:

$$\mathbf{F}^2 = \mathbf{G}^2 = \tfrac{1}{4}(n^2 - 1)\,, \tag{B.44}$$

$$n \leftrightarrow 2f + 1\,, \tag{B.45}$$

$$n \leftrightarrow 2g + 1\,. \tag{B.46}$$

For m, we have simply $F_z + G_z = L_z$. Therefore

$$n \leftrightarrow 2f + 1\,, \qquad F_z + G_z \leftrightarrow m\,. \tag{B.47}$$

B.6 The SO(2, 1) Lie algebra

So far, we have only considered the zero-field hydrogenic problem. This system was described using the commutation relationships pertaining to the SO(4) Lie algebra, which is a symmetry algebra of the zero-field hydrogenic atom since all of its elements commute with the Hamiltonian. However, inserting the hydrogenic atom into a magnetic field produces an extra term in the Hamiltonian, the diamagnetic term, that breaks the SO(4) symmetry because a particular direction (usually defined as the z axis) is singled out, so many of the generators of the SO(4) Lie algebra no longer commute with the Hamiltonian. Furthermore, even in the zero-field case many of these operators do not commute with L_z, so the SO(4) Lie algebra does not preserve the magnetic quantum number m either.

As we mentioned at the start of this appendix, we will find it convenient to express the Schrödinger equation in a basis that can be generated by operators that preserve m. Consider the transformation of the Schrödinger equation in dilated (scaled according to the energy) semi-parabolic coordinates

$$\mu \equiv (-2E)^{1/4}\sqrt{r + z}\,, \quad \nu \equiv (-2E)^{1/4}\sqrt{r - z}\,, \quad \Psi(\mathbf{r}) = \frac{e^{im\phi}\Psi(\mu, \nu)}{\sqrt{2\pi}}\,. \tag{B.48}$$

The resulting Schrödinger equation

$$\left(\frac{\partial^2}{\partial\mu^2}+\frac{1}{\mu}\frac{\partial}{\partial\mu}-\frac{m^2}{\mu^2}-\mu^2+\frac{\partial^2}{\partial\nu^2}+\frac{1}{\nu}\frac{\partial}{\partial\nu}-\frac{m^2}{\nu^2}-\nu^2+\frac{4}{\sqrt{-2E}}\right)\Psi(\mu,\nu)=0. \quad \text{(B.49)}$$

In introductory physics it is well-known that the Schrödinger equation of a two-dimensional simple harmonic oscillator (SHO) is

$$\left(\frac{\partial^2}{\partial\rho^2}+\frac{1}{\rho}\frac{\partial}{\partial\rho}-\frac{m^2}{\rho^2}-\rho^2+\frac{2}{\sqrt{-2E}}\right)\Psi(\rho)=0, \quad \text{(B.50)}$$

so the Schrödinger equation of a hydgrogenic atom, in dilated semi-parabolic coordinates, behaves exactly like two independent particles bound in a two-dimensional simple harmonic oscillator potential. The diamagnetic term mixes the two coordinates μ and ν, but we will concern ourselves with this later.

For the two-dimensional SHO of Eq. (B.50), Englefield[178] derived the set of Hermitian operators

$$S_1=\frac{1}{4}\left(\frac{\partial}{\partial\mu}+\frac{1}{\mu}\frac{\partial}{\partial\mu}-\frac{m^2}{\mu^2}+\mu^2\right), \quad \text{(B.51)}$$

$$S_2=\frac{1}{4}\left(-\frac{\partial}{\partial\mu}-\frac{1}{\mu}\frac{\partial}{\partial\mu}+\frac{m^2}{\mu^2}+\mu^2\right), \quad \text{(B.52)}$$

$$S_3=\frac{i}{2}\left(1+\mu\frac{\partial}{\partial\mu}\right), \quad \text{(B.53)}$$

that generate the SO(2, 1) Lie algebra, defined by

$$[S_1,S_3]=-iS_2\,,\quad [S_3,S_2]=iS_1\,,\quad [S_2,S_1]=iS_3\,. \quad \text{(B.54)}$$

The Casimir operator is given by

$$S^2=S_1^2+S_2^2-S_3^2=\tfrac{1}{4}(1-m^2). \quad \text{(B.55)}$$

Although a bit pedantic, we will also note that for the coordinate ν:

$$T_1 = \frac{1}{4}\left(\frac{\partial}{\partial\nu} + \frac{1}{\nu}\frac{\partial}{\partial\nu} - \frac{m^2}{\nu^2} + \nu^2\right), \tag{B.56}$$

$$T_2 = \frac{1}{4}\left(-\frac{\partial}{\partial\nu} - \frac{1}{\nu}\frac{\partial}{\partial\nu} + \frac{m^2}{\nu^2} + \nu^2\right), \tag{B.57}$$

$$T_3 = \frac{i}{2}\left(1 + \nu\frac{\partial}{\partial\nu}\right). \tag{B.58}$$

The corresponding Casimir operator is clearly

$$T^2 = T_1^2 + T_2^2 - T_3^2 = \tfrac{1}{4}(1 - m^2). \tag{B.59}$$

The two Lie algebras in this section clearly commute — they directly sum to produce the SO(2, 2) Lie algebra.

B.7 The SO(2, 2) Lie algebra and its application to diamagnetic hydrogen

Going back to earlier in the chapter we noted that because $[F_i, L_z] \neq 0$ for all i (nor does $[G_i, L_z]$ for that matter), we could not expect the operators corresponding to the SO(4) Lie algebra to conserve m. However, we would like to examine the energy spectrum of diamagnetic hydrogen in a single m-subspace, and the important point to note about the SO(2, 2) Lie algebra that we just determined is that it is a representation of the zero-field hydrogen problem, expressed in dilated semi-parabolic coordinates, that preserves m under all operations.

At this point we have reached a crossroads. On the one hand, we have a SO(4) Lie algebra representation of diamagnetic hydrogen that preserves n under all operations, but not m. On the other hand, we have a SO(2, 2) representation of the same problem that preserves m under all operations, but not n. However, there is an overlap between the two

Lie algebras that consists of a subset of operators that preserve both m and n. It turns out that this subset describes an isomorphism between the two subsets of operators:

$$S^{\pm}T^{\mp} \leftrightarrow -F^{\pm}G^{\mp}\,, \tag{B.60}$$

$$S_z + T_z \leftrightarrow n = 2f + 1\,, \tag{B.61}$$

$$S_z - T_z \leftrightarrow F_z - G_z\,, \tag{B.62}$$

$$m \leftrightarrow F_z + G_z\,. \tag{B.63}$$

In terms of the SO(2, 2) Lie algebra the diamagnetic term is given by

$$V(\mu,\nu) = \frac{B^2}{32E^2}(\mu^4\nu^2 + \mu^2\nu^4) = B^2(S_z + S_x)(T_z + T_x)(S_z + T_z + S_x + T_x). \tag{B.64}$$

Note that all operators in $V(\mu,\nu)$ preserve m, but not n. However, we now apply first-order perturbation theory to the Hamiltonian. By expanding $V(\mu,\nu)$ and discarding all terms that do not preserve n, the result will be guaranteed to be a first-order invariant. So to first-order in B^2, we have

$$V(\mu,\nu) \rightarrow \frac{B^2}{16E^2}(S_z + T_z)(S^2 + T^2 + 6S_zT_z + 2S^+T^- + 2S^-T^+)\,. \tag{B.65}$$

This expression for the diamagnetic term, although not exact, preserves both quantum numbers. Since there is an isomorphism between the operators in Eq. (B.65) and the m, n-preserving operators in the SO(4) Lie algebra, we can simply re-express the potential energy in Eq. (B.65) in terms of those operators:

$$V(\mu,\nu) = \frac{n^2B^2}{16}(3n^2 + 1 - 4F_z^2 - G_z^2 + 4F_zG_z - 4F^+G^- - 4F^-G^+) \tag{B.66}$$

$$= \frac{n^2B^2}{16}(n^2 + 3 + m^2 + 4A^2 - 5A_z^2). \tag{B.67}$$

Finally, we have derived the first-order invariant of the diamagnetic hydrogen problem, which is expressed in Chap. 2 as Eqs. (2.2) and (2.3).

Appendix C

Description of the Ground State of the One-dimensional Hydrogenic Atom.

Suppose we are given a normalizable function $\chi(x)$ defined over the interval $(0, \infty)$. We will now show that the scalar product $\langle R|\chi\rangle$ of this function with the ground state of the one-dimensional hydrogenic atom vanishes. The following follows the treatment of Andrews. (Ref. [96].) Here we use the shorthand notation (setting the Bohr radius $a_0 = 1$)

$$|R_{k\to 0}\rangle = \lim_{k\to 0} \frac{1}{\sqrt{k}} e^{-x/k}. \tag{C.1}$$

We first break the integration over all space into two parts by choosing a positive value a such that

$$\langle R_{k\to 0}|\chi\rangle = \langle R_{k\to 0}|\chi\rangle_0^{ak/2} + \langle R_{k\to 0}|\chi\rangle_{ak/2}^{\infty}, \tag{C.2}$$

where the notation $\langle\cdots\rangle_b^c$ means to integrate from b to c.

Next we label each integral term as

$$I_1 \equiv \langle R_{k\to 0}|\chi\rangle_0^{ak/2}, \qquad I_2 \equiv \langle R_{k\to 0}\chi\rangle_{ak/2}^{\infty}. \tag{C.3}$$

The Schwarz inequality states that for each integral,

$$|I_1|^2 \le \langle R_{k\to 0}|R_{k\to 0}\rangle_0^{ak/2} \langle\chi|\chi\rangle_0^{ak/2}, \qquad |I_2|^2 \le \langle R_{k\to 0}|R_{k\to 0}\rangle_{ak/2}^{\infty} \langle\chi|\chi\rangle_{ak/2}^{\infty}. \tag{C.4}$$

Since

$$\langle R_{k\to 0}|R_{k\to 0}\rangle_0^{ak/2} = \lim_{k\to 0}\frac{1}{k}\int_0^{ak/2} e^{-2x/k}\,dx = \frac{1}{2}(1-e^{-a}) = \frac{1}{2}-\frac{e^{-a}}{2} < \frac{1}{2}, \quad \text{(C.5)}$$

then

$$|I_1|^2 < \frac{1}{2}\langle\chi|\chi\rangle_0^{ak/2}. \quad \text{(C.6)}$$

Also, since

$$\langle R_{k\to 0}|R_{k\to 0}\rangle_{ak/2}^{\infty} = \lim_{k\to 0}\frac{1}{k}\int_{ak/2}^{\infty} e^{-2x/k}\,dx = \frac{1}{2}e^{-a} \quad \text{(C.7)}$$

then

$$|I_2|^2 \le \frac{1}{2}e^{-a}\langle\chi|\chi\rangle_{ak/2}^{\infty} < \frac{1}{2}e^{-a}\langle\chi|\chi\rangle. \quad \text{(C.8)}$$

Now consider the $|I_2|^2$ term. Since $\chi(x)$ is normalizable, $\langle\chi|\chi\rangle = N$, where $N > 0$ is finite. Therefore, we can always find a sufficiently small value of ϵ and a sufficiently large value of $a = A$ such that

$$|I_2|^2 < \frac{N}{2}e^{-A} < \frac{1}{4}\epsilon, \quad \text{(C.9)}$$

no matter how small we choose ϵ. With $a = A$ then k can always be made small enough (remember that $k \to 0$) so that

$$|I_1|^2 \le \frac{1}{2}\langle\chi|\chi\rangle_0^{ak/2} < \frac{1}{4}\epsilon. \quad \text{(C.10)}$$

Now we can consider the square of the scalar product $\langle R_{k\to 0}|\chi\rangle$,

$$|\langle R_{k\to 0}|\chi\rangle|^2 = |I_1 + I_2|^2. \quad \text{(C.11)}$$

However, by examining our previously determined results

$$|I_1 + I_2|^2 = |I_1|^2 + |I_2|^2 \pm 2|I_1||I_2| < \frac{1}{2}\epsilon \pm 2|I_1||I_2| < \epsilon \tag{C.12}$$

we can see that

$$|\langle R_{k\to 0}|\chi\rangle|^2 < \epsilon. \tag{C.13}$$

Since we are free to choose ϵ as small as we wish we therefore have found that

$$\langle R_{k\to 0}|\chi\rangle \to 0, \tag{C.14}$$

which means there is no overlap between the ground state of a one-dimensional hydrogenic atom and any normalizable function.

The consequences of this result are two-fold:

1. In a one-dimensional Coulombic basis, the expansion coefficient c_0 of a normalizable function $\chi(x)$ is given by

$$c_0 = \langle R_{k\to 0}|\chi\rangle\,. \tag{C.15}$$

   Therefore $c_0 = 0$, regardless of the choice of $\chi(x)$ so the ground state is not needed for completeness in the set of one-dimensional hydrogenic wave functions.

2. Since any operator $\hat{O}$ in Hilbert space operates on normalizable functions to produce other normalizable functions; that is

$$\hat{O}\chi(x) = \chi'(x), \tag{C.16}$$

   then the matrix element

$$\langle R_{k\to 0}|\hat{O}|\chi\rangle = \langle R_{k\to 0}|\chi'\rangle \to 0, \tag{C.17}$$

so the matrix element of any Hermitian operator taken between the ground state and any normalizable function vanishes.

With the above results in mind, *we can safely conclude that the ground state of the one-dimensional hydrogenic atom is nonphysical.* However, we must keep in mind that this result does not hold for finite B-fields, since the potential energy function describing motion along the z-axis in finite fields is not truly Coulombic.

Appendix D

The Coupling Potential.

The following is a detailed derivation of the results found in J. Simola and J. Viertamo, J. Phys. B **11**, 3309 (1978) and H. Friedrich, Phys. Rev. A **26**, 1827 (1982).

Here we study the coupling potential [Eq. (2.41) in Sec. 2.2.1], which links the excited states corresponding to motion along the x,y-plane and along $\hat{\mathbf{z}}$, in the limit of large $|z|$. We will find that for large $|z|$ the coupling potential assumes a diagonal form approaching that of a one-dimensional Coulombic potential

$$V(z) = -\frac{1}{|z|}. \tag{D.1}$$

This means that the coupling potential becomes asymptotic to the z-axis as $|z| \to \infty$, which implies an infinite number of bound states for motion along the z-axis. Furthermore, we will see that $V(z)$ models the behavior of the electron more effectively as the magnetic field strengthens.

We rewrite the coupling potential as

$$\mathcal{V}^m_{N',N}(x) \equiv -\sqrt{\frac{2}{B}}\, V^m_{N',N}(z) = \int_0^\infty \frac{P_{N',m}(\xi) P_{N,m}(\xi)\, \xi^{|m|} e^{-\xi}}{\sqrt{\xi + x^2}}\, d\xi, \tag{D.2}$$

where $\xi = B\rho^2/2$, $x = \sqrt{B/2}\, z$, and $P_{N,m}(\xi)$ is related to the Landau wave function by[183]

$$\Omega_{N,m} = \sqrt{B}\, e^{-\xi/2} \xi^{|m|/2} P_{N,m}(\xi). \tag{D.3}$$

The exact form of $P_{N,m}(\xi)$ is[183]

$$P_{N,m}(\xi) = \frac{1}{\sqrt{S!N!}} \sum_{k=0}^{\min(S,N)} \frac{(-1)^k}{k!} \frac{N!}{(N-k)!} \frac{S!}{(S-k)!} \xi^{\min(S,N)-k}$$
$$= \sum_{k=0}^{\min(S,N)} A_{k,N,m}\, \xi^{\min(S,N)-k} \tag{D.4}$$

where $S \equiv N-m$.

For large $|x|$ (in other words, large $|z|$) we can expand the denominator in Eq. (D.2) as

$$\frac{1}{\sqrt{\xi + x^2}} = \frac{1}{|x|} \sum_{k=0}^{\infty} (-1)^k \frac{(2k-1)!!}{2^k k!} \left(\frac{\xi}{x^2}\right)^k = \frac{1}{|x|} \sum_{k=0}^{\infty} C_k \left(\frac{\xi}{x^2}\right)^k, \tag{D.5}$$

where we let $C_k = (-1)^k(2k-1!!)/2^k k!$. We note that $C_0 = 1$ and $C_1 = -\frac{1}{2}$. Now the coupling potential is

$$\mathcal{V}^m_{N',N}(x) = \frac{1}{|x|} \sum_{k=0}^{\infty} \left[C_k \left(\frac{1}{x^2}\right)^k \int_0^{\infty} P_{N',m}(\xi) P_{N,m}(\xi)\, \xi^{|m|} \xi^k e^{-\xi}\, d\xi \right]. \tag{D.6}$$

The polynomials $P_{N,m}(\xi)$ are orthonormal when integrated with the factor $\xi^{|m|}e^{-\xi}$, thus

$$\int_0^{\infty} P_{N',m}(\xi) P_{N,m}(\xi)\, \xi^{|m|} e^{-\xi}\, d\xi = \delta_{N',N}. \tag{D.7}$$

If we fix the value of N' we can find the values of N for which $V^m_{N',N}(z)$ is nonzero. With N' fixed the only way for integral

$$I \equiv \int_0^{\infty} P_{N',m}(\xi) P_{N,m}(\xi)\, \xi^{|m|} \xi^k e^{-\xi}\, d\xi = \int_0^{\infty} P_{N',m}(\xi) F_{N,m}(\xi)\, \xi^{|m|} e^{-\xi}\, d\xi, \tag{D.8}$$

in Eq. (D.6) to be nonzero is for $P_{N',m}(\xi)$ to be of equal or higher order than $P_{N,m}(\xi)\,\xi^k \equiv F_{N,m}(\xi)$. The polynomial $P_{N',m}(\xi)$ is of the order $\mathcal{O}(N') = \min(S', N') - k$ and $F_{N,m}(\xi) = P_{N,m}(\xi)\,\xi^k$ is of the order $\mathcal{O}(N) = \min(S, N)$. Therefore we require

$$\min(S, N) < \min(S', N') - k. \tag{D.9}$$

If $m<0$ then $\min(S, N)=N$ and $\min(S', N')=N'$. Thus

$$(\text{for } I \neq 0) \qquad k \geq N' - N. \tag{D.10}$$

Now suppose $m>0$ so that $\min(S, N)=S=N-m$ and $\min(S', N')=N'-m$. We find the same result as above.

We could just as easily focused on N rather than N'. In this case $P_{N,m}(\xi)$ must be of equal or higher order than $P_{N',m}(\xi)\xi^k$. Since N' and N are essentially dummy variables, we can see that in this case

$$(\text{for } I \neq 0) \qquad k \geq N - N'. \tag{D.11}$$

We can combine these two results to find that $\mathcal{V}^m_{N',N}(x) \neq 0$ only if

$$|N' - N| \geq k. \tag{D.12}$$

this means the summation in Eq. (D.6) can be started at $k=|N'-N|$:

$$\mathcal{V}^m_{N',N}(x) = \frac{1}{|x|}\left\{\sum_{k=|N'-N|}^{\infty}\left[C_k\left(\frac{1}{x^2}\right)^k \int_0^{\infty} P_{N',m}(\xi)P_{N,m}(\xi)\,\xi^{|m|}\xi^k e^{-\xi}\,d\xi\right]\right\}. \tag{D.13}$$

Now it is desirable to change back to the original ρ and z coordinates so that

$$\begin{aligned} V^m_{N',N}(z) = -\sqrt{\frac{2}{B}}\mathcal{V}^m_{N',N}(z) &= \frac{1}{|z|}\left[\sum_{k=|N'-N|}^{\infty}\frac{C_k}{z^{2k}}\int_0^{\infty}\rho^{2k}\Omega_{N',m}(\rho)\Omega_{N,m}(\rho)\rho\,d\rho\right] \\ &= -\frac{1}{|z|}\left[\sum_{k=|N'-N|}^{\infty}\frac{C_k}{z^{2k}}\langle\Omega_{N'}|\rho^{2k}|\Omega_N\rangle\right]. \end{aligned} \tag{D.14}$$

D.1 Diagonal approximation

In the diagonal (adiabatic) approximation ($N = N'$) the first two terms are

$$V^m_{N,N}(z) \approx -\frac{1}{|z|}\left[C_0\langle\Omega|\Omega\rangle + \frac{C_1}{z^2}\langle\Omega|\rho^2|\Omega\rangle\right] = -\frac{1}{|z|}\left[1 - \frac{1}{2z^2}\langle\rho^2\rangle\right]. \qquad \text{(D.15)}$$

If we factor $8/B^2$ out of the ρ^2 expectation value in the last term we note that this transforms into the expectation value of the Landau potential energy function

$$V(\rho) = \frac{B^2}{8}\rho^2. \qquad \text{(D.16)}$$

Thus

$$V^m_{N,N}(z) \approx -\frac{1}{|z|}\left(1 - \frac{1}{2z^2}\frac{8}{B^2}\left\langle\Omega\left|\frac{B^2}{8}\rho^2\right|\Omega\right\rangle\right) = -\frac{1}{|z|}\left(1 - \frac{4}{B^2z^2}\langle V(\rho)\rangle\right). \qquad \text{(D.17)}$$

The virial theorem states that for time-independent Hamiltonians, $\langle V\rangle = \langle T\rangle = \frac{1}{2}\langle T + V\rangle$ if the potential energy function V is of second order.[184] Therefore

$$V^m_{N,N}(z) \approx \quad -\frac{1}{|z|}\left(1 - \frac{2}{B^2z^2}\langle T + V\rangle\right) = -\frac{1}{|z|}\left(1 - \frac{2}{B^2z^2}E_{N,m}\right). \qquad \text{(D.18)}$$

Remember that the Landau energy $E_{N,m}$ is linearly proportional to B. [See Eq. (2.25).] As stated in the main text, for sufficiently large $|z|$, in the diagonal approximation the coupling potential approaches the one-dimensional Coulombic potential. Furthermore, the second order correction is proportional to the Landau energy, but this correction falls off by a factor of $1/B^2$. Therefore, in the limit of large field strengths the Coulomb potential $V(r)$ becomes increasingly modeled by a one-dimensional hydrogenic atom.

D.2 Off-diagonal approximation

We still have yet to consider the off-diagonal (nonadiabiatic) terms. These occur when $k=|N'-N|\neq 0$. From Eq. (D.14) we have for $N-N'=1$,

$$\begin{aligned} V^m_{N',N}(z) = & -\frac{1}{|z|}\sum_{k=1}^{\infty}\frac{C_k}{z^{2k}}\langle\Omega_{N'}|\rho^{2k}|\Omega_N\rangle \\ = & -\frac{1}{|z|}\sum_{k=1}^{\infty}\left[\frac{C_1}{z^2}\int_0^{\infty}\Omega^*_{N'}(\rho)\Omega_N(\rho)\,\rho^3\,d\rho+\frac{C_2}{z^4}\int_0^{\infty}\Omega^*_{N'}(\rho)\Omega_N(\rho)\,\rho^5\,d\rho+\cdots\right] \\ = & -\frac{1}{|z|}\sum_{k=1}^{\infty}\left[\frac{2C_1}{z^2B}\int_0^{\infty}e^{-\xi}\xi^m P_{N',m}(\xi)P_{N,m}(\xi)\xi\,d\xi\right. \\ & \left.+\frac{4C_2}{z^4B^3}\int_0^{\infty}e^{-\xi}\xi^m P_{N',m}(\xi)P_{N,m}(\xi)\xi^2\,d\xi+\cdots\right] \end{aligned} \tag{D.19}$$

Each integral is simply a constant with respect to z and B, so we can see that as $B\rightarrow\infty$ all of the off-diagonal terms vanish. Therefore, in the limit of infinite field strengths the coupling potential uncouples in terms of the ρ and z degrees of freedom.

Appendix E

The Landau-Zener Transition Probability

The contents of this chapter were written for my Specialist's exam in December, 1997. I include this work because it is relevant to future research that is discussed in this dissertation.

E.1 A simplified model

As with many systems, the easiest way to understand the fundamentals of Landau-Zener tunneling is to consider a simple example. The simplest system that displays many of the most important points about Landau-Zener tunneling is a spin-half particle (an electron for example) suspended in two crossed magnetic fields, one of which is varying with time. At first, we will consider only one field, which will be held constant, and add in the second (also constant) field as a complicating factor. Then, we will consider what happens when the first field varies with time.

E.1.1 The unpertubed (uncoupled) system: Electron in a constant magnetic field

Consider an electron suspended in a magnetic field $B_{\parallel}$ that points in a direction we define as the z-axis. (The $\parallel$ symbol means *pointing along the z-axis.*) We first assume that the total spin vector of the electron points in the $+\hat{\mathbf{z}}$ direction. We define this spin orientation as spin-*up* and denote the spin-up eigenstates of this unperturbed system with the spinor

$\chi_\uparrow^\dagger = (1, 0)$. If we define the zero-point energy as that energy when $B_\parallel = 0$, then the total unperturbed energy of the spin-up electron is given by

$$E_\uparrow = \mu B_\parallel, \tag{E.1}$$

where μ, the magnitude of the magnetic moment of the electron, is a positive constant.[188] Since this energy is proportional to the magnetic field strength, then if we sample the energy at different values of $B_\parallel$ we will trace a straight line of positive slope, as shown in Fig. E.1.[189]

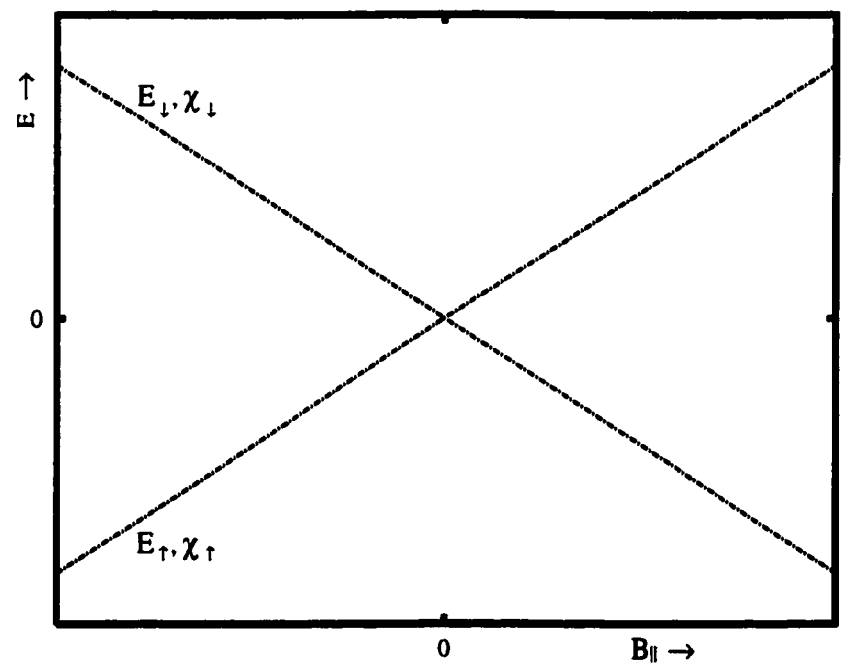

Figure E.1: Energy levels $E_\uparrow$ and $E_\downarrow$ relating to Eqs. (E.1) and (E.2).

Now consider the same system, but with the spin vector pointing in the $-\hat{\mathbf{z}}$ direction (spin-*down*). The spin-down unperturbed eigenstate is described by the spinor $\chi_\downarrow^\dagger = (0, 1)$. In this case,

$$E_\downarrow = -\mu B_\parallel, \tag{E.2}$$

and the energy similarly traces out a straight line when sampled at different values of $B_\parallel$, but with a negative slope. In Fig. E.1 we show both energy levels together. The two levels cross at a physical (real) value of $B_\parallel$ which we call a *level* crossing, which occurs here at $B_\parallel = 0$.

The Hamiltonian for this system is given by

$$\mathcal{H}_0 = \mu \mathbf{S} \cdot \mathbf{B} = \mu B_\parallel \hat{S}_z = \mu \begin{pmatrix} B_\parallel & 0 \\ 0 & -B_\parallel \end{pmatrix}, \tag{E.3}$$

where $\mathbf{S} = \hat{S}_z \hat{\mathbf{z}}$ is the total spin-vector of the electron, so that the time-independent Schrödinger equation is

$$\mu \begin{pmatrix} B_\parallel & 0 \\ 0 & -B_\parallel \end{pmatrix} \chi_{\uparrow\downarrow} = E_{\uparrow\downarrow} \chi_{\uparrow\downarrow}. \tag{E.4}$$

Note from Eq. (E.4) that the two unperturbed eigenstates $\chi_\uparrow$ and $\chi_\downarrow$ are not coupled, since

$$\langle \chi_\downarrow \,|\, \mathcal{H}_0 \,|\, \chi_\uparrow \rangle = 0, \tag{E.5}$$

which is why the two energy levels cross without affecting each other.

At this point, the level crossing between the two energy levels is not very interesting. However, let us consider what happens if we include a second magnetic field to the system.

E.1.2 The perturbed (coupled) system: electron in two crossed and constant magnetic fields

Suppose we directed a second constant magnetic field $B_\perp$ perpendicular to $B_\parallel$. Now the Hamiltonian is

$$\mathcal{H} = \mu \mathbf{S} \cdot \mathbf{B} = \mu B_\parallel \hat{S}_z + \mu B_\perp \hat{S}_x = \mu \begin{pmatrix} B_\parallel & B_\perp \\ B_\perp & -B_\parallel \end{pmatrix} \tag{E.6}$$

and therefore the time-independent Schroedinger equation is

$$\mu \begin{pmatrix} B_\parallel & B_\perp \\ B_\perp & -B_\parallel \end{pmatrix} \Psi_\pm = E_\pm \Psi_\pm. \tag{E.7}$$

(We could have chosen $\hat{S}_y$ instead of $\hat{S}_x$. Neither the $x-$ or $y-$axis is preferred over the

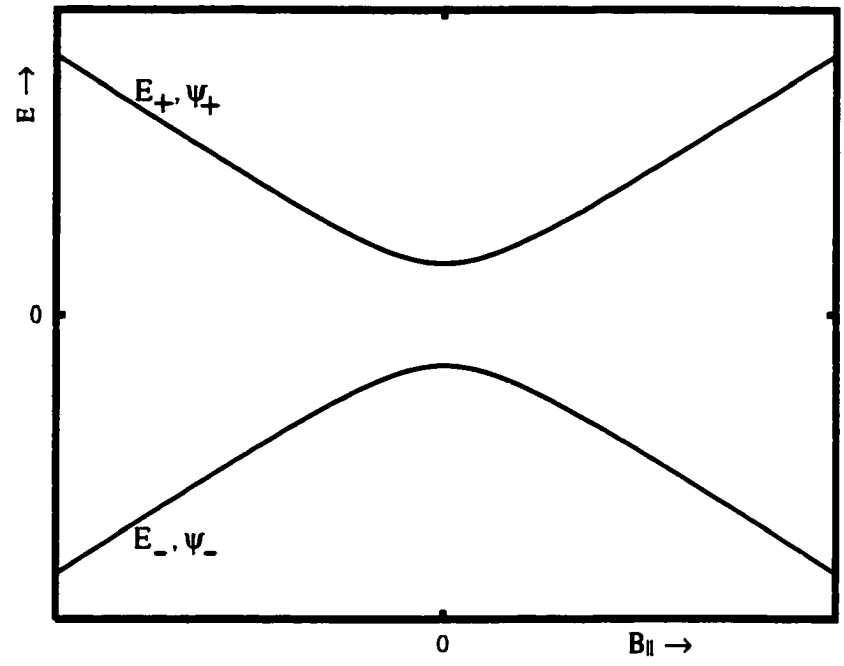

Figure E.2: The coupled energy levels E_+ and E_- relating to Eq. (E.8). Note that the lower curve is associated with Ψ_- and the upper curve Ψ_+ for all values of $B_\parallel$.

other due to the symmetry of the unperturbed system.) Since the perturbed Hamiltonian $\mathcal{H}$ is not diagonal, then the eigenstates $\Psi_\pm$ of $\mathcal{H}$ are not the same as the eigenstates $\chi_{\uparrow\downarrow}$ of $\mathcal{H}_0$. However, we can find the eigenstates in Eq. (E.7) by diagonalizing $\mathcal{H}$, producing the following values for the physical parameters:

$$E_\pm = \pm\mu\sqrt{B_\parallel^2 + B_\perp^2}, \tag{E.8}$$

$$\Psi_+ = N(B_\parallel, B_\perp)\begin{pmatrix} \frac{1}{B_\perp}\left[B_\parallel + \sqrt{B_\parallel^2 + B_\perp^2}\right] \\ 1 \end{pmatrix} \tag{E.9}$$

$$\Psi_- = N(B_\parallel, B_\perp)\begin{pmatrix} 1 \\ -\frac{1}{B_\perp}\left[B_\parallel + \sqrt{B_\parallel^2 - B_\perp^2}\right] \end{pmatrix}, \tag{E.10}$$

where $N(B_\parallel, B_\perp)$ is the normalization factor, which ensures that the probability of finding the electron with either spin up or down is one. Note that Ψ_+ and Ψ_- are orthogonal.

If we sample the energy E_+ in Eq. (E.8) at different values of $B_\parallel$ (remember $B_\perp$ is a constant) then we will trace out the upper curve shown in Fig. E.2. Not only is this curve not a straight line, but at $B = 0$ the energy, which was initially decreasing, begins to increase. The curve for E_- has just the opposite effect, as shown by the upper curve in the same plot. Not only do the two energy levels *not* cross[190] they appear to repel each other. This phenomenon is known as an *avoided crossing*.

The behavior just discussed is entirely consistent with the Wigner-von Neumann no-crossing theorem,[184] which states that two energy levels cannot cross if their respective states are (1) coupled by the Hamiltonian of the system *and* (2) of the same parity. (Actually, two levels can cross even if they satisfy both criteria. As shown in Sec. E.5, however, such a crossing would be very unlikely.) We show in Sec. E.5 that the $\chi_{\uparrow\downarrow}$ and $\Psi_\pm$ states all have the same parity. However, in the perturbed system the two eigenstates are coupled, unlike the unperturbed system. Therefore when the perpendicular field $B_\perp$ is applied to the system, the resulting Hamiltonian couples the two eigenstates and so avoided crossings replace level crossings.

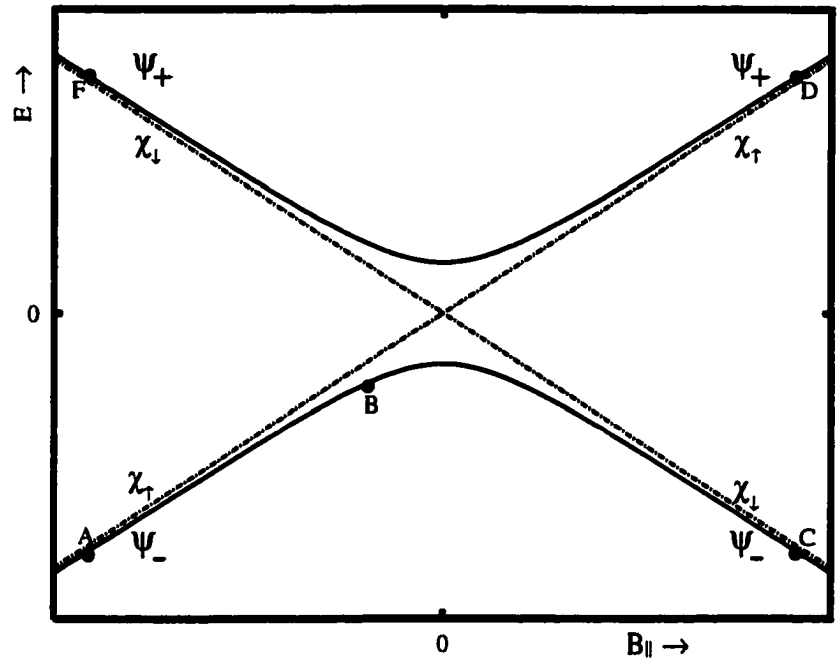

Figure E.3: A view of the energy levels in Figs. E.1 and E.2 superimposed. The points A, B, C, D, and F are referred to in text.

We can get a better understanding of what is happening if we superimpose the uncoupled energy levels in Fig. E.1 with the coupled energy levels in Fig. E.2, as shown in Fig. E.3. We can see that for sufficiently large $|B_\parallel|$ both the perturbed and unperturbed energy levels are nearly the same value. In fact, if we examine the Hamiltonian in Eq. (E.7) it is not hard to see why: the Hamiltonian becomes nearly diagonal when $|B_\parallel| \gg |B_\perp|$. Since in this limit the coupled Hamiltonian becomes nearly the same as the uncoupled Hamiltonian, then we can also say that in this limit the eigenstates $\Psi_\pm$ in Eqs. (E.9) and (E.10) approach the appropriate unperturbed eigenstates $\chi_{\uparrow\downarrow}$.

In summary, $\mathcal{H} \rightarrow \mathcal{H}_0$ as $B_\parallel \rightarrow \pm\infty$. As $B_\parallel \rightarrow +\infty$:

$$\Psi_+ \longrightarrow \chi_\uparrow, \quad \Psi_- \longrightarrow \chi_\downarrow, \quad E_+ \longrightarrow E_\uparrow, \quad E_- \longrightarrow E_\downarrow. \tag{E.11}$$

Similarly, as $B_\parallel \to -\infty$:

$$\Psi_+ \longrightarrow \chi_\downarrow, \quad \Psi_- \longrightarrow \chi_\uparrow, \quad E_+ \longrightarrow E_\downarrow, \quad E_- \longrightarrow E_\uparrow. \tag{E.12}$$

If we keep in mind that the perturbed eigenstates $\Psi_\pm$ can be expanded in terms of the unperturbed eigenstates $\chi_{\uparrow\downarrow}$, for example

$$\Psi_- = c_\uparrow \chi_\uparrow + c_\downarrow \chi_\downarrow, \tag{E.13}$$

where the coefficients $c_{\uparrow\downarrow}$ are functions of $B_\parallel$, then we can even describe what this means physically by thinking of the statistical nature of the problem in terms of ensembles. If we start the system out at pt. A in Fig. E.3 the *character* of the system, which we define as being either spin-up or spin-down, will be nearly all spin-up, with a little spin-down mixed in. In terms of ensembles, we say that when $B_\parallel$ points in the negative z-direction and has enormous strength in comparison to $B_\perp$, we can prepare the system such that nearly all of the systems in the ensemble will be expected to be spin-up, with the remaining few spin-down. If we take this system but fix the magnetic field at a less negative value, (for example, pt. B in Fig. E.3) we will find more spin-down states included in the ensemble. When we reach the avoided crossing center, exactly half the states will be spin-up and the other half spin-down. Finally, if we fix $B_\parallel$ at pt. C most of the states will be spin-down. *So we can say that the character of the system (spin-up or spin-down) switches across the avoided crossing center.*

The energy level curves corresponding to $E_\pm$ are called the *adiabatic* curves of the system, and the $\Psi_\pm$ are the adiabatic states. Conversely, the unperturbed energy levels $E_{\uparrow\downarrow}$ are called the *diabatic* curves of the system, and the $\chi_{\uparrow\downarrow}$ states the diabatic states.

Up to this point, we have only considered constant magnetic fields, with the system evaluated at different values of $B_\parallel$. Now we will see what happens when $B_\parallel$ varies with time.

E.1.3 Time evolution of the perturbed and unperturbed systems

Consider the magnetic field $B_{\|}$ to be a function of time. If a system described by the perturbed Hamiltonian $\mathcal{H}(t)$ is initially started at t_o in the (say) perturbed eigenstate Ψ_+, then at some later time t the system will be in the state

$$\Phi(t) = U(t, t_o)\Psi_+(t_o), \tag{E.14}$$

where $U(t, t_o)$ is the time-evolution operator of the system. Using arguments detailed in Sec. E.6, we can show that when the magnetic field is changed as a function of time, the state $\Phi(t)$ has a nonzero probability of being the Ψ_- state at time t, rather than the initial state Ψ_+. In other words, the overlap

$$\langle \Psi_-(t_o)|\Psi_+(t)\rangle = \langle \Psi_-(t_o)|U(t, t_o)|\Psi_-(t_o)\rangle, \tag{E.15}$$

is in general nonzero as long as the system evolves with time. (As also shown in Sec. E.6, this overlap vanishes as the evolution of the system becomes increasingly adiabatic — the time it takes to go from t_o to t becomes infinite.) Since this possibility applies to infinitesimally small changes in time as well, then changing $B_{\|}$ with time causes continual mixing between the two states, and therefore there is a chance that in this situation the state will transform from what was initially the Ψ_- state to the Ψ_+ state, and even back again.

The question now becomes "If we sweep the magnetic field $B_{\|}$ at a particular rate, what is the *probability* that the system will be found in the same state long after the avoided crossing has been traversed?" We will see that not only does the answer depend on the relative magnitudes of the diagonal and off-diagonal elements of the Hamiltonian, but it will also depend on how fast we sweep the magnetic field. Even later, we will find even more considerations to include when we further generalize the problem.

E.1.4 The Landau-Zener probability

The probability for the system to remain in the same unperturbed (diabatic) state as the system evolves past an avoided crossing was first derived by Zener.[192] The treatment by Wannier is similar, and it is this treatment that we will consider in the following.[193] Both assume a linear relationship between the variable parameter and time.

We can always express the initial state of the system as a linear combination of spin-up and spin-down unperturbed eigenstates,

$$\Psi(t) = c_\uparrow(t)\chi_\uparrow + c_\downarrow(t)\chi_\downarrow. \tag{E.16}$$

If we are sufficiently far from the avoided crossing we can approximate the initial state of the system as being purely spin-up or spin-down, as evidenced by the relations in (E.11) and (E.12). Let us assume that at $t \to +\infty$ the system is in the spin-up state $\chi_\uparrow$, that is $|c_\uparrow(+\infty)| = 1$ and $|c_\downarrow(+\infty)| = 0$.[194]

The probability that the system will be in the $\chi_\uparrow$ state at $t \to -\infty$ (pt. A in Fig. E.3) is given by $|c_+(-\infty)|^2$. Assuming that $B_\parallel$ changes linearly with time, $B_\parallel = \lambda t$, the Hamiltonian becomes

$$\mathcal{H}(t) = \mu\begin{pmatrix} \lambda t & B_\perp \\ B_\perp & -\lambda t \end{pmatrix}. \tag{E.17}$$

To find $|c_\uparrow(-\infty)|^2$ we must now consider the time-dependent Schrödinger equation,

$$\begin{pmatrix} \lambda t & B_\perp \\ B_\perp & -\lambda t \end{pmatrix}\begin{pmatrix} c_\uparrow \\ c_\downarrow \end{pmatrix} = i\hbar\frac{d}{dt}\begin{pmatrix} c_\uparrow \\ c_\downarrow \end{pmatrix}, \tag{E.18}$$

where we have set $\mu = 1$. (The magnetic fields will be measured in energy units.) Writing out the equations resulting from the above we find

$$\lambda t c_\uparrow + B_\perp c_\downarrow = i\hbar\frac{d}{dt}c_\uparrow, \qquad -\lambda t c_\downarrow + B_\perp c_\uparrow = i\hbar\frac{d}{dt}c_\downarrow, \tag{E.19}$$

Solving for $c_\downarrow$ in the first equation and substituting it into the other we obtain a second-order differential equation,

$$\frac{d^2}{dt^2}c_\uparrow(t) + \left(\frac{\lambda^2 t^2}{4\hbar^2} + \frac{B_\perp^2}{4\hbar^2} + \frac{i\lambda}{2\hbar}\right) c_\uparrow(t) = 0, \tag{E.20}$$

a special type of confluent hypergeometric equation called a parabolic cylinder equation. The exact form of the two solutions for $c_\uparrow$, given in terms of Whittaker functions[195], are of little concern to us; instead we are more interested in their asymptotic forms. Only one of the (asymptotic) solutions,

$$c_\uparrow(t) \sim e^{-\frac{i}{4\hbar}\left[\lambda t^2 - (B_\perp^2/\lambda)\ln t\right]}, \qquad t \to \infty, \tag{E.21}$$

obeys the boundary condition that at $t \to +\infty$ the system is in the state $\chi_\uparrow$. This asymptotic solution is also valid for $t \to -\infty$ provided we make the substitution[193]

$$-t \to e^{-i\pi}|t|. \tag{E.22}$$

Upon doing so, our asymptotic relation becomes

$$c_\uparrow(t) \sim e^{-\frac{1}{4\hbar}\left[i\lambda t^2 - i(B_\perp^2/\lambda)\ln|t| + \frac{\pi B_\perp^2}{\lambda}\right]}, \qquad t \to -\infty. \tag{E.23}$$

Therefore, the Landau-Zener transition probability is

$$P(\uparrow) = |c_\uparrow(-\infty)|^2 = \exp\left[-\frac{\pi B_\perp^2}{4\lambda\hbar}\right] \tag{E.24}$$

As we can see, the probability of remaining in the same state increases as the coupling field $B_\perp$ vanishes . This is expected since the Hamiltonian becomes nearly diagonal for sufficiently small $B_\perp$, and so the system behaves almost like the unperturbed system. Likewise, the probability of remaining in the same state increases as λ (the sweep rate of the magnetic field) increases. This is the *diabatic* (or *sudden*) limit, and results from having the magnetic field change so rapidly that the character of the state, defined by the orientation

of its spin vector in relation to the z-axis, never has a chance to switch. (Wannier called this the "inertial path."[193])

As $\lambda \to 0$ the probability $P(\uparrow)$ vanishes and the system will be found in the other state, $\chi_\downarrow$, at $B_\parallel \to -\infty$. In other words, the system will follow the upper curve in Fig. E.3 to pt. F, switching character across the avoided crossing. This is the *adiabatic* limit because it corresponds to such a slow evolution of the system that time can be treated like an ordinary parameter in the time-*independent* Schrödinger equation. In other words, in this limit we are not solving a time-dependent problem but rather an infinite number of time-independent problems, each evaluated at a different value of $B_\parallel$.

Note also that $P(\uparrow) \to 0$ as $\hbar \to 0$, the classical limit; barrier penetration is a purely quantum-mechanical effect.

Notice that in order for the system to be found in the same spin-state as $B_\parallel$ is swept from $-\infty$ to $+\infty$ (or in the other direction) the nonphysical (classically forbidden) region between the two coupled energy levels must be traversed. This tunneling between levels is the basis behind the term Landau-Zener *tunneling*.

There is a physical description of our results that is useful. The electron in our system is being acted upon by two perpendicular magnetic fields, one which points along the $\hat{\mathbf{z}}$-axis, $B_\parallel$, and another perpendicular to the $\hat{\mathbf{z}}$-axis, $B_\perp$. If $B_\parallel$ is sufficiently large, then the effects of $B_\perp$ are minimized and the electron (essentially) reacts as if it is only acted upon by $B_\parallel$. In this situation, we can (in effect) start the electron in a spin-up state, and assume that the net magnetic field points in the $+z$-direction. In other words, we are starting the system near pt. D in Fig. E.3. However, if $B_\parallel$ is weakened at a finite rate, the effects of $B_\perp$ become more prominent and the electron's spin vector begins to precess about the total magnetic field $\mathbf{B}_\perp + \mathbf{B}_\parallel$. In this situation, there is an increased probability that the electron will be found in the spin-down state. Once $B_\parallel$ has changed direction it begins to grow in magnitude, and the state of the system becomes increasingly spin-down. The slower the field is weakened, the more likely the system will be able to evolve accordingly, and

therefore the more more likely the system will be found in the spin-down state once the avoided crossing has been traversed. In this case the system is approaching the adiabatic limit, following the lower curve in Fig. E.3.

However, if the magnetic field direction is changed rapidly, the spin-vector will not have a chance to change direction accordingly, and electron will be "caught" in the state where its spin vector points in the positive z-direction (spin-up). This corresponds to the fact that as $\lambda \to \infty$ the system remains in the same state — the diabatic limit. This is why Wannier called this evolution of the system the "inertial path."

The Landau-Zener transition probability refers only to initial and final conditions at $\pm\infty$. However, if we start the system in the $\chi_\uparrow$ state at a very negative value of t_o, we can calculate the probability $|c(t)|^2$ of remaining in the same state *as a function of time* by numerically solving the time-dependent Schrödinger equation in Eq. (E.18). We can see in Fig. E.4 that in certain situations the probability to remain in the original state can oscillate as $B_\parallel$ is changed. As seen in the figure, the probability of remaining in the same unperturbed state as the avoided crossing is traversed vanishes as $\gamma \equiv \hbar\lambda/B_\perp^2$ becomes small, corresponding to the large $B_\perp$ and small λ and $\hbar$ limits, as we previously discussed.

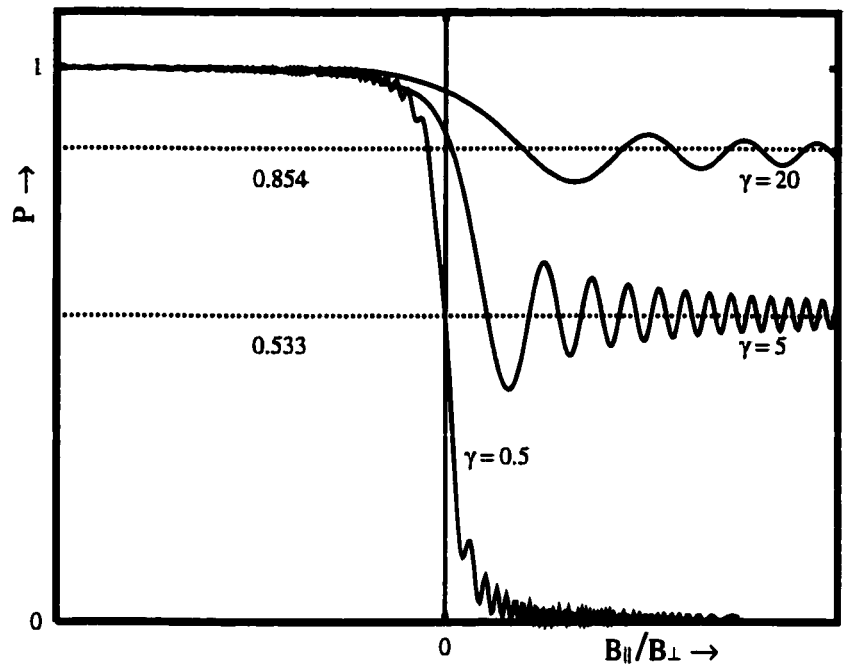

Figure E.4: The probability to remain in the original diabatic state as the magnetic field $B_\parallel$ is swept linearly with time, where $\gamma \equiv \hbar\lambda/B_\perp^2$. Note that the horizontal axis is expressed in terms of the ratio between $B_\parallel$ and $B_\perp$, where $B_\perp$ is fixed according to the value of γ. The resulting data represents a numerical solution of Eq. (E.18) with the initial condition that $c_\uparrow(-\infty) = 1$. A very similar plot is shown in Mullen, *et al.*[191]

E.2 A More general model

Before we examine a more general model we should first discuss the effects each term in the Hamiltonian matrix has on the physical properties of the system. First, if a constant term C is added to both diagonal elements,

$$\mu\begin{pmatrix} B_\parallel & B_\perp \\ B_\perp & -B_\parallel \end{pmatrix} \longrightarrow \mu\begin{pmatrix} B_\parallel + C & B_\perp \\ B_\perp & -B_\parallel + C \end{pmatrix}, \tag{E.25}$$

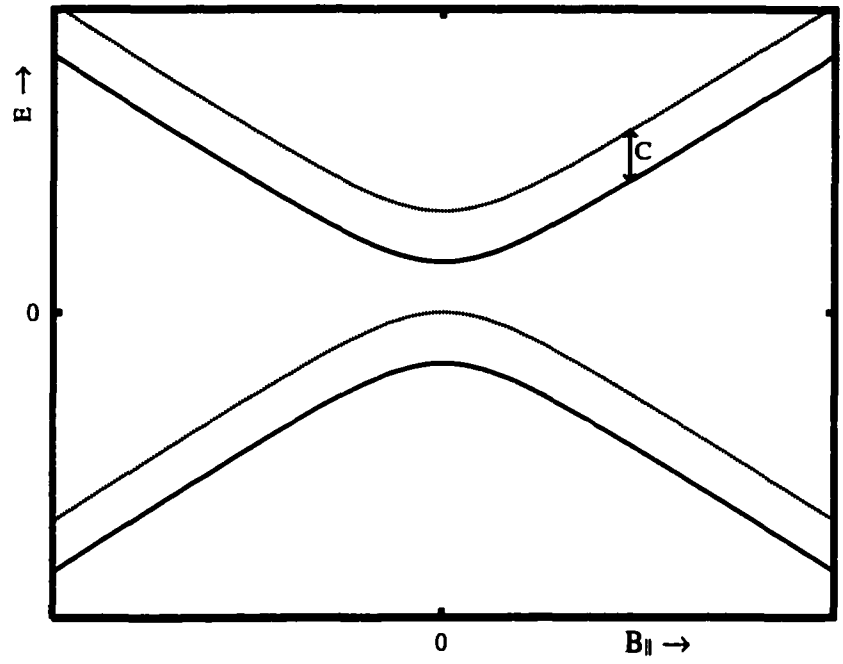

Figure E.5: Effects on the energy levels due to a shift in the diagonal elements of the Hamiltonian, shown in Eqs. (E.25) and (E.26).

the effect will be an overall shifting up or down by a value C of the energy levels, as shown in Fig. E.5. The transition probabilities we are concerned with depend only on energy level *separation*, therefore we can ignore these terms if they appear. Note that adding a term to both diagonal elements is the same as including a time-dependent phase factor to both eigenstates,

$$\Psi_{\pm} \longrightarrow e^{iCt}\Psi_{\pm} \quad \Longleftrightarrow \quad \mathcal{H} \longrightarrow \mathcal{H} + C\mathbf{1}, \tag{E.26}$$

where $\mathbf{1}$ is the identity matrix. We can take advantage of this freedom to include or ignore such a phase factor whenever it is convenient.

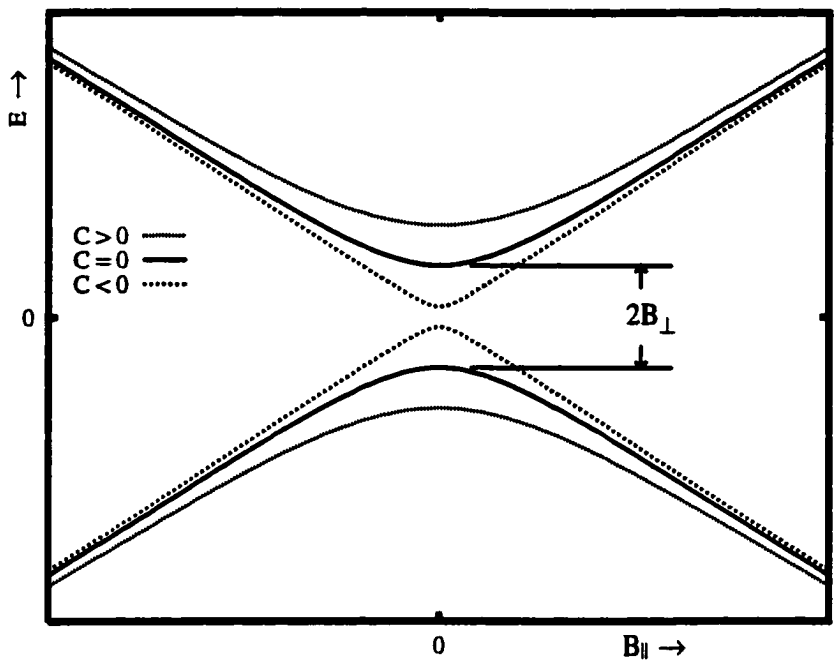

Figure E.6: Effects on the energy levels due to a shift in the off-diagonal elements of the Hamiltonian, shown in Eq. (E.27).

If a term C is added to the off-diagonal elements,

$$\mu\begin{pmatrix} B_\parallel & B_\perp \\ B_\perp & -B_\parallel \end{pmatrix} \longrightarrow \mu\begin{pmatrix} B_\parallel & B_\perp + C \\ B_\perp + C & -B_\parallel \end{pmatrix}, \tag{E.27}$$

this will either sharpen or flatten the avoided crossing without shifting the center of the crossing, as shown in Fig. E.6. We can even quantify this effect by nothing that the separation between energy levels at $B_\parallel = 0$, at least in this simple example, is $2B_\perp$. (This relation is roughly true for most Landau-Zener problems. In fact, it is one of the assumptions that we will use later to derive the Landau-Zener probability.

Finally, if each diagonal element is changed by the same constant factor

$$\mu\begin{pmatrix} B_\parallel & B_\perp \\ B_\perp & -B_\parallel \end{pmatrix} \longrightarrow \mu\begin{pmatrix} B_\parallel + C & B_\perp \\ B_\perp & -(B_\parallel + C) \end{pmatrix}, \tag{E.28}$$

the only effect will be a shifting of the avoided crossing with respect to $B_{\|}$, as shown in Fig. E.7. In this case, the transition probability will be unchanged, as long as the values of $B_{\|}$ on the horizontal axis are adjusted accordingly.

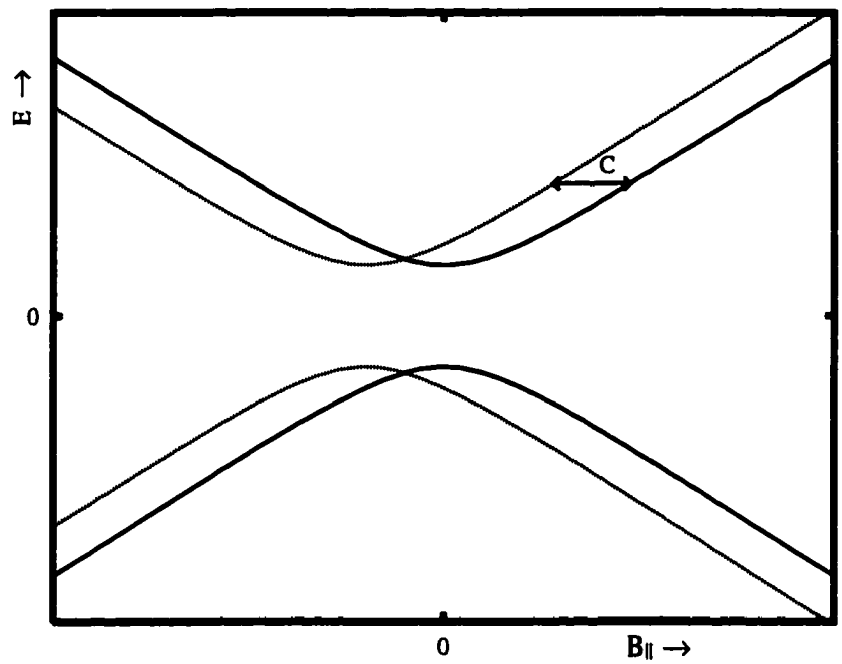

Figure E.7: Effects on the energy levels due to a shift in the diagonal elements of the Hamiltonian, shown in Eq. (E.28).

With this discussion in mind we can now consider a more genral problem and how the generalizations effect the results for the Landau-Zener transition probability. A typical example of a more general problem[196] is where an unperturbed system is described by a Hamiltonian H_0 such that, at any particular value of the variable parameter s,

$$H_0(s)\phi_1(s) = \widetilde{E}_1(s)\phi_1(s), \qquad H_0(s)\phi_2(s) = \widetilde{E}_2(s)\phi_2(s). \tag{E.29}$$

In the simple model, the uncoupled spin eigenstates $\chi_{\uparrow\downarrow}$ would correspond to $\phi_{1,2}$ and $B_{\|}$ would correspond to the variable parameter s. Another definition of s that commonly appears is the distance between two atoms or molecules in a scattering process. Note that here

the unperturbed states are functions of s, whereas in the simple model the unperturbed spin-states were constant for all $B_{\parallel}$. The two eigenstates ϕ_i, where i refers to the two degrees of freedom, are linearly independent since both are solutions of the same differential equation. Therefore we would expect *level* crossings between the two corresponding energy levels. However, unlike the simple model we cannot necessarily expect the unperturbed energy levels to be linear functions of the variable parameter.

Now suppose the system is perturbed by another Hamiltonian $\delta H(s)$ which couples the two degrees of freedom (in a manner similar to the coupling created by $B_{\perp}$, except here the coupling term is a function of s). Let us define the total Hamiltonian (which Lubin *et al.*[196] call the *adiabatic* Hamiltonian) as

$$H_a(s) \equiv H_0(s) + \delta H(s) \tag{E.30}$$

and the *corrected* energies as

$$\varepsilon_1 \equiv \langle \phi_1 \,|\, H_a \,|\, \phi_1 \rangle, \quad \varepsilon_2 \equiv \langle \phi_2 \,|\, H_a \,|\, \phi_2 \rangle. \tag{E.31}$$

The relationship between the corrected energies ε_i and the unperturbed eigenenergies $\widetilde{E}_i$ is

$$\varepsilon_i = \widetilde{E}_i + \langle \phi_i \,|\, \delta H \,|\, \phi_i \rangle, \tag{E.32}$$

so the ε_i are simply first-order corrections to the unperturbed energies $\widetilde{E}_i$. The ε_i are *not* the adiabatic energies of the system, which result from a diagonalization of the total Hamiltonian, so we expect some mixing to enter the time-independent Schroedinger equations corresponding to ϕ_1 and ϕ_2. We can therefore, for ϕ_1, assume an equation of the form

$$H_a(s)\phi_1(s) = \varepsilon_1(s)\phi_1(s) + \varepsilon_{12}(s)\phi_2(s), \tag{E.33}$$

where $\varepsilon_{12}(s)$ represents the amount of mixing contributed by the state $\phi_2(s)$. It is straightforward to show that the complementary equation is

$$H_a(s)\phi_2(s) = \varepsilon_2(s)\phi_2(s) + \varepsilon_{12}^*(s)\phi_1(s). \tag{E.34}$$

By projecting ϕ_2 onto Eq. (E.33) we find that

$$\varepsilon_{12}(s) = \langle \phi_2(s) \,|\, H_a \,|\, \phi_1(s) \rangle = \langle \phi_2(s) \,|\, \delta H(s) \,|\, \phi_1(s) \rangle. \tag{E.35}$$

The actual eigenstate of $\mathcal{H}_a$ will be a linear combination of ϕ_1 and ϕ_2,

$$\Psi(s) = C_1(s)\phi_1(s) + C_2(s)\phi_2(s), \tag{E.36}$$

so the time-dependent Schrödinger equation, $H_a\Psi = i\hbar\,\partial\Psi/\partial t$, becomes

$$H_a(s)\Big(C_1(s)\phi_1(s) + C_2(s)\phi_2(s)\Big) = i\hbar\frac{\partial}{\partial t}\Big(C_1(s)\phi_1(s) + C_2(s)\phi_2(s)\Big), \tag{E.37}$$

such that

$$C_1(s)\Big(\varepsilon_1(s)\phi_1(s) + \varepsilon_{12}(s)\phi_2(s)\Big) + C_2(s)\Big(\varepsilon_2(s)\phi_2(s) + \varepsilon_{12}^*(s)\phi_1(s)\Big) \tag{E.38}$$

$$= i\hbar\dot{s}\Big(C_1'(s)\phi_1(s) + C_1(s)\phi_1'(s)\Big) + i\hbar\dot{s}\Big(C_2'(s)\phi_2(s) + C_2(s)\phi_2'(s)\Big), \tag{E.39}$$

where primes indicate differentiation with respect to s. By projecting both $\phi_1(s)$ and $\phi_2(s)$ onto the above equation we obtain two coupled differential equations,

$$i\hbar\dot{s}\Big(C_1'(s) + \langle \phi_1(s) \,|\, \phi_1'(s) \rangle C_1(s) + \langle \phi_1(s) \,|\, \phi_2'(s) \rangle C_2(s)\Big) = \varepsilon_1(s)C_1(s) + \varepsilon_{12}^*(s)C_2(s), \tag{E.40}$$

$$i\hbar\dot{s}\Big(C_2'(s) + \langle \phi_2(s) \,|\, \phi_2'(s) \rangle C_2(s) + \langle \phi_2(s) \,|\, \phi_1'(s) \rangle C_1(s)\Big) = \varepsilon_2(s)C_2(s) + \varepsilon_{12}(s)C_1(s). \tag{E.41}$$

In matrix form

$$i\hbar\dot{s}\frac{d}{ds}\begin{pmatrix} C_1 \\ C_2 \end{pmatrix} = \begin{pmatrix} \varepsilon_1 - i\hbar\dot{s}\langle\phi_1 \,|\, \phi_1'\rangle & \varepsilon_{12}^* - i\hbar\dot{s}\langle\phi_1 \,|\, \phi_2'\rangle \\ \varepsilon_{12} - i\hbar\dot{s}\langle\phi_1 \,|\, \phi_2'\rangle & \varepsilon_2 - i\hbar\dot{s}\langle\phi_2 \,|\, \phi_2'\rangle \end{pmatrix}\begin{pmatrix} C_1 \\ C_2 \end{pmatrix}. \tag{E.42}$$

The $\langle\phi_1 \,|\phi_1'\rangle$ and $\langle\phi_2 \,|\phi_2'\rangle$ terms in the Hamiltonian are purely imaginary, since

$$\langle\phi_1 \,|\phi_1'\rangle = -\langle\phi_1' \,|\phi_1\rangle = -\langle\phi_1 \,|\phi_1'\rangle^*. \tag{E.43}$$

Therefore, we can set (say) $\langle\phi_1 \,|\phi_1'\rangle = i\alpha(s)$, where $\alpha(s)$ is real-valued. As demonstrated in Eq. (E.25), the eigenstates are only defined up to an arbitrary s-dependent phase, which we can demonstrate by inserting the mapping $\phi_i(s) \rightarrow \phi_i(s)e^{i\theta(s)}$ into the Schroedinger equation above and ignoring the constant added to the diagonal terms.[197] Therefore $\alpha(s)$ is arbitrary as well, so we choose $\alpha(s)$ in such a way that

$$\varepsilon_1(s) = i\hbar\dot{s}\langle\phi_2 \,|\, \phi_2'\rangle. \tag{E.44}$$

(This is also discussed in Schiff.[198]) Using the same reasoning, we can set $\varepsilon_2(s) = i\hbar\dot{s}\langle\phi_1 \,|\, \phi_1'\rangle$ so that the matrix equation becomes

$$i\hbar\dot{s}\frac{d}{ds}\begin{pmatrix} C_1 \\ C_2 \end{pmatrix} = \begin{pmatrix} \varepsilon_1 - \varepsilon_2 & \varepsilon_{12}^* - i\hbar\dot{s}\langle\phi_1 \,|\, \phi_2'\rangle \\ \varepsilon_{12} - i\hbar\dot{s}\langle\phi_1 \,|\, \phi_2'\rangle & -\left(\varepsilon_1 - \varepsilon_2\right) \end{pmatrix}\begin{pmatrix} C_1 \\ C_2 \end{pmatrix}. \tag{E.45}$$

At this point no approximations have been made as long as the system is truly two-level. The above relation is a general formulation of the Landau-Zener problem involving two interacting energy levels, as long as only one parameter is being varied. Let us now summarize how the two systems — the general model and the simple model introduced earlier — differ:

1. The unperturbed energy levels of interest are not necessarily the eigenenergies of the unperturbed Hamiltonian, but rather the first-order *corrections* to those eigenenergies. In the simple model, there was no difference between the two energies since

$$\varepsilon_\uparrow \equiv E_\uparrow + \mu B_\perp \langle \phi_\uparrow \,|\, \hat{S}_x \,|\, \phi_\uparrow \rangle = E_\uparrow. \tag{E.46}$$

In fact, the unperturbed energy levels do not necessarily cross for a physical value of the variable parameter (see Mullen *et al.*[202] for an example), but we will assume they do.

2. The corrected energies ε_i in the general model are not necessarily linear functions of the variable parameter.

3. The uncoupled eigenstates ϕ_i are in general functions of the variable parameter, unlike the spin-states in the simple model.

4. An extra term $i\hbar\dot{s}\langle\phi_1 \,|\, \phi_2'\rangle$ is subtracted from the off-diagonal elements of the Hamiltonian in the general model. This term didn't appear in the simple model since the spin eigenstates were not functions of $B_\parallel$. From our previous discussion, and from Fig. E.6, we expect that this added term will narrow or widen the barrier between the two energy levels, therefore affecting the Zener probability amplitude.

The Hamiltonian used by Wannier and Zener, from which the Zener probability was derived, is of the form

$$\begin{pmatrix} H_{11} & H_{12} \\ H_{12} & -H_{11} \end{pmatrix}, \tag{E.47}$$

where H_{11} was a linear function of time and H_{12} was a constant. Such a form is a naturally developed in the earlier problem of a half-integer spin placed in a magnetic field, mainly because in the simple model the unperturbed spin-states were field-independent and the coupling H_{12} constant. At this point, neither assumption has been used. Therefore, to put the Hamiltonian in Eq. (E.45) in this form, some approximations will have to be employed:

1. The rate of change of the variable parameter is nearly constant. In other words, $\dot{s}$ can be replaced by λ, a constant. (In the simple model λ corresponded to $dB_\parallel/dt$.) If s is an

externally controlled parameter, such as $B_{\parallel}$ in the simple model, then we can specify this requirement — no assumption is needed.

2. We assume that a region s_{Zen} centered about the point where $\varepsilon_1 = \varepsilon_2$ (which we define to be $s = 0$) exists such that $\varepsilon_1 - \varepsilon_2$ is large in comparison to $|\varepsilon_c|$ outside this region. Even if the unperturbed energy levels $\varepsilon_i(s)$ have shallow approaches, we assume that we can always enlarge the region of interest to encompass s_{Zen}. This condition could be violated if there are multiple avoided crossings placed close to each other, or if the avoided crossing center is displaced significantly from $s = 0$. Mullen and colleagues[191] estimated the sizes of s_{Zen} in both the diabatic and adiabatic limits. We will discuss their results shortly.

Therefore, the Hamiltonian in Eq. (E.45) is essentially diagonal for all s outside the s_{Zen} region. Since uncoupled Hamiltonians cannot induce transitions between adiabatic states, we can assume that all of the transitions occur within s_{Zen}, and therefore only concern ourselves with the Hamiltonian describing the system within this region.

3. Other than $\varepsilon_1 - \varepsilon_2$, all parameters have slow s-dependence. We can therefore ignore their derivatives with respect to s, and also approximate each parameter by its first nonvanishing term in their expansion about $s = 0$. For $\varepsilon_1 - \varepsilon_2$ we assume that its s-dependence is at most not much greater than linear. Therefore, we can ignore any second-order (or higher) derivatives of this term.

From the second assumption both $\varepsilon_1 - \varepsilon_2$ and the coupling term $\varepsilon_C \equiv \varepsilon_{12} - i\hbar\alpha\langle\phi_1 \mid \phi_2'\rangle$ in Eq. (E.45) can be replaced by the first nonvanishing term in its expansion about $s = 0$. Since we assumed that ε_1 and ε_2 cross at $s = 0$ then

$$\varepsilon_1 - \varepsilon_2 \approx [\varepsilon_1'(0) - \varepsilon_2'(0)]\, s = \eta s, \tag{E.48}$$

where $\eta \equiv \varepsilon_1'(0) - \varepsilon_2'(0)$. Furthermore, as long as we can ignore the $\langle \phi_1 \mid \phi_2' \rangle$ term then we can approximate ε_c as $\varepsilon_{12}(0)$. Using the above assumptions, our Hamiltonian is now of the form

$$i\hbar\lambda \frac{d}{ds} \begin{pmatrix} C_1 \\ C_2 \end{pmatrix} = \begin{pmatrix} \eta s & \varepsilon_{12}^*(0) \\ \varepsilon_{12}(0) & -\eta s \end{pmatrix} \begin{pmatrix} C_1 \\ C_2 \end{pmatrix}. \tag{E.49}$$

This is the matrix equation solved in the simple model and by Zener and Wannier. From our previous result for the simple model, we can see that if we started the system in the ϕ_1 state at $t \to -\infty$, then the probability of remaining in the same state at $t \to \infty$ is

$$P(1) = \exp\left[-\frac{\pi|\varepsilon_{12}|^2}{\hbar\eta\lambda}\right]. \tag{E.50}$$

Notice that the rate at which the corrected energies ε_1 and ε_2 approach each other, given by η, now becomes an important factor when determining the Zener probability amplitude. The steeper the rate, the more chance the system has of tunneling through the barrier and thus remaining in the same state.

E.3 The implications of Zener's assumptions

We will now relax some of Zener's assumptions and see what physical effects will occur when evaluating the Zener probability amplitude. As long as we do not violate any of Zener's three assumptions, then we should be able to simply modify the Zener probability amplitude accordingly.

The first assumption we will relax is the requirement that $\langle \phi_1 \mid \phi_2' \rangle$ be negligible. We can see the impact that this term has on the Schrödinger equation by transforming the Schrödinger equation to a new basis. Let us first reexpress the coupling terms in the original Hamiltonian. Since they are complex-valued and complex-conjugate, we can redefine them using DeMoivre's theorem as,

$$\varepsilon_c^*(s) = |\varepsilon_c(s)|\, e^{i\Theta(s)} \quad \varepsilon_c(s) = |\varepsilon_c(s)|\, e^{-\Theta(s)}, \tag{E.51}$$

where $\varepsilon_c \equiv \varepsilon_{12} - i\hbar\lambda\langle\phi_1(s) \mid \phi_2'(s)\rangle$, and

$$\Theta(s) = \tan^{-1}\left[\frac{\hbar\lambda|\langle\phi_1(s) \mid \phi_2'(s)\rangle|}{|\varepsilon_{12}(s)|}\right], \quad |\varepsilon_c(s)| = \sqrt{|\varepsilon_{12}(s)|^2 + \hbar\lambda^2|\langle\phi_1(s) \mid \phi_2'(s)\rangle|^2}. \tag{E.52}$$

The subsequent matrix can be simplified by transforming the expansion coefficients with respect to the same phase,

$$C_1 \to C_1 e^{i\Theta(s)/2}, \quad C_2 \to C_2 e^{-i\Theta(s)/2}. \tag{E.53}$$

The freedom to redefine the expansion coefficients in this manner relies on the fact that $|C_1|^2$ and $|C_2|^2$ — the probabilities of being in the respective states ϕ_1 and ϕ_2 — are invariant under such a transformation. In this new basis the Schrödinger equation becomes

$$i\hbar\lambda\frac{d}{ds}\begin{pmatrix} C_1 \\ C_2 \end{pmatrix} = \begin{pmatrix} \varepsilon_1 - \varepsilon_2 + \frac{\hbar}{2}\lambda\Theta'(s,\lambda) & |\varepsilon_c(s)| \\ |\varepsilon_c(s)| & -\left[\varepsilon_1 - \varepsilon_2 + \frac{\hbar}{2}\lambda\Theta'(s,\lambda)\right] \end{pmatrix}\begin{pmatrix} C_1 \\ C_2 \end{pmatrix}. \tag{E.54}$$

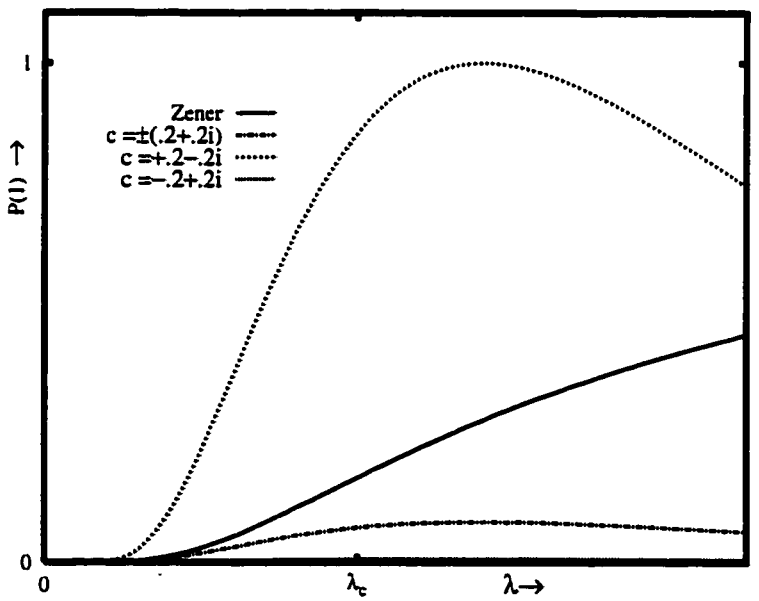

Figure E.8: The Zener probability, Eq. (E.57), to remain in the same diabatic state, ϕ_1 when the coupling $\langle\phi_1(0) \mid \phi_2'(0)\rangle$ is nonzero. In the key, c stands for the value of $\langle\phi_1(0) \mid \phi_2'(0)\rangle$, expressed as a complex number. The Zener transition corresponds to $\langle\phi_1(0) \mid \phi_2'(0)\rangle = 0$.

From Eqs. (E.52) can see that if $\langle\phi_1(s) \mid \phi_2'(s)\rangle$ is nonzero, then the second term in the radical for $|\varepsilon_c|$ can become large in the large λ limit. At this point, we cannot approximate $\varepsilon_{12} \approx \varepsilon_{12}(0)$ and one of Zener's assumptions fails. However, because of the square root in the definition of $|\varepsilon_c(s)|$ we know that as long as $|\langle\phi_1(s) \mid \phi_2'(s)\rangle|$ is not too much larger than $|\varepsilon_{12}|$ then $|\varepsilon_c(s)$ will not increase by a significant factor. In fact, Lubin *et al.*[196] defined the characteristic sweep rate λ_c as

$$\lambda_c \equiv \frac{|\varepsilon_{12}|}{\hbar|\langle\phi_1(s) \mid \phi_2'(s)\rangle|}. \tag{E.55}$$

If $\langle\phi_1(s) \mid \phi_2'(s)\rangle \neq 0$, we can still satisfy Zener's assumptions as long as the sweep rate is not increased significantly over λ_c. Obviously the diabatic limit (which relied on $\lambda \to \infty$) does not apply in this situation. We can even predict what effect this will all have if we assume that we can ignore the variations of $\langle\phi_1(s) \mid \phi_2'(s)\rangle$ with respect to s. (In other words, the overlap between $\phi_1(s)$ and $\phi_2'(s)$ is not zero, but it is still roughly constant.) In that case, we can still expand ε_{12} about $s = 0$, producing

$$\varepsilon_{12}(s) \approx \varepsilon_{12}(0) - i\lambda\hbar\langle\phi_1(0) \mid \phi_2'(0)\rangle. \tag{E.56}$$

Since Zener's assumptions still hold, we can simply modify the result in Eq. (E.50) to incorporate the new off-diagonal terms,

$$P(1) = \exp\left[-\frac{\pi}{\eta}\left(\frac{|\varepsilon_{12}(0)|^2}{\hbar\lambda} - 2\,\mathrm{Im}\left(\varepsilon_{12}(0)\langle\phi_1(0) \mid \phi_2'(0)\rangle^*\right) + \hbar\lambda|\langle\phi_1(0) \mid \phi_2'(0)\rangle|^2\right)\right]. \tag{E.57}$$

In this case, the probability is no longer a monotonic function of λ but we must keep in mind that the above result is not valid for $\lambda \gg \lambda_c$, and λ_c is the point at which the probability begins to decrease. What I found surprising in this research was how varied the effects that the relative strength of the second term in Eq. (E.56) had on the transition probability, as demonstrated in Fig. E.8.

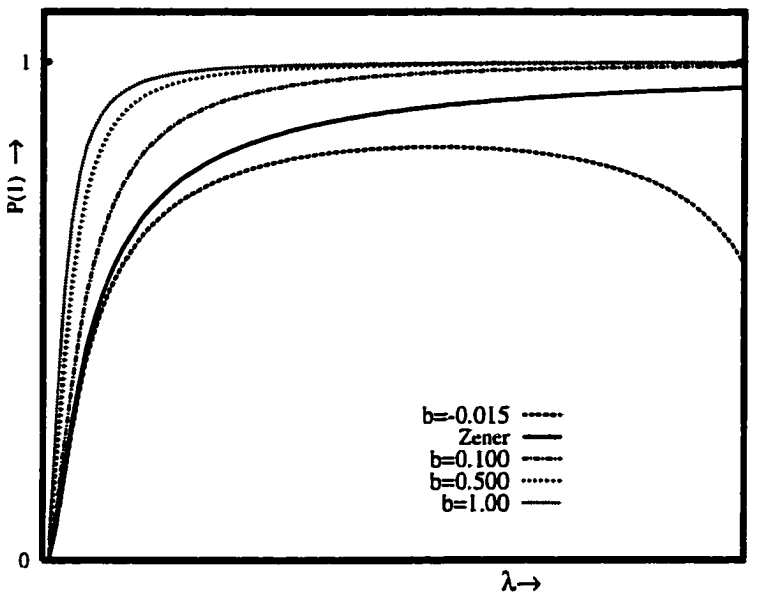

Figure E.9: Effects on the energy levels due to linear relationship between Θ' and s, as shown in Eq. (E.60).

Now suppose that the magnitude of the coupling term in Eq. (E.45) is s-independent, but the phase is not. In other words,

$$\varepsilon_c(s) = |\varepsilon_c|\, e^{i\theta(s)}, \quad |\varepsilon_c| = \text{constant}. \tag{E.58}$$

By looking at the Hamiltonian in Eq. (E.54) we can see that the adiabatic energy levels will be the same, no matter what functional dependence $\Theta(s)$ has on s, since the adiabatic levels are found by setting $\lambda = 0$ and solving the time-independent Schrödinger equation. If $\Theta'(s)$ is a constant, then the Zener transition probability amplitude will be given by Eq. (E.50). As we learned earlier in Eq. (E.28) and Fig. E.7, all that will occur is a shift in the avoided crossing center with respect to the variable parameter. However, if $\Theta'(s)$ is a linear function of s, that is $\Theta'(s) = bs$ where b is a constant, then all we have to do is redefine the diagonal terms as

$$\eta s \longrightarrow (\eta + b)s. \tag{E.59}$$

The Zener transition probability is modified accordingly, so that

$$P(1) = \exp\left[-\frac{\pi|\varepsilon_{12}|^2}{\hbar(\eta + b)\lambda}\right]. \tag{E.60}$$

So in this example, two different systems can have the exact same adiabatic spectrum but completely different transition probabilities, depending on the value of b. See Fig. E.9.

E.4 Discussion

We have seen that the simple model of an electron suspended in a magnetic field has many hidden assumptions that makes deriving the Landau-Zener transition probability fairly simple. When a more general system is considered, not only do the first-order corrections to the unperturbed energy levels become an important consideration, but the nature of the coupling between the off-diagonal terms can have large effects on the transition probabiliy. Two different systems can have the same adiabatic levels and still exhibit great differences in transition probabilities.

E.5 Parities of the Spin-up and Spin-down Eigenstates

This section was originally the first appendix in the original Specialist Exam writeup.

To find out how the parities of the spin-up and spin-down eigenstates relate we apply the lowering operator S_- to the spin-up state:

$$S_-\chi_\uparrow = \hbar\chi_\downarrow. \tag{E.61}$$

Applying the parity operator Π to both sides,

$$\Pi S_-\chi_\uparrow = \hbar\Pi\chi_\downarrow, \tag{E.62}$$

and noting that the the parity operator is unitary, $\Pi^{-1} = \Pi^{\dagger}$, we find

$$\Pi S_{-}\Pi^{-1}\Pi\chi_{\downarrow} = \Pi S_{-}\Pi^{\dagger}\Pi\chi_{\downarrow} = \hbar\Pi\chi_{\downarrow} \quad \longrightarrow \quad S_{-}\Pi\chi_{\uparrow} = \hbar\Pi\chi_{\downarrow}, \tag{E.63}$$

because the raising operator is invariant under a unitary transformation. Because the eigenstates of S_z have definite parity, then we can define $\pi_{\uparrow}$ and $\pi_{\downarrow}$ such that

$$\Pi\chi_{\uparrow} = \pi_{\uparrow}\chi_{\uparrow} \qquad \Pi\chi_{\downarrow} = \pi_{\downarrow}\chi_{\downarrow}. \tag{E.64}$$

From Eq. (E.63) we obtain $\pi_{\uparrow}S_{-}\chi_{\uparrow} = \hbar\pi_{\downarrow}\chi_{\downarrow}$. But $S_{-}\chi_{\uparrow} = \hbar\chi_{\downarrow}$, so $\pi_{\uparrow}\hbar\chi_{\downarrow} = \hbar\pi_{\downarrow}\chi_{\downarrow}$. Therefore

$$\pi_{\uparrow} = \pi_{\downarrow}, \tag{E.65}$$

and we have shown that the parity of the $\chi_{\uparrow}$ and $\chi_{\downarrow}$ states are the same. Since the perturbed eigenstates Ψ_{+} and Ψ_{-} are simply linear combinations of these unperturbed spin-states, all which have the same parity, then we can also say that Ψ_{+} and Ψ_{-} also have the same parity.

Now we can discuss the Wigner-von Neumann no-crossing theorem. For a two-level system the time-independent Schrödinger equation will be of the form

$$\begin{pmatrix} H_{11}(s) & H_{12}(s) \\ H_{12}(s)^{*} & H_{22}(s) \end{pmatrix}\begin{pmatrix} \Phi_1(s) \\ \Phi_2(s) \end{pmatrix} = E_{\pm}(s)\begin{pmatrix} \Phi_1(s) \\ \Phi_2(s) \end{pmatrix}, \tag{E.66}$$

where s is a variable parameter. The eigenvalues are

$$E_{\pm}(s) = \frac{H_{11}(s) + H_{22}(s)}{2} \pm \frac{1}{2}\sqrt{(H_{11}(s) - H_{22}(s))^2 + |H_{12}(s)|^2}. \tag{E.67}$$

For the two energy levels to become degenerate, the square-root term must vanish. However, the radical is a sum of squares, so the only way for the square-root to vanish at some value of the variable parameter s is for (1) $H_{11}(s) = H_{22}(s)$ *and* (2) $H_{12}(s) = 0$. However, if the two states Φ_1 and Φ_2 are of the same parity, then in general the second condition is not satisfied and we cannot expect to find a value of s where the energies are degenerate.

(It could be that a value of s exists such that H_{12} *and* $H_{11} - H_{22} = 0$, which would produce a level crossing between two levels correspondint to coupled states of the same parity. But this is an unlikely occurrence.) In that case, we expect avoided crossings, not level crossings. However, if the two states are not coupled by the Hamiltonian, then the second condition is already satisfied. In that case, any value of s where $H_{11} = H_{22}$ will be location of a level crossing.

In summary, the energy levels corresponding to states of the same parity that are coupled by the Hamiltonian of the system will not cross for any physical (real) value of the variable parameter.

E.6 The Adiabatic Limit

This section was originally the second appendix in the original Specialist Exam writeup. It is mostly the work of Martin Dunn, and I take little credit for it.

The proof that a time-varying parameter induces transitions between adiabatic states relies on one assumption — in the adiabatic limit no such transitions take place. Even though this assumption is expected, I will now offer a proof of this assumption.

The time-dependent Schrödinger equation for the system we are considering is

$$\begin{pmatrix} \lambda t & c \\ c & -\lambda t \end{pmatrix} \Psi(\lambda, t) = i\hbar \frac{d}{dt} \Psi(\lambda, t), \tag{E.68}$$

where λ is the sweep rate in the relation $s = \lambda t$ and s is the variable parameter. (In the simple model, $B_\perp$ would correspond to the off-diagonal term c and $B_\parallel$ would correspond to s.) In general, we can always express the state $\Psi(t)$ in terms of a time-dependent phase factor, which will also be a function of the sweep rate λ. Therefore, we write

$$\Psi(\lambda, t) = e^{-i\alpha(\lambda,t)} \Phi(\lambda, t), \tag{E.69}$$

where $\langle \Phi \mid \Phi \rangle = 1$ to conserve probability. Therefore

$$\frac{d}{dt}\Psi(\lambda,t) = e^{-i\alpha(\lambda,t)}\left[-i\left(\frac{d}{dt}\alpha(\lambda,t)\right)\Phi(\lambda,t) + \frac{d}{dt}\Phi(\lambda,t)\right] \tag{E.70}$$

$$= e^{-i\alpha(\lambda,t)}\left[-i\lambda\left(\frac{d}{ds}\alpha(\lambda,\frac{s}{\lambda})\right)\Phi_{\pm}(\lambda,\frac{s}{\lambda}) + \lambda\frac{d}{ds}\Phi(\lambda,\frac{s}{\lambda}) + \lambda\frac{d}{ds}\Phi_{\pm}(\lambda,\frac{s}{\lambda})\right]. \tag{E.71}$$

Now our time-dependent Schrödinger equation is (canceling the exponential terms)

$$\begin{pmatrix} s & c \\ c & -st \end{pmatrix}\Phi_{\pm}(\lambda,\frac{s}{\lambda}) = \hbar\lambda\left(\frac{d}{ds}\alpha(\lambda,\frac{s}{\lambda})\right)\Phi_{\pm}(\lambda,\frac{s}{\lambda}) + i\hbar\lambda\frac{d}{ds}\Phi_{\pm}(\lambda,\frac{s}{\lambda}). \tag{E.72}$$

Since the Hamiltonian is Hermitian it can always be diagonalized by a real, orthogonal, unitary matrix U, therefore

$$\begin{pmatrix} E_{+}(s) & 0 \\ 0 & E_{-}(s) \end{pmatrix}U(s)\Phi_{\pm}(\lambda,\frac{s}{\lambda}) = \hbar\lambda\left(\frac{d}{ds}\alpha(\lambda,\frac{s}{\lambda})\right)U(s)\Phi_{\pm}(\lambda,\frac{s}{\lambda}) + i\hbar\lambda\left(\frac{d}{ds}U(s)\Phi_{\pm}(\lambda,\frac{s}{\lambda})\right). \tag{E.73}$$

Since $\langle \Phi_{\pm} \mid \Phi_{\pm} \rangle = 1$ then

$$\lim_{\lambda\to 0}\left[i\hbar\lambda\left(\frac{d}{ds}U\right)\Phi_{\pm}\right] = 0, \tag{E.74}$$

and we lose the last term in the time-dependent Schrödinger equation in this limit. We now have two uncoupled differential equations,

$$\left[E_{\pm}(s) - \hbar\lambda\frac{d}{ds}\alpha + i\hbar\lambda\frac{d}{ds}\right](U\Phi)_{\pm} = 0, \tag{E.75}$$

where $(U\Phi)^{*}_{\pm}(U\Phi)_{\pm} = 1$. The phase factor α is completely arbitrary, so we choose a particular value of α such that $(U\Phi)_{\pm} = 1$. Then

$$(d/ds)(U\Phi)_{\pm} = 0 \tag{E.76}$$

and

$$\left[E_{\pm}(s) - \hbar\lambda\frac{d}{ds}\alpha\right] = 0. \tag{E.77}$$

From Eqs. (E.74) and (E.76) we can see that

$$\lim_{\lambda \to 0} i\hbar\lambda \frac{d}{ds}\Phi_{\pm} = 0 \tag{E.78}$$

and our time-dependent Schrödinger equation becomes in the limit $\lambda \to 0$

$$\begin{pmatrix} s & c \\ c & -s \end{pmatrix} \Phi_{\pm}(0, \infty) = E_{\pm}(s)\Phi_{\pm}(0, \infty). \tag{E.79}$$

But

$$\frac{d}{ds}\alpha = \frac{E_{\pm}(s)}{\hbar\lambda} \quad \longrightarrow \quad \alpha = \frac{1}{\hbar\lambda}\int_{s_o}^{s} E_{\pm}(s')\, ds', \tag{E.80}$$

which is infinite as $\lambda \to 0$. Therefore, in the adiabatic limit

$$\Psi(0, \infty) = \begin{pmatrix} \text{infinite} \\ \text{phase} \end{pmatrix} \times \begin{pmatrix} \text{adiabatic} \\ \text{wavefunction} \end{pmatrix}. \tag{E.81}$$

In the adiabatic limit, the state of the system does not switch to another state, but rather is nothing more than the original state multiplied by an infinite phase factor.

Now consider the system to be in the adiabatic state Ψ_1 when the parameter of the system s is at some initial value s_o. We assume that s is varying infinitely slowly (adiabatically). If the system evolves adiabatically, then at some later value of s we assume that the system will be in the same state Ψ_1. In other words, the adiabatic evolution operator U_a takes us from our initial state at s_o to the same state at s

$$\Psi_1(s) = U_a(s_o, s)\Psi_1(s_o) \tag{E.82}$$

If the system varies nonadiabatically, then at some later value of time the system will be found in the state

$$\Psi(t) = U(t, t_o)\Psi_1(t_o) \tag{E.83}$$

If we can show that the final state $\Psi(t)$ is *not* the same as $\Psi_1(t)$, then we have shown that the final state must be a mixture of Ψ_1 and some other state. Therefore, we will have shown that the time-evolution operator mixes the states as time evolves in the system.

If the final states for both the adiabatic and nonadiabatic evolutions are the same, then the two evolution operators must be proportional to each other, so at the most they can vary by some time-dependent phase $e^{i(t,t_o)}$,

$$U(t,t_o) = e^{i(t,t_o)}U(s,s_o). \tag{E.84}$$

The two Hamiltonions describing the system at different values of t do not commute, so the exact form for the time-evolution operator is rather complicated. However, the first two terms in the expansion of the time-evolution operator are not complicated:

$$U(t,t_o) = \mathbf{1} - \frac{i}{\hbar}\int_{t_o}^{t} H(t')\,dt'. \tag{E.85}$$

If $U(s,s_o)$ is indeed proportional to $U(t,t_o)$, then the two operators must commute. However, they in do not. This can be seen by examing the commutation between $U(s,s_o)$ and the first two terms in $U(t,t_o)$,

$$\left[U(s,s_o), \mathbf{1} - \frac{i}{\hbar}\int_{t_o}^{t} H(t')\,dt'\right] = -\left[U(s,s_o), \frac{i}{\hbar}\int_{t_o}^{t} H(t')\,dt'\right] \neq 0. \tag{E.86}$$

Even if the above commutation relation does equal 0 for some time t, it certainly cannot equal 0 for all time. Naturally the above relies on only the first two terms of $U(t,t_o)$, but if it fails to commute for the first two terms it would be extremely unlikely that it would commute for the sum of all the terms in the expansion.

Therefore, the adiabatic and nonadiabatic evolution operators cannot be simply proportional to each other, and therefore the final state when the system evolves nonadiabatically cannot be purely Ψ_1. Therefore, varying the external parameter with time mixes the states.

Appendix F

Avoided Crossings as $|m|$ is Swept while the Unscaled Field Strength B is Held Constant: Details

Originally appeared as the Appendix in J.R. Walkup, M. Dunn, D.K. Watson, Phys. Rev. A **58**, 4668-4682 (1998).

F.1 Rewriting the energy level characterization in Terms of the Unscaled Field Strength and the Solutions of Eq. (4.11) for Fixed Physical Field Strength

When re-expressed in terms of B and δ, the $\tilde{\delta}_{\pm}(\widetilde{B})$ of Eqs. (4.10) and (4.11) are functions of both B *and* δ (see Eq. (3.3)), that is $\tilde{\delta}_{\pm}(B,\delta)$. Consider expanding $\tilde{\delta}_{\pm}(B,\delta)$ about a point δ_c while B is held fixed, where δ_c is a solution of Eq. (4.13) for fixed B. Then

$$\begin{aligned}\tilde{\delta}_{\pm}(B,\delta) &= \tilde{\delta}_{\pm}(B,\delta_c) + \left.\frac{d\tilde{\delta}_{\pm}(B,\delta)}{d\delta}\right|_{\delta=\delta_c}(\delta-\delta_c) \\ &\quad + \text{higher order terms in } (\delta-\delta_c)\,. \end{aligned} \tag{F.1}$$

Now $\tilde{\delta}_{\pm}(B,\delta_c) = \tilde{\delta}_{\pm}(\widetilde{B}_c)$ is the solution of $\Delta E(\delta,\widetilde{B}_c) = 0 = \Delta E(\delta,B)$ (see Eqs. (4.11) and (4.13)), that is $\tilde{\delta}_{\pm}(B,\delta_c) = \delta_c$, where $c{=}\pm$. Therefore

$$\begin{aligned}\tilde{\delta}_{\pm}(B,\delta) &= \delta_{\pm} + \left.\frac{d\tilde{\delta}_{\pm}(B,\delta)}{d\delta}\right|_{\delta=\delta_c}(\delta-\delta_{\pm}) \\ &\quad + \text{higher order terms in } (\delta-\delta_{\pm})\,. \end{aligned} \tag{F.2}$$

This means that

$$\sqrt{\delta - \tilde{\delta}_{\pm}(\widetilde{B})} = \sqrt{A(B,\delta)\,(\delta - \delta_{\pm}(B))} \tag{F.3}$$

where $A(B,\delta)$ is finite at $\delta = \delta_{\pm}(B)$, and Eq. (4.10) becomes

$$E_{\pm}(\delta, B) = E_a(\delta, B) \pm E_b(\delta, B)\sqrt{\delta - \delta_+(B)}\,\sqrt{\delta - \delta_-(B)}\,,$$

(see for example Eq. (4.10)) where the $\delta_{\pm}(B)$ are solutions of Eq. (4.13).

F.1.1 Derivation of the approximate relationship of Eq. (4.16) from Eq. (4.13)

A good approximation for the $\Re e(\delta_{\pm}(B))$, the real part of the solutions of Eq. (4.13) for fixed B, may be obtained from the positions of the branch points in the complex plane for fixed $\widetilde{B}$, the solutions $\tilde{\delta}_{\pm}(\widetilde{B})$ of Eq. (4.11). Equation (4.12) determines where an avoided crossing will be found as $\widetilde{B}$ held fixed. According to Eq. (3.3) this corresponds to an unscaled magnetic field $B = \left[\Re e(\tilde{\delta}_{\pm}(\widetilde{B}))\right]^3 \widetilde{B}$. By using this value of B in Eq. (4.13) we obtain the positions of the branch points in the complex δ-plane for this value of B. Therefore from Eq. (4.15) we obtain the position of the avoided crossings as B is held to this value. However, the value of B at $\tilde{\delta}_{\pm}(\widetilde{B})$, the branch-point position with $\widetilde{B}$ held fixed, is not $\left[\Re e(\tilde{\delta}_{\pm}(\widetilde{B}))\right]^3 \widetilde{B}$ but rather $\left[\tilde{\delta}_{\pm}(\widetilde{B})\right]^3 \widetilde{B}$. Thus the $\tilde{\delta}_{\pm}(\widetilde{B})$ are the solutions of Eq. (4.13) with $B = \left[\tilde{\delta}_{\pm}(\widetilde{B})\right]^3 \widetilde{B}$. Nevertheless, these are close to $\left[\Re e(\tilde{\delta}_{\pm}(\widetilde{B}))\right]^3 \widetilde{B}$ since $\left|\Re e(\tilde{\delta}_{\pm}(\widetilde{B}))\right| \gg \left|\Im m(\tilde{\delta}_{\pm}(\widetilde{B}))\right|$. Therefore, assuming that the solutions of Eq. (4.13) are not extremely sensitive to the precise value of B,

$$\delta_{\pm}\left(\left[\Re e(\tilde{\delta}_{\pm}(\widetilde{B}))\right]^3 \widetilde{B}\right) \approx \tilde{\delta}_{\pm}(\widetilde{B}). \tag{F.4}$$

Therefore from Eq. (4.15)

$${}^{AC}\delta_c\left(\left[\Re e(\tilde{\delta}_{\pm}(\widetilde{B}))\right]^3 \widetilde{B}\right) \approx \Re e(\tilde{\delta}_{\pm}(\widetilde{B}))\,.$$

Appendix G

Quadratic Padé Approximants

Originally appeared as Appendix A in J. R. Walkup, M. Dunn, and D. K. Watson, J. Math. Phys. **41**, 216 (2000).

To analyze the divergent energy series we employ both linear Padés and quadratic Padés[185]. Quadratic Padés have a functional form which enables them to incorporate explicitly square-root branch point singularities; in addition linear Padés $S_{[L/M]}$ (see below) are determined by the requirement that

$$Q\,E - P \sim 0\,,$$

where E is the energy series, P is an L^{th} order polynomial, Q is an M^{th} order polynomial with zeroth-order coefficient $q_0 \equiv 1$, and "~ 0" means "asymptotic[126] to 0 up to and including order $L+M$." Therefore the energy series E is asymptotic to the rational function of polynomials, or linear Padés,

$$S_{[L/M]} = \frac{P}{Q}\,,$$

up to and including order $L + M$. In other words,

$$E \sim S_{[L/M]}\,.$$

The value of $S_{[L/M]}$ for a specific value of the perturbation parameter is the $[L/M]$ linear Padé sum of the energy expansion at that value of the perturbation parameter. By introducing a third polynomial R of order N, we can determine the quadratic Padés $S_{[L/M/N]}$ from the equation

$$Q\,E^2 - P\,E + R \sim 0\,,$$

where '~ 0' means asymptotic to 0 up to and including order $L + M + N + 1$. Therefore

$$E \sim S_{[L/M/N]}\,, \qquad S_{[L/M/N]} = \frac{1}{2}\left(\frac{P}{Q} + \frac{\sqrt{(P^2 - 4QR)}}{Q}\right)\,. \tag{G.1}$$

The square-root term in Eq. (G.1) requires that $S_{[L/M/N]}$ be a multivalued function with two branches.[186] Equation (G.1) holds for only one of these two branches. The value of $S_{[L/M/N]}$ for some value of the perturbation parameter is the $[L/M/N]$ quadratic Padé sum of the energy expansion at that value of the perturbation parameter. Although quadratic Padé summation is useful in its own right for summing series of functions with branch points, we simply use it to locate such branch points. The branch points are given by the zeros of $P^2 - 4QR$, which have a stable position as L, M, and N are varied in a regular fashion so that $L + M + N + 1$ increases.

Appendix H

Verification of Branch Points at the Origin at the Fermi Resonance

Originally appeared as Appendix B in J.R. Walkup, M. Dunn, and D.K. Watson, J. Math. Phys. **41**, 216 (2000).

At the Fermi resonance, $\delta = 0$ and $E^+(0, \widetilde{B}) = E^-(0, \widetilde{B})$. Therefore, there are two possibilities:

1. At least one branch point is found at the origin. (The coefficient $C(\delta, \widetilde{B})$ or $F(\delta, \widetilde{B})$ in front of the nonzero $\sqrt{\delta - \tilde{\delta}^{\pm}(\widetilde{B})}$ term in Eq. (5.4) must be 0. This possibility imposes no constraint on $G(\delta, \widetilde{B})$ in Eq. (5.5), since $\delta - \tilde{\delta}^{-}(\widetilde{B}) = 0$.)
2. Neither branch point is found at the origin. (This requires that $C(\delta, \widetilde{B}) = F(\delta, \widetilde{B}) = 0$ in Eq. (5.4) and $G(\delta, \widetilde{B}) = 0$ in Eq. (5.5).)

To see which of these two possibilities is correct, we only need to examine the magnitude of the coefficients in the δ-expansions for $E^{\pm}(\delta, \widetilde{B})$ near the Fermi resonance. If the coefficients diverge without bound as $\widetilde{B}$ approaches the Fermi resonance, then at least one of the singularities approaches the origin and the first possibility is correct. This is what occurs for both the 2:1 and 4:1 Fermi resonances (see Table H.1); one or more branch points converge onto the origin at the Fermi resonance.

For the 2:1 Fermi resonance, we can even show *analytically* the presence of a branch point at the origin when the 2:1 Fermi-resonance degeneracy condition between the $|11\rangle$

Table H.1: Fourth-order energy coefficients (see Eq. (3.9)) of the $|11\rangle$ state as functions of $\widetilde{B}$ in the large-$\widetilde{B}$ limit. The numbers in parentheses indicate the power of ten multiplying the entry.

$\widetilde{B}$ [a]	$\widetilde{E}^{(8)}$
10 000	1.3356583551610437 (6)
20 000	9.2198129717014880 (6)
30 000	2.5008272699694642 (7)
40 000	4.9098907630423283 (7)
50 000	8.1664939726775076 (7)
60 000	1.2278772158146093 (8)
70 000	1.7250282491805636 (8)
80 000	2.3082038846347921 (8)
90 000	2.9773544049674207 (8)

[a] Note that the scaled field strengths listed are extremely large physically, even for large values of $|m|$. From $B=\delta^3\widetilde{B}$, the scaled strength $\widetilde{B}=10\,000$ corresponds to nearly 7500 tesla when $|m|=33$. At $|m|=0$ this field strength is on the order of 10^8 tesla. (!)

and $|03\rangle$ states is met exactly. This can be achieved using degenerate perturbation theory (see Appendix I), the required method when two zeroth-order states are degenerate. Although degenerate perturbation theory proceeds in almost exactly the same fashion as nondegenerate perturbation theory once the zeroth-order state has been determined, the fact that the zeroth-order state is a linear superposition of both the $|11\rangle$ and $|03\rangle$ states means that the usual arguments for the coefficients of the odd powers of $\delta^{1/2}$ in the energy series being 0 in nondegenerate perturbation theory break down for degenerate perturbation theory (see the text following Eqs. (3.9) and (3.11)). This confirms the presence of a branch point at the origin when the 2:1 Fermi-resonance degeneracy condition is exactly satisfied.

The application of degenerate perturbation theory to the 4:1 Fermi resonance is a little different from the ordinary. See Sec. 5.4.2 and Appendix G.

Appendix I

Branch Point Behavior via Degenerate Perturbation Theory

Originally appeared as Appendix C in J.R. Walkup, M. Dunn, and D.K. Watson, J. Math. Phys. **41**, 216 (2000).

The harmonic Hamiltonian has the same form as a two-dimensional SHO, therefore we expand the perturbed states in the two-dimensional SHO basis $|\nu_1\nu_2\rangle$. The $|11\rangle$ state is involved in both crossings under consideration. The other is either the $|03\rangle$ state (2:1 Fermi resonance) or the $|05\rangle$ state (4:1 Fermi resonance). Therefore, for the two-fold degeneracies we consider, we expand the nth perturbed eigensolutions to second order in $\delta^{\frac{1}{2}}$ as[187]

$$|\Phi_n\rangle = c_{n1}^{(0)}|1\rangle + c_{n2}^{(0)}|2\rangle + \delta^{\frac{1}{2}}\sum_{m=3}^{\infty} c_{nm}^{(1)}|m\rangle + \delta\sum_{m=3}^{\infty} c_{nm}^{(2)}|m\rangle, \qquad E_n = E_n^{(0)} + \delta^{\frac{1}{2}}E_n^{(1)} + \delta E_n^{(2)}. \tag{I.1}$$

Here $|1\rangle \equiv |11\rangle$, $|2\rangle$ refers to either the $|03\rangle$ or the $|05\rangle$ state (depending on which crossing we are considering) and the $|m\rangle$ number all unperturbed states other than $|1\rangle$ and $|2\rangle$.

The first-order correction to the harmonic Hamiltonian, $\mathcal{H}^{(1)}$, contains the following set of annihilation/creation operators a_i:

$$\mathcal{H}^{(1)} : \left\{a_1^3\mathrm{I}_2,\ a_1\mathrm{I}_2,\ \tilde{a}_1^3\mathrm{I}_2,\ \tilde{a}_1\mathrm{I}_2,\ a_1a_2^2,\ a_1\tilde{a}_2^2,\ \tilde{a}_1a_2^2,\ \tilde{a}_1\tilde{a}_2^2\right\}, \tag{I.2}$$

where I_1 and I_2 refer to diagonal operators operating on the first and second quanta, respectively.

Now consider first-order degenerate perturbation theory. Since there are no purely diagonal terms, $\mathcal{H}^{(1)}_{11} = \mathcal{H}^{(1)}_{22} = 0$. Therefore $E^{(1)}_n = \pm|\mathcal{H}^{(1)}_{12}|$. For the 2:1 Fermi resonance, $E^{(1)}_n \neq 0$ because $\langle 11|\mathcal{H}^{(1)}|03\rangle \neq 0$. However, $\langle 11|\mathcal{H}^{(1)}|05\rangle = 0$.

For the 4:1 Fermi resonance ($|2\rangle \equiv |05\rangle$) we cannot determine either of the expansion coefficients $c^{(0)}_{n1}$ or $c^{(0)}_{n2}$ at first order since $\mathcal{H}^{(1)}_{11} = \mathcal{H}^{(1)}_{22} = \mathcal{H}^{(1)}_{12} = \mathcal{H}^{(1)}_{21} = 0$, so we now resort to the next order of perturbation theory to determine the zeroth-order states at the degeneracy.

The first-order perturbed wave function coefficients are given by

$$c^{(1)}_{nm} = \frac{c^{(0)}_{n1}\mathcal{H}^{(1)}_{m1} + c^{(0)}_{n2}\mathcal{H}^{(1)}_{m2}}{E^{(0)}_n - E^{(0)}_m}, \qquad \mathcal{H}^{(\alpha)}_{ij} \equiv \langle i\,|\mathcal{H}^{(\alpha)}|\,j\rangle\,. \tag{I.3}$$

According to Eq. (I.2), there are only nine possible $|m\rangle$ for $c^{(1)}_{nm} \neq 0$:

$$|m\rangle \in (|01\rangle, |21\rangle, |23\rangle, |41\rangle, |03\rangle, |13\rangle, |15\rangle, |17\rangle, |35\rangle). \tag{I.4}$$

The first five states in the set above are connected by $\mathcal{H}^{(1)}$ to $|05\rangle$, whereas the final four are connected by $\mathcal{H}^{(1)}$ to $|11\rangle$. It is important to note that *no* $|m\rangle$ state simultaneously connects $\mathcal{H}^{(1)}$ to both $|05\rangle$ *and* $|11\rangle$.

The second-order perturbation[119]

$$\mathcal{H}^{(2)} = {}^{0}v_{2,4}\,x_1^4 + {}^{1}v_{2,4}\,x_1^2x_2^2 + {}^{2}v_{2,4}\,x_2^4 + v_{2,2}\,x_1^2 + v_{2,0} \tag{I.5}$$

contains the following annihilation/creation operators:

$$\mathcal{H}^{(2)} : \Big\{a_1^4\mathrm{I}_2,\ a_1^2\mathrm{I}_2,\ \widetilde{a}_1^2\mathrm{I}_2,\ \widetilde{a}_1^4\mathrm{I}_2,\ a_1^2a_2^2,\ a_1^2\widetilde{a}_2^2,\ \widetilde{a}_1^2\widetilde{a}_2^2,\ \mathrm{I}_1a_2^2,\ \mathrm{I}_1\widetilde{a}_2^2,\ \widetilde{a}_1^2a_2^2,\ \mathrm{I}_1a_2^4,\ \mathrm{I}_1\widetilde{a}_2^4,\ \mathrm{I}_1\mathrm{I}_2,\ \Big\}. \tag{I.6}$$

At second order we have the coupled equations[187]

$$\sum_{m=3}^{\infty} c^{(1)}_{nm}\mathcal{H}^{(1)}_{sm} + \sum_{\ell=1}^{2} c^{(0)}_{n\ell}\mathcal{H}^{(2)}_{s\ell} = \sum_{\ell=1}^{2} c^{(0)}_{n\ell}E^{(2)}_n\langle s|\ell\rangle, \tag{I.7}$$

where $\langle s|\ell\rangle = \delta_{s\ell}$. For s corresponding to $|11\rangle$,

$$\sum_{m=3}^{\infty} c_{nm}^{(1)}\mathcal{H}_{1m}^{(1)} + c_{n1}^{(0)}\mathcal{H}_{11}^{(2)} + c_{n2}^{(0)}\mathcal{H}_{12}^{(2)} = c_{n1}^{(0)}E_n^{(2)}, \tag{I.8}$$

and for s corresponding to $|05\rangle$,

$$\sum_{m=3}^{\infty} c_{nm}^{(1)}\mathcal{H}_{2m}^{(1)} + c_{n1}^{(0)}\mathcal{H}_{21}^{(2)}11 + c_{n2}^{(0)}\mathcal{H}_{22}^{(2)} = c_{n2}^{(0)}E_n^{(2)}. \tag{I.9}$$

From Eq. (I.3), the first-order wave function coefficients $c_{nm}^{(1)}$ are functions of $c_{n1}^{(0)}$ and $c_{n2}^{(0)}$. Therefore, the first term on the left side in Eq. (I.8) is given by

$$\sum_{m=3}^{\infty} c_{nm}^{(1)}\mathcal{H}_{1m}^{(1)} = \sum_{m=3}^{\infty}\left[\frac{c_{n1}^{(0)}\mathcal{H}_{m1}^{(1)} + c_{n2}^{(0)}\mathcal{H}_{m2}^{(1)}}{E_n^{(0)} - E_m^{(0)}}\right]\mathcal{H}_{1m}^{(1)}. \tag{I.10}$$

But we know that $\mathcal{H}_{m2}^{(1)}\mathcal{H}_{1m}^{(1)} = \langle m|\mathcal{H}^{(1)}|05\rangle\langle 11|\mathcal{H}^{(1)}|m\rangle = 0$, since $\mathcal{H}^{(1)}$ cannot simultaneously connect $|m\rangle$ to $|11\rangle$ *and* $|05\rangle$. Therefore

$$\sum_{m=3}^{\infty} c_{nm}^{(1)}\mathcal{H}_{1m}^{(1)} = \sum_{m=3}^{\infty}\frac{|\mathcal{H}_{m1}^{(1)}|^2}{E_n^{(0)} - E_m^{(0)}}c_{n1}^{(0)}. \tag{I.11}$$

Similarly, the first term on the left side of Eq. (I.9) becomes

$$\sum_{m=3}^{\infty} c_{nm}^{(2)}\mathcal{H}_{2m}^{(1)} = \sum_{m=3}^{\infty}\frac{|\mathcal{H}_{m2}^{(1)}|^2}{E_n^{(0)} - E_m^{(0)}}c_{n2}^{(0)}. \tag{I.12}$$

Combining like coefficients of $c_{n1}^{(0)}$ and $c_{n2}^{(0)}$ in Eqs. (I.8) and (I.9) we find

$$\begin{pmatrix} M_{11}\mathcal{H}_{12}^{(2)} \\ \mathcal{H}_{21}^{(2)}M_{22} \end{pmatrix}\begin{pmatrix} c_{n1}^{(0)} \\ c_{n2}^{(0)} \end{pmatrix} = 0, \tag{I.13}$$

where

$$M_{11} \equiv \sum_{m=3}^{\infty}\frac{|\mathcal{H}_{m1}^{(1)}|^2}{E_{nm}^{(0)}} + \mathcal{H}_{11}^{(2)} - E_n^{(2)}, \qquad M_{22} \equiv \sum_{m=3}^{\infty}\frac{|\mathcal{H}_{m2}^{(1)}|^2}{E_{nm}^{(0)}} + \mathcal{H}_{22}^{(2)} - E_n^{(2)}. \tag{I.14}$$

However, $\mathcal{H}^{(2)}$ cannot connect states $|11\rangle$ and $|05\rangle$ since none of the raising/lowering operators in $\mathcal{H}^{(2)}$ raise or lower ν_1 by only one quanta. This means that the matrix operator in Eq. (I.13) is diagonal with eigenvectors

$$\begin{pmatrix} c_{n1}^{(0)} \\ 0 \end{pmatrix} \text{ and } \begin{pmatrix} 0 \\ c_{n2}^{(0)} \end{pmatrix}. \tag{I.15}$$

Therefore, the zeroth-order wave functions of degenerate perturbation theory for the states of the 4:1 Fermi resonance at exact degeneracy are not composed of a linear combination of the $|05\rangle$ and $|11\rangle$ harmonic functions, but instead consists of only *one* of the two harmonic functions.

In summary, *no* branch points connect the two states at the 4:1 Fermi resonance. This explains the branch point annihilation at the Fermi resonance in Fig. 4.6. From the above arguments this branch-point annihilation should exist for the 6:1, 8:1, 10:1, ... Fermi resonances as well, although this has not been confirmed. On the other hand, the interaction between the $|11\rangle$ and $|03\rangle$ states, which connect at first order, does not feature branch point annihilation at the 2:1 Fermi resonance, and therefore both mixing coefficients are nonzero for all field strengths.

Appendix J

Optimization of Economized Rational Approximants: The *Mathematica* Source Code

The source code below is an abbreviated version of the actual *Mathematica* code used to find the optimal value of α (denoted "alpha" in the code). The values of the constants entered in this example find an approximate optimal α in about a minute on a Pentium II computer. More precise values of α_0 would require finer meshes in both α and s and would therefore take longer to complete. Note that the function we are optimizing in the code below is $\tanh(x)$, evaluated at $x_0 = 4$.

J.1 OptimalAlpha.nb

Test of the Economized Rational Approximants (ERAs)

Some Preliminaries

```
In[1]:= Needs["Calculus`Pade`"];
In[2]:= Needs["Statistics`LinearRegression`"];
```

Now we define our test function (func[x]) and the value of the parameter (x0) at which this function will be evaluated. The function era[a,n] is the [n/n] economized rational approximant evaluated at x0. The parameter (a) is the tunable ERA parameter denoted alpha in the text. Note that era[0,n] is equivalent to the [n/n] Pade approximant. eraTable[alpha] is a list of the rERAs up to some maximum order maxOrder. The variable numPrecision establishes the desired precision of certain subsequent calculations. To speed up the ensuing search, it is best to set the lower limit (n) in eraTable[alpha] to be four less than the upper limit.

```
In[3]:= maxOrder=14; x0=4; numPrecision=20;
In[4]:= func[x_]:=Tanh[x];
In[5]:= era[a_,n_]:=EconomizedRationalApproximation[
```

```
            func[x], {x, {-a, a}, n, n}];
In[6]:= eraTable[a_]:=Table[era[a_,n_], {n, 0, maxOrder}];
```

fitEquation[s] takes the sequence of ERAs and finds an exponential fit given a particular value of s in its exponential. The function Regress[ ][[2]][[2]] calculates the regression for the chosen value of s and sets it equal to regression[s]. ShowOutput[alpha,s] is simply a formatting function for the output. It is easiest to understand simply by running the program and examining the output.

```
In[7]:= fitEquation[s_]:=NumberForm[Fit[
            sequence, -1, Exp[-s n], n], numPrecision
In[8]:= regression[s_]:=
            Regress[sequence, -0.1, Exp[-s n], n][[2]][[2]]
In[9]:= ShowOutput[alpha_, s_] :=
            Print[ N[a, 4],   , N[s] , "F(n) = ",
               fitEquation[s], N[sequence, numPrecision] ];
```

Now we calculate the sequence of ERAs. The variables alphaI and alphaF are the initial and final values of alpha, which is incremented in steps of alphaStep in the outer While[] loop. The inner While[] loopo selects the best power law equation - expressed as an exponential Exp[-s n] - to fit the resulting table of values (notice that we do not try to fit the entire ERA sequence, only those values corresponding to the highest four orders). The variables sI and sF are the initial and final values of the parameter s in the exponential, with sStep the increment. All are user-defined. Initially, it is best to set sF=sI and only sum over alpha. Then after examining the resulting plots for the range of alpha where convergence is roughly exponential the sum over s can be performed.

```
In[10]:= alphaI = 0;  alphaStep = 1;  alphaF = 10;
In[11]:= sI = 2/10;  sStep = 1/10;  sF = 4;
In[12]:= a=alphaI
In[13]:= While[ a <= alphaF,  (* Outer loop. *)
          sequence = Take[ eraTable[a], -4];
          ListPlot[ sequence, PlotRange -> All,
               PlotJoined -> True];
          s=sI; regTemp = 0;
          While[ s <= sF,
             If[ regression[s] > 0.9999999,
               ShowOutput[a, s];
             ];
             s+=sStep;
             regTemp = regression[s];
          ];
          a+=alphaStep;
        ]
        Print["Complete"];
```

Appendix K

The Matrix Method

A summary of the computer algorithm of Dunn, *et al.*[105] used to generate the energy coefficients of the dimensional perturbation series. Note: This appendix is included for completeness for those that may want to implement it in the future – I was *not* involved in the development of this algorithm. Note that the source code, with subroutines and make file, are included at the end of this appendix. This source code was originally written by Tim Germann, which I later modified for my own purpose.

Main program

```
c Matrix Method for the hydrogen atom in a magnetic field
c with two degrees of freedom

 PROGRAM MATRIX_H_MAG
 IMPLICIT NONE

 include 'qcommon.h'

 REAL*16 T2(96,96), T3(96), sqt(96), R2(96)

 INTEGER maxj, state(2), i, j, n, i1, i2, k
 INTEGER smax, iarr(3), imin, B
 LOGICAL evenE, savewf
 REAL*16 energy,omega(2),temp,rho,Breal
 character*5 Bchar
 character*1 nschar1, nschar2
 character*18 filly

 COMMON /ARRAYS/ U1,U2,U3,energy,ptr,T1,T2,T3,sqt,R2
 COMMON /WVF/ A, asize

 write(*,*) 'state=?'
```

```
 read(*,*) state(1),state(2)
 state(1) = state(1)+1
 state(2) = state(2)+1

c 'Coeffs' is a file containing a table of B values and
c order for each value of B
 open(unit=1,file='Blist',form='formatted',status='old')
 read(1,*)
 read(1,*)
 read(1,*)
 read(1,*)
 read(1,*)

 do 200 k = 1,599
 call setup(maxj,state,omega,B,rho,Breal)

C Initialize arrays sqt and R2 for use in recursion
C .  multiplications

 do i = 1,LEN
    sqt(i)=qsqrt(1.q0*i)
    R2(i)=qsqrt(1.q0*i*(i+1))
 end do

 write(nschar1,12) state(1)-1
 write(nschar2,12) state(2)-1

 write(Bchar,11) B
 if (B.lt.10000) Bchar(1:1) = '0'
 if (B.lt.1000) Bchar(2:2) = '0'
 if (B.lt.100) Bchar(3:3) = '0'
 if (B.lt.10) Bchar(4:4) = '0'
11 format(i5)
12 format(i1)
 filly = 'ecoeffq.'//nschar1//nschar2//Bchar//'P'
 write(*,*) filly
 open(unit=13,file=filly,form='formatted',status='unknown')
 smax=state(1)
 if (state(2).gt.smax) smax = state(2)

 asize(0) = smax
 do i1 = 1,smax
    do i2 = 1,smax
       a(0,i1,i2) = 0.
       T1(i1,i2) = 0.
    end do
 end do
 a(0,state(1),state(2)) = 1.
 T1(state(1),state(2)) = 1.

 j = 0
 do while ((j.lt.maxj).and.(asize(j).le.LEN))
    asize(j+1) = asize(j) + 3
    j = j+1
```

```
 end do

 if (j.lt.maxj) then
    asize(j) = LEN
c  write(*,*) 'NOTE: wavefunction truncation begins with ',
c  .         'a(',j,')'
    do i1 = j+1,maxj
      asize(i1) = asize(i1-1) - 3
      if (asize(i1).lt.smax) then
c        write(*,*) 'WARNING: incorrect energy coeffs will'
c        write(*,*) 'appear beginning with E(',(i1+1)/2,')'
        maxj = 2*((i1-1)/2)
      endif
    end do
 endif

 do n = 1, maxj
    do i1 = 1,asize(n)
       do i2 = 1,asize(n)
          A(n,i1,i2) = 0.
       end do
    end do
 end do

 savewf = 0

 write(13,*)  state(1)-1,' ', state(2)-1
 write(13,*)  B
 write(13,*) 'pmin = ',0, '  pmax =',maxj/2
 write(13,*)
 write(13,*) 'Energy coefficients...'
 write(13,*) '---------- '
 write(13,40) energy(-1)
 write(13,40) energy(0)

 evenE = .FALSE.

C   ********************
C   **** MAIN LOOP ****
C   ********************

 do 900 n = 0, maxj-1

C Compute H*A terms from A(n) to A(n+1), A(n+2), ...

    CALL compute_H_A(n,maxj+2)

C Extract energy coefficients on every other iteration

    if(evenE) energy((n+1)/2)=-A(n+1,state(1),state(2))

C Final corrections to wavefunction tensor

    do j = 1,(n+1)/2
```

```
        i = n+1-2*j
        do i1 = 1, imin(asize(i),asize(n+1))
           do i2 = 1, imin(asize(i),asize(n+1))
              if (A(i,i1,i2).ne.0.q0) A(n+1,i1,i2) =
     .            A(n+1,i1,i2) + A(i,i1,i2) * energy(j)
           end do
        end do
     end do

     do i1 = 1,asize(n+1)
       do i2 = 1,asize(n+1)
         if (A(n+1,i1,i2).ne.0.q0) then
           temp=omega(1)*(i1-state(1))+omega(2)*(i2-state(2))
           if (temp.eq.0.q0) temp = 1.q0
           A(n+1,i1,i2) = A(n+1,i1,i2) / temp
           if (savewf) write(10+n+1,*) i1,i2,A(n+1,i1,i2)
         endif
         T1(i1,i2) = A(n+1,i1,i2)
       end do
     end do

     if (evenE) then
        call itime(iarr)
        write(13,40) energy((n+1)/2)
     endif

     evenE = .not.evenE

900  continue
   write(13,*)
   write(13,50)  omega(1)
   write(13,60)  omega(2)
   write(13,70)  omega(1)/omega(2)
   write(13,80)  omega(2)/omega(1)
   write(13,90)  rho

200  end do

  20  format(i2,':',i2,':',i2)
  30  format(7x,d41.33)
  40  format(7x,d41.33)
  50  format(9x, 'w_1 = ', f)
  60  format(9x, 'w_2 = ', f)
  70  format(5x, 'w_1/w_2 = ', f)
  80  format(5x, 'w_2/w_1 = ', f)
  90  format(5x, 'rho = ', f)
 142  format(2x,i2,2x,e,3x,i2,':',i2,':',i2)
 955  format(2i5,e)

  close(unit=1)
  close(unit=13)

  end
```

Header file: COMMON.H

```
C----- constants (max order in sqrt(1/D)
c----- and array dimension (LENxLEN))
      integer SIZE, LEN
C 20th order, up to 5 quanta of excitation
C      data SIZE, LEN /40,66/
C 25th order, up to 4 (?) quanta
c     data SIZE, LEN /50,80/
C 30th order, up to 5 quanta of excitation
       data SIZE, LEN /60,96/

C----- wavefunction tensors and temporary storage
C               A(0:SIZE,LEN,LEN)
C 20th order
C      REAL*16 A(0:40,66,66), T1(66,66)
C      INTEGER asize(0:40)
C 25th order
c     REAL*16 A(0:50,80,80), T1(80,80)
c     INTEGER asize(0:50)
C 30th order
       REAL*16 A(0:60,96,96), T1(96,96)
       INTEGER asize(0:60)

C----- potential expansion coefficients
C----- and associated pointers
C  For order k in 1/D, U1 should be allocated
C  with k(k+4) elements.
C 20th order
C      REAL*16 U1(480), U2(40), U3(2:40), energy(-1:20)
C      INTEGER ptr(40)
C 25th order
c     REAL*16 U1(725), U2(50), U3(2:50), energy(-1:25)
c     INTEGER ptr(50)
C 30th order
       REAL*16 U1(1020), U2(60), U3(2:60), energy(-1:30)
       INTEGER ptr(60)
```

Subroutine: SETUP

```
 SUBROUTINE SETUP(maxj,state,omega,B,rho,Breal)
 IMPLICIT NONE

 include 'qcommon.h'

c REAL*16 bnom(0:79,0:79),twofact(0:79),rhofact(0:79)
c REAL*16 bnomhalf(0:79)

 REAL*16 bnom(0:95,0:95),twofact(0:95),rhofact(0:95)
 REAL*16 bnomhalf(0:95)
```

```
 REAL*16 ZERO, ONE, tol
 DATA ZERO, ONE, tol /0.q0, 1.q0, 1.q-26/

 INTEGER i,j,l, state(2), n(2), r, maxj, ptr, B
 REAL*16 rho, drho, func, prefact, rhoinv, omega(2), V0
 REAL*16 fact0j, fact0l, ominv, omfact, Breal
c
 COMMON /ARRAYS/ U1,U2,U3,energy,ptr,T1,bnom,
1      twofact,rhofact,bnomhalf
 COMMON /WVF/ A, asize

C  Input various parameters
 open(unit=1,file='~/thesis/CoeffBlist',
1    form='formatted',status='old')
 read(1,*) B,maxj
 write(*,*) 'a'


 Breal = B*1000.q0
c I am unsure whether the following is correct.
 n(1) = state(1)-1
 n(2) = state(2)-1
 maxj = maxj*2

C Find minimum of the effective potential
c I commented out the rootseeking for and used Mathematica
 rho = 0.5q0
 drho = rho
 do while (qabs(drho/rho).gt.tol)
    func = Breal*Breal*rho**4 + 4.q0*rho - ONE
    drho = -func / (4.q0 * rho**3 * Breal*Breal + 4.q0)
    rho = rho + drho
    write(*,*) rho
 enddo
c write(*,*) 'rho(minimum)=?'
c read(*,*) rho

C Set up powers of 2 and rho:

 twofact(0) = ONE
 rhofact(0) = ONE
 rhoinv = ONE / rho
c Changed upper limit of do limit from maxj+2 to 50
 do i = 1,maxj+2
    twofact(i) = 2.q0 * twofact(i-1)
    rhofact(i) = rhoinv * rhofact(i-1)
 enddo
 rhofact(maxj+3) = rhoinv * rhofact(maxj+2)
c To print rhofact()
c   do i = 1, maxj+2
c   write(*,*) rhofact(4)
c enddo
```

```
C Evaluate analytic expressions

 energy(-1)=(rhofact(2)+Breal*Breal*rho*rho)/8.q0-rhofact(1)
 write(*,*) 'rhofact(2) = ', rhofact(2)
 write(*,*) 'Breal = ', Breal
 write(*,*) 'rho = ', rho
 write(*,*) 'rhofact(1)=', rhofact(1)
 write(*,*) 'energy(-1)=',  Breal*Breal
 omega(1)=qsqrt(0.75q0*rhofact(4)
.    -2.q0*rhofact(3)+Breal*Breal/4.q0)
 omega(2)=qsqrt(rhofact(3))
 V0 = - rhofact(2) * 0.5q0
 energy(0)=V0+(n(1)+0.5q0)*omega(1)+(n(2)+0.5q0)*omega(2)

C Set up arrays of binomial coefficients

 do j = 0,maxj+2
    bnom(j,0) = ONE
    do i = 1, j/2
       bnom(j,i) = bnom(j,i-1) * (j+ONE-i) / (ONE*i)
    enddo
    do i = 0, j/2
       bnom(j,j-i) = bnom(j,i)
    enddo
 enddo

 bnomhalf(0) = ONE
 do j = 1, maxj+2
    bnomhalf(j) = bnomhalf(j-1) * (0.5q0 - j) / (ONE*j)
 enddo


C Potential expansion coefficients

 ptr(1) = 1
 do j = 2,maxj
    ptr(j) = ptr(j-1) + (j+3)/2
 end do
 prefact = -rhofact(2) / twofact(3)

 do j = 3, maxj+2

  do l = 0, j/2
     U1(ptr(j-2)+l) = ZERO
     do r = l, j/2
       U1(ptr(j-2)+l) = U1(ptr(j-2)+l) - bnom(j-r,r)*
.       bnom(r,l)*twofact(j-2*r)*rhofact(j+1)*bnomhalf(j-r)
     enddo
  enddo

    U1(ptr(j-2))=U1(ptr(j-2))+prefact*rhofact(j)*(j+ONE)
    U2(j-2)=-4.q0*prefact*rhofact(j-2)*(j-ONE)
    if (j.ge.4) U3(j-2)=3.q0*prefact*rhofact(j-4)*(j-3.q0)
    prefact = -prefact
```

```
 enddo

C Multiply by sqrt(1/2*omega) factors
C which appear in the x matrices

 ominv = qsqrt(ONE / (2.q0*omega(1)))
 omfact = omega(1) / omega(2)
 fact0j = ominv / (2.q0*omega(1))

 do j = 3, maxj+2
    fact0l = fact0j
    do l = 0,j/2
       U1(ptr(j-2)+l) = fact0l*U1(ptr(j-2)+l)
       fact0l = fact0l * omfact
    enddo
    fact0j = fact0j*ominv
 enddo

 U2(1) = U2(1) * ominv
 fact0l = ONE / (2.q0*omega(1))
 fact0j = ONE
 do j = 2, maxj
    U2(j) = fact0j*fact0l*U2(j)
    U3(j) = fact0j*U3(j)
    fact0j = fact0j * ominv
 enddo

 end
```

Subroutine: COMPUTE

```
C This subroutine takes the tensor T1, which is initialized
C with a copy of the tensor a(n) prior to the subroutine
C call, and computes all product tensors of the form
C
C         /  m1       m2 \
C        |  x    *   x    | a
C         \  1         2 /   n
C
C which contribute to a(n+1), a(n+2), ..., a(maxj).  To
C follow the notation in the implementation section of Dunn
C et al., twok is sent the value maxj+2.  (The program
C counts the order in 1/D beginning with the E(-1) infinite-
C dimensional term, but this is usually referred to as the
C zeroth term, Bender et al. being one exception to this.
C Therefore, the slight discrepency in counting terms.)
C
 SUBROUTINE compute_H_A(n,twok)
 IMPLICIT NONE

 include 'qcommon.h'

C 20th order
```

```
C   REAL*16 T2(66,66), T3(66), sqt(66), R2(66)
C 25th order
c  REAL*16 T2(80,80), T3(80), sqt(80), R2(80)
C 30th order
 REAL*16 T2(96,96), T3(96), sqt(96), R2(96)

C----- local variables
 INTEGER m1,m2,i1,i2,m,axis1,axis2,lim1,lim2,n,twok,imin

 COMMON /ARRAYS/ U1,U2,U3,energy,ptr,T1,T2,T3,sqt,R2
 COMMON /WVF/ A, asize

C
C NOTE: m2 loop is outermost to minimize
C the number of (more costly)
C          /     2 \
C         | I * x   | operations.
C          \     2 /
C
 axis2 = asize(n)
 do m2 = 0, twok-n, 2
C T2 = T1
    axis1 = asize(n)
    do i1 = 1,axis1
       do i2 = 1,axis2
          T2(i1,i2) = T1(i1,i2)
       end do
    end do

    do m1 = 0, twok-n-m2
       m = m1+m2+n

       if (m2.eq.0) then
          if (m.le.(twok-4)) then
C
C                                        /  m1      \
C a     =  a     -  v          |  x    * I   | a
C  m+2      m+2      m1+2,m1   \  1       /   n
C
            lim1 = imin(axis1,asize(m+2))
            lim2 = imin(axis2,asize(m+2))
            do i1 = 1,lim1
               do i2 = 1,lim2
                  if (T2(i1,i2).ne.0.q0) A(m+2,i1,i2) =
.                    A(m+2,i1,i2) - U3(m1+2)*T2(i1,i2)
               end do
            end do
         endif
               if ((m1.ne.0).and.(m.le.(twok-2))) then
C
C                          /  m1      \
C a   =  a   -  v       |  x    * I   | a
C  m      m      m1,m1   \  1       /   n
C
```

```
               lim1 = imin(axis1,asize(m))
               lim2 = imin(axis2,asize(m))
               do i1 = 1,lim1
                  do i2 = 1,lim2
                     if (T2(i1,i2).ne.0.q0) A(m,i1,i2) =
.                         A(m,i1,i2) - U2(m1)*T2(i1,i2)
                  end do
               end do
            endif
         endif

         if ((m1+m2).ge.3) then
C
C                    m2/2                      /  m1    m2 \
C a      =  a     -     v                     |  x   * x    | a
C  m-2       m-2          m1+m2-2,m1+m2       \  1     2  /   n
C
            lim1 = imin(axis1,asize(m-2))
            lim2 = imin(axis2,asize(m-2))
            do i1 = 1,lim1
              do i2 = 1,lim2
               if (T2(i1,i2).ne.0.q0) A(m-2,i1,i2) =
.                A(m-2,i1,i2)-U1(ptr(m1+m2-2)+m2/2)*T2(i1,i2)
              end do
            end do
         endif

C         /     \
C T   = | x * I | T
C  2    \ 1   /   2
         do i2 = 1,axis2
            do i1 = 2,axis1
               T3(i1-1) = sqt(i1-1)*T2(i1,i2)
            end do
            T3(axis1) = 0.
            if (axis1.lt.LEN) T2(axis1+1,i2) = sqt(axis1)*
.                T2(axis1,i2)
            do i1 = axis1,2,-1
               T2(i1,i2) = T3(i1) + sqt(i1-1)*T2(i1-1,i2)
            end do
            T2(1,i2) = T3(1)
         end do
         axis1 = axis1 + 1
         if (axis1.gt.LEN) axis1 = LEN
      end do

C         /     2 \
C T   = | I * x   | T
C  1    \     2 /   1
      do i1 = 1,axis1
         do i2 = 3,axis2
            T3(i2-2) = R2(i2-2)*T1(i1,i2)
         end do
         if (axis2.gt.1) T3(axis2-1) = 0.
```

```
      do i2 = axis2,imin(axis2+2,LEN)
         T3(i2) = 0.
      end do
      do i2 = 1,imin(axis2,LEN-2)
         T3(i2+2) = T3(i2+2) + R2(i2)*T1(i1,i2)
      end do
      do i2 = 1,axis2
         T1(i1,i2) = (2*i2-1)*T1(i1,i2) + T3(i2)
      end do
      if (axis2.lt.LEN) T1(i1,axis2+1) = T3(axis2+1)
      if ((axis2+1).lt.LEN) T1(i1,axis2+2) = T3(axis2+2)
   end do
   axis2 = axis2 + 2
   if (axis2.gt.LEN) axis2 = LEN
end do
return
end

function imin(i,j)
integer imin,i,j
imin = i
if (j.lt.i) imin = j
return
end
```

Make file

```
SOURCES= H-mag.f setup.f comp_H_A.f
#PROGRAM= H-mag

#quadruple precision version
SOURCES= qH-mag.f qsetup.f qcomp_H_A.f
PROGRAM= qH-mag

OBJECTS= $(SOURCES:.f=.o)

# -g allows dbx debugging,
# -C produces code checking array bounds
#OPTIONS = -g -C
# To optimize debugged version of the code
OPTIONS= -O3

all debug profile: $(PROGRAM)

$(PROGRAM): $(OBJECTS)
   f77 $(OPTIONS) -o $@ $(OBJECTS)

%.o: %.f
   f77 $(OPTIONS) -c $<

clean:
   rm -f $(PROGRAM) $(OBJECTS) $(LINTFILES) $(SOURCECODE)
```